



UNIVERSIDADE ESTADUAL DE CAMPINAS
IFGW – Instituto de Física “Gleb Wataghin”

PAULO EDUARDO MENEGASSO FILHO

**ACOPLAMENTO HIPERFINO COMO SONDA DE HIBRIDIZAÇÃO EM
SISTEMAS DE ELÉTRONS FORTEMENTE CORRELACIONADOS**

**HYPERFINE COUPLING INTERACTION AS A PROBE OF SCES
HYBRIDIZATION**

CAMPINAS

2021

PAULO EDUARDO MENEGASSO FILHO

**HYPERFINE COUPLING INTERACTION AS A PROBE OF
SCES HYBRIDIZATION**

**ACOPLAMENTO HIPERFINO COMO SONDA DE
HIBRIDIZAÇÃO EM SISTEMAS DE ELÉTRONS
FORTEMENTE CORRELACIONADOS**

Tese apresentada ao Instituto de Física “Gleb Wataghin” da Universidade Estadual de Campinas como parte dos requisitos exigidos para a obtenção do título de Doutor em Ciências, na área de Física.

Thesis presented to the Gleb Wataghin Physics Institute of the University of Campinas in partial fulfillment of the requirements for the degree of Doctor in Science, the area of Physics.

Orientador: Ricardo Rodrigues Urbano

Este trabalho corresponde à versão final da tese defendida pelo aluno Paulo Eduardo Menegasso Filho e orientada pelo Prof. Dr. Ricardo Rodrigues Urbano.

Campinas

2021

Ficha catalográfica
Universidade Estadual de Campinas
Biblioteca do Instituto de Física Gleb Wataghin
Lucimeire de Oliveira Silva da Rocha - CRB 8/9174

M524h Menegasso Filho, Paulo Eduardo, 1990-
Hyperfine coupling interaction as a probe of SCES hybridization / Paulo Eduardo Menegasso Filho. – Campinas, SP : [s.n.], 2021.

Orientador: Ricardo Rodrigues Urbano.
Tese (doutorado) – Universidade Estadual de Campinas, Instituto de Física Gleb Wataghin.

1. Férmions pesados. 2. Ressonância magnética. 3. Matéria condensada.
I. Urbano, Ricardo Rodrigues, 1974-. II. Universidade Estadual de Campinas. Instituto de Física Gleb Wataghin. III. Título.

Informações para Biblioteca Digital

Título em outro idioma: Acoplamento hiperfino como sonda de hibridização em sistemas de elétrons fortemente correlacionados

Palavras-chave em inglês:

Heavy fermions

Magnetic resonance

Condensed matter

Área de concentração: Física

Titulação: Doutor em Ciências

Banca examinadora:

Ricardo Rodrigues Urbano [Orientador]

Ricardo Luís Doretto

Jonathas de Paula Siqueira

José Gerivaldo dos Santos Duque

Nelson Orlando Moreno Salazar

Data de defesa: 09-06-2021

Programa de Pós-Graduação: Física

Identificação e informações acadêmicas do(a) aluno(a)

- ORCID do autor: <https://orcid.org/0000-0002-6501-7140>

- Currículo Lattes do autor: <http://lattes.cnpq.br/6350667377496252>

MEMBROS DA COMISSÃO JULGADORA DA TESE DE DOUTORADO DE **PAULO EDUARDO MENEGASSO FILHO – RA 164192** APRESENTADA E APROVADA AO INSTITUTO DE FÍSICA “GLEB WATAGHIN”, DA UNIVERSIDADE ESTADUAL DE CAMPINAS, EM 09 / 06 / 2021.

COMISSÃO JULGADORA:

- Prof. Dr. Ricardo Rodrigues Urbano – Orientador – DEQ/IFGW/UNICAMP
- Prof. Dr. Ricardo Luis Doretto – DFMC/IFGW/UNICAMP
- Prof. Dr. Jonathas de Paula Siqueira – DEQ/IFGW/UNICAMP
- Prof. Dr. José Gerivaldo dos Santos Duque – DF/UFES
- Prof. Dr. Nelson Orlando Moreno Salazar – DF/UFES

OBS.: Ata da defesa com as respectivas assinaturas dos membros encontra-se no SIGA/Sistema de Fluxo de Dissertação/Tese e na Secretaria do Programa da Unidade.

This work is dedicated to all families that lost loved ones during the Covid-19 pandemic

Acknowledgment

Overall others, I thank God for everything He has done for me, not only during this Ph.D. but also through all events in my life.

I also thank my advisor, Prof. Dr. Ricardo R. Urbano, for all his strong support during this work, which would not be possible without all his teachings and mentoring, both academic and for life. I also thank his great patience, which he had to use often with me, and enthusiasm in, not just Science, but all aspects of knowledge.

There are also other Professors, who have contributed enormously to this project and I have my best esteem. Among them, I would like to especially thank Professor Carlos Rettori, for all knowledge he shared with me, not only but mostly in ESR, crystalline electrical field, and solid-state physics in general; Professors Pascoal Pagliuso and Cris Adriano for all their teachings in sample growth, characterization, especially in heavy fermions compounds. Also, my many thanks to Professor Thiago Branquinho, who taught me how to carry out high-resolution NMR experiments and welcomed me a bunch of times to his lab at UFABC to perform experiments on nanoparticles systems. I also thank professor Mariano de Souza, from Unesp-RC for fruitful discussions regarding Fabre-Bechgaard salts. Last but not least, I'd like to thank Professor Nicholas Curro, from UC-Davis, who has welcomed me to his NMR lab, where we carried out a lot of, in his own words, "exciting experiments".

I also would like to thank my fiancée, Tamires, for all emotional support (and, to be honest, some help with data organization as well). Hope we can finally get married now after completing my Ph.D. degree... love you.

Thanks to my parents, Eliana and Paulo, and also to my little sister, Camila, for all their unconditional help, not only during this period but through my entire life.

To my childhood friends Danilo and Henrique. For all the great times we have shared since elementary school.

To my extended list of friends through all groups I participated during these last four years, that I'm going to order chronologically: Guilherme, Davi, Isadora, Lina, Eduardo, Ali, and Michael, from our magnetic resonance group within GPOMS; Camilo, Jean, Kevin, Mario, Matheus

(Goiba), Denise, Gabriel, Rodolfo, Rogério, Henrique, Carlos, André, Danilo, and Kousik, from GPOMS; Zeppelin, Tanat, Victoria, Louis, Zewei, Sarah and Igor from UC-Davis.

Also, my thanks to all personel at Unicamp who have provided us a lot of quality life. I especially thank Marcia, who helped a lot with my paperwork obligations with FAPESP, and Isabel, that always cleans the mess we make in the labs.

Finally, I would like to thank all the teachers and professors I have interacted with in my life. It could try to list all of them here but I would rather not since I'm afraid of being unfair and forget someone. Unfortunately, education is not a priority in Brazilian society and they are neither rewarded nor recognized as they should and deserve. From my prospects, however, I like to emphasize that achieving such a goal in my academic career would not be possible without the aid, support, teachings, and goodwill of all these people.

This study was financed in part by the Coordenação de Aperfeiçoamento de Pessoal de Nível Superior - Brasil (CAPES) - Finance Code 001. Grant number 1584096/2016.

Finally, I acknowledge Fundação de Amparo à Pesquisa do Estado de São Paulo - FAPESP (grants number 2016/14436-3 and 2012/05903-6) for the main financial support of this project.

Resumo

Sistemas com fenômenos eletrônicos coletivos, como Magnetismo e Supercondutividade, são atualmente um tema de alto interesse dentro da Física da Matéria Condensada. Dentre estes sistemas, nesta tese, darei ênfase aos compostos de férmions pesados da família $(\text{Ce,Nd})M\text{In}_5$ ($M=\text{Ir}$, Rh and Co). Além de supercondutividade não-convencional, os férmions pesados são sistemas modelos na exploração de fases ordenadas magneticamente e do efeito Kondo. Ainda, existem neles fortes efeitos de campo elétrico cristalino, que devem ser levados em consideração para compreender o estado fundamental desses sistemas. Membros da família 115 são convenientes para investigação dessas interações, uma vez que permitem substituição química em sítios distintos. Nossa investigação principal levou à resultados que mostrar que o campo elétrico cristalina tem um papel fundamental nos orbitais eletrônicos f do Ce. Propomos uma lei de escala que relaciona o acoplamento hiperfino entre elétrons do Ce e núcleos de In com o parâmetro α da função de onda do estado fundamental de CEF, que se mostra verdadeira para substituição química, pressão hidrostática e campos magnéticos extremos na família $\text{Ce}M\text{In}_5$.

Estudos de ressonância magnética em outros compostos que resultaram em contribuições científicas também são brevemente mencionados.

Assim, nos sistemas descritos acima, experimentos de caracterização cristalográfica, magnética e termodinâmica proveram um forte suporte à investigações de Ressonância Magnética Nuclear, por meio de deslocamento em sítios específicos, Knight shift e dinâmica de spin (taxas de relaxação spin-spin e spin-rede), em função da temperatura, campo magnético, pressão química e anisotropia. Ainda, experimentos de Ressonância de Spin Eletrônico também foram realizados para complementar os resultados de NMR, corroborando com as conclusões e abrindo novas perspectivas para estudos futuros.

Abstract

Systems with collective phenomena of electrons, such as Magnetism and Superconductivity are currently of high interest within Condensed Matter Physics. Among the physical systems investigated in this Thesis, I highlight the heavy fermion compounds of $(\text{Ce,Nd})M\text{In}_5$ ($M=\text{Ir, Rh}$ and Co) family. Besides non-conventional superconductivity, the heavy fermions are model systems to exploration of magnetically ordered phases and the Kondo effect. On top of that, there are also the crystalline electric field (CEF) effects that must be taken into account to understand the ground state properties of these systems. Members of the 115s heavy fermions family are convenient since they allow chemical substitution at distinct sites.

Our main investigations leading to the result that CEF plays a crucial role on the Ce f -electron orbitals. We propose here a scaling rule that relates the hyperfine coupling between electrons of Ce and nuclei of In with the wavefunction parameter α of the CEF ground state, which holds true for chemical doping, hydrostatic pressure and extreme magnetic field in the $\text{Ce}M\text{In}_5$ family. NMR studies on other compounds that resulted in scientific contributions were also mentioned.

Thus, on the systems described above, crystallographic, magnetic and thermodynamic characterization experiments provided strong support to the systematic Nuclear Magnetic Resonance (NMR) investigation, by means of the site specific magnetic shift, Knight shift and spin dynamics (spin-spin and spin-lattice relaxation rates) as function of temperature, magnetic field, chemical pressure and anisotropy. Moreover, Electron Spin Resonance (ESR) experiments have been also carried out and the results were very important to complement the NMR results, corroborating with most conclusions and opening up new perspectives for future investigations.

List of Illustrations

1.1	Formation of the Hubbard bands as a function of $\frac{U}{t}$ value. This figure was extracted from [29] and W represents t in Eq. 1.2.5. Once the ratio $\frac{U}{t}$ increases, the Hubbard bands splits, as described in the main text.	29
1.2	Spin, orbital and total angular momentum for the Lanthanide series with 3+ valence. The red dots represent the calculated magnetic moment in terms of μ_B . A clear relation between \vec{J} and $\vec{\mu}$ is observed.	32
1.3	Behavior of inverse χ as a function of temperature for typical magnetic orderings.	34
1.4	Zeeman effect diagram for a) a simple case of an atom with nuclear spin $I = 1/2$ and b) a more complex case of an atom with nuclear spin $I = 9/2$	36
1.5	Graph of J as a function of ΔR in the RKKY interaction model. Note that J coupling changes as a function of the atomic distance. In other words, the AFM or FM interaction between magnetic impurities changes as a function of the distance between them.	37
1.6	a) CEF effects on 3d octahedral and tetrahedral symmetries with especial emphasis to Co^{3+} . Red circles represents electron with spin up while blue ones stands for electron with spin down. Note that CEF effects may change the effective spin S_{eff} depending on the symmetry. Since the effective spin can be measured through ESR experiments, it is a smoking gun experiment to determine the CEF state. b) CEF effects on the 4f rare-earth cerium, with the approximate gap values, extracted from [37].	41
1.7	Scheme of the direct (A) and transferred (B) hyperfine coupling on generic atoms	42
2.1	Representative of an absorption spectrum. Spins with a gap $h\nu_i$ between spin up and spin down states are expected on ν_i position in frequency. The intensity at higher energy is expected to be higher than at low energy.	45
2.2	Main parameters of a Lorentzian lineshape on a magnetic resonance spectra. The gaussian shape is shown in a dashed line employing comparison. ΔB represents the linewidth at half-height, B_{Res} is the resonance field. The line intensity is proportional to the integrated area and represents the spin susceptibility.	47
2.3	a) MR Spectrum of a given spin system. b) Effects of the hyperfine splitting over the electronic spin. In this case, the nucleus have the same probability to be aligned parallel or anti-parallel with the external field. c) Effects of the hyperfine coupling on the spectra when the up state is favoured. d) Hyperfine coupling effects when all nuclear spins are parallel to the external field.	49

LIST OF ILLUSTRATIONS

2.4 Energy levels of a $\frac{3}{2}$ nuclear spin. The EFG splits the levels $|\pm\frac{1}{2}\rangle$ and $|\pm\frac{3}{2}\rangle$, which gives rise to one absorption at ν . The Zeeman effect (under external magnetic field) further breaks the degeneracy between + and - levels, giving rise to more transitions. 52

2.5 a) Scheme of a closed-cycle cryostat. The probe must be in the most homogeneous magnetic field region, typically near the center of the magnet. The red and orange circles is zoomed into b), which is a photo of a probe used in the experiments. The top posses the leadings to the spectrometer, while the brass cap at the bottom end prevents the sample to accidentally fall inside the cryostat and also works as a Faraday's cage shielding. c) Stands for a picture of a copper coil. Although this is not the best example of a sample, due to the crossed turns, which induced inhomogenety in the magnetic field. 54

2.6 a) Voltage versus time signal collected from the NMR coils when measuring a given nucleus of interest. The signal are submitted to FFTs and then converted to the frequency domain. b) Sum of the three signals from a), which is typically the result observed in an NMR experiment. By submitting the signal to a FFT, the results in frequency domain are observed. Normally, the individual separation of each part of the molecule can be separated only by high-resolution NMR experiments. 56

2.7 a) Magnetization *versus* time curves for M_{xy} (red), which gives access to T_2 , and M_z (blue), which provides information associated with T_1 . b) Depicts the process of coherence loss. In the first sketch to the left, all spins are pointing at the same direction, thus the magnetization on the plane is maximum. As the system evolves in time, spins come across the coherence loss process and the transversal magnetization (M_{xy}) vanishes. This process is not independent from spin-lattice relaxation, which means that the modulus M is also reduced. The total magnetization is shown in c), reproduced from [42]. 61

2.8 Pulse sequences for different kind of NMR experiments. a) is the simplest one to obtain the Free Induction Decay (FID), which gives rise to the NMR spectra after a Fourier Transform. b) is the spin-echo (Hann-echo), which also results in the NMR spectra but with more time resolution for faster relaxation times, as described in the main text. c) is the inversion recovery sequence for T_1 and d) the saturation recovery, also for measuring T_1 . e) Depicts the sequence employed for the measurement of T_2 . The inset shows the z-axis longitudinal magnetization M_z *versus* time as a log scale for a T_1 measurement, as described in the main text. 62

2.9 Block diagram of the NMR experimental configuration, described with details in the main text. 65

2.10 Block diagram of the NMR detection system, described with details in the main text. 67

2.11 Panoramic view of the NMR laboratory at GPOMS - IFGW - Unicamp. 69

3.1 Kmetko-Smith diagram of $3d$ to $5f$ elements, reproduced from [56, 57]. Increased electronic localization favors magnetism, while electronic localization tends to favor superconductivity. In the bottom, examples of $3d$, $5f$ and $4f$ are shown, with the first possessing more delocalized electrons while the latter more localized ones. 72

3.2 Electrical resistivity of $Ce_xLa_{1-x}Cu_6$ as a function of temperature for several doping levels, extracted from [58]. The Ce-rich sample establishes a Kondo lattice and the magnetic atoms are not treated as an impurity, establishing the Kondo coherence, as described in the main text. As Ce gets diluted on the sample, the coherence regime breaks up and the magnetic impurity Kondo behavior is recovered. 74

LIST OF ILLUSTRATIONS

3.3 The Doniach phase diagram [60], showing the competition between Kondo and RKKY interactions, the former favoring superconductivity and the latter a magnetically ordered phase. Note that at a critical $JN(E)$ value, a Quantum Critical Point (QCP) emerges [64]. It is proposed in the literature that such a QCP would be also necessary for the superconducting phase in HFs [65]. It should be pointed out, however, that the Doniach phase diagram does not capture the CEF effects, but is still a good toy model to understand most physical properties of the heavy fermion materials. 75

3.4 Ce-115 unitary tetragonal cell. This is a planar compound alternating between Ce-In, pure In, and M planes, as depicted. Note that there are two possible indium sites: In(1), in the Ce-In plane, which is common in other series of Ce-based heavy fermions as $CeIn_3$ and Ce_2MIn_8 , and In(2), which is outside the Ce-In plane. 76

3.5 Phase diagram of $CeMIn_5$ family, extracted from [66]. Note that the $\frac{a}{c}$ ratio scales well with the superconducting transition temperature T_C outside the magnetic phase, where this scaling breaks down. 77

3.6 Scaling between α and the transition temperature of $CeMIn_5$ compounds. Note the orbital anisotropy on the bottom of the figure, which means that oblate orbitals ($M = Co$ and Ir) tend to favor superconductivity, while stronger in-plane interactions ($M = Rh$) favors antiferromagnetism. 78

3.7 Moment direction as a function of B_{20} CEF parameter, extracted from [72]. The discrepancy between Ce and Nd compounds is huge for small values of B_{20} . Typical B_{20} parameters for $CeMIn_5$ are within the red range as shown. 78

3.8 a) Illustration of the flux method, used to grow $CeMIn_5$ samples. b) The temperature ramps employed. Surprisingly, larger samples have been obtained through the faster cooling ramp (in blue), at least for the system with Nd doping. c) $CeRhIn_5$ sample grown through the flux method. It has been cut to the typical size of $2x1x0.5\text{ mm}^3$ and polished to remove the residual indium flux on the surface. 80

3.10 Bulk magnetization along c -axis of $CeRh_{1-x}Ir_xIn_5$. The solid lines are mean-field CEF fits, from where the α parameter can be extracted. 82

3.9 X-ray diffraction patterns for $CeRh_{1-x}Ir_xIn_5$ samples. Red arrows indicate In flux lines. Literature data from [76] for means of comparison. 83

3.11 ^{115}In NMR spectra of $CeRh_{1-x}Ir_xIn_5$ for distinct doping levels at $T = 5\text{ K}$ and with $B = 11.7\text{ T}$. The red arrows indicate the position for the $-1/2$ to $1/2$ spin transition for In(1) site. Multiple lines can be observed due to a small angular deviation from $H_0//c$. Simulations of the spectra reveal that such deviation is not higher than 6 degrees, in the worst scenario, which would not be enough to change the Knight shift expressively. The orange dashed line indicates the position of the main resonance for pure In. The copper signal near 132 MHz arises from the RF coil. 86

3.12 ^{115}In NMR spectra of $CeRh_{1-x}Ir_xIn_5$ for distinct doping levels at several temperatures. The blue signal stands for In(1), while the red ones represent In(2). For $x = 0.8$ and 0.25 , a satellite In(1) transition was measured instead of the central line to overcome the overlap with the In(2) signal. This has been taken into account for the calculation of the Knight shift. The obtained ν_Q of about 6 MHz, is the value expected for these compounds [78]. 88

LIST OF ILLUSTRATIONS

3.13 Knight shift K_1 (circle) for In(1) and K_2 (square) for In(2) as a function of temperature for $\text{CeRh}_{1-x}\text{Ir}_x\text{In}_5$. The distinct temperature dependencies is a confirmation that the magnetic field is indeed aligned with c -axis. Results for pure CeRhIn_5 are consistent with those already reported [79]. Results for CeIrIn_5 are extracted from [79]. The dashed lines stands for the magnetization measurements, with the color matching the x values. 89

3.14 In(1) Knight shift versus magnetic susceptibility for $\text{CeRh}_{1-x}\text{Ir}_x\text{In}_5$ and CeCoIn_5 . The linear fit, represented as the lines, at high temperature range allows to extract the hyperfine coupling parameter B_1 , which is proportional to the angular coefficient. Results for pure CeMIn_5 are in agreement with the literature [79]. 90

3.15 In (1) Hyperfine coupling B_1 as a function of the α coefficient (taken from [66]). A linear scaling was observed throughout all members of the CeMIn_5 family. The red solid line is a guide to the eyes. 91

3.16 Hyperfine coupling of In(1) and In(2) as a function of α coefficient of the ground state wave function. A linear scaling was observed for both In sites. On the right axis, the ratio between the hyperfine coupling specific to each In site is shown. 93

3.17 ^{115}In NMR spectra of a) $\text{Ce}_{0.97}\text{Nd}_{0.03}\text{IrIn}_5$ at 4.2 K. The insets show satellite lines of In(1). b) $\text{Ce}_{0.97}\text{Nd}_{0.03}\text{IrIn}_5$ spectra for distinct temperatures up to 55 K, with their respective Lorentzian fit. The left resonance refers to a metallic In transition and is not relevant for our analysis. The orange line is a guide to the eyes for better visualization of the line displacement with the temperature. c) $\text{Ce}_{0.97}\text{Nd}_{0.03}\text{RhIn}_5$ spectra for distinct temperatures up to 35 K, with their respective fit. Below 22.5 K, both In sites were observed (In(1) in green and In(2) in blue). Note, once again, the lines to the left of the spectra comes from metallic In. d) shows another representation of the structure to emphasize the site differentiation for In. 95

3.18 Comparison between Knight shift and magnetic susceptibility for (a) $\text{Ce}_{0.97}\text{Nd}_{0.03}\text{IrIn}_5$ and (b) $\text{Ce}_{0.97}\text{Nd}_{0.03}\text{RhIn}_5$. A comparison between pure (data provided by Professor Nicholas Curro) and Nd-doped systems is emphasized in (a). The notorious divergence between K and χ shifts to higher temperatures with Nd doping. The very same happens to $M = \text{Rh}$ compound. 96

3.19 Knight shift as a function of magnetic susceptibility with their linear fit in the paramagnetic phase for (a) $\text{Ce}_{0.97}\text{Nd}_{0.03}\text{IrIn}_5$ and (b) $\text{Ce}_{0.97}\text{Nd}_{0.03}\text{RhIn}_5$. The hyperfine coupling is reduced with the substitution of Ce for Nd, as discussed in the main text. The fitting “from paper” in (a) is found at [79]. 97

3.20 Hyperfine coupling versus α^2 with Nd doped data included. For $M = \text{Rh}$, the α^2 value is 0.14 and for $M = \text{Ir}$ it is 0.38 Also one can sketch the Ce orbitals by possessing this α values and, in fact, Nd doped orbitals are more out-of-plane. 98

3.21 Hyperfine coupling versus α^2 with CeRhIn_5 NMR data under pressure (extracted from [82]). One can observe that the scaling holds true. Red line stands for the linear fit, while the blue one assumes a second order term. In terms of the least square method, the linear approximation is quite better. 99

3.22 Scaling between the squared ground state wave function constant α and the external pressure for CeRhIn_5 , assuming a 2^{nd} order relation between them. 100

3.23 Hyperfine coupling versus α^2 for under pressure CeRhIn_5 or high magnetic field data included (extracted from [82] and [78]). The resultant Ce orbitals for α values addressing the pure compounds are also presented. The redish highlighted stripe is guide to the eyes. 101

LIST OF ILLUSTRATIONS

3.24 Phase diagram of $CeMIn_5$ family, modified from [68], with the Ce's orbitals representation from the data obtained in this thesis and related reports. 102

4.1 Magnetic susceptibility (panel a) and specific heat (panel b) versus temperature for $GdIn_3$ bulk and nanowire, investigated in our group, according to [83]. The results show an impressive reduction on T_N , indicating that physical confinement induces severe changes on the material's physical properties. 107

4.2 a) Energy levels of Er^{3+} , Yb^{3+} and Tm^{3+} electron system. The intermediate levels are metastable and can be reached by the absorption of a low-energy photon. However, if the electron absorbs another low-energy photon, it is promoted to a higher energy level. Then, the electron tends to decay, releasing all absorbed energy at once, leading to a higher energy emitted phonon. Figure depicted after [85]. b) Schematic (simplified) view of the upconversion process. 108

B.1 Photograph of Zavoisky's experimental setup for the first ESR experiments ever performed. Figure taken from [91]. 125

B.2 Schematic function of the microwave bridge. (1) is the MW source; (2) and (3) are the power attenuators, (4) is the circulator, (5) is the resonance cavity (which stays out of the bridge), (6) is the electromagnet (actually it is not a part of the microwave bridge, but it is in the figure for reference), (7) is the lock-in amplifier of the reference arm (8) and (9) is the receptor diode. A detailed description of each component is presented in the main text. 126

B.3 Photograph of the ESR setup used at GPOMS - IFGW - Unicamp for the experiments described in this thesis. 129

D.1 a) Scheme of the magnetic fields \vec{H}_0 and \vec{H}_1 inside the magnet coils. b) Rotating frame. Note that $\hat{e}_z = \hat{e}'_z$, but \hat{e}'_x and \hat{e}'_y rotates around the z axis. 136

D.2 Stages $|\Psi_1\rangle$, $|\Psi_2\rangle$ and $|\Psi_3\rangle$ represented accordingly to the pulse sequence. Time evolution of the state is given by Schrödinger's equation. 140

E.1 Illustration of the four leads method to measure resistivity. This is the conventional method to ensure no wiring contribution to low-resistivity samples. 142

I.1 ^{19}F MAS spectra for 7 nm rare-earth doped $NaYF_4$ at rotating frequency of 15 kHz. The asterisks are spinning sidebands and the sharp resonance line near -140 ppm is from residual NaF on the NPs surface, which can be eliminated by washing the NPs. 173

I.2 a) In-plane relative magnetization for ^{19}F as a function of time for RE doped $NaYF_4$ for a series of RE. The fitting to obtaining the spin-spin relaxation times are shown. b) Out of plane relative magnetization for ^{19}F as a function of time for RE doped $NaYF_4$. The fitting to obtaining the spin-lattice relaxation times are shown. 174

List of Tables

3.1	In(1) Knight shift (K_1), In(2) Knight shift(K_2), squared Γ_7 coefficient (α^2) and hyperfine couplings for In(1) (B_1) and In(2) (B_2) for the Ce115 family. The α values were extracted from [66] and agrees very well to the values obtained by our magnetization fittings.	85
I.1	Spin-lattice and spin-spin relaxation times for RE doped nanoparticles, for both ^{19}F and ^{23}Na sites.	175

Abbreviations List

BCS Bardeen, Cooper, Schrieffer theory for superconductivity.

RVB Resonant Valence Bond theory.

QCP Quantum Critical Point.

CEF Crystalline Electrical Field.

SCES Strongly Correlated Electron Systems.

NMR Nuclear Magnetic Resonance.

EFG Electric Field Gradient.

RKKY Ruderman-Kittel-Kasuya-Yoshida theory.

FM Ferromagnetism or Ferromagnetic.

AFM Antiferromagnetism or Antiferromagnetic.

ESR Electron Spin Resonance.

MR Magnetic Resonance.

FWHM Full Width at Half Maximum.

NQR Nuclear Quadrupolar Resonance.

RF Radio Frequency.

FFT Fast Fourier Transform.

FID Free Induction Decay.

FT Fourier Transform.

MAS-NMR Magic Angle Spinning Nuclear Magnetic Resonance.

XAS X-Ray Absorption Spectroscopy.

PPMS Physical Properties Measurement System.

MPMS Magnetic properties measurement system.

VSM Vibrating Sample Magnetometer.

NP Nanoparticles or Nanoparticle.

Contents

Dedicatória	5
Acknowledgment	6
General Introduction	21
1 Theoretical Aspects	26
1.1 Actually, What is a Heavy Fermion?	27
1.2 Electronic Correlation: The Free Electron Model and Beyond	29
1.3 Origin of Atomic Moments	31
1.4 Nuclear Magnetism	35
1.5 RKKY Interaction	36
1.6 The Kondo Effect	38
1.7 Crystal Electric Field (CEF)	39
1.8 The Hyperfine Coupling	42
2 Magnetic Resonance	44
2.1 Introduction and Generalities	44
2.1.1 Dipolar and Quadrupolar Interactions	50
2.2 NMR 101	52
2.2.1 Chemical and Knight Shift	58
2.2.2 Controlling the spin ensemble with pulses	59
2.2.3 Radiofrequency Pulse Sequences	62
2.2.4 Fundamentals of NMR Experiments	65
2.2.5 The Tank Circuit	66
3 The Heavy Fermions of Ce-115 Family	71
3.1 Motivation and Objectives	71
3.2 State of the Art	76
3.3 Methodology, Results and Discussion	79
3.3.1 Sample Growth	79
3.3.2 Sample Characterization: XRD and Magnetic Susceptibility	82
3.3.3 Intermetallic Doped Compounds	84
3.3.4 Nd Doped Compounds	92

CONTENTS

3.3.5	Addressing the CeRhIn ₅ Under Extreme Conditions in the Scaling Rule	97
3.4	Conclusion and Perspectives	102
4	Investigations in Other Systems of Interest	105
4.1	Insulating Nanoparticles	105
4.1.1	Introduction and Motivation	106
4.2	Cobalt-Based Ludwigites	110
4.3	Systems Investigated in Collaborations	111
4.3.1	YCd ₆ Quasi-Periodic Crystals	111
4.3.2	Single Crystals of MgB ₂	111
4.3.3	Er doped Au Nanoparticles	111
4.3.4	SmB ₆ Topological Insulators	112
4.3.5	La ₃ Ir ₄ Sn ₁₃ Heavy Fermions	112
4.3.6	TmVO ₄ Oxides	113
4.3.7	Fabre Bechgaard Organic Conductors	113
5	General Conclusions and Forewords	114
	References	117
A	Sandwich Ph. D. at UC - Davis	123
B	Fundamental of continuous wave ESR experiments	125
B.1	The ESR Microwave Bridge	126
B.2	The ESR Resonant Cavity	128
B.3	Magnetic Field	128
B.4	Temperature Control	130
C	Microwave and Radiofrequency Generators	131
C.1	Microwave Generation	131
C.2	Radiofrequency Generation	133
D	NMR Hamiltonians and pulse sequences	134
E	Complementary Experimental Techniques	141
E.1	X-ray Diffraction	141
E.2	Electrical Resistivity	142
E.3	Specific Heat	143
E.4	Magnetic Measurements	143
F	Mathematica Code for Orbital Sketching	145
G	Scientific resultant from the investigations on this thesis	148
H	Scientific Work on Heavy Fermions	150

CONTENTS

I Detailed study on Insulating Nanoparticles	159
I.1 Rare-earth doping	173
J Scientific Work on SmB₆	176
K Scientific Work on Cobalt Based Ludwigites	185
L Scientific Events	192

General Introduction

Physics is a huge Science devoted to explaining the very fundamental properties of nature. From tiny sub-particles that form the atoms to the great galaxies in the universe, and arguably even in multiverses, there are physicists researching, both in theory and experiments. The work presented in this Ph.D. thesis is however restricted to an intermediate size scale, at the spectral window of Condensed Matter Physics, which represents nowadays a very attractive field in Physics subject. Although there are very interesting studies in Condensed Matter varying from Bose-Einstein condensation [1, 2] to Superfluidity (overview, Ref. [3]), remarkable efforts have been done in understanding exotic quantum phenomenon: the superconductivity.

Particularly, Solid State Physics is perhaps the most studied field in Condensed Matter Physics area, not just because it is a wide subject, ranging from small cold clusters of atoms to huge neutron stars in outer space, but also for the tremendous potential for technological applications.

Within this framework, superconductivity was discovered by Heike K. Onnes more than a century ago in 1911 [4, 5], just three years after liquefying helium [6, 7]. Since then, the superconductivity has been served as motivation for physicists around the world. A prove of that is the vast list of superconductors found in the last century with critical temperatures up to 250 K, under external pressure [8]. More recently, experiments with pressurized systems revealed Room Temperature superconducting phase transitions [9]. This quest for high-temperature superconductivity is strongly motivated by technological applications on transport and mainly efficient (zero resistance) energy transference.

There were several milestones in the history of superconductivity since Onnes discovery. The first notable fact was the Meissner-Ochsenfeld effect [10], which has found that an external magnetic field is expelled from a superconductor. This effect is actually what differs a superconductor from a perfect conductor with null electrical resistivity. Further, in 1957, Bardeen, Cooper and Schrieffer proposed their famous BCS theory [11], stating that superconductivity arises from a pair of electrons whose attraction is mediated by lattice vibrations. They were capable of explaining the pairing mechanism of all superconductors discovered since then but erroneously predicted with the very same theory that the highest critical temperature achievable would not surpass much more than 40 K, killing any expectation of achieving the dream of a room critical temperature superconductor. In fact, for a great period of time, the record for BCS critical temperature was 42 K, on MgB_2 compound [12].

Fortunately, about twelve years later, in 1979, Bednorz and Müller discovered the superconducting cuprates and they presented a couple of different properties from all other superconductors so far [13]. First of all, they were insulating oxides at room temperature. Further, they are Mott insulators [14], contradicting the expectation that a metallic high-temperature state would be necessary to achieve superconductivity. Second of all: it is very hard to control the level of oxygen within a sample synthesis, leading to vacancies and defects and thus to the excess of impurity, also believed to compete with superconductivity. Last, but not least, the pairing mechanism was not mediated by phonons, leading to the very first case of a superconductor that could not be explained by the well-known BCS theory. It was the birth of the so-called unconventional superconductivity.

Although an open question, there is some theories that attempt to explain the unconventional superconductivity. Among them, it's worth citing the Resonance Valence Bond (RVB) theory, by P. Anderson [15] and, the spin fluctuation theory proposed by Monthoux, Balatsky and Pines [16]. Besides incomplete, the latter is much more accepted by the scientific community and states that a magnetic state, usually antiferromagnetically ordered, must be present in the vicinity of unconventional superconductivity. More recent studies claim that superconductivity arises from a

quantum critical point (QCP) at the very edge of an antiferromagnetic state [17].

From the experimental point of view, what can be done is to search for novel materials that would work as a “playground” to understand the physical phenomena and test them in the real world. Fortunately, for the issue related with unconventional superconductivity *vs* magnetism scenario there is a very convenient material known since the 80’s: the cerium based heavy fermions (e.g. 115 family), which will be discussed in details in this thesis. They are layered compounds that exhibit unconventional superconductivity in the vicinity of antiferromagnetism and a QCP.

Moreover, these systems feature a ground electronic state affected by Crystalline Electrical Field (CEF) effects and the main goal here is to demonstrate that such effects are crucial to understand and explain the properties of the 115-heavy fermion family, including the superconductivity originated from a $4f$ electron. Historically, CEF effects were underestimated due to a small energy scale and thus neglected in the first theoretical models of such systems (for a complete review, refer to [18]). However, as one of the main conclusion of this thesis, it will be shown that CEF has a very strong impact on the hyperfine coupling, which determines how strong is the interaction between Ce $4f$ electrons and their vicinity, through drastic changes of the $4f$ wavefunctions.

Dimensionality restrictions may affect the electronic wavefunctions, changing the behavior of the materials, usually leading to what is called “low dimensional materials”. The heavy fermions studied in this thesis, for instance, present $4f$ electrons “bounded” to the structural Ce-In layers, displaying the so-called 2D electronic character. On top of that, one can also add more bounds to the electron’s mobility. One way to do so is to limit the physical dimension of the material. That’s the main idea behind the hunt for thin films (2D), nanowires (1D) and nanoparticles (0D), which has been the main project of our research group in the IFGW-Unicamp.

In that sense, we have also devoted a part of this study to the exploration of insulating nanoparticles of NaYF_4 . The Y site accepts any other rare-earth elements on the composition, as is shown later on in the text, and consists of an excellent environment to explore $4f$ CEF effects on restricted

electronic dimensions. Most of the studies, however, were done on the undoped NaYF_4 compound, to understand how such dimensionalization can be probed by magnetic resonance. This work led to relevant contributions for future research in our group since it proved that NMR and ESR are quite sensitive techniques for studying nanostructured materials [19].

Furthermore, the studies of CEF effects have been extended on this thesis to a distinct system: the cobalt boron oxides of the $\text{Co}_3\text{O}_2\text{BO}_3$ family, in which the CEF effects induces magnetic transitions. So far, to the best of our knowledge, no superconductivity was observed for these systems, but they do exhibit complex magnetism that leads to frustrated phases. The main results on these systems show a high-spin to low-spin transition [20, 21].

In short, this thesis aim in the heavy fermion materials with cobalt boron oxides and nanoparticles being explored as satellite matters, firstly not related to the focus, but with shared similarities in the fundamental aspects.

The chapters in this thesis are divided as follows:

Chapter 1: Presents the theoretical fundamentals to understand the underlying physics of the explored compounds in this work.

Chapter 2: Presents a brief introduction to magnetic resonance, from the theoretical and experimental point of view.

Chapter 3: Introduces and shows the state of the art, motivation, methodology and results obtained for the heavy fermion compounds of the 115s family.

Chapter 4: Briefly describe the work performed in other systems of interest, giving focus on the insulating NaYF_4 nanoparticles and the cobalt boron oxides of the $\text{Co}_3\text{O}_2\text{BO}_3$ family, who lead to scientific publications.

Chapter 5: Finally presents the general conclusions and future perspectives of this work.

The Appendix A is a short overview about my sandwich at University of California, in a collaboration program (seed grant) between UC and Unicamp

Appendix B through F presents several experimental and theoretical aspects that are relevant to the thesis, but were not discussed the main body, in order to do not extend it too much;

Appendix G is the list of scientific works generated by this work.

Appendix H through K presents papers and additional discussions the topics addressed in the main text.

Finally, appendix L is the list of scientific conferences attended throughout the period.

Chapter 1

Theoretical Aspects

This chapter is devoted to present basic theoretical aspects and concepts necessary to understanding the experimental techniques and results presented in this thesis. Electronic correlations, magnetism, magnetic interactions, crystalline electric field effects, ultimately related to the subjects under investigation, are some of the topics discussed here. The phenomena are discussed here in a general approach and how they effectively affect the system of interest are discussed on the specific chapters

Electrons under extreme conditions, such as low temperatures, high magnetic fields and strong internal electronic interactions with conduction electrons may exhibit unusual physical properties. Now, imagine that, on top of all that the electron itself couples with magnetic particle, developing effective masses ranging from 100 to 1000 times the mass of an electron in conventional metals as copper or gold. Such materials are called “heavy fermions” and interesting properties may arise from these “massive electrons”, such as unconventional superconductivity, quantum criticality, magnetism, and topological behavior to mention just a few. This section is devoted to the study of cerium based heavy fermions of the $CeMIn_5$ family (where M stands for Co, Rh, or Ir) from the NMR perspective.

1.1 Actually, What is a Heavy Fermion?

The term “heavy fermion” may sound a little strange to the ears. From basic Physics it is known that materials are made of protons, neutrons, and electrons, being all them, fermions. In that sense, “heavy fermion” means the same as “heavy electron”. So, an immediate question that arises is: “How can an electron be heavier?”. The unexpected and very impressive answer is “No, they do not”, and this story began with Andres, Graebner, and Ott, in 1975 [22]. They investigated the behavior of CeAl_3 under low-temperature conditions and found out a specific heat coefficient of γ 1620 mJ mole/ K^2 , which is roughly 1000 times larger than the γ value for metallic copper [23].

It is known from basic solid-state physics [23] that the specific heat can be described mainly by a linear electronic and a cubic phononic dependency with temperature, i. e.:

$$c_p = \gamma T + \beta T^3. \quad (1.1.1)$$

The most important term is the electronic one with γ known as the Sommerfeld’s coefficient, which is defined as:

$$\gamma = \frac{\pi^2}{2} \frac{k_B^2}{\epsilon_F} n, \quad (1.1.2)$$

where ϵ_F is the Fermi energy, which for metals is given by:

$$\epsilon_F = \frac{\hbar^2 k_F^2}{2m_E}. \quad (1.1.3)$$

So, combining Eqs. 1.1.2 and 1.1.3, the Sommerfeld’s coefficient depends only on fundamental constants and the electron mass m_E . Hence, the only possible reason a material presents a high γ is presenting an effective mass larger than that of a free electron. And that is unique because one can see such behavior in heavy fermion materials: Electrons roughly presents the effective mass of a proton. That is exactly what happens and the term “heavy fermions” was firstly used by Steglich [24] one year later from Andres experiments.

The physical reason behind this enhancement of the specific heat coefficient γ lies in the 4f/5f hybridization, which will be discussed in more detail in the following.

To discuss the hybridization, take a concrete example: Cerium. It is a silvery-white metal of the rare-earth family, whose symbol is Ce and atomic number 58. So, its electronic configuration is [Xe] 4f¹ 5d¹ 6s², with the 6s² electrons usually participating in the conduction band, while the 4f¹ ones more closely bonded to the nuclei. Hence, the hybridization process occurs when the 4f electrons start to interact with the conduction electrons in the material. Such interaction leads to the enhancement of the electronic component of the specific heat, since the 4f electrons, which now is “part” of the conduction band, is still strongly coupled to the nuclei, in a competition between localization and delocalization. To make an analogy, imagine a fast runner trying to run bounded to a heavy chain. It will be much more difficult for the runner to move in this situation. It is important to note, however, that not all electrons in a heavy fermion present high effective mass, just those coupled to the 4f ones, since only they carry the bond with the nuclei. Following the same analogy, some runners would be bounded to the chains, while others would be free to move.

In the last two decades, heavy fermion compounds have attracted great attention from the scientific community due to the discovery of intermetallic antiferromagnetism and unconventional superconductivity, tunable by external control parameters as magnetic field, pressure or even chemical doping [25, 26, 27]. This antiferromagnetic state is separated from the heavy fermion ground state by a quantum critical point, which is a singularity in the phase diagram that could lead not only to unconventional superconductivity but to other novel states of matter as well, as discussed in the next section.

1.2 Electronic Correlation: The Free Electron Model and Beyond

Free electrons in solids are, at a first approximation, treated as a particle with zero potential energy in a cube with L^3 volume, such that its wave function is given by [28]:

$$\Psi_n(\vec{r}) = A \sin \frac{\pi n_x x}{L} \sin \frac{\pi n_y y}{L} \sin \frac{\pi n_z z}{L}. \quad (1.2.1)$$

Periodic boundary condition, which is $\Psi_n(\vec{r} + L) = \Psi_n(\vec{r})$, limits the possible values for the argument on the sine functions so that:

$$k_i = \frac{n_i \pi}{L}; n_i = 0, \pm 2, \pm 4, \dots \quad (1.2.2)$$

The eigenenergies are given by:

$$E_K = \frac{\hbar^2}{2m} \vec{k}^2, \quad (1.2.3)$$

which leads to a spherical Fermi surface [23], from which physical properties such as the heat capacity (C) can be derived. It has the form

$$C = \alpha T + AT^3, \quad (1.2.4)$$

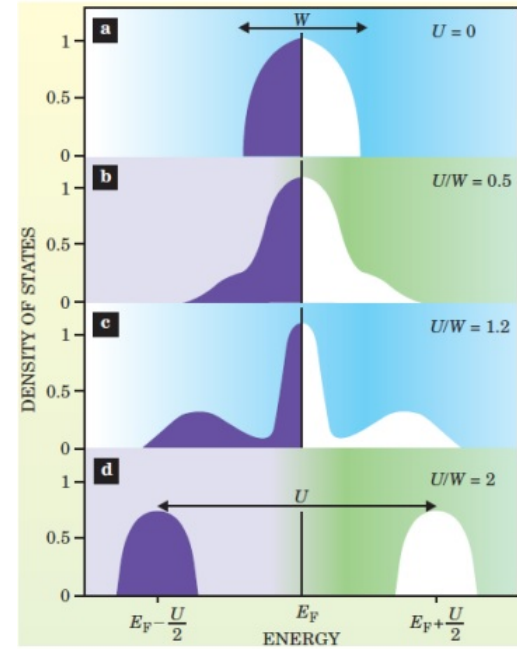


Figure 1.1: Formation of the Hubbard bands as a function of $\frac{U}{t}$ value. This figure was extracted from [29] and W represents t in Eq.1.2.5. Once the ratio $\frac{U}{t}$ increases, the Hubbard bands splits, as described in the main text.

One can also derive the thermodynamic properties as done in fundamental solid-state physics textbooks and the electrical resistivity, as discussed later in this chapter. However, all those cal-

where α , the Sommerfeld coefficient, is related to the electronic contribution and A to the phononic one.

culations are valid in a regime with no atomic potentials. If one is to add a potential U , the Hamiltonian becomes very complicated and, in most cases, there are no exact solutions. Some examples are the Kronig-Penney model which modulates the nuclear interactions as a periodic square potential, and the tight-binding model, which modulates them as Dirac's delta function [23]. Further, there are specific cases where far beyond the atomic potential must be taken into account to treat the problem. These materials are so-called Strongly Correlated Electron Systems (SCES) since the electron-electron interactions plays an important role in the description of their physical properties.

The simplest model to describe electronic correlation is the Hubbard model [30], proposed in 1963. This model describes electrons moving along the sites of a given lattice with hopping energy t , which favors electron mobility between lattice sites and a Coulomb interaction (U), which favors electronic localization. U is also always positive. When $\frac{U}{t} = 0$, the density of states is that of a pure metal, as shown in Fig. 1.1a (this figure was reproduced from [29] with t represented as W). As $\frac{U}{t}$ increases, the half-ellipse is deformed (panel b) and the upper and lower Hubbard bands appear at $E_F - \frac{U}{2}$ and $E_F + \frac{U}{2}$, where E_F is the Fermi energy. When $\frac{U}{t}$ is high enough, there is a complete separation between these bands, and an insulating state is established.

The Hubbard hamiltonian is given by:

$$H = \sum_{i,j} t_{i,j} c_{i,S}^\dagger c_{j,S} + \sum_i U_i n_{i\uparrow} n_{i\downarrow}, \quad (1.2.5)$$

in which $c_{i,S}^\dagger$ is the creation operator for an electron with spin S and $c_{j,S}$ is the destruction operator. Note that the electron destructed at site j is created at site i . This term ‘‘hops’’ the electron from j to i . $n_{i,\uparrow}$ and $n_{i,\downarrow}$ are the electron number operators at i site respectively with spin up and spin down states (note there is nothing at j site) so this is called the ‘‘in-site’’ Hubbard repulsion.

As a matter of fact, the Hubbard model can also be extended by adding an inter-site Coulomb

repulsion term $V_{i,j}$, which stands for:

$$H_{ext} = \sum_{i,j} V_{i,j} n_{i\uparrow}, n_{j\downarrow}, \quad (1.2.6)$$

where n_i and n_j stands for the number of spins at i and j sites, regardless their spins. This extension to the Hubbard hamiltonian is required to explain the charge ordering effect that happens in the $\text{Co}_3\text{O}_2\text{BO}_3$ compound. However, for general strong correlation, which is the most common case, Eq. 1.2.5 satisfies well the problem description.

1.3 Origin of Atomic Moments

Magnetic moments of a given solid have three principal contributions:

- two electronic components: One associated with electrons spin and orbital angular momentum;
- nuclear, which presents only spin component;

Electrons states are defined by their quantum numbers n , l , m_l and m_s [28]. The maximum number of electrons in a given electronic shell is defined by Pauli's principle, meaning that two different electrons may not share the same energy state, *i. e.*, have the same quantum numbers.

The orbital contribution to the total angular momentum is calculated as if the electrons are moving in a circular wire of the electrons orbit diameter. Thus

$$\vec{\mu}_l = -\frac{|e|\hbar}{2m} \vec{l} \longrightarrow |\vec{\mu}_l| = \mu_B \sqrt{l(l+1)} \quad (1.3.1)$$

where μ_B is the Bohr magneton given by $\mu_B = \frac{|e|\hbar}{2m}$ and evaluated as 9.274×10^{-24} J/T. e is the electronic charge (1.602×10^{-19} C), m is its mass (9.109×10^{-31} kg) and \hbar is the Plank constant over 2π (1.054×10^{-34} J.s). The projection of the magnetic moment along the magnetic field \vec{B} ,

which can be taken along the z -axis without loss of generality, can be simplified as $\mu_{lz} = -m_l \mu_B$.

The spin contribution is given by:

$$\vec{\mu}_s = -g \frac{|e| \hbar}{2m} \vec{s} \longrightarrow |\vec{\mu}_s| = g \mu_B \sqrt{s(s+1)} \quad (1.3.2)$$

in which g is the Landé factor (2.0023 for free electrons) and the angular projection along field axis is $\mu_{sz} = -g_e m_s \mu_B$.

The Hamiltonian of a magnetic moment in a given magnetic field strength H , such that $\vec{B} = \mu_0 \vec{H}$ and μ_0 the vacuum permeability, is given by:

$$\hat{H} = -\vec{\mu} \cdot \vec{B}. \quad (1.3.3)$$

For an atom, the most intuitive way to evaluate quantities is to sum over all microscopic entities, so that, the total angular orbital momentum (\vec{L}) and total spin angular momentum (\vec{S}) are given by:

$$\vec{L} = \sum_i \vec{l}_i \quad \text{and} \quad \vec{S} = \sum_i \vec{s}_i. \quad (1.3.4)$$

These two quantities can be coupled through the so-called spin-orbit interaction. In this case, it is better to consider the total angular momentum $\vec{J} = \vec{L} + \vec{S}$.

It looks very complicated to evaluate the total angular momentum of heavier atoms. An anion of much interest due to its magnetic properties for instance is Gd^{3+} which has 54 electrons that will hardly fit in eq. 1.3.4. Fortunately for the scientist that works with Gd^{3+} and other complex atoms, not all electrons contribute

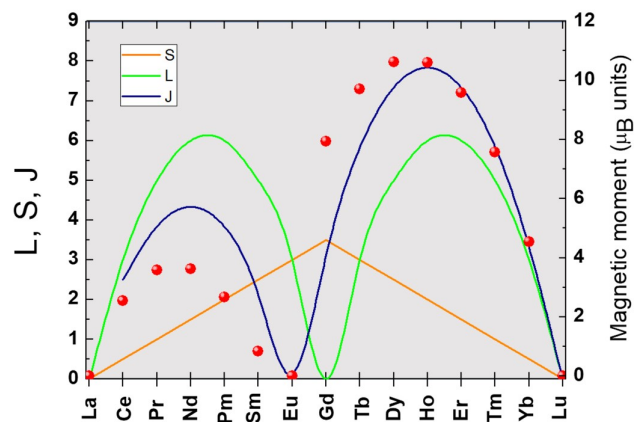


Figure 1.2: Spin, orbital and total angular momentum for the Lanthanide series with 3+ valence. The red dots represent the calculated magnetic moment in terms of μ_B . A clear relation between \vec{J} and $\vec{\mu}$ is observed.

to the bulk magnetism of a given material, but just the unpaired electrons. Here, a “pair” is defined as two electrons with the same n , l and m_l quantum numbers but different m_s numbers. Therefore, it is noted that inner electronic shells do not contribute to magnetism since closed shells have an even number of electrons with opposite m_s . Electronic magnetism thus arises from electrons on the most external shell. The occupation of these shells is given by Hund’s rule and will not be discussed extensively here.

One of the very important “sources” of magnetism in bulk solids are the rare-earth elements of the Lanthanide series, more commonly named as rare-earth, which have incomplete $4f$ shell and whose magnetic properties are defined in Fig. 1.2. Supposing that a given sample has unpaired electronic spins, they can give rise to a series of interesting magnetic states. The most common ones observed in nature are:

- *Diamagnetism*: there is no permanent moment, but they can be induced under magnetic fields, in which, the moments align in the opposite direction to \vec{B} ;
- *Paramagnetism*: the atomic magnetic moments point in random directions without external field. With applied magnetic field, they align parallel to \vec{B} . There is a particular case for metals, in which the electrons are also screened, leading to the so-called temperature dependent Pauli paramagnetism;
- *Ferromagnetism*: characterized by a strong coupling between the magnetic moments, they can be aligned even in the absence of an external magnetic field. The material with such characteristic is a permanent magnet, *i. e.*, it presents a spontaneous magnetization;
- *Antiferromagnetism*: it is also an ordered state, but the electron pair has spins antiparallel to each other, being one spin up and another spin down, leading to zero net magnetization.

The description above represents idealized phenomena and is generally not the case in real samples, since the temperature increase tends to randomize the directions of the spins. So, the most common case observed in nature is paramagnetism at higher temperatures, while magnetic ordering is often achieved through phase transitions at lower temperatures. Such transitions can be observed by measuring the magnetic susceptibility as function of temperature. The typical results are summarized in Fig. 1.3.

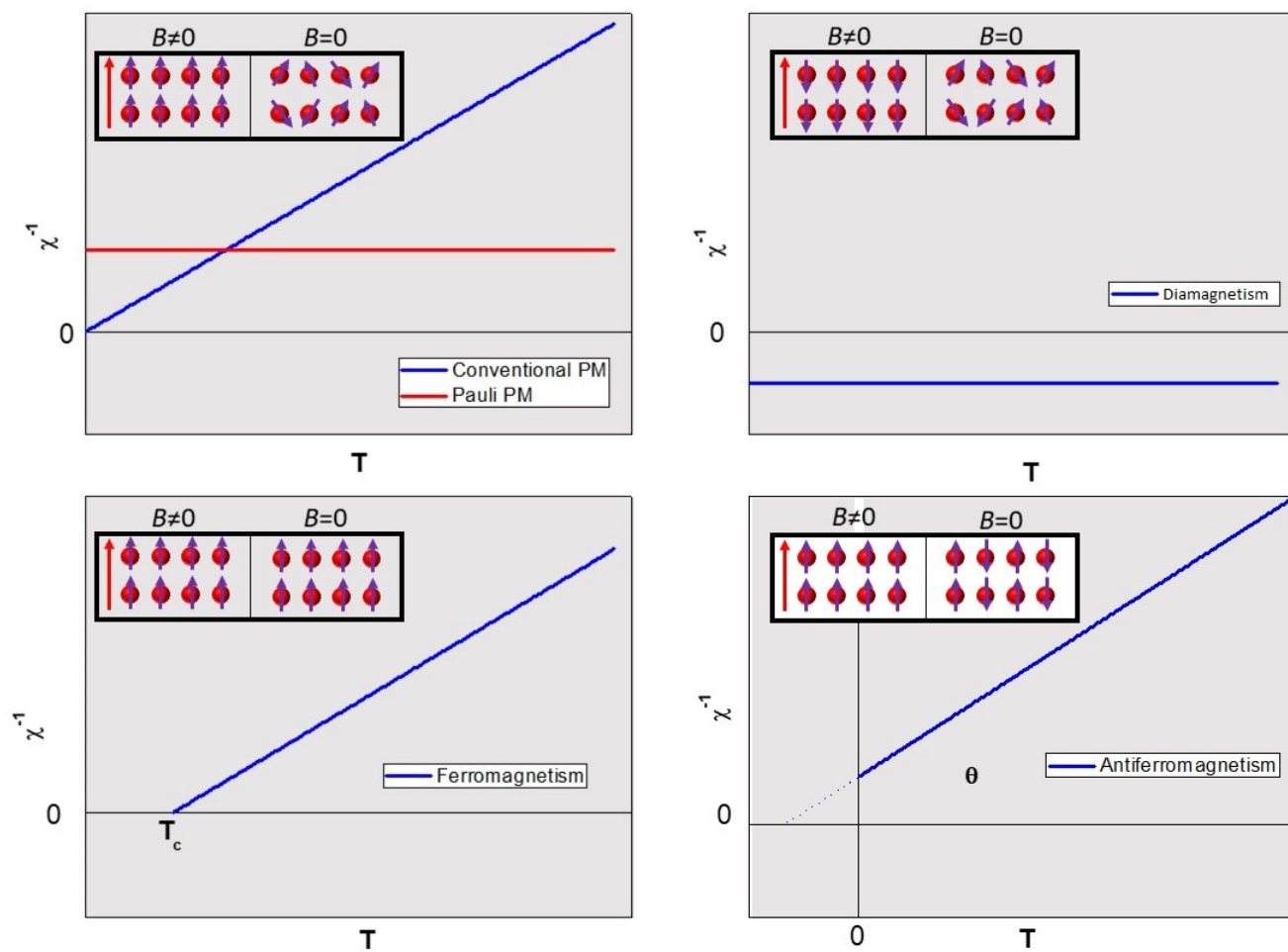


Figure 1.3: Behavior of inverse χ as a function of temperature for typical magnetic orderings.

1.4 Nuclear Magnetism

Like electrons, nuclei possess fundamental intrinsic physical properties, among them, orbital and spin magnetic momentum. Compared with L and S , those feature a very small intensity (about 0.1%) and do not contribute to macroscopic properties, such as bulk magnetization. However, even this small total momentum can be used as probes to investigate the microscopic structure without disturbing it, working only as a tiny perturbation. In NMR, the probe is the spin ground state (I) that arises from the nuclei, thus it is very important to understand our main object of study: The nucleus.

In the most recent standard model [31], while electrons (e^-) are fundamental particles of nature, nuclei are more complex, being composed by protons (p^+) and neutrons (n^0), which are by themselves formed of three quarks each, intermediated by gluons. Quarks are fermions, which means they have half-integer spin, leading protons and neutrons to have a $1/2$ and $3/2$ spin state, the second being an excited state, not reached by typical NMR energies (they can be however accessed via Mössbauer spectroscopy [32]). Therefore, neutrons and protons will be treated in this text as particles of spin $1/2$.

The nuclei, main objects of our NMR studies, have therefore:

- mass, given by the total number of n^0 and p^+ ;
- positive electrical charge given by the number of p^+ times the fundamental charge;
- intrinsic magnetic moment;
- spin, given by the sum of n^0 and p^+ spin, according to Hund's rule.

It is not trivial, however, to determine the ground state for the nuclear spin, which is generically

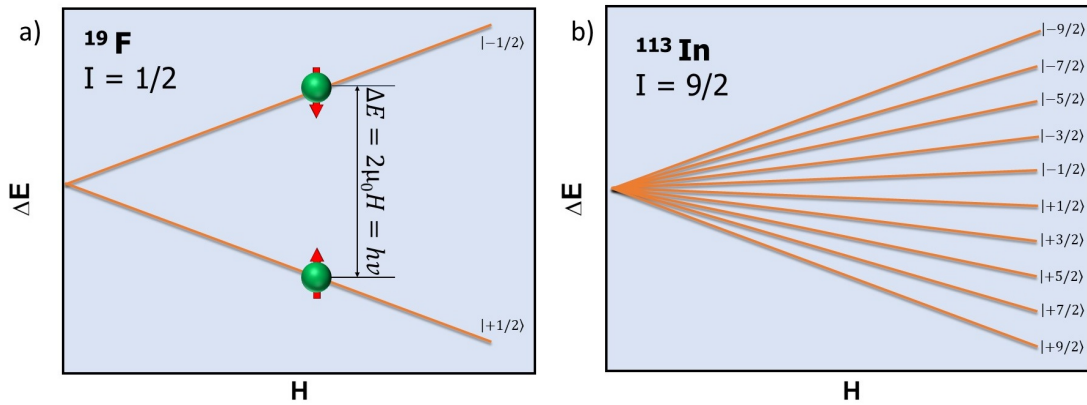


Figure 1.4: Zeeman effect diagram for a) a simple case of an atom with nuclear spin $I = 1/2$ and b) a more complex case of an atom with nuclear spin $I = 9/2$.

measured experimentally. Nuclei with odd atomic number will always present semi-integer spin and are, in principle, observable by NMR, while even atomic number ones have integer spin, which may be zero (not observable) or not.

The nuclear spin states are also, as electrons spin states, $(2I+1)$ -fold degenerate, and thus susceptible to Zeeman splitting via magnetic fields. In figure 1.4 the cases of Zeeman splitting of two nuclei investigated in this study, the ^{19}F and ^{113}In are depicted. It is also worth mentioning that the Zeeman effect is perturbative and more accurate for low magnetic fields.

While the first has the simplest diagram, featuring just two levels and one possible transition, the latter is substantially more complex, given the ^{113}In nuclear spin $9/2$, presenting ten possible energy levels and nine nuclear transitions (the allowed transitions must satisfy $\Delta m = \pm 1$). The energy separation between the energy levels depends on the nuclear gyromagnetic ratio and obviously on the field strength, but the NMR energy scale is typically below the energy separation between the ground state and the first excited state. Note that in the levels diagram in Figs. 1.4(a) and (b), neither spin-orbit coupling (LS) nor Electric Field Gradient (EFG) effects have been considered.

1.5 RKKY Interaction

Several other examples of magnetic interactions may happen in solids. Meaningful to note here for the work presented later on is the Ruderman-Kittel-Kasuya-Yoshida (RKKY) interaction, which is a coupling of the f or d electron spins mediated by conduction electrons [33, 34, 35].

Such interaction has an indirect exchange coupling characteristic. The Hamiltonian can become very complex (Eq 3.1 on [35]) and consider terms for inter d electron spins interactions, internuclear spin and d -electrons to nuclear spin energies. Fortunately, one can characterize the RKKY interaction by means of an effective coupling coefficient j given by:

$$J(\Delta\vec{R}) = 9\pi \left(\frac{J^2}{E_F} \right) F(2k_F\Delta\vec{R}), \quad (1.5.1)$$

where

$$F(x) = \frac{x \cos x - \sin x}{x^4}, \quad (1.5.2)$$

and ΔR is the distance between magnetic moments, E_F and k_F are the Fermi surface energy and radius respectively. As shown in Fig. 1.5, the RKKY interaction oscillates around positive and negative values. So, depending on the distance between the magnetic moments, the interaction can have a ferromagnetic (FM) or an antiferromagnetic (AFM) character.

The RKKY interaction is crucial to understanding the state of the art behind the Ce-115 heavy fermion compounds discussed in this thesis, along with the Kondo effect, discussed in the next section.

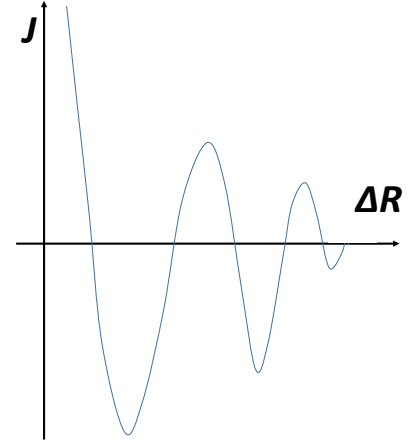


Figure 1.5: Graph of J as a function of ΔR in the RKKY interaction model. Note that J coupling changes as a function of the atomic distance. In other words, the AFM or FM interaction between magnetic impurities changes as a function of the distance between them.

1.6 The Kondo Effect

At higher temperatures, the resistivity becomes linearly proportional to T . In other words, the total resistivity of a material has a constant term ρ_0 , which depends basically on the samples purity and a T -dependent term that arises from the electron-phonon or electron-electron scattering.

The electrical resistivity of single elementary metals is well known from Matienssen's law [23] as:

$$\rho = \alpha T^5 + c\rho_0, \quad (1.6.1)$$

for temperature lower than the Debye Θ_D .

However, when diluted magnetic impurities are inserted on the metal, they will induce extra scattering centers, and an additional contribution to the resistivity, which has a logarithmic temperature dependence. This effect was explained by J. Kondo [23] and was hence named “the Kondo effect”, which shows that the contribution to electrical resistivity is:

$$\rho_K = \frac{3zJ}{E_F} \ln T, \quad (1.6.2)$$

where J is the exchange energy between the magnetic moments, z is the number of nearest magnetic neighbours and E_F is the Fermi energy. By combining eq. 1.6.1 and 1.6.2, then:

$$\frac{d\rho}{dT} = 5\alpha T^4 + \frac{3zJ}{E_F T}. \quad (1.6.3)$$

So, it is possible to have a critical point when

$$T_K = \left(-0.6 \frac{zJ}{\alpha E_F} \right)^{\frac{1}{5}}, \quad (1.6.4)$$

which is positive since J is negative. The Kondo temperature T_K is in the order of several kelvins, in which a conductivity minimum slightly dependent on the concentration of the magnetic dilution centering is observed for several simple metals like Co, Au, Mn, Fe, among others [23].

1.7 Crystal Electric Field (CEF)

As pointed out before, many effects can take place on crystalline materials and affect their properties in different ways. Another example of such effects with extreme relevance on this thesis is the Crystalline Electrical Field (CEF), which has small but quite effective contributions on most rare-earth based compounds, as the Ce-115 heavy fermions and 3d based compounds as the $\text{Co}_3\text{O}_2\text{BO}_3$ ludwigites. As the term “electrical” suggests, the CEF arises from Coulomb interactions, whose Hamiltonian is:

$$H = q_i V(\vec{r}_i \vec{R}_j) = \sum_i \frac{q_i q_j}{|\vec{R}_j - \vec{r}_i|}, \quad (1.7.1)$$

where q_i is the electrical charge on the \vec{r}_i position, interacting with its surroundings: The n charges q_j , at \vec{R}_j . It is worth remembering that the CEF hamiltonian developed here uses a punctual charge model, so that, the potential solves the Laplace equation. It is possible to expand the potential in terms of the Legendre’s polynomials:

$$\sum_j \frac{1}{|\vec{R} - \vec{r}|} = \sum_{n=0}^{\infty} \frac{r^n}{R^{n+1}} P_n^0(\cos \theta). \quad (1.7.2)$$

Note that, when one treats the problem with Legendre’s polynomials, the spherical coordinates are implicit. It is a very good choice since the coefficients can be written in terms of the spherical harmonic, as:

$$P_n^0(\cos \theta) = \frac{4\pi}{2n+1} \sum_{m=-n}^n (-1)^m Y_n^{-m}(\theta_j, \phi_j) Y_n^m(\theta_k, \phi_k), \quad (1.7.3)$$

leading the Hamiltonian in Eq. 1.7.1 to:

$$H = \sum_0^{\infty} \sum_{m,i} r_i^n A_{n,m} Y_{n,m}(\theta_i, \phi_i), \quad (1.7.4)$$

with

$$A_{n,m} = \sum_j \frac{4\pi}{(2n+1)} q_i q_j \frac{Y_{n,m}(\theta_j, \phi_j)}{R_j^{n+1}}. \quad (1.7.5)$$

The values chosen for m and n are restricted to the symmetry of the lattice and the electronic orbitals. In general, terms with *odd* m are zero and can be ignored. Higher-order terms ($m > 8$) can also be ignored since they are very small. Y_{00} is a constant and will not be taken into account.

In order to transform Eq. 1.7.4 into something like Eq. 1.7.6, the Wigner-Eckart theorem [28] must be used. What it does is transform the position operators in spherical coordinates (from the spherical harmonics) to magnetic moment operators in cartesian coordinates (Stevens' Operators).

The most common discussions of CEF in literature make use of the Stevens' Operators, O_n^m to describe the hamiltonian in such a way that:

$$H = \sum_{n=0}^{\infty} \sum_{m=-n}^n B_n^m O_n^m. \quad (1.7.6)$$

For the term Y_{20} the transformation is done like:

$$Y_{20} = \sum_k (3z_k^2 - r_k^2) = \alpha_J \langle r^2 \rangle [3J_z^2 - J(J+1)] = \alpha_J \langle r^2 \rangle O_2^0, \quad (1.7.7)$$

where α_J is a constant which carries information on the J couplings.

Although the math behind are very complex, it is easy to understand, in principle, the effects of CEF hamiltonian on a solid: It simply breaks the $2J+1$ degeneracy of the ground state. Such effects may happen in d or f electrons, and fortunately both are important in this thesis, so, two examples of CEF effects are given: In the cobalt atom, which will be relevant to the study of the ludwigites, and the cerium, fundamental for the studies on CeMIn_5 heavy fermions. In the case of a $3d$ electronic shell, as Co, there are five possible orbital states: d_{z^2} , $d_{x^2-y^2}$, d_{xy} , d_{xz} and d_{yz} . At tetrahedral punctual symmetry, the degeneracy is broken favoring the states d_{z^2} and $d_{x^2-y^2}$. The doublet is hence named e_g , while d_{xy} , d_{xz} and d_{yz} energy level is increased, forming the high energy triplet state t_{2g} . For clearness, the splitting is shown in Fig. 1.6a. The electronic filling of Co^{3+} (with 6 electrons on $3d$ bands) is also presented on tetrahedral and octahedral punctual symmetries as examples. Note that, when the punctual symmetry changes, so do the energy levels e_g and t_{2g} .

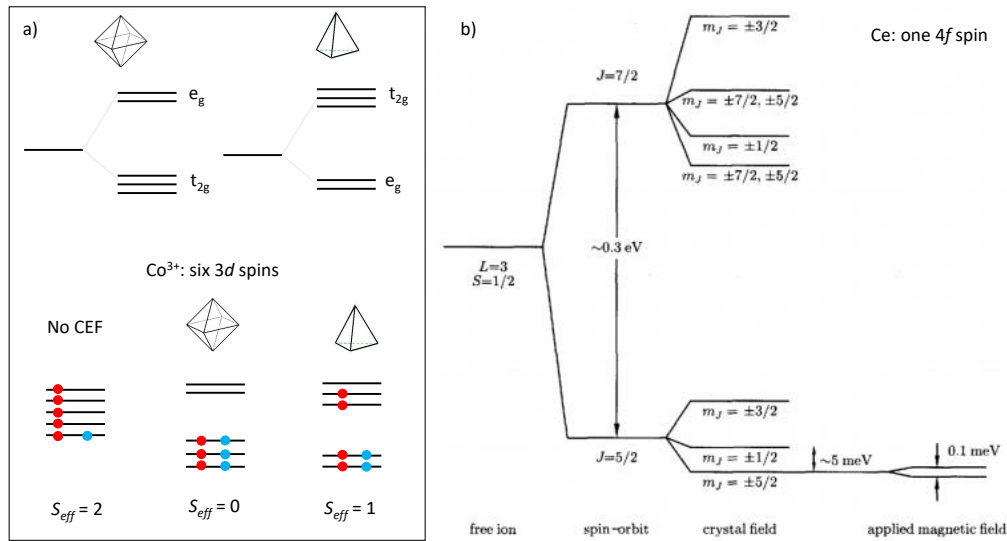


Figure 1.6: *a)* CEF effects on 3d octahedral and tetrahedral symmetries with especial emphasis to Co^{3+} . Red circles represents electron with spin up while blue ones stands for electron with spin down. Note that CEF effects may change the effective spin S_{eff} depending on the symmetry. Since the effective spin can be measured through ESR experiments, it is a smoking gun experiment to determine the CEF state. *b)* CEF effects on the 4f rare-earth cerium, with the approximate gap values, extracted from [37].

For the case of rare-earths, the CEF is much weaker and it is treated as a perturbation on the spin-orbit coupling. Fig. 1.6*b*, extracted from [37], depicts the case of cerium atom with its typical energies. With $L = 3$ and $S = \frac{1}{2}$, there are two possible J states: The low energy state $\frac{5}{2}$ and the high energy state $\frac{7}{2}$, which are approximately 0.3 eV apart. The CEF effects lift the degeneracy of the m_j states. Note however that the splitting is of the order of 5 meV, more than one hundred times smaller than the spin-orbit splitting, such that the CEF is usually not strong enough to mix J levels, as it may do in 3d compounds. The figure also presents the further splitting of the Zeeman effect, which is in the order of 0.1 meV, and it is basically what one measures during an ESR or NMR experiment. That is why these techniques are pretty useful for measuring CEF effects, especially for rare-earth atoms. It's worth pointing out that the so called low-spin state, when electrons occupy the bottom set of levels is favored when the Coulomb interaction becomes stronger than the Pauli exclusion principle. When Pauli interactions are stronger than electrical repulsion, the electrons populates the systems as if no gap has been opened. This is the so called

high spin state.

1.8 The Hyperfine Coupling

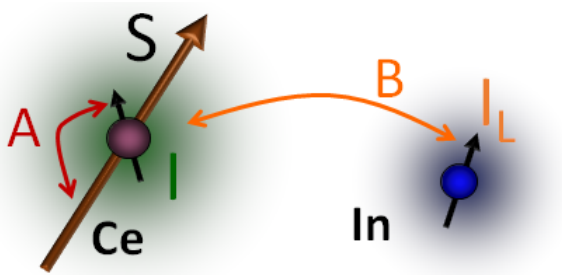


Figure 1.7: Scheme of the direct (A) and transferred (B) hyperfine coupling on generic atoms

The hyperfine coupling is defined as the interaction between a nuclear and an electronic spin inside a solid. Fig.1.7 is a schematic view of the process. There are two distinct process: The direct, which is the interaction within the same atom (represented by A) and the transferred, which is the interaction within different atoms (represented by B).

Although very simple in concept, the hyperfine coupling can be measured through a delicate analysis using Knight shift and magnetic susceptibility data.

The main investigation on this thesis is related to the transferred hyperfine coupling between Ce and In in Ce-115 heavy fermions family. It is worth mentioning that in this study, we were interested in the electron orbitals of Cerium. However, Ce is very hard to be seen by NMR experiments, given its low gyromagnetic ratio. Fortunately, there is a more suitable nuclei to measure in Ce-115s: In. Although it is not trivial, since In has a high nuclear spin ($\frac{9}{2}$), it is possible to measure it and extracts the transferred hyperfine coupling B from the nuclei of In and the conduction electron from Ce.

In order to do so, one must perform the Clogston-Jaccarino fitting, which associates Knight Shift K (a parameter obtained via NMR, as discussed in section 2.2.1) and magnetic susceptibility

χ in a linear relation in the paramagnetic regime by the equation:

$$K = K_0 + C.\chi. \quad (1.8.1)$$

where K_0 stands for a constant which carries non-electronic contributions to the Knight shift and C is a constant, which is proportional to the hyperfine coupling, as follows:

$$C = \frac{B}{N_A \mu_B}, \quad (1.8.2)$$

with N_A is the Avogadro number and μ_B , the Bohr magneton.

It is worth emphasising that B is the transferred hyperfine coupling, If one wants to be measuring the direct hyperfine coupling, he must measure the Knight shift upon Ce site.

Our main achieve in this work was to relate B and the evolution of the Ce's f electron, establishing an scaling rule that worked across all Ce-115s family, including results under extreme conditions of pressure and magnetic field, as discussed in chapter 3.

Chapter 2

Magnetic Resonance

This chapter is devoted to present the fundamental aspects of nuclear magnetic resonance, which is the main technique used in this thesis. The presented discussion is based on several references, [38, 39, 40, 41, 42, 43, 44], papers [45, 46] and thesis [47, 48, 49, 50, 51, 52]. It is intended to provide the fundamentals to a non-familiar public for understanding the terms, the general theory, and how an NMR experiment can be performed. Complementary experimental techniques, such as electrical resistivity, X-ray, specific heat and magnetization, also performed on the course of this thesis, are presented in appendix E. The appendix B is also dedicated to Electron Spin Resonance (ESR), since it was performed to confirm some results in this thesis.

2.1 Introduction and Generalities

Spectroscopy is defined as any kind of experiment in which a difference in energy levels ΔE is measured in some way. The experimental determination of such energy levels allows us to identify related physical properties from the material under investigation.

If a given particle, atom, spin, or any other entity has two energy levels, it may “switch” between these levels by receiving (absorbing) or delivering energy which, in spectroscopy, generally comes from a photon. The famous Planck’s relation $E = h\nu$, in which the energy E of an electromagnetic wave is related with its frequency ν by the Planck’s constant h , is the key

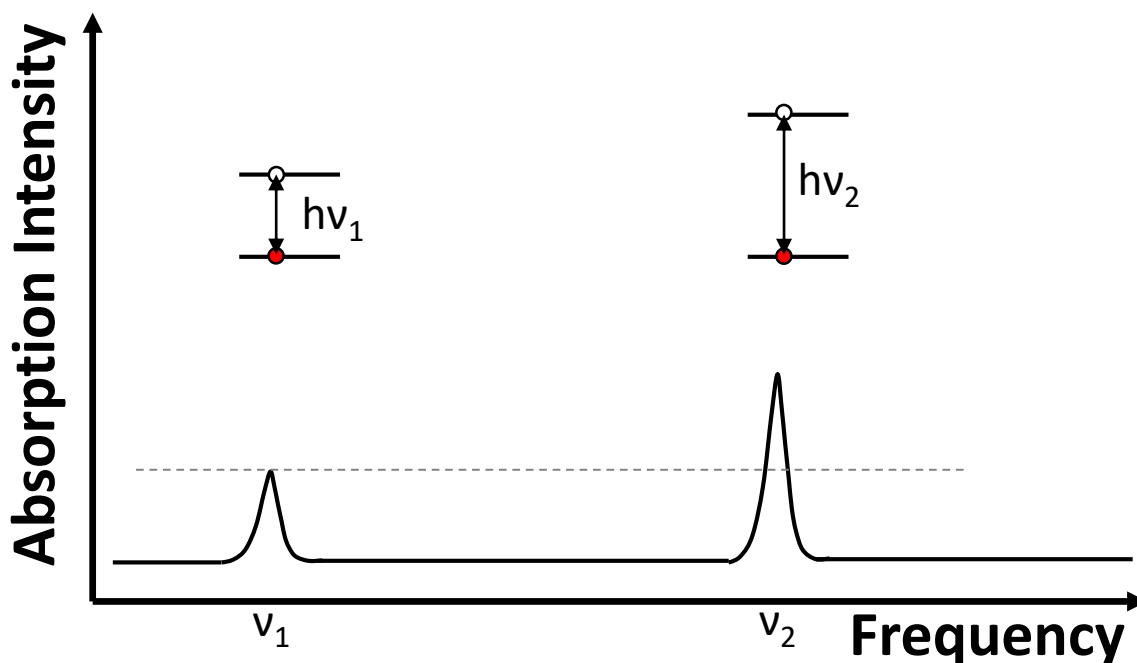


Figure 2.1: Representative of an absorption spectrum. Spins with a gap $h\nu_i$ between spin up and spin down states are expected on ν_i position in frequency. The intensity at higher energy is expected to be higher than at low energy.

equation to spectroscopy. The secret is to match exactly the energy of the electromagnetic wave E with the energy gap between two distinct levels ΔE ; so that $\Delta E = h\nu$. Depending on the energy scale of interest, there is an associated spectrum of electromagnetic waves. In this thesis, I focused on the study of low-energy spectroscopy, using waves on a radiofrequency range (dozens of MHz for NMR) and microwave range (a few GHz for ESR). However, when it comes to more energetic transitions, frequencies on the range of ultraviolet light can be also used for spectroscopy.

Generally, when doing spectroscopy experiments, the energy gap is constant and one sweeps through a range of frequencies to determine the exact frequency in which E matches ΔE . This would represent an absorption peak on the spectra, like those depicted in Fig. 2.1, where the first atom has a gap to the excited level of $h\nu_1$ and will absorb energy and thus resonate on the frequency ν_1 . The same statement is valid for the atom with excited state in $h\nu_2$. Since the linear relation between ΔE and ν , higher energy transitions needs higher frequencies to reach.

For the magnetic resonance, there is however a different way to perform the experiments. The energy difference arises from the interaction between a nuclear (for NMR) or electronic (for ESR) spin with an external magnetic field due to the Zeeman interaction. Since the spin acts as a small magnet, it has an interaction with the external magnetic field, which from now on is defined as H_0 , and it will align parallel or anti-parallel to such a field. This is the simplest case of an effective spin $\frac{1}{2}$; which could have two different spin projections: $m_S = +\frac{1}{2}$ and $m_S = -\frac{1}{2}$, leading to two distinct energy levels (in general, $m_S = +\frac{1}{2}$ is the lower energy ground state, since the spin is pointing towards the field). However, mainly for NMR, the case can be more complex since the nuclear spin can range from 0 to $\frac{9}{2}$ (in steps of $\frac{1}{2}$). A point which is worth emphasizing is that nuclei with zero spin is NMR vegetable, i. e., it does not present a NMR signal, however, nuclei with another spin I will have $2I + 1$ accessible level under magnetic field and thus $2I$ possible transitions.

For the moment, the simplest case of a spin $\frac{1}{2}$ will be considered, since it can be generalized to higher spin values. Also, the interaction of the spin with H_0 is given by the Zeeman Hamiltonian:

$$\hat{H} = -\vec{S} \cdot \vec{H}_0. \quad (2.1.1)$$

Thus, the energy of such distinct levels in the electronic case is given by:

$$E_e = g\mu_B H_0 m_s, \quad (2.1.2)$$

assuming that the magnetic field is pointing towards the z axis. μ_B is the Bohr magneton and g is the Landé factor. For the nuclear case, the vector \vec{S} on eq.2.1.1 is substituted by \vec{I} and thus the energy of distinct levels is:

$$E_N = \Gamma H_0 m_I, \quad (2.1.3)$$

in which Γ is the gyromagnetic ratio. Note that, in both cases, the energy can be written as a constant times $H_0 m_{S,I}$. So, in the following, just the electronic case is discussed, but all conclusions may be automatically extended to the nuclear case.

Since the energy of both levels is defined by eq. 2.1.2, one can write: $E_e^+ = g\mu_B H_0 \frac{1}{2}$ and $E_e^- = g\mu_B H_0 \frac{-1}{2}$; and than, the energy gap $\Delta E_e = E_e^+ - E_e^-$:

$$\Delta E_e = g\mu_B H_0, \quad (2.1.4)$$

and although simple, this equation has an outstanding result: one can manipulate the gap on the energy levels by changing the external magnetic field H_0 .

Equation 2.1.4 allows us to consider the possibility of taking a spectrum differently: As in most continuous wave spectrometers one can keep the frequency ν constant and vary the external magnetic field H_0 . An absorption will only happen when:

$$h\nu = g\mu_B H_0. \quad (2.1.5)$$

This equation is often called **resonance condition**. Note that there are infinite values of the pair (ν, H_0) that can satisfy the resonance condition. This is specially interesting for ESR experiments (discussed on the appendix B), which allows experiments on different bands. To address it shortly here, the most common is the X-Band with a microwave frequency near 9.2 GHz, which would lead to a resonance field near 3350 G (for $g=2$). This is the most used frequency band (more details later on in this section). There are however lower energy bands: L ($\nu_L \approx 1.1$ GHz with $B_L \approx 390$ G) and S ($\nu_S \approx 4.0$ GHz with $B_S \approx 1430$ G) but generally the spectra are noisier due to weaker Zeeman interaction. Also there are higher energy bands such as K ($\nu_K \approx 24.0$ GHz with $B_K \approx 9000$ G), Q ($\nu_Q \approx 34.0$ GHz with $B_Q \approx 12100$ G) and W ($\nu_W \approx 94.0$ GHz with $B_W \approx 33500$ G)

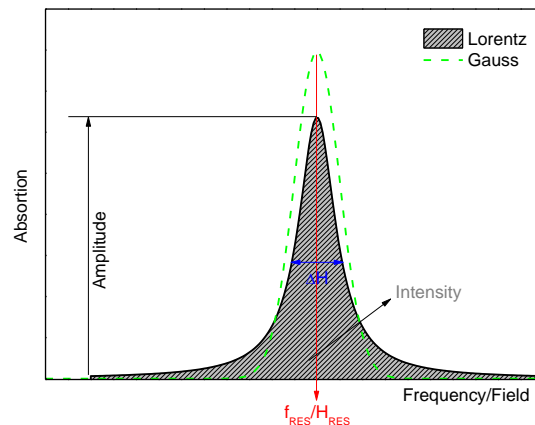


Figure 2.2: Main parameters of a Lorentzian lineshape on a magnetic resonance spectra. The gaussian shape is shown in a dashed line employing comparison. ΔB represents the linewidth at half-height, B_{Res} is the resonance field. The line intensity is proportional to the integrated area and represents the spin susceptibility.

but experiments are more complex, since higher magnetic field is required and special cavities and setup must be employed. The resonant cavity for high-frequency bands is more sensitive and as discussed in the experimental section, even small samples may disturb it enough to ruin the experimental conditions.

For NMR, in principle the number of pairs that satisfy the resonance condition is also infinity, although the cryostats generally come with a constant (non-sweepable) magnet. A common value of magnetic field recently is $H_0 = 11.7\text{ T}$, but it is not the only value. The user has to adjust the tank circuit to the desired resonance frequency. Specially designed systems such as ours, however, have the option to sweep the magnetic field H_0 allowing the user to control this experimental parameter.

So far only the absorption signal position in the MR spectra was discussed, which is given by its relative g or Γ factor, but there is also another important feature: The lineshape. First, for a homogeneous resonance of an insulating paramagnetic sample, a Lorentzian shape is observed. Inhomogeneity distorts the Lorentzian shape and distributions of internal magnetic fields in the sample would lead to a Gaussian lineshape. By distribution of internal fields, one may understand any gradient of electric or magnetic fields present inside the material.

The signal intensity of the absorption line (its area) also carries important information and is proportional to the concentration of the resonating spins. By knowing the precise number of resonant spins of a standard sample, one can measure a sample of interest under the same experimental conditions and by comparison, estimate the number of resonating spins.

Another important parameter is the full width at half maximum (FWHM), which is closely related to the spin-spin relaxation time (T_2). More precisely, the broader the line, the faster is T_2 . A resonance line and its main parameters are depicted in Fig. 2.2.

Other external factors could also have a strong influence on the absorption lines. For a concrete example, there is the hyperfine interaction which can be evaluated. Suppose that the electron is very close to a nucleus of hydrogen ($I = \frac{1}{2}$) inside the sample. The hydrogen nuclei's magnetic

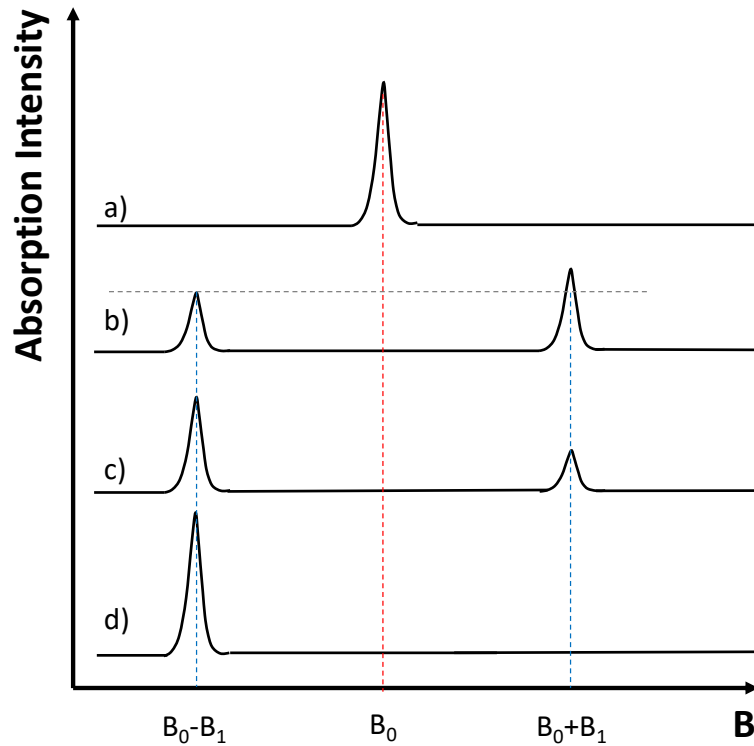


Figure 2.3: *a)* MR Spectrum of a given spin system. *b)* Effects of the hyperfine splitting over the electronic spin. In this case, the nucleus have the same probability to be aligned parallel or anti-parallel with the external field. *c)* Effects of the hyperfine coupling on the spectra when the up state is favoured. *d)* Hyperfine coupling effects when all nuclear spins are parallel to the external field.

moment will provide an internal magnetic field H_{HF} . The measured electron than is under an effective magnetic field, given by:

$$H_{eff} = H_0 \pm H_{HF}. \quad (2.1.6)$$

The \pm signal arises from the fact that the nuclei can be aligned parallel to the magnetic field (which is the negative sign) or antiparallel to H_0 (which is the positive sign). That would shift the resonance according to the most probable configuration (Fig. 2.3).

When carrying out a magnetic resonance spectroscopy experiment, two parameters were not taken into account until now. First: The spins are not insulated, i. e., an ensemble of nuclei is under investigation instead of just one, and second, although the up spin state has lower energy, not all the spins are in such state due to thermal effects which induce disorder in the ensemble. Suppose that there is N^+ spins up and N^- spins down at a given temperature T , such that $N =$

$N^+ + N^-$. The equilibrium population is:

$$\frac{N_0^-}{N_0^+} = e^{-\frac{\Delta E}{k_B T}}, \quad (2.1.7)$$

in which k_B is the Boltzmann constant. Thus, the larger is the difference between populations, the more spins will change their energy levels when the resonance condition is met. This generally leads to a more sizable experimental signal. This effect explains why it is preferable to have a larger magnetic field (which increases ΔE at eq.2.1.7) and a lower temperature for MR experiments.

For magnetic resonance experiments there are also two distinct ways to experiment: Continuous wave (c. w.) and by pulsed sequences, both with their advantages and disadvantages. In the former, the radiation is applied to the spin ensemble and the external field is swept continuously. However, the relaxation time cannot be measured directly on c.w. experiments.

The NMR experiments presented in this thesis have been done with pulse sequences. The radiofrequency pulses “manipulate” the spin system, as shown later in this text, preparing the desirable spin state before the measurement. By employing this method, one can unravel precise information about the relaxation times, but need to be very careful with the acquiring time, to prevent signal losses.

2.1.1 Dipolar and Quadrupolar Interactions

It was shown early how the hyperfine coupling can affect the MR signal of a given spin ensemble. Now, consider how a MR spectrum is affected by more general interactions: The magnetic dipoles and electric quadrupoles interactions.

If two nuclear spins are separated by a distance \vec{r} , the dipolar interaction will create an additional internal magnetic field $H_{int} = \mu_N/r^3$ (where μ_N is the nuclear magneton). The order of magnitude of this term is about a few Gauss, but even a small field like this (when compared to the external magnetic field) can change the precession rate of the spins. That is the reason why

the spectrum is not just a singularity in the resonance frequency but rather it spreads out through a range of frequencies around ν_0 (i. e. the spectrum has a sizable linewidth).

The electronic lattice around the nuclear spin also contributes to the Hamiltonian with a term proportional to the electric field gradient (EFG). The nuclear spin $\frac{1}{2}$ has a spherical charge distribution and so are unaffected by quadrupolar effects, but nuclei with spin higher than $\frac{1}{2}$ have a quadrupolar moment Q which interacts with the electrical field gradient. Such interaction is given by:

$$V_{a,b} = \frac{\partial^2 V}{\partial x_a \partial x_b}, \quad (2.1.8)$$

where V is the electrostatic potential at the nuclei center. The quadrupolar Hamiltonian is given by:

$$H_Q = \frac{eQV_{zz}}{4I(2I-1)} \left[(3\hat{I}_z^2 - \hat{I}^2) + \frac{|V_{xx}| - |V_{yy}|}{|V_{zz}|} (\hat{I}_x^2 - \hat{I}_y^2) \right], \quad (2.1.9)$$

in which the term $\frac{|V_{xx}| - |V_{yy}|}{|V_{zz}|}$ is called the asymmetry parameter of the EFG and is represented by η . The quadrupolar hamiltonian is interesting in the sense that no external magnetic field is needed to break the degeneracy of the energy levels. For a sample with strong EFG, Nuclear Quadrupolar Resonance (NQR) can be done. The degeneracy is lifted by EFG between the states $m = \pm\frac{1}{2}$, $m = \pm\frac{3}{2}$, $m = \pm\frac{5}{2}$ and so on. An energy diagram for the simplest case $I = \frac{3}{2}$ can be seen in Fig. 2.4.

The central resonance peak is called central transition and the other ones are named satellite transitions. The quadrupolar character is of the second order for the central $-\frac{1}{2}$ to $\frac{1}{2}$ transition but it is proportional to the order of the transition otherwise. In other words, the intensity of the lines became attenuated as the distance (in frequency or field) to the central line grows. The linewidth is also increased for higher transition satellites.

Also, there is a special kind of magnetic resonance that may happen when the system undergoes a magnetic ordering: The so-called Zero Field NMR. This can be done even without an external magnetic field applied but is different from NQR in the sense that, on the former, the degeneracy is lifted by an EFG, i.e., magnetic field is absent. On Zero Field NMR, the magnetic field is internal

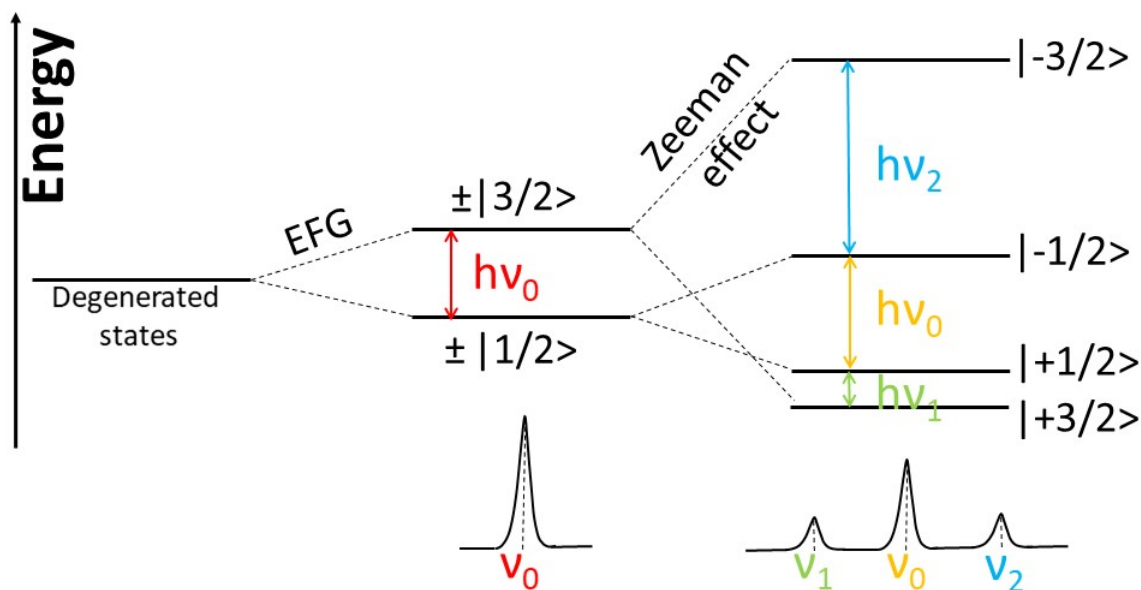


Figure 2.4: Energy levels of a $\frac{3}{2}$ nuclear spin. The EFG splits the levels $|\pm\frac{1}{2}\rangle$ and $|\pm\frac{3}{2}\rangle$, which gives rise to one absorption at ν . The Zeeman effect (under external magnetic field) further breaks the degeneracy between + and – levels, giving rise to more transitions.

to the sample and it is responsible for lifting the degeneracy by Zeeman interaction.

2.2 NMR 101

Since MR spectroscopy is based on the very same phenomena, all the theory previously presented in this chapter can be generalized for NMR. With this in mind, this section is devoted to explaining the particular behavior of the nuclei spin and how such behavior can be translated into an NMR spectrum. However, it is worth pointing out that a nuclear spin has 1831 times **less** energy than an electron spin, so, detecting a nuclear spin signal is significantly harder than an electronic one.

Later on in this section, details on the detection equipment are discussed, but there are three very basic NMR components that must be discussed here: The magnet, the probe, and the coil detecting solenoid. It is worth pointing that the magnet for an NMR experiment is not a regular superconducting magnet, as one may have in a MPMS. Although it is possible to measure NMR

inside a MPMS, a much more **homogeneous** magnetic field is desired and necessary. If the magnetic field is not homogeneous enough, different parts of the sample may essay distinct magnetic field strength, which can be quite hurtful for an NMR experiment since it can cause a spurious broadening in the spectrum (that in some cases is already large).

The probe consists of a long non-magnetic tube. The top stays out of the cryostat, while the bottom, which contains the mounted probe along with the tank circuit. The part that contains the sample must be inserted exactly in a position to match the center of the magnet, to have the most homogeneous possible magnetic field. Such position may be determined with millimetric precision, and, to do so, experiments on a standard sample must be performed. Basically, the spectrum of the sample is taken for different positions and the signal response determines the most homogeneous position. This is often calibrated with a well known standard sample. A representation of the probe position inside an NMR cryostat is presented in Fig. 2.5a, while the details of the probe itself are shown in Fig. 2.5b.

The third and maybe the most vital part of an NMR experiment is the coil. It consists basically of a metallic enameled wire winding as a solenoid that wraps the entire sample. The terminations of the wire are connected to the RLC circuit, making it a tank circuit (more details on this chapter). It must be noted that the coil is responsible not only for the inductivity of the circuit but also for a significant part of the resistivity. When performing solid-state NMR experiments, like the ones presented in this thesis, the coils are manufactured for each different sample and some care must be taken: Firstly, it is vitally important that the coils cover all the sample extensions. As will be seen later, the coil is responsible for applying the radiofrequency magnetic field to the sample. As happens with the field from the magnet, the RF magnetic field must be as homogeneous as possible and so border effects, which happens when part of the sample is out of the coil, can completely ruin an NMR experiment. It is worth to point out that the probes for solid state NMR are especially designed for this kind of experiments. A detail lies in the capacitors, that must be variable, to ensure the frequency tuning, and cryogenic, to ensure that they will not freeze and consequently break at low temperatures. In this sense, the perfect coil is a compromise between

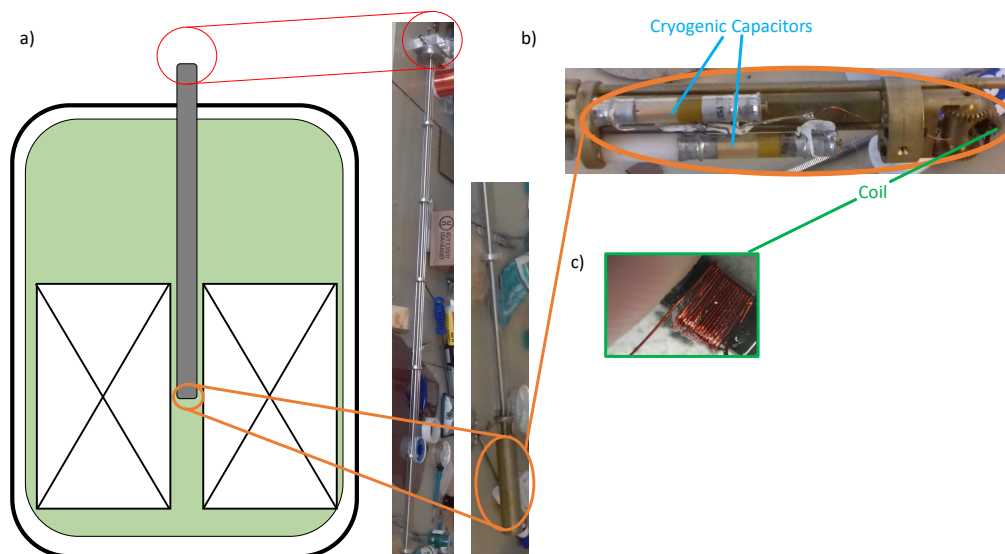


Figure 2.5: a) Scheme of a closed-cycle cryostat. The probe must be in the most homogeneous magnetic field region, typically near the center of the magnet. The red and orange circles is zoomed into b), which is a photo of a probe used in the experiments. The top posses the leadings to the spectrometer, while the brass cap at the bottom end prevents the sample to accidentally fall inside the cryostat and also works as a Faraday's cage shielding. c) Stands for a picture of a copper coil. Although this is not the best example of a sample, due to the crossed turns, which induced inhomogenity in the magnetic field.

filling factor and magnetic field homogeneity. The perfect condition would be a complete filling factor, but only near the coil center.

Second important point is that the sample may not be allowed to move inside the coil. If the sample is moving, the magnetic field, again, not constant during an experiment, which can (and probably will) induce a spurious signal. Also, care must be taken on how the sample is prevented from moving inside the coil. Using glue may induce unwanted uniaxial pressure or stress in the sample, which is not desired since it can change the physical properties of the samples.

Thus, supposing everything is fine with the magnet, the probe is positioned at the right height and is not made of ferromagnetic material, and also that the coil has been prepared with care, one can finally moved to take the NMR spectrum of a given nucleus. Hereafter, it will be shown the movement of an atomic spin translated into a signal and then into a spectrum. An example of coil is shown in Fig. 2.5c.

It was already stated, but it is good to point out again, that a spin, nuclear or electronic, behaves like a small magnet. In the presence of a strong magnetic field, which is provided by the superconducting magnet, this small magnet probe a perturbation and thus start “moving”. One may know for experience that in the presence of a magnetic field, magnetic materials will start moving towards that field direction. This is more or less the principle of a fridge magnet, which stays attached to the fridge, no matter what. However, the nuclei spin does not behave like a fridge magnet for a simple reason: The nuclei inside the material are not allowed to move. So, the nuclear spin “wants” to move and get closer to the magnetic field, but it is bounded “inside” the nuclei. In the macroscopic world, there is an object that has more or less the same principle: A compass needle. The needle would move towards the north pole if it was free to move, however, since it is bounded to the compass, the only thing it can do is to spin around.

This is the same case of the nuclear spin: The spins around the direction of the magnetic field, in a precession motion, almost like a spinning top. The precession frequency depends basically on the magnetic field strength and is named as Larmor frequency. It defines the gyromagnetic ratio of a nucleus (for more details, Appendix D and sections 2.3.2 and 2.3.3). For this moment, however, it is sufficient to understand that the higher the Larmor frequency is, the stronger the response signal will be.

The fact that magnetic field impacts the Larmor frequency have a severe consequence: Large molecules and even solids may have a local magnetic field. By that, one can understand a magnetic field that is generated by some part of the molecule or solid. Another part of it may feel this field and have the Larmor frequency changed. Note that this effect has the very same origin as the inhomogeneity of the external magnetic field, but unlike the former, it is not to be cast aside, since it is not a spurious effect, but a real feature of the sample/molecule. Also, the molecular field is used to explain many features in high-resolution NMR, which is not the main concern of this thesis.

One important thing to keep in mind is that a conventional NMR experiment has approximately

10^{17} spins precessing. So, one can treat this ensemble of precessing spins as a net magnetization on the sample. That is another reason why the coil is crucially important to the experiment: Changes in the net magnetization may (and will) induce a voltage in the coil. This voltage is amplified and stored as a dc voltage versus time signal and this is the NMR data. This voltage *versus* time signal is submitted to a Fast Fourier Transform (FFT) and the time domain is converted into the frequency domain, which is defined as an NMR spectrum. An example of the process is illustrated in Fig. 2.6a.

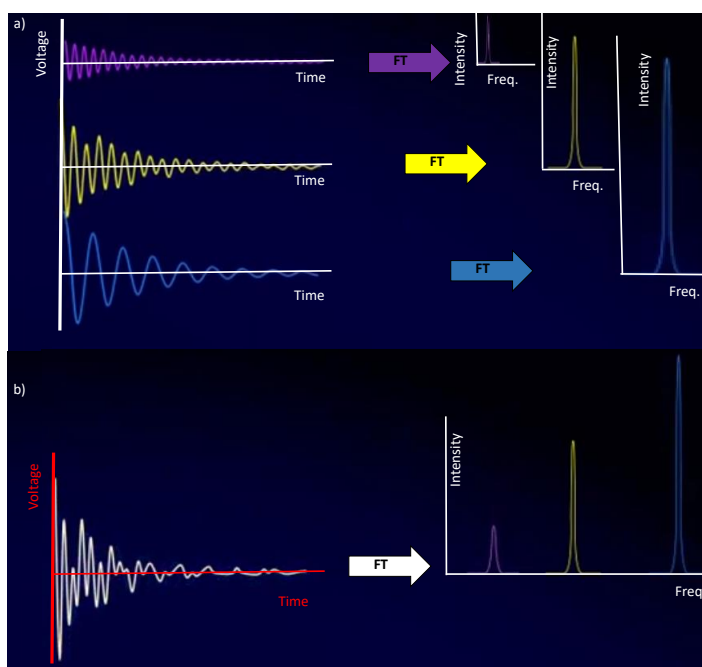


Figure 2.6: a) Voltage versus time signal collected from the NMR coils when measuring a given nucleus of interest. The signals are submitted to FFTs and then converted to the frequency domain. b) Sum of the three signals from a), which is typically the result observed in an NMR experiment. By submitting the signal to a FFT, the results in the frequency domain are observed. Normally, the individual separation of each part of the molecule can be separated only by high-resolution NMR experiments.

But what would happen if different spins, of the same nuclei, have distinct internal fields due to molecular internal magnetic fields? In this case, each of them will produce a different voltage response, but since a conventional NMR experiment has just one coil and just one sample, the signal is composed by the N different signals that N different clusters of spins would generate, as depicted in Fig. 2.6b. Fortunately, the FFT is capable of separating them into quite distinct peaks

in the NMR spectrum, since each internal field gives rise to a distinct chemical shift, which will be explored with more details shortly in this chapter.

The different chemical shifts are the key to high-resolution NMR, i. e., NMR performed in molecules to determine the types of bonds and atomic distances. In this type of NMR, generally quadrupolar effects and conducting electrons effects are ruled out and the sample response is purely magnetic (due to Zeeman effect). This was not exactly the case for solids. In general, a small internal magnetic field in solids is hidden by large EFGs. The result of this strong EFG is that all spins in the ensemble has virtually the same effective magnetic field and thus precess with the same frequency and produces the same voltage *versus* time signal, leading to a homogeneous spectrum. The downside is that EFG broadens the spectrum, increasing the linewidth.

NMR in solids, or solid-state NMR, is sometimes referred in the literature as low-resolution NMR. It is worth emphasizing that “low-resolution” stands for a small resolution in the time domain and has nothing to do with the experiments sensitivity (which is virtually the same as high-resolution NMR).

Another fundamental difference is that high-resolution NMR often is employed to measure the hydrogen site. Since hydrogen has the highest gyromagnetic ratio on the whole periodic table, their nuclear spins are more susceptible to the external (molecular) magnetic field, giving rise to more separation in the spectra than other atoms. On the other hand, low-resolution experiments can be applied to virtually any atom in the periodic table, even ones with a small gyromagnetic ratio, as Sb or even Y.

It is important yet to point out that, while both experiments are a different matter of performing NMR, they give rise to very distinct results. Researchers of high-resolution NMR are often interested in molecular distances, bonds, and J -coupling, while solid state NMR excels at obtaining hyperfine couplings and relaxation rates. In this sense, both are complementary stances of the same technique. Hereafter, the focus will be given to pulsed solid state NMR.

2.2.1 Chemical and Knight Shift

The NMR shifts are defined as a displacement from the expected position (in frequency or field) of the absorption line due to parameters of the lattice. Both arise from the interaction of the nuclei with the electron's angular momentum. The chemical shift is the interaction with the orbital component while the Knight shift is associated with the spin component. Typically, the first is temperature independent, while the latter depends on T . While the chemical shift is very important at biology NMR, since its capability to determine the structure of substances in a very precise way, this thesis sticks to discussions of the Knight shift, which has an origin that interests the most: The hyperfine coupling.

The Hamiltonian of the hyperfine coupling is:

$$\hat{H} = \hat{I} \cdot \hat{A} \cdot \hat{S}. \quad (2.2.1)$$

where A is the hyperfine coupling matrix. In the presence of a magnetic field, one must add the Zeeman Hamiltonian which leads to an effective \hat{H}_{eff} :

$$\hat{H}_{eff} = \mu_0 \gamma \hat{I} \cdot \vec{H}_{eff} = \mu_0 \gamma (1 + K) \hat{I} \cdot \vec{H}_0, \quad (2.2.2)$$

in which K is the Knight shift. Another important conclusion is that K varies linearly with the electronic magnetic susceptibility. In other words, if one plot K versus χ , the angular coefficient of the straight line is proportional to the hyperfine coupling A , such that:

$$K \propto A \chi + K_0, \quad (2.2.3)$$

where K_0 is a constant. This is known as the Clogston-Jaccarino relation.

At some cases, A can be exchanged by B . Note that A and B (direct and transferred) hyperfine couplings can be measured by NMR experiments, depending on which electron is contributing to the magnetic susceptibility and which nuclear site's Knight shift is taken into account.

As an example, suppose a given material XY , where X is an atom and Y is an other. Suppose also that it has a sizable magnetic susceptibility and it is strongly governed by electrons from X . If one measures K for X nuclei, the Clogston-Jaccarino relation will lead to coupling constant A . Instead, if K for nuclei Y was measured, the relation would lead to coupling constant B . In this work, mainly on $CeMIn_5$, the electron which contributes to the magnetic susceptibility comes from Ce , while the Knight shift was measured at In site, leading us to the transferred hyperfine coupling between Ce and In .

The Knight shift can be determined experimentally from the NMR spectra by:

$$f_{obs} = \gamma H_0(1 + K). \quad (2.2.4)$$

Eq. 2.2.4 needs to have an additional term σ for the chemical shift, but generally, in metals, thus $K \gg \sigma$, so that the approximation is still valid.

2.2.2 Controlling the spin ensemble with pulses

The spin ensemble is responsible for the nuclear magnetization of the samples. The core of pulsed NMR experiments is that such magnetization can be controlled by RF pulses. The calculation on how this can be exactly done is performed in Appendix D, but the main results obtained will be discussed hereafter in this section, so that, a few arguments will be provided without proof to make the reading more pleasant to non-specialists.

There are two parameters to be controlled in an NMR RF pulse: The power (intensity) and length (in time). These parameters are used to create two relevant pulses: The short pulse (90 degrees or $\frac{\pi}{2}$ -pulse) and the long pulse (180 degrees or π -pulse). Their names are quite proper since the effect of the first is to rotate the magnetization by 90 degrees, while the second rotates the pulse by 180 degrees. In an equilibrium situation, i.e., without any pulse applied, the net magnetization of the spin ensemble remains pointing towards the magnetic field direction.

For the sake of simplicity and without loss of generality, consider $\vec{M}_0 = M\hat{z}$. If a short pulse is applied in that situation, the magnetization rotates 90 degrees and stands directly in the xy plane. If the system is allowed to rest after this pulse, i.e., no more pulse is applied, the hamiltonian evolution shows that the magnetization stays forever rotating in the xy plane. This result is obtained through an approximation: A spin does not exchange energy, which is a false assumption.

There are two effects however that are not captured by the set of equations presented in Appendix D since they involve a non-conservative process of energy exchange with the lattice:

i) there is coherence loss over time;

ii) there is a change in the spin populations even in the absence of RF pulses. In other words, after the short pulse, the magnetization does not lays forever on the xy plane, but it decays and tends to realign with H_0 . Such decaying is exponential as shown on Fig. 2.7a and is governed by the spin-spin relaxation time T_2 and the spin-lattice relaxation time T_1 :

$$M_{xy}(t) = M_{xy}(0)e^{-\frac{t}{T_2}}, \quad (2.2.5)$$

$$M_z(t) = M_0 \left(1 - e^{-\frac{t}{T_1}} \right). \quad (2.2.6)$$

In the former equations, 2.2.5, the energy is conservative in the spin system, what happens is that the individual spins have different angular velocities around z -axis due to sample inhomogeneities, as shown in Fig. 2.7b

In the second process 2.2.6, the energy is not conserved on the spin ensemble. Since the ground state, parallel to z -axis has lower energy than the plane, the spins must “get rid” of this additional energy to the lattice. The relaxation processes do not happen independently, but simultaneously, so if one would sketch the spacial magnetization returning to z -axis after a 90 degrees pulse, it would look like Fig. 2.7c. The relaxation processes require complex pulses sequences to measure different properties of the systems of interest, as the examples on the next section.

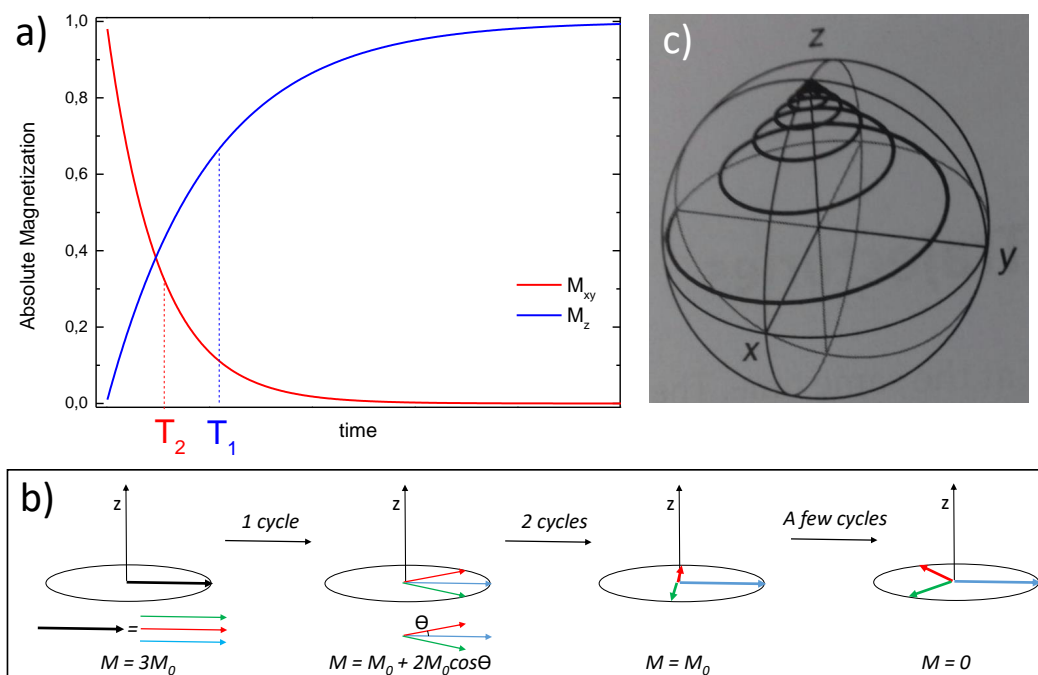


Figure 2.7: a) Magnetization *versus* time curves for M_{xy} (red), which gives access to T_2 , and M_z (blue), which provides information associated with T_1 . b) Depicts the process of coherence loss. In the first sketch to the left, all spins are pointing at the same direction, thus the magnetization on the plane is maximum. As the system evolves in time, spins come across the coherence loss process and the transversal magnetization (M_{xy}) vanishes. This process is not independent from spin-lattice relaxation, which means that the modulus M is also reduced. The total magnetization is shown in c), reproduced from [42].

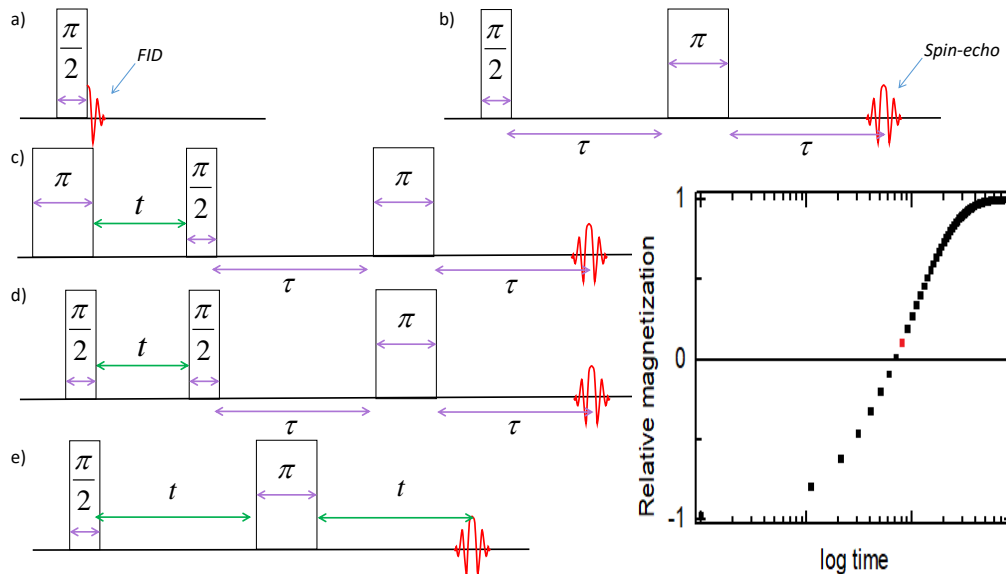


Figure 2.8: Pulse sequences for different kind of NMR experiments. *a)* is the simplest one to obtain the Free Induction Decay (FID), which gives rise to the NMR spectra after a Fourier Transform. *b)* is the spin-echo (Hahn-echo), which also results in the NMR spectra but with more time resolution for faster relaxation times, as described in the main text. *c)* is the inversion recovery sequence for T_1 and *d)* the saturation recovery, also for measuring T_1 . *e)* Depicts the sequence employed for the measurement of T_2 . The inset shows the z-axis longitudinal magnetization M_z versus time as a log scale for a T_1 measurement, as described in the main text.

2.2.3 Radiofrequency Pulse Sequences

Hereafter, the NMR pulse sequences employed to obtain the results in this thesis are discussed. There is virtually an infinite number of pulse sequences one can employ to access excited states, forbidden transitions, out-of-resonance process, J -couplings, and much more complex properties. Here, however, only the simplest cases are analyzed and depicted in Fig. 2.8. Panel *a)* stands for the most simple measurement one can perform to obtain an NMR spectrum: The Free Induction Decay (FID). In this kind of experiment, the acquisition is performed just after a simple $\frac{\pi}{2}$ pulse. The magnetization changes as Fig. 2.7c and such changes are picked up as a dc voltage in the coil. Therefore, when the decay is very fast, i.e., the T_2 relaxation time is short, this method would not be fast enough to measure, since the spins might lose coherence before the measure is performed. In such cases, it is possible to employ the spin-echo sequence, depicted in Fig. 2.8b to overcome the coherence loss problems.

The spin-echo applies a second π pulse in a time τ after the first one, which is used to regain

the spin coherence. To illustrate that, imagine that two individual spins are precessing on the xy plane clockwise and that the velocity of the first spin ω_A is higher than the velocity of the second one ω_B . After the time τ , spin A changed its position by θ_A , while spin B changed θ_B . When they move backwards, after the same time τ , spin A would have moved $-\theta_A$, and will be at its origin just after the 90 degrees pulse. The very same happens to spin B and any other spin in the system regardless of its angular velocity. So, 2τ after the first $\frac{\pi}{2}$ pulse, all spins will refocus and regain coherence. At this time, the acquisition is made for maximum signal.

A variation of this method is the Carr-Purcell sequence, in which the π pulse is repeated a great number of times before the acquisition. Although powerful, this technique was not applied to the experiments in this thesis, given the huge time it takes and since the samples presented a measurable signal using simpler methods.

To measure spin-lattice relaxation time T_1 there are two possible pulse sequences: The inversion recovery and the saturation methods (Fig. 2.8c and Fig. 2.8d, respectively). Both of them consist of applying a pulse before an echo measurement. For the former, a π pulse is applied while for the second, a $\frac{\pi}{2}$ pulse is used. The π pulse would invert all spin population from the up state to the down state, then a time t waits before the echo and when the measure is done, the first point to the left in Fig. 2.8c inset. If this time t is increased by a small amount, the magnetization measured will be a bit smaller, giving rise to the second point on the graph. This happens because while t is waited the spin ensemble is relaxing from $|\beta\rangle$ to $|\alpha\rangle$. So, after the first $\frac{\pi}{2}$ pulse on the echo sequence, the spins will not be exactly in the plane. The more one waits, the more out of the plane the spins are and the weaker is the signal. Eventually, a time will be reached in which the magnetization will be the majority in the plane after t wait, and so no signal is observed. As t keeps increasing, M starts to increase again (the purple point in Fig. 2.8c inset), and afterward it will increase until enough time for the spins to relax completely after t waits. At this point, saturation is achieved. Any measure waiting more time than this will result in the very same magnetization value.

The saturation method follows the very same concept but starting with a $\frac{\pi}{2}$ pulse, implying that the “negative” magnetization branch does not happen. Instead, one sees the graph depicted in Fig. 2.7a for magnetization in z -axis versus time. This saturation method is, in general, less precise than the inversion recovery. However, for samples with fast spin-lattice relaxation, often one cannot inverse all spins. For this cases, saturation method is indicated.

For measuring T_2 one would just need to take sequential echos increasing the time constant τ between the pulses. As result, as more time passes, fewer spins will refocus after 2τ and the magnetization on xy plane will drop, as depicted in Fig. 2.7a.

Physically speaking, T_1 is an important measurement in solid-state NMR since it is quite related to internal fields at the atomic site. If the field fluctuates with a correlation time τ_0 , the T_1 can be anisotropic and has the expression:

$$\frac{1}{T_{1,i}} = \frac{3}{2}\gamma^2(h_j^2 + h_k^2)\tau_0, \quad (2.2.7)$$

where i, j and k are the crystallographic directions and h means the strength of field fluctuations. Such fluctuating magnetic field arises from the hyperfine interaction with the electronic spins, as shown by Moriya [53], then it is possible to rewrite the eq. 2.2.7 as:

$$\frac{1}{T_{1,\alpha}} = \frac{\gamma^2 k_B T}{2\mu_B^2} \lim_{\omega \rightarrow 0} \sum_{\vec{q}, \alpha' \neq \alpha} |A_{\alpha', \alpha'}^2| \frac{\chi_{\alpha', \alpha'}(\vec{q}, \omega)}{\omega}. \quad (2.2.8)$$

$\chi_{\alpha', \alpha'}$ is the component of the imaginary electron spin susceptibility with wavevector \vec{q} and frequency ω . Note that this expression refers to the A.C. magnetic susceptibility. $A_{\alpha', \alpha'}$ stands for the components in the hyperfine coupling matrix and the limit of small ω values can be used since the Larmor frequency is in a much lower energy scale than the other fluctuations.

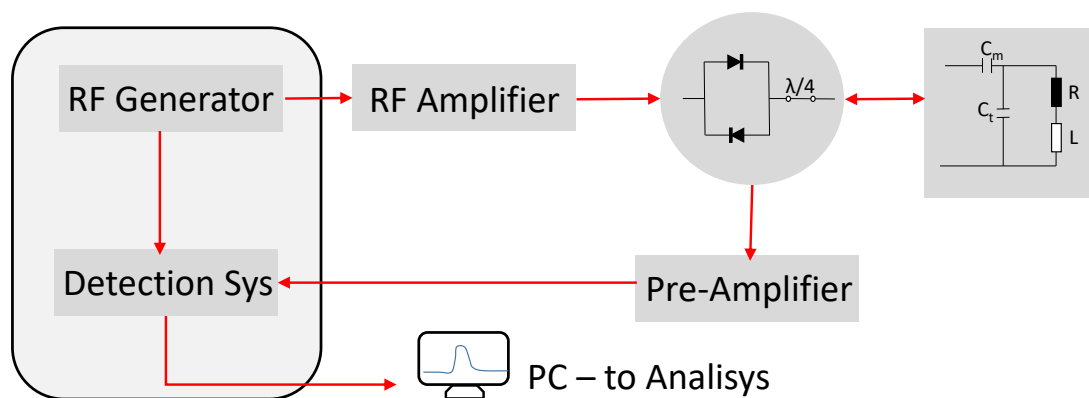


Figure 2.9: Block diagram of the NMR experimental configuration, described with details in the main text.

T_1 is also related to the density of states at the Fermi level by

$$\frac{1}{T_1 T} \propto N(E_F)^2. \quad (2.2.9)$$

2.2.4 Fundamentals of NMR Experiments

The diagram of the spectrometer design is shown in Fig. 2.9.

The RF pulse, generated inside the spectrometer, must be amplified to reach the desired power levels, in an opposite process that happens on the ESR circuit attenuator. The power can be as high as 1 kW. The pulse strength inside an NMR solenoid can be calculated as [49] $H_1 = \sqrt{\frac{10PQ}{\nu V}}$, in which P is the power and ν the frequency of the microwave. Q is the quality factor of the tank circuit and V the solenoid volume. The duplexer works as a circulator allowing the signal to pass from the amplifier to the coil and from the coil to the detection system. This can be done by using two diodes in parallel but in opposite directions. In series to this diodes is a piece of coax cable with length equal to $\frac{1}{4}$ of the RF wavelength, which is called quarter-wave cable. This cable can change its impedance according to the incoming RF power since the amount of waves reflected depends on the impedance match. The effect is that the quarter-wave cable works like a switch: When the signal comes from the power amplifier it opens and no signal goes to the detector. When the signal comes from the coil it closes and the signal goes to the detector.

2.2.5 The Tank Circuit

The changes on the nuclear magnetization of a sample during a NMR pulse sequence are tiny. To be more specific, in the order of some microvolts or even nanovolts. Then, a very sensitive circuit must be used to detect it. Thus, we make use of the resonant properties of a RLC circuit, which is also referred as tank circuit.

C_m and C_t stands respectively for the matching and tuning capacitors, L is the coil which carries the sample inside and will be responsible for providing the H_1 magnetic oscillating field and also pick up the coil signal. It's always desired that the coils are build in such a way that the sample is slightly tight inside. So that, fewer space will be blank, increasing the so called filling factor, which leads to a better signal: Since the distance between the coil and the sample is small, the magnetic fields are more intense and homogeneous.

In general, the circuit have an impedance of $50\ \Omega$, which matches the coax impedance. This would lead the capacitor values to be in the range of several picofarads. Usually, cryogenic capacitors on the 3-100 pF range are used. Since temperature can change the nominal values of the components, its desirable to have capacitors with such wide variation range.

For the coil, the inductance is approximatly given by $L = \frac{\mu_0 N^2 A}{l}$. Typical coils are made of copper, although silver coils could also been used since Cu has a strong and characterist NMR signal, with 4 to 6 mm lenght and 10 to 15 turns. However, all these parameters can change a lot under different conditions, such as sample size and orientation. In practical terms, manufacturing NMR coils is more a try and error process than predicting the exact one by the formula above.

The Detection System

The detection system mentioned in Fig. 2.9 will be discussed in more details now. A diagram of its operation is shown in Fig. 2.10. The amplifier and pre-amplifier before the heterodyne are low-noise electronic devices whose function is to increase electronically the weak signal which comes from the samples to higher levels of voltage so that the conventional electronics might work ef-

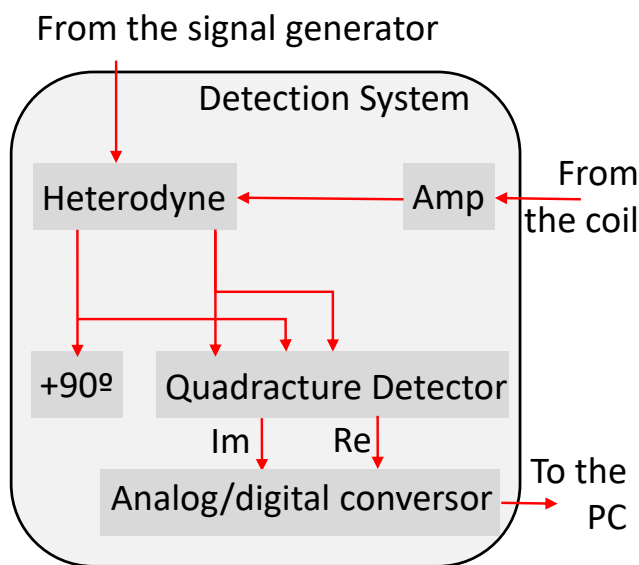


Figure 2.10: Block diagram of the NMR detection system, described with details in the main text.

fectively with them. The heterodyne do more or less the same thing, but in frequency domain: It takes the signal at Larmor frequency and transforms it into an identical one, but at a lower frequency. The responsible for that is an element called mixer. It multiplies the incoming signal by a sine function and as a result, it gets the signal split into two other: One at a higher frequency and another at lower ones, following the relation:

$$2 \cos \theta_1 \cos \theta_2 = \cos(\theta_1 + \theta_2) + \cos(\theta_1 - \theta_2). \quad (2.2.10)$$

The high-frequency signal is filtered out and just the lower one is allowed to proceed.

Now, the next part is the quadrature detection. It is responsible to divide the signal into its real and imaginary parts. This is quite important in NMR since the real part can be associated with one of the axis on xy plane and the imaginary part on the other one. However, to measure both parts one would need to mount the sample inside two coils, orthogonally disposed between each other with two distinct tank circuits. It is already a challenge to mount the sample inside one coil so, fortunately, there is an easier method: The real and imaginary parts of the signal are

dephased by 90 degrees, so, what the spectrometer does at quadrature detection is to duplicate the signal. The signal comes from the sample and its phase is compared with the generated one. The difference of phase ϕ is then attributed to the real part, and a second signal with phase $\phi + \frac{\pi}{2}$ is then created and treated as the imaginary part. These signals are then converted from voltages to digital data and send to the computer for analysis.

Fast Fourier Transform

NMR experiments are performed in time domain, but generally, the analysis should be done and the results are shown in frequency (or magnetic field) domain. This can be achieved by performing the Fast Fourier Transform (FFT) algorithm [54], which computes a discrete Fourier Transform for a sequence of data.

The FT is defined as a transformation from the space t to space ω performed by:

$$F(\omega) = \int_{-\infty}^{+\infty} f(t)e^{-i\omega t} dt, \quad (2.2.11)$$

but a discrete FT does not use a function $f(t)$, but instead a series of points $x_i(t)$, such that:

$$X_i(\omega) = \sum_{i=0}^n x_i(t)e^{-i\omega t}. \quad (2.2.12)$$

Generally, a spectrum is composed of 1024 or 2048 pairs of points in time domain, and doing the discrete FT for any of them could be very time-consuming. The FFT process reduces the time cost of the whole transformation to a couple of milliseconds, by factoring the Discrete Fourier Transform (DFT) matrix into a product of its diagonal terms. The computational time is reduced from $O(N^2)$ to $O(N \log N)$; where N is the number of data points. Considering the 2048 points from the spectra and supposing that the DFT of one point would cost $1 \mu\text{s}$, the FFT process speeds up from 4.2s to less than 7ms!



Figure 2.11: Panoramic view of the NMR laboratory at GPOMS - IFGW - Unicamp.

The usage of FFTs is not restricted to NMR but covers lots of branches in data analysis. The algorithm is considered by many the most important numerical algorithm of the whole history.

Temperature Control

The cryostat used for most of the NMR experiments is a JANIS open cycle ^4He Dewar equipped with a sweepable magnet, capable of achieving 12.1 T. To keep the magnet cold enough, it is inserted into the helium bath. To cool the sample, there is a needle valve between the liquid helium bath and the sample chamber. The cooling power can be controlled by opening or closing this valve and a heater. The inter and outer vacuum chambers ensure thermal insulation.

Some experiments were also performed in an Oxford 11.7T permanent magnet, while developing a PhD sandwich at UC-Davis with Professor Nicholas Curro. The magnet is also inserted in ^4He bath and a liquid nitrogen jacket is used to prevent too much helium boil-off. Apart from this system, a closed cycle JANIS cryostat is mounted inside the magnet. So the sample cooling and magnet cooling are controlled by independent systems.

An analogous cryostat has been employed in the MAS-NMR experiments also reported here for the measurements in the NaYF_4 nanoparticles. The equipment belongs to UFABC multiusers laboratory, and the experiments was performed under a fruitful collaboration with Professor Thiago Branquinho. Such experiments however were performed only at room temperature.

Our experimental setup for NMR experiments at Unicamp is presented in Fig. 2.11.

Chapter 3

The Heavy Fermions of Ce-115 Family

It will be shown in this chapter that CEF has a strong impact on the fundamental properties of Ce-115 heavy fermions, especially the hyperfine coupling between Ce $4f$ electrons and the In nuclei. A general scaling rule between the electronic orbitals (driven by CEF) and the hyperfine coupling is proposed as the main result of the thesis.

3.1 Motivation and Objectives

Electronic correlations and thus heavy electrons may arise under electron confinement. In other words, the more localized an electron is, more likely it is to behave as a heavy electron in this class of materials. Such trend is summarized on the Kmetko-Smith diagram [55], depicted in Fig. 3.1. At the bottom of the figure, there is a representation of the $3d$, $5f$ and $4f$ wavefunction. The $3d$ electrons tend to be less localized, favoring superconductivity while $4f$ electrons tend to be more localized, favoring magnetic ordering. Between them, there are the $5f$ electrons. It is not so simple though, and some $3d$ materials, such as Ni or Co, also favor magnetic states, but the diagram helps to predict some of the fundamental properties of a given system.

Looking at the diagram, one can observe that the magnetic moment increases moving up-left. Ce, U, and some other atoms stand in a very particular position: They are localized enough to increase the magnetic moment of the host materials, but not enough to annihilate unconventional

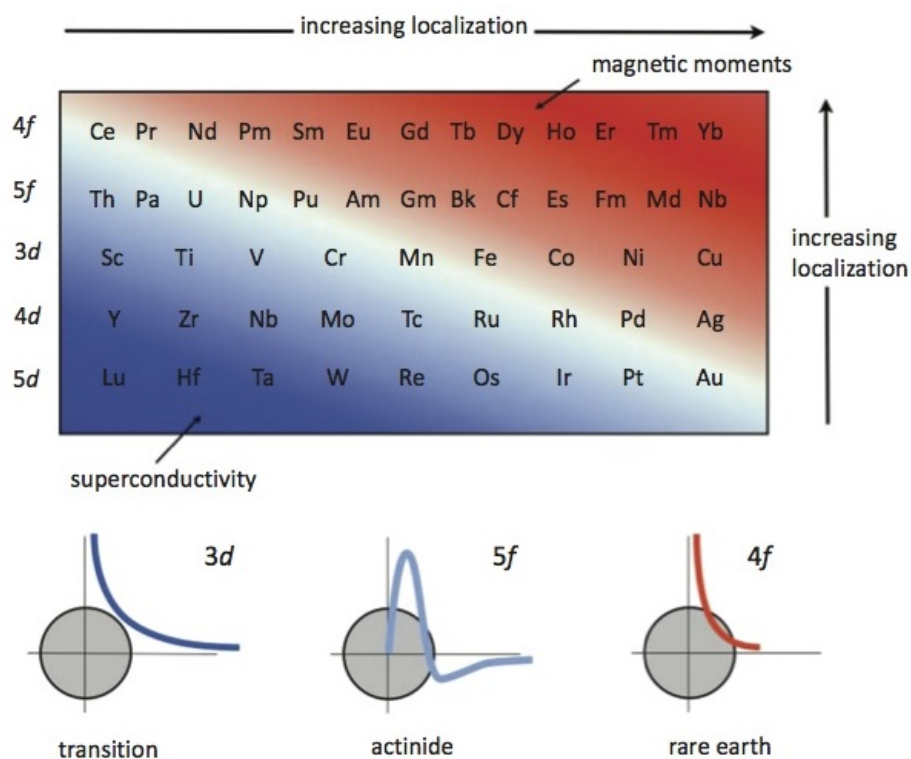


Figure 3.1: Kmetko-Smith diagram of $3d$ to $5f$ elements, reproduced from [56, 57]. Increased electronic localization favors magnetism, while electronic localization tends to favor superconductivity. In the bottom, examples of $3d$, $5f$ and $4f$ are shown, with the first possessing more delocalized electrons while the latter more localized ones.

superconductivity, being excellent systems to study the interplay between magnetism and superconductivity. Furthermore, another advantage of Ce-based compounds is that the atom has only one f electron in the valence shell.

Generally, heavy fermion compounds are conductors and their heavy electrons form a lattice immersed into a sea of conducting electrons. The interaction between localized magnetic moments happens then by a exchange interaction already discussed in chapter 1: The Kondo interaction. The $4f$ electrons of Ce have $l=3$ and $s=\frac{1}{2}$, which leads to a $j=\frac{5}{2}$ ground state and $2J+1=6$ degenerated orbitals, with magnetic moment $M=2.64\mu_B$ [18].

The Hamiltonian of the Kondo model is given by:

$$H = \sum_k \epsilon_k \sigma_{k,\alpha}^\dagger \vec{\sigma}_{k,\alpha} + J \psi^\dagger(0) \vec{\Sigma} \psi(0) \cdot \vec{S}, \quad (3.1.1)$$

where the first term takes into account the electronic hopping, as already observed in the Hubbard Hamiltonian in Eq.1.2.5, and the second term (also referred as ΔH [18]) stands for the exchange interaction, with $\psi^\dagger(0) = N^{-\frac{1}{2}} \sum_i \sigma_{i,\alpha}^\dagger$, which creates a conducting electron, while $\psi(0) = N^{-\frac{1}{2}} \sum_i \sigma_{i,\alpha}$ annihilates it. This term is very similar to Hubbard's U , but the interaction is governed by magnetic (spin) instead of Coulomb (charge) interactions.

Now, it is very important to point out that the single impurity Kondo model treats well the case of diluted magnetic impurities in a metallic matrix. Generally for most heavy fermions, however, it is a bit different: The magnetic moments of cerium are not single impurities but a lattice. So, inside the material, the Kondo effect leads to the development of a long-range coherence. The main change during this low-temperature coherence phase is that the Kondo singlet scatters the electron elastically, conserving its momentum, which leads to a drop in the electrical resistivity. A good example is the case of La-doped CeCu₆ [58]. La is a common silent dopant into Ce-based heavy fermions since La and Ce are iso-electronic, with no electron in the f shells. So, when the percentage of Ce approaches zero, the regime of a dilute magnetic moment is recovered and

the coherence destroyed. Fig.3.2 depicts the electrical resistivity as a function of temperature for $\text{La}_{1-x}\text{Ce}_x\text{Cu}_6$. One can observe that as the Ce concentration x tends to zero, the expected behavior of a Kondo impurity is achieved.

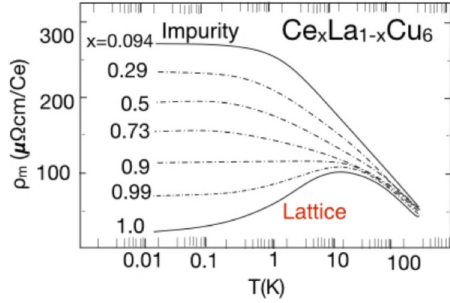


Figure 3.2: Electrical resistivity of $\text{Ce}_x\text{La}_{1-x}\text{Cu}_6$ as a function of temperature for several doping levels, extracted from [58]. The Ce-rich sample establishes a Kondo lattice and the magnetic atoms are not treated as an impurity, establishing the Kondo coherence, as described in the main text. As Ce gets diluted on the sample, the coherence regime breaks up and the magnetic impurity Kondo behavior is recovered.

The interaction throughout the Kondo lattice however carries an antiferromagnetic coupling constant J , which leads to another phenomenon already described in chapter 1: The RKKY interaction. Mott and Doniach [59, 60] have shown that there are mainly two relevant energy scales in heavy fermions: The RKKY, which is proportional to $J^2N(E)$, where J is the coupling constant and $N(E)$ the density of states at the Fermi level, and the Kondo, proportional to $e^{-\frac{1}{2JN(E)}}$. At low $JN(E)$ range, RKKY energy scale prevails and the dominant effect is a long-range antiferromagnetic order, while for higher values of $JN(E)$, the Kondo effect dominates, leading to a non-ordered ground state which can, in principle, be a superconducting one. This scenario is roughly represented by the Doniach phase diagram, briefly mentioned in chapter 1 and depicted with more details in Fig. 3.3. Doniach has also predicted the existence of a quantum critical point in the transition between

the magnetically ordered and disordered phases, which later was confirmed experimentally for heavy fermions like $(\text{Ce,Au})\text{Cu}_6$ and CeRhIn_5 under pressure [61, 62, 63].

Although very effective, it is arguable that Doniach’s scenario does not accurately applied to every possible heavy fermion compound. It seems that something is missing. The main goal of this thesis is to provide the “missing bond” in the model: The crucial role of the CEF effects over the ground state of heavy fermions like Ce-115, which has been turned down so far in the

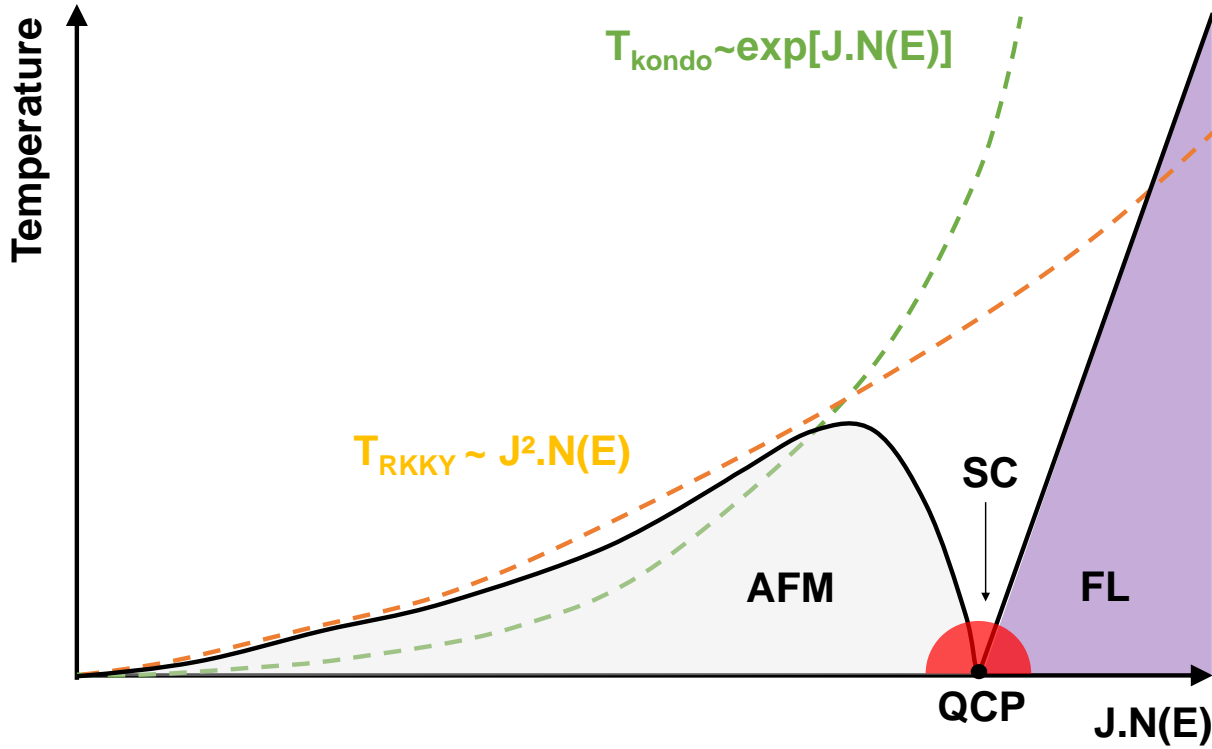


Figure 3.3: The Doniach phase diagram [60], showing the competition between Kondo and RKKY interactions, the former favoring superconductivity and the latter a magnetically ordered phase. Note that at a critical $JN(E)$ value, a Quantum Critical Point (QCP) emerges [64]. It is proposed in the literature that such a QCP would be also necessary for the superconducting phase in HFs [65]. It should be pointed out, however, that the Doniach phase diagram does not capture the CEF effects, but is still a good toy model to understand most physical properties of the heavy fermion materials.

models. It will be shown through a detailed analysis of the hyperfine coupling that, at least for the $CeMIn_5$ family, the CEF has an important contribution. Despite its smaller energy scale compared to Kondo and RKKY ones, it is inherent to form the electronic ground state of Ce, leading to a severe impact on its physical properties as demonstrated in the following sections.

3.2 State of the Art

$CeMIn_5$ crystallizes in the tetragonal structure presented in Fig. 3.4. Note that there are two different sites for indium atoms: One, called In(1), in the cerium planes, and an other, named In(2) along c direction. The system has strong out-of-plane anisotropy (along c axis) which is expected for a tetragonal compound.

The temperature versus concentration phase diagram is shown in Fig. 3.5, reproduced from [66], which was adapted from a series of reports [67, 68, 69, 70]. At ambient pressure, $CeCoIn_5$ and $CeIrIn_5$ are superconductors with T_C of 2.3 K [70] and 0.4 K [68], while $CeRhIn_5$ has an incommensurate antiferromagnetic ordering with $T_N = 3.8$ K. Through substitutions studies at the M site [68], it has been shown that when Rh is replaced by Ir, a commensurate magnetic phase arises co-existing with the incommensurate one as well as with superconductivity. However, for Co substitution, this matter is still under debate. Eventually, upon doping, superconductivity arises.

It has been pointed out by some authors [71] that the ratio $\frac{a}{c}$ of lattice parameters is related to superconductivity. As shown in the

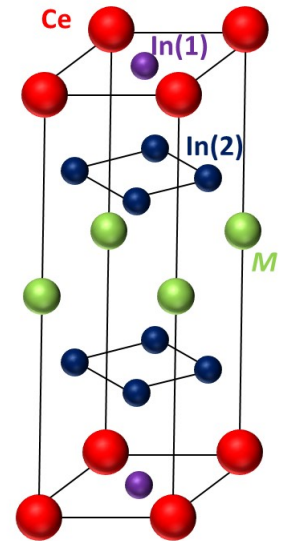


Figure 3.4: Ce-115 unitary tetragonal cell. This is a planar compound alternating between Ce-In, pure In, and M planes, as depicted. Note that there are two possible indium sites: In(1), in the Ce-In plane, which is common in other series of Ce-based heavy fermions as $CeIn_3$ and Ce_2MIn_8 , and In(2), which is outside the Ce-In plane.

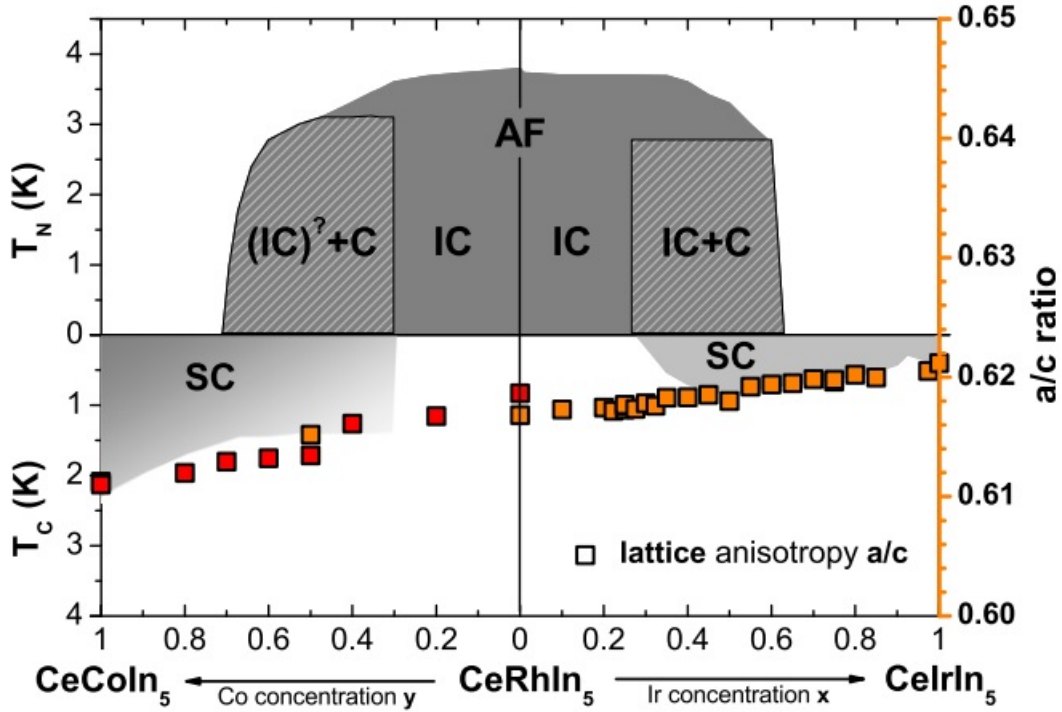


Figure 3.5: Phase diagram of $CeMIn_5$ family, extracted from [66]. Note that the $\frac{a}{c}$ ratio scales well with the superconducting transition temperature T_C outside the magnetic phase, where this scaling breaks down.

phase diagram of Fig. 3.5, it seems that such relation remain valid, but only outside the AFM phase. There is also a breakdown in the Rh-Ir and Co-Rh initial branch of superconductivity, evidencing that the ratio $\frac{a}{c}$ is not a sufficiently good parameter for predicting SC phases in the vicinity of antiferromagnetism. So, in this thesis, it is proposed that another ingredient must be considered: The Crystalline Electric Field (CEF). There are a few examples and prediction on how the CEF modifies the Ce ground state in the literature. A relevant reference is the work of Willers *et al* [66]. They performed X-Ray absorption spectroscopy (XAS) experiments on $CeRh_{1-x}Ir_xIn_5$ to determine the ground state wavefunction of these compounds. It is well known that CEF in this systems leads to a Krammers doublet ground state Γ_7 with:

$$\Gamma_7 = \alpha \left| \pm \frac{5}{2} \right\rangle + \beta \left| \pm \frac{3}{2} \right\rangle, \quad (3.2.1)$$

where the coefficients α and β satisfy the relation $\alpha^2 + \beta^2 = 1$.

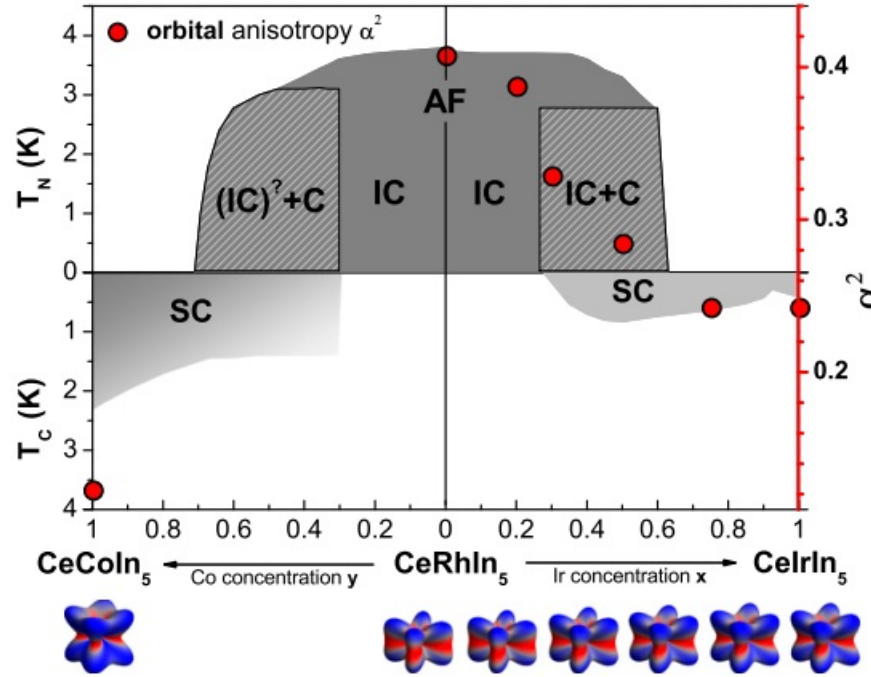


Figure 3.6: Scaling between α and the transition temperature of CeMIn_5 compounds. Note the orbital anisotropy on the bottom of the figure, which means that oblate orbitals ($M = \text{Co}$ and Ir) tend to favor superconductivity, while stronger in-plane interactions ($M = \text{Rh}$) favors antiferromagnetism.

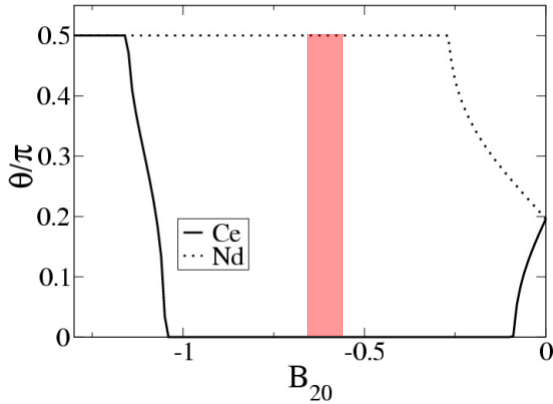


Figure 3.7: Moment direction as a function of B_{20} CEF parameter, extracted from [72]. The discrepancy between Ce and Nd compounds is huge for small values of B_{20} . Typical B_{20} parameters for CeMIn_5 are within the red range as shown.

Willers and coworkers have determined the wavefunction coefficients as a function of the Ir doping and the results are depicted in Fig.3.6 (extracted from [66]), which shows a monotonic evolution of α with T_N and T_C . Also, one can observe the orbital representation for Γ_7 as a function of the doping at M site in the bottom of the figure. It seems to be very clear that when the in-plane interactions are stronger (meaning higher α), AFM is favored. Also, when out-of-plane interactions are stronger, superconductivity usually takes place.

This can be intimately related to the magnetic moment direction inside the solid, as suggested by recent work with neodymium substitution at the cerium site, eventually leading to magnetic frustration [73]. In Fig. 3.7, reproduced from [72], one can observe the momentum direction θ (which represents the angle between the moments alignment with $x - y$ plane) as a function of the tetragonal CEF hamiltonian parameter B_{20} . Note that for a wide range, highlighted, only the substitution of Ce by Nd would “flip” the moment out of the plane. This is an unexpected effect and strong evidence that the CEF itself, which changes upon substitution of Ce for Nd, can alter relevant physical properties and drive changes in the magnetic structure.

3.3 Methodology, Results and Discussion

Hereafter, the main NMR results on Ce-based 115 compounds are depicted. They were divided into two main investigations: The Nd doping at the Ce atomic site in $CeMIn_5$ and the intermetallic substitution of Rh for Ir at the M site.

3.3.1 Sample Growth

In order to grow high quality single crystals of $Ce_xNd_{1-x}Rh_{1-y}Ir_yIn_5$, the metallic flux method has been employed [74]. This method consists of the following steps: First, a stoichiometric ratio of all elements, except indium, is measured and put into an alumina (Al_2O_3) ceramic crucible. Then, excess indium (around 4 times the stoichiometric quantity) is added in small pieces. The crucible is covered with quartz wool and sealed inside a quartz tube. A representation of the setup is shown in Fig. 3.8a. The element chosen as metallic flux generally has the lowest melting point among them. In the case of these samples, the indium is already present in the compound, however, when this is not the case, an extrinsic low melting point element may also be used.

The setup is heated up in an automatically controlled oven following the temperature ramp represented in Fig. 3.8b. Primary, it is heated up from room temperature to 1100 Celsius degrees at a rate of 200 C/h. The mixture is kept at 1100 C for four hours and then the cooling process starts, at a fixed rate: 3 C/h to yield large and 20 C/h to yield small Nd doped single crystals. For the

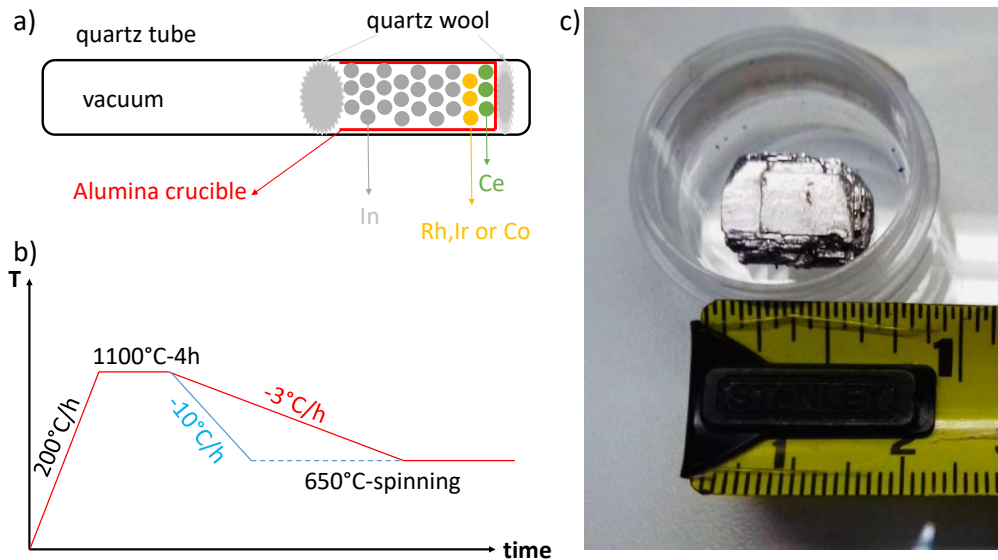


Figure 3.8: a) Illustration of the flux method, used to grow $CeMIn_5$ samples. b) The temperature ramps employed. Surprisingly, larger samples have been obtained through the faster cooling ramp (in blue), at least for the system with Nd doping. c) $CeRhIn_5$ sample grown through the flux method. It has been cut to the typical size of $2 \times 1 \times 0.5 \text{ mm}^3$ and polished to remove the residual indium flux on the surface.

intermetallic doping crystals, only the 3 C/h was used. At 650 C/h , the cooling process is stopped and the samples are removed from the oven. It is important to point out that, at this temperature, the indium flux is still liquid. The sealed quartz tube is then inserted into a centrifuge and rotated at 1500 to 2000 rpm for two minutes. During this time, the system continues to cooldown while the liquid In flux passes through the quartz wool.

After the spinning, the sample is integrally solid and close to room temperature. An example of the final product is shown in Fig. 3.8c.

It is possible and common that some In flux remain on the sample surfaces, and it can be quite prejudicial to an experiment like NMR. That is why it is always recommended to polish the crystals grown by metallic flux method.

The metallic flux growth method is very useful since the withdraw process of samples at high temperatures prevents the growth of unwanted low-temperature phases. The X-ray diffraction

data of $\text{CeRh}_{1-x}\text{Ir}_x\text{In}_5$ in Fig. 3.9 showed a perfect tetragonal phase for all measured crystals, as reported in the literature [75]. There is however a minor presence of metallic In flux detected in some diffractograms (indicated by the red arrows), possibly from interlayer in-flux incursion.

3.3.2 Sample Characterization: XRD and Magnetic Susceptibility

The powder X-ray diffraction (XRD) measurements of the samples were performed in a Bruker Phaser D2 diffractometer with Cu $K\alpha$ radiation ($\lambda = 1.5418 \text{ \AA}$) using a silicon plate with zero background. The 2θ Scan range was set as 15-70 degrees with a step of 0.05 degrees and a count time of 2s. The diffraction pattern was compared with the expected one from the literature for this family [76] and the tetragonal phase was confirmed without evidence of spurious phases. Data is shown in Fig. 3.9.

The magnetic susceptibility experiments were carried out on a commercial Quantum Design PPMS-14T, with an insert for VSM magnetization measurements in the range $3 \text{ K} < T < 300 \text{ K}$, under a magnetic field of 8 T. The samples were attached to the sample holder using Duco cement, which signal was subtracted from the raw data. The sample has been mounted for the susceptibility experiments to have the c axis parallel to the external magnetic field. Results are depicted in Fig. 3.10. The solid lines are fits to the high-temperature data using a mean-field model reported at [72]. The bulk magnetic susceptibility, χ , in $\text{CeRh}_{1-x}\text{Ir}_x\text{In}_5$ varies strongly between 4 K and 300 K, reflecting the localized nature of the Ce $4f$ electrons. For $T > 50 \text{ K}$, χ is well-described by local moments in a tetragonal crystal field, with an effective exchange interaction, as discussed in [72]. This behavior is modified at low temperatures due to the crystal

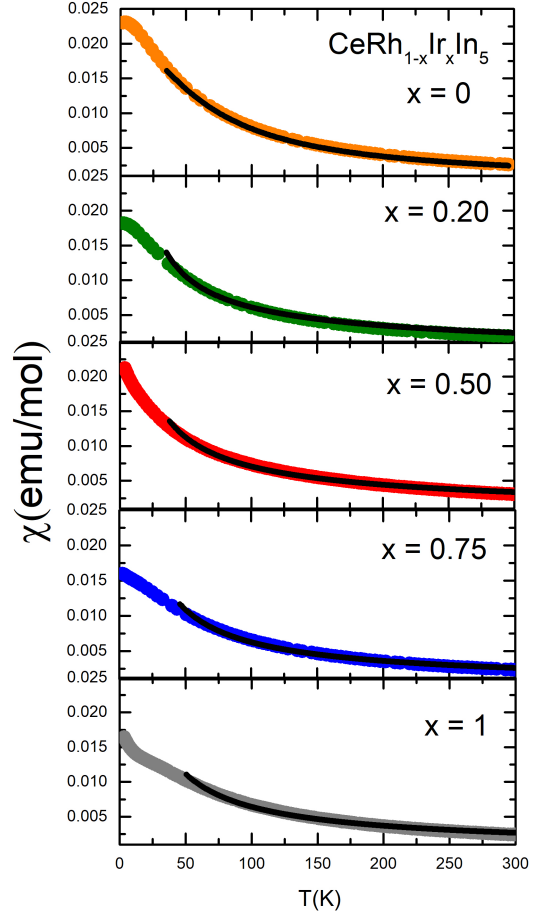


Figure 3.10: Bulk magnetization along c -axis of $\text{CeRh}_{1-x}\text{Ir}_x\text{In}_5$. The solid lines are mean-field CEF fits, from where the α parameter can be extracted.

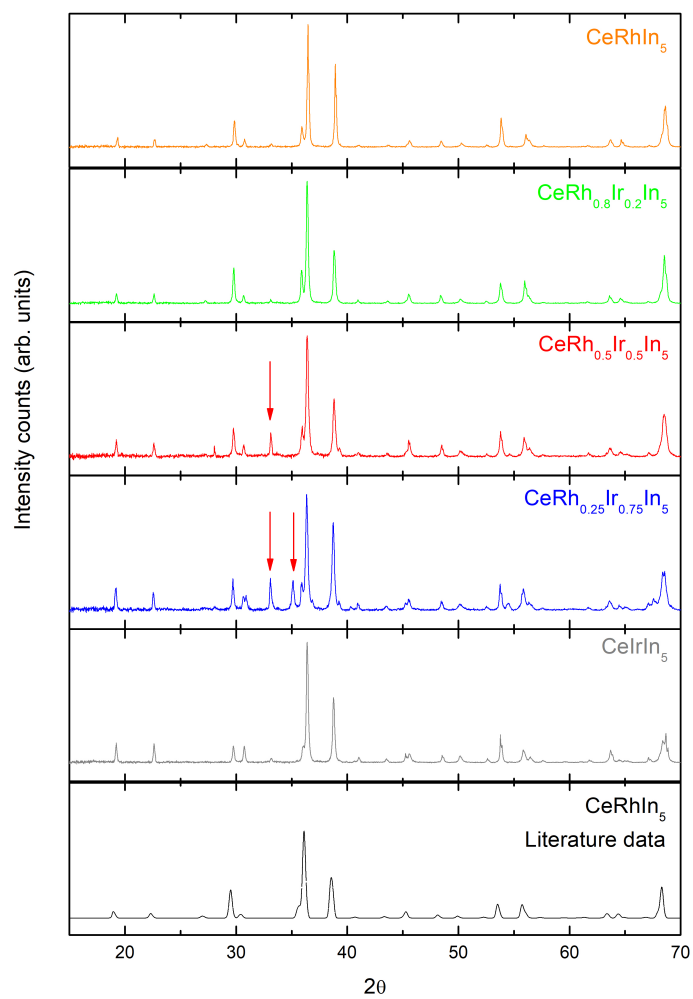


Figure 3.9: X-ray diffraction patterns for $\text{CeRh}_{1-x}\text{Ir}_x\text{In}_5$ samples. Red arrows indicate In flux lines. Literature data from [76] for means of comparison.

field splitting, the Kondo interaction, and the exchange interaction among the Ce orbitals, all of which depend on the doping, x . As x increases the ground state evolves from antiferromagnetic below $T_N = 3.8$ K ($x = 0$) to superconducting below $T_c = 0.4$ K ($x = 1$), with a possible quantum phase transition near $x = 0.3$ [77].

3.3.3 Intermetallic Doped Compounds

Most of the ^{115}In ($\frac{\gamma}{2\pi} = 9.317$ MHz/T, $I = \frac{9}{2}$) NMR experiments displayed in this section were carried out during two visits (in a sandwich Ph.D. program) to the University of California - Davis under the supervision of Professor Nicholas Curro. An Oxford 11.7 T permanent magnet, equipped with a Janis closed-cycle cryostat was used for these measurements. The In NMR spectra were taken between $4\text{ K} < T < 300\text{ K}$, with a TecMag Appolo spectrometer and a 0.3 kW power supply. A few experiments were also performed in the MR group setup at Unicamp, which consists of a Janis open cycle cryostat equipped with a sweepable magnet, with operational capability between $-12.1\text{ T} < H < 12.1\text{ T}$, although the magnetic field used was kept at 11.7 T to ensure consistency. A TecMag RedStone spectrometer and a 1 kW power supply were employed.

The NMR coils for the tank circuit were made with copper enameled (formvar) wires and the tank circuits covered the frequency range of $80 < f < 140$ MHz with at least 20 dB of RF coupling. The coil diameter was chosen to tightly fit the sample dimensions to prevent vibration and improve the filling factor. The external magnetic field was applied along the c direction. The In NMR spectra were obtained using an auto-tuner frequency sweep sequence, with manual tuning being checked out every 2 MHz to ensure the best possible coupling. The spin-echo pulse sequences were set with short pulse lengths (varying from 1.9 and 2.2 μs depending on the sample). Besides short delay times (about 15 ms), due to fast spin-lattice relaxation times were used in most measurements.

Fig. 3.11 presents the ^{115}In NMR spectra at 5 K for a series of different doping levels of Rh in $\text{CeRh}_{1-x}\text{Ir}_x\text{In}_5$ ($x = 1, 0.8, 0.5, 0.25$ and 0). One can observe a severe broadening of the resonance

Table 3.1: In(1) Knight shift (K_1), In(2) Knight shift(K_2), squared Γ_7 coefficient (α^2) and hyperfine couplings for In(1) (B_1) and In(2) (B_2) for the Ce115 family. The α values were extracted from [66] and agrees very well to the values obtained by our magnetization fittings.

x	K_1(5 K)	K_2(5 K)	α^2	B_1(kOe/μ_B)	B_2(kOe/μ_B)
1	8.28	4.2	0.3969	21.4	8.8
0.8	6.89	7.66	0.3844	20	9.8
0.5	6.28	6.23	0.2809	16.7	13.9
0.25	6.27	9.65	0.2401	15	-
0	4.84	10.6	0.2401	13.8	15.8

peaks upon doping, which is a consequence of higher inhomogeneity, due to the mixing of Rh and Ir. Given the tetragonal $CeMIn_5$ structure, one would expect more intense lines for In(2) than for In(1), mainly because In(2) is four times more abundant per unit cell. That is the case of pure $CeRhIn_5$. Interestingly enough, when Ir doping level increases, also the relativity intensity of the peaks become more even, except for the pure Ir compound. The spectra were well simulated by exact diagonalization of the Nuclear Hamiltonian. The fitting equation is fairly complex to be written here, but it basically fits a Lorentzian (or Gaussian) to each of the spectra, by using nuclear properties, and add them up.

Small misalignments concerning $c//H_0$ direction, of about 2 degrees, for the $x = 0.8$, and of 6 degrees for $x = 0.5$, were detected by the simulations. Such deviation is responsible for double In(2) peaks observed in the spectra, e. g. in Fig. 3.11, has no significant impact on the In(1) Knight shift, since the In(1) angular dependence on Knight shift is very smooth for an angle smaller than 10 degrees [50]. Nevertheless, one could not rule out internal twinning but this would rather affect the linewidth, not the Knight shift, which is the main concern here.

The values of In(1) Knight shift, $K_1(5\text{ K})$, are presented in Table I, along with In(2) Knight shift (K_2), both also at 5 K, the α coefficient of the Γ_7 fundamental state squared, and the hyperfine coupling constant for both In sites (B_1 and B_2 of this series which are relevant to our discussions hereafter presented).

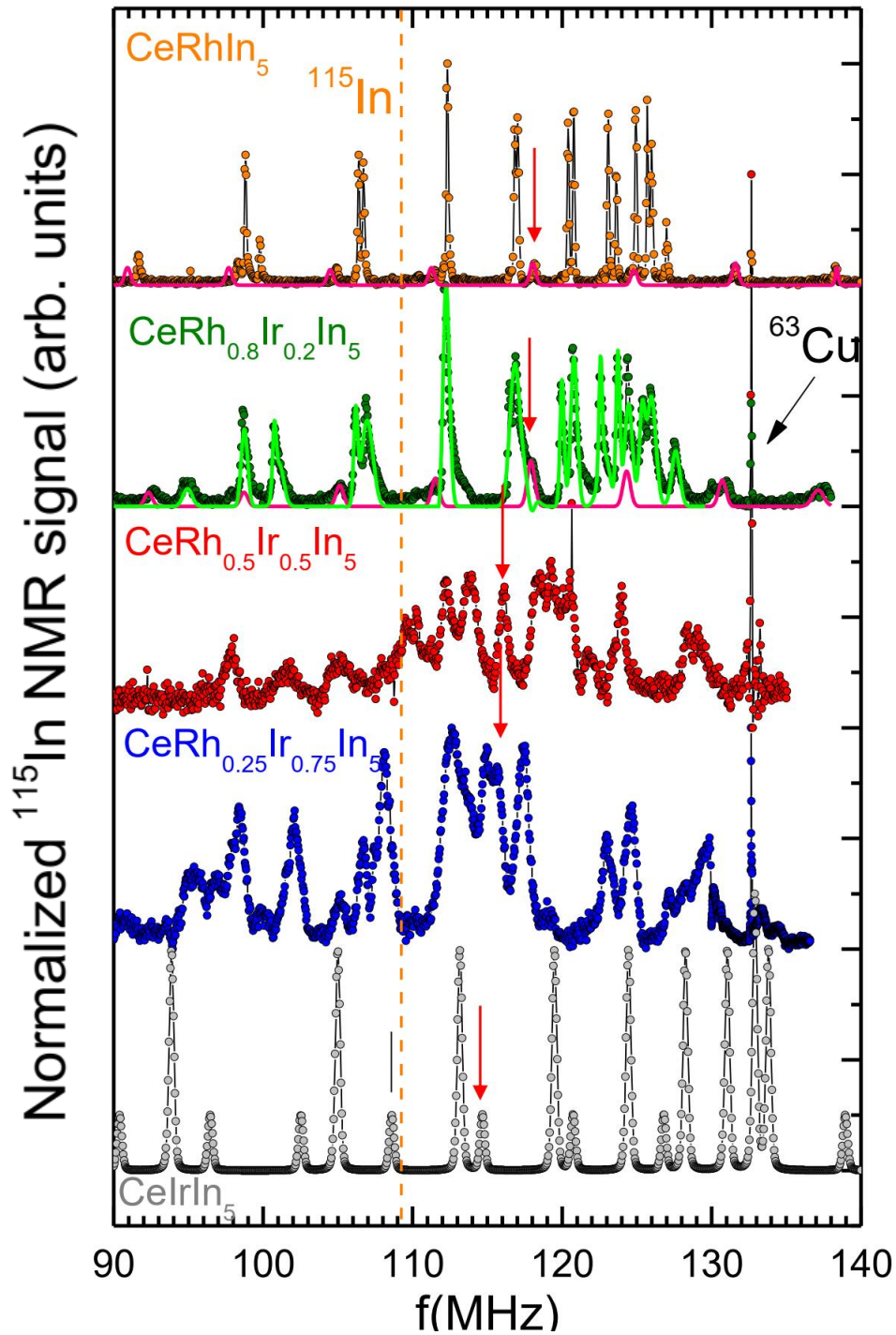


Figure 3.11: ^{115}In NMR spectra of $\text{CeRh}_{1-x}\text{Ir}_x\text{In}_5$ for distinct doping levels at $T = 5\text{ K}$ and with $B = 11.7\text{ T}$. The red arrows indicate the position for the $-1/2$ to $1/2$ spin transition for In(1) site. Multiple lines can be observed due to a small angular deviation from $H_0//c$. Simulations of the spectra reveal that such deviation is not higher than 6 degrees, in the worst scenario, which would not be enough to change the Knight shift expressively. The orange dashed line indicates the position of the main resonance for pure In. The copper signal near 132 MHz arises from the RF coil.

The In(1) and In(2) NMR spectra for the intermetallic samples presented in Fig 3.12 were measured for distinct temperatures. The distinct temperature dependencies of In(1) and In(2) resonances also helped to identify their signals. This can be seen more easily for $x = 0.2$ sample, whose In(1) signal in blue deviates more than the In(2) one, in red.

From these results, the Knight shift K_1 and K_2 , respectively for In(1) and In(2) as a function of temperature was obtained according to Eq. 3.3.1.

$$f_{obs}^{(i)} = \gamma H_0 [1 + K_{(i)}] \pm n\nu_Q, \quad \text{with } i = 1, 2 \quad (3.3.1)$$

where γ is the Larmor frequency of Indium and H_0 the applied magnetic field. The real frequency in which the NMR signal was observed is f_{obs} . K and ν_Q stand for the Knight shift and quadrupolar frequency of the specific In site respectively, and n is an integer that represents the order of the transition. For instance, the transition $-\frac{3}{2}$ to $-\frac{1}{2}$ has $n = 1$, while $\frac{5}{2}$ to $\frac{3}{2}$ has $n = -2$, and so on. The Knight shifts as a function of temperature for In(1) and In(2) are shown in Fig. 3.13, along with their magnetic susceptibility.

According to the NMR Hamiltonian in the paramagnetic phase, the Knight shift must scale well with the magnetic susceptibility, and such behavior is observed for CeMIn_5 , as shown in Fig. 3.14. The fit of the linear part in the Clogston-Jaccarino graph [80] provides the hyperfine coupling B , according to the equation $K \propto K_0 + B\chi$, in which K_0 is a fitting constant. The obtained values for B_1 and B_2 are also presented in Table I. Moreover, one can observe that the temperature range in which the fitting is valid depends on the Ir substitution level. This is however related to the magnetic ordering, which occurs just at lower temperatures for x closer to 1 compound. In fact, T^* , the temperature in which divergence between K and χ is observed, is higher for pure Ir samples Fig. 3.14.

From the values in Table 3.1, one can notice an increasing B_2 and decreasing B_1 upon Ir substitution. Due to the material's structure, it is equivalent to say that the hybridization is more planar

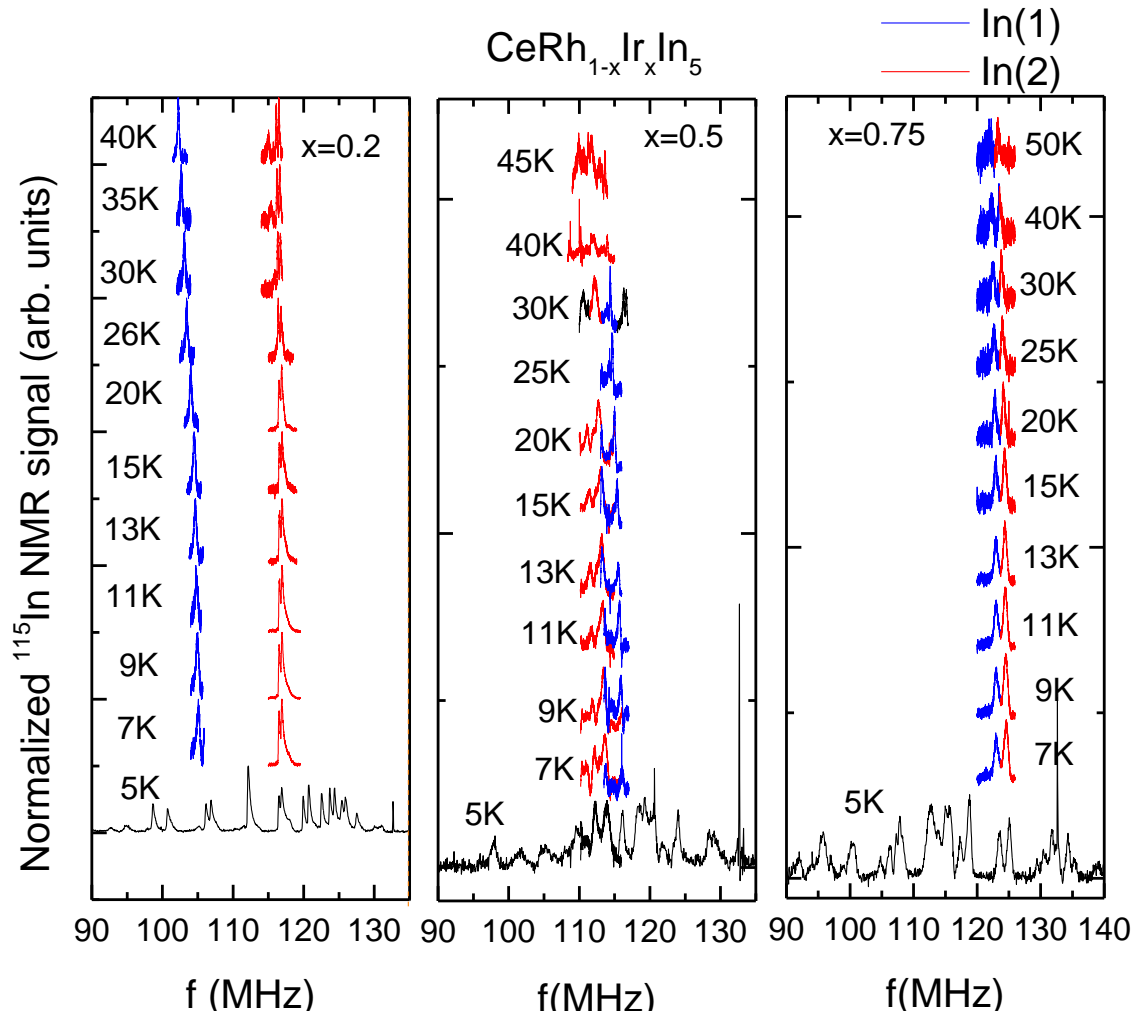


Figure 3.12: ^{115}In NMR spectra of $\text{CeRh}_{1-x}\text{Ir}_x\text{In}_5$ for distinct doping levels at several temperatures. The blue signal stands for In(1), while the red ones represent In(2). For $x = 0.8$ and 0.25 , a satellite In(1) transition was measured instead of the central line to overcome the overlap with the In(2) signal. This has been taken into account for the calculation of the Knight shift. The obtained ν_Q of about 6 MHz, is the value expected for these compounds [78].

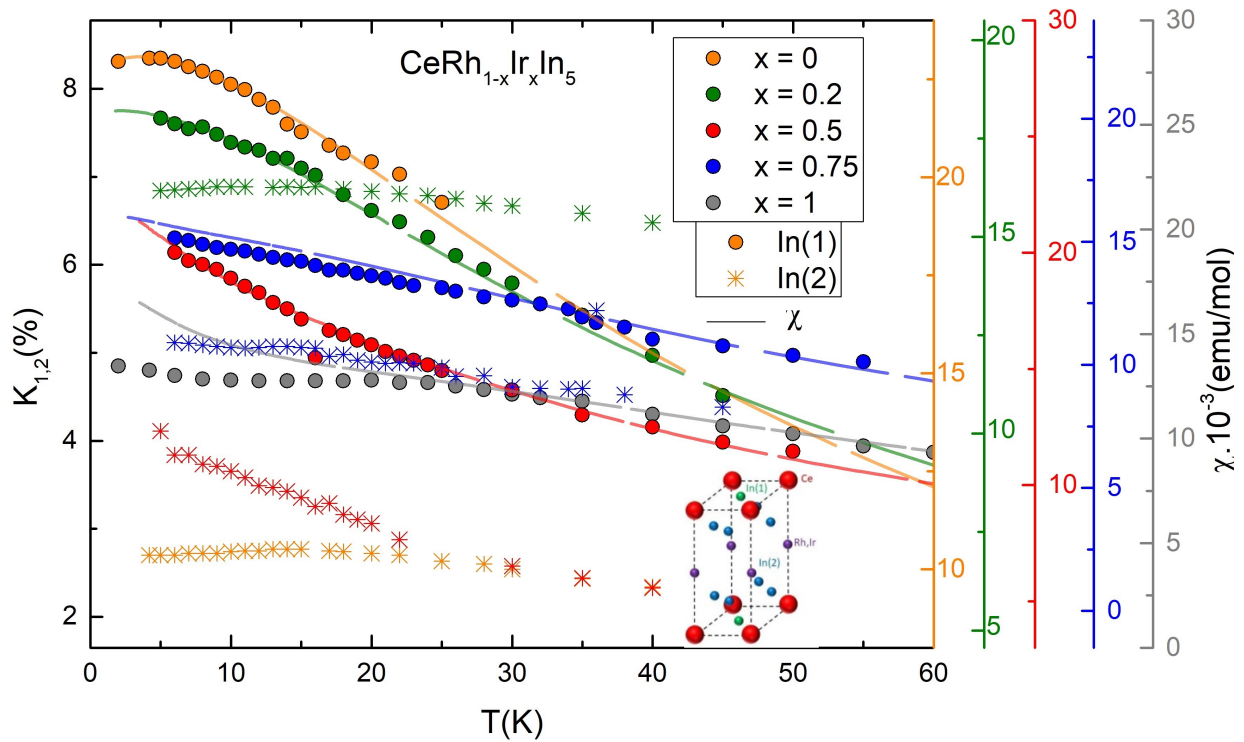


Figure 3.13: Knight shift K_1 (circle) for In(1) and K_2 (square) for In(2) as a function of temperature for $\text{CeRh}_{1-x}\text{Ir}_x\text{In}_5$. The distinct temperature dependencies is a confirmation that the magnetic field is indeed aligned with c -axis. Results for pure CeRhIn_5 are consistent with those already reported [79]. Results for CeIrIn_5 are extracted from [79]. The dashed lines stands for the magnetization measurements, with the color matching the x values.

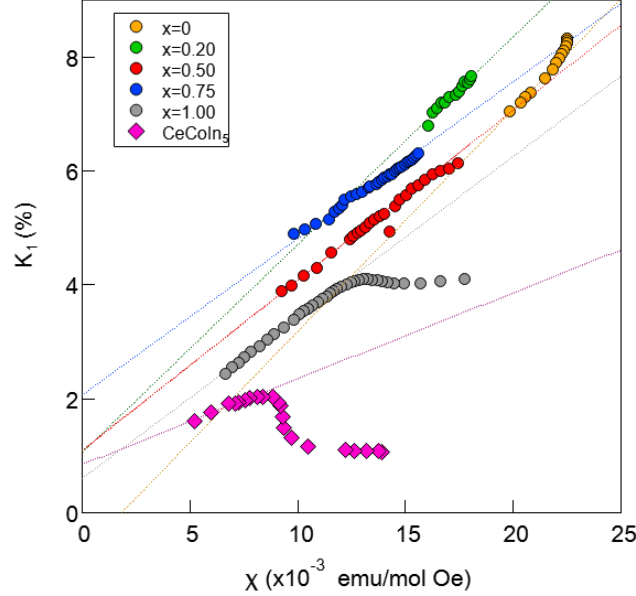


Figure 3.14: $\ln(1)$ Knight shift versus magnetic susceptibility for $\text{CeRh}_{1-x}\text{Ir}_x\text{In}_5$ and CeCoIn_5 . The linear fit, represented as the lines, at high temperature range allows to extract the hyperfine coupling parameter B_1 , which is proportional to the angular coefficient. Results for pure CeMIn_5 are in agreement with the literature [79].

in compounds with more Rh. This is also consistent with the observations drawn by Willers *et al.* [66], who measured the CEF ground state wavefunction of Ce115 compounds by XAS and have shown that the parameter α , in eq. 3.1.1 increases with larger Rh content. Since the CEF ground state is a $\Gamma_7^{1,2}$, it is clear that a higher α , that is a parameter related to the $|\frac{5}{2}\rangle$ orbital, favors planar interaction in the $4f$ orbitals. Furthermore, a linear scaling between B_1 and α , which is presented in Fig. 3.15 is strikingly observed for all CeMIn_5 compounds investigated in this thesis. It is important to note that the α values used here are experimentally obtained [66], but they were also calculated using a model that takes into account the RKKY interaction and CEF effects. The Kondo effect is accounted as an effective mean-field. Although the simplistic model, the calculated α values are in excellent agreement with the experimental ones. The choice for using the experimental values of α for the scaling in Fig. 3.15 is to keep the result as experimental as possible and develop an empirical framework.

The fitting equation to the scaling rule, that related the hyperfine coupling with the α parameter is:

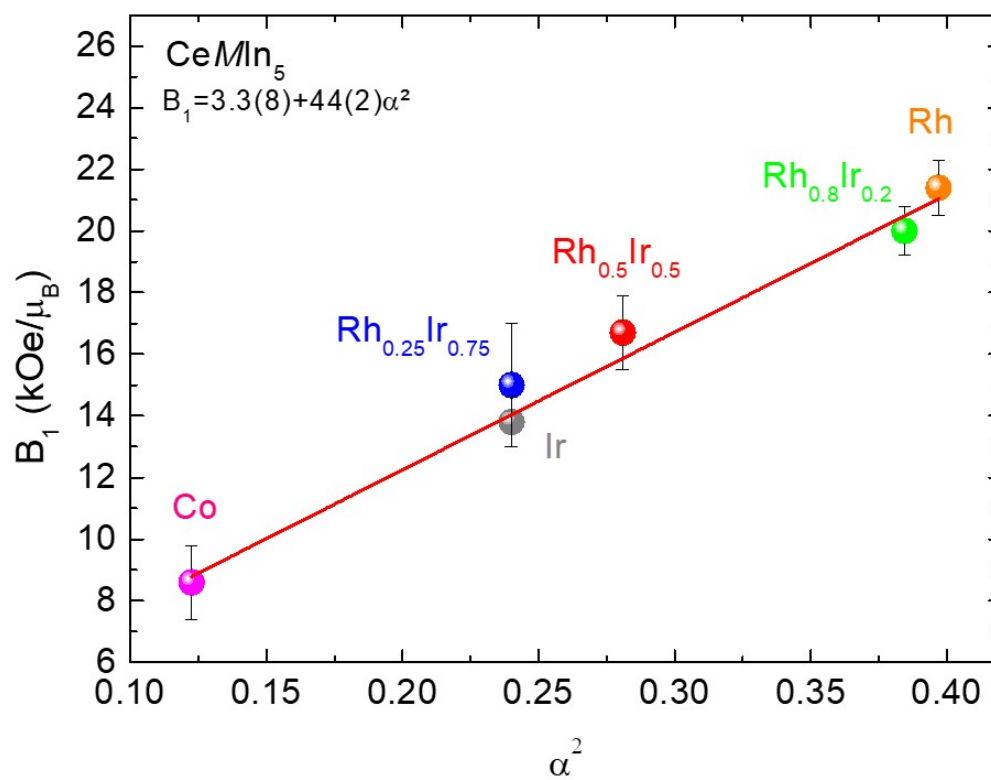


Figure 3.15: In (1) Hyperfine coupling B_1 as a function of the α coefficient (taken from [66]). A linear scaling was observed throughout all members of the CeMIn_5 family. The red solid line is a guide to the eyes.

$$B_1 = 3.3 + 44\alpha^2 \quad (3.3.2)$$

This result demonstrates that the hyperfine coupling is strongly dependent on the Crystal Electric Field in this family of materials and so that the CEF effects have a severe impact not only over the ground state but also over the most relevant physical properties of such systems, despite its smaller energy scale compared to Kondo and RKKY interactions. Through this novel and general NMR procedure, one can extract information from the Ce $4f$ ground state itself simply by measuring the hyperfine coupling constant B_1 . One will still need to perform calculations or alternatively carry out neutron diffraction or X-Ray Absorption Spectroscopy experiments to access α . In other words, microscopic NMR measurements are a powerful technique able to grant access to the actual Ce's orbital wave function (ground state). This is interesting not only from the point of view of the Ce115 heavy fermions but more generalized, for being capable of unraveling any system's orbital wavefunction if similar scaling rule is verified.

Fig. 3.16 presents the scaling for the In(2) hyperfine coupling B_2 , which decreases with increasing α . This is an expected behavior since this parameter shows that out-of-plane interaction is decreasing with the increasing dominance of the $|5/2\rangle$ orbital in great agreement with the discussed scenario.

Next section, another study that emphasizes the power of this scaling rule is discussed.

3.3.4 Nd Doped Compounds

By knowing the scaling rule between the hyperfine coupling constant and the α coefficient for the ground state wave function, NMR experiments on other $CeMIn_5$ compounds may also lead to a better comprehension of their $4f$ electronic orbitals.

It is known that Ce substitution for Nd changes the CEF ground state and favors out-of-plane magnetic interactions [72, 73]. That happens due to a change in the effective magnetic moment

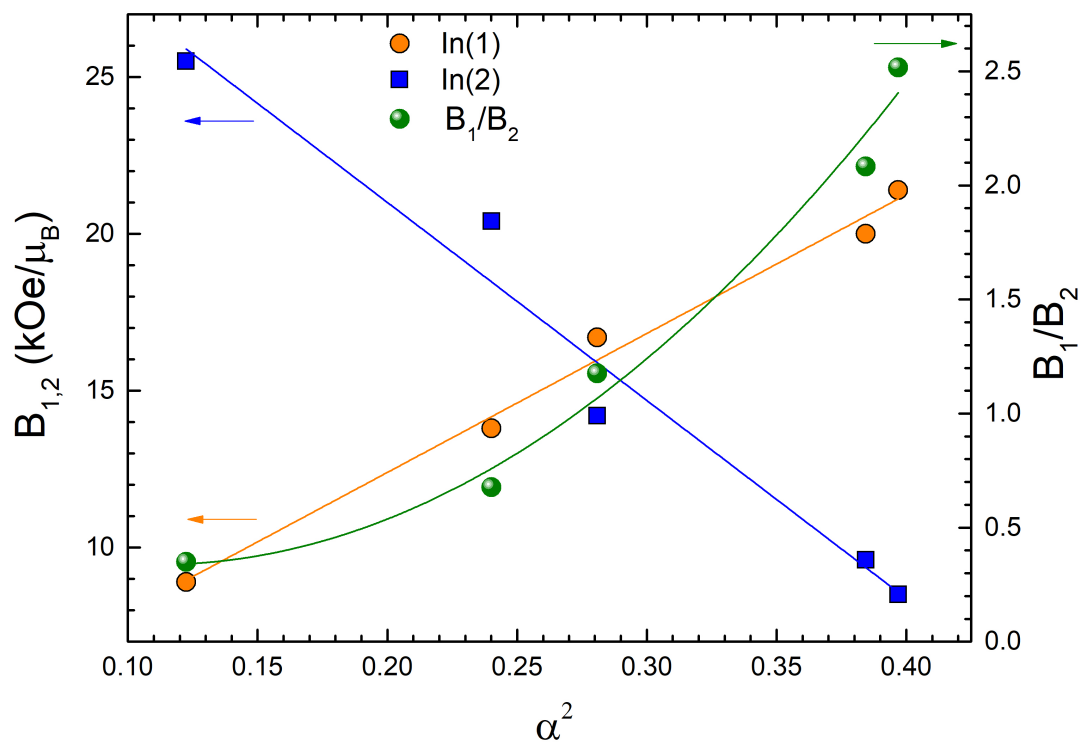


Figure 3.16: Hyperfine coupling of In(1) and In(2) as a function of α coefficient of the ground state wave function. A linear scaling was observed for both In sites. On the right axis, the ratio between the hyperfine coupling specific to each In site is shown.

J upon Nd doping. However, it is still to be known how the electronic spins behave in slightly doped compounds like $\text{Ce}_{0.97}\text{Nd}_{0.03}M\text{In}_5$. This part of the study aimed to find it out by performing Knight shift measurements and using the scaling rule as a toy model to predict the modified $4f$ wavefunctions.

$\text{Ce}_{0.97}\text{Nd}_{0.03}M\text{In}_5$ with $M = \text{Rh}, \text{Ir}$ samples were grown employing the In flux method, with the very same temperature ramps as before. XRD and magnetic susceptibility experiments were performed to certify that there were no spurious phases. For the NMR experiments, a constant magnetic field of 11.72 T was applied along c direction.

The NMR results are presented in Figs. 3.17*b* and *c*, emphasizing that for $M = \text{Rh}$, the signal-to-noise ratio was better allowing the observation of In(1) and In(2) signals. The NMR measurements were taken at the satellite resonance, corresponding to the $\frac{3}{2} \rightarrow \frac{1}{2}$ transition, as shown for $M = \text{Ir}$ case in Fig. 3.17*a*, at 4 K. Note that not all In flux was successfully removed from the sample and there were additional sharp resonance lines associated to it in the spectra. Nevertheless, one may undoubtedly identify the In(1) signal due to three main reasons:

- i*) the observation of satellites, presented in the inset, equally split by approximately 8.4 MHz, it is a strong indication for In(1) signal when $H_0//c$ (In(2) signal does not split equally due to not null ν_Q).
- ii*) the disagreement in the linewidth and intensity of the referred signal from the sample with those of metallic In flux and
- iii*) the line displacement (Knight shift) as a function of temperature different from that expected for ^{115}In metallic flux.

After certifying that the In(1) NMR spectra were measured, experiments as a function of temperature for the main transition up to approximately 60 K were performed, when the In signal became extremely weak due to thermal disorder of the spin populations. Despite the low signal-to-noise ratio compared to typical NMR results, the Lorentzian line fitting allowed to determine the Knight shift. A strong divergence between the observed K_1 with those from undoped samples

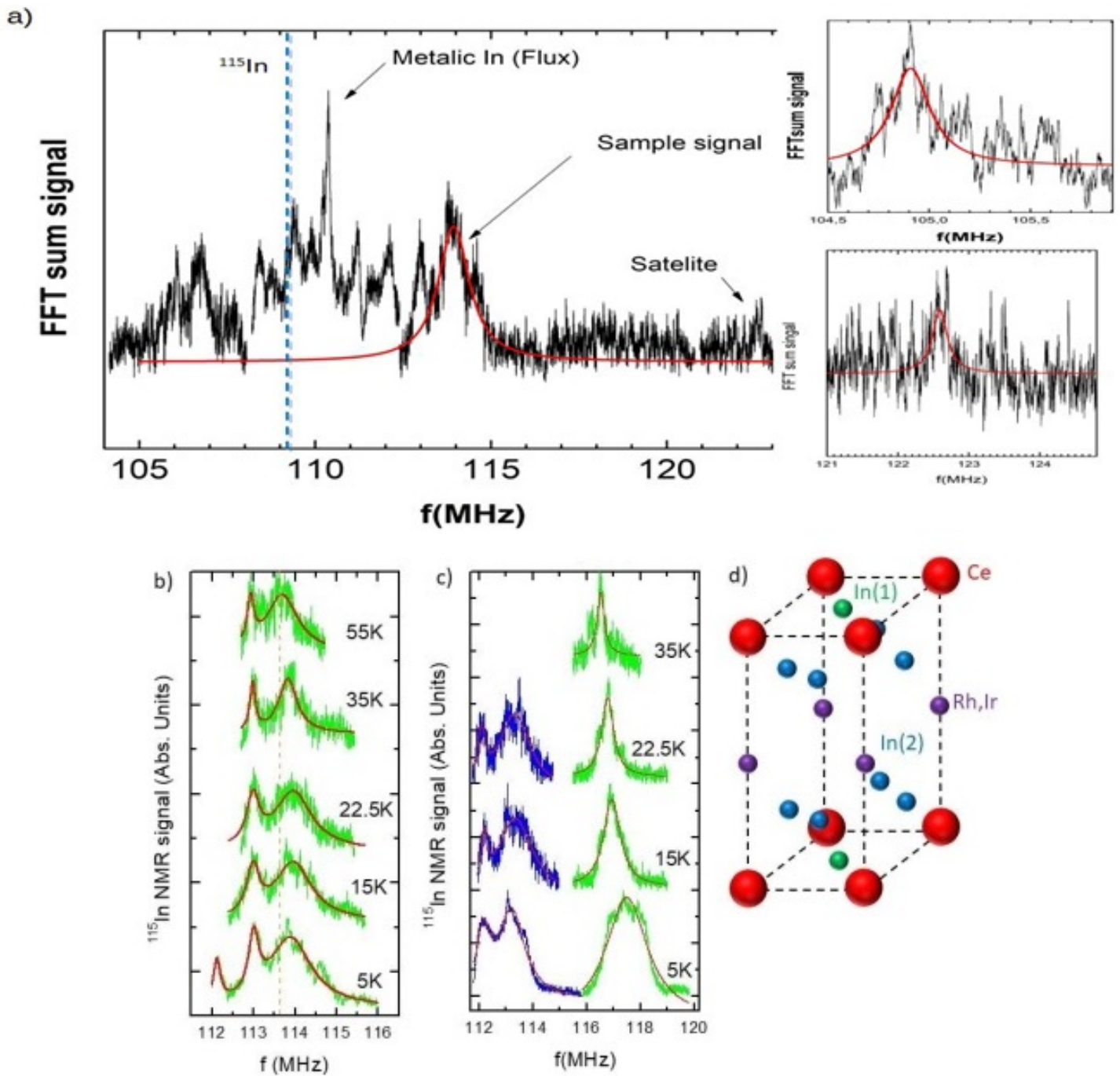


Figure 3.17: ^{115}In NMR spectra of a) $\text{Ce}_{0.97}\text{Nd}_{0.03}\text{IrIn}_5$ at 4.2K. The insets show satellite lines of In(1). b) $\text{Ce}_{0.97}\text{Nd}_{0.03}\text{IrIn}_5$ spectra for distinct temperatures up to 55K, with their respective Lorentzian fit. The left resonance refers to a metallic In transition and is not relevant for our analysis. The orange line is a guide to the eyes for better visualization of the line displacement with the temperature. c) $\text{Ce}_{0.97}\text{Nd}_{0.03}\text{RhIn}_5$ spectra for distinct temperatures up to 35K, with their respective fit. Below 22.5K, both In sites were observed (In(1) in green and In(2) in blue). Note, once again, the lines to the left of the spectra comes from metallic In. d) shows another representation of the structure to emphasize the site differentiation for In.

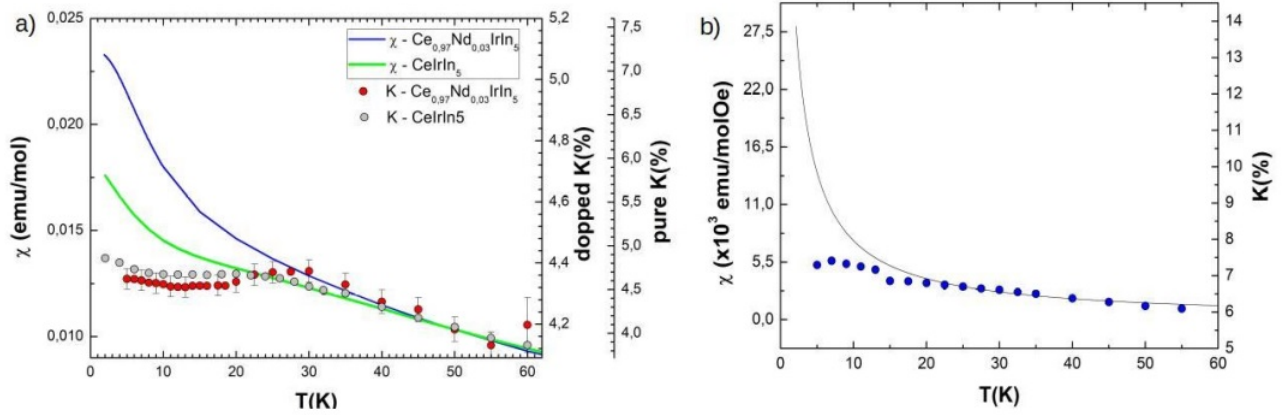


Figure 3.18: Comparison between Knight shift and magnetic susceptibility for (a) $\text{Ce}_{0.97}\text{Nd}_{0.03}\text{IrIn}_5$ and (b) $\text{Ce}_{0.97}\text{Nd}_{0.03}\text{RhIn}_5$. A comparison between pure (data provided by Professor Nicholas Curro) and Nd-doped systems is emphasized in (a). The notorious divergence between K and χ shifts to higher temperatures with Nd doping. The very same happens to $M = \text{Rh}$ compound.

[79] was found. For $M = \text{Ir}$, K_1 was shifted from 4.6% (pure compound) to 4.2% in the Nd doped, as shown in Fig. 3.18. This difference is more pronounced for $M = \text{Rh}$, with K_1 changing from 8.2% (pure) to 7.5% (doped) at 4 K. Note that in both cases the Knight shift was suppressed.

For most metallic systems, the Knight shift should scale linearly with the magnetic susceptibility. However, in many heavy fermion compounds a deviation from this behavior is observed at low temperatures, defining what is called T^* , which is the temperature in which the coherence of the Kondo effect is established. The results presented in Fig. 3.18 demonstrate that such temperature is increased upon Nd doping from 25 K to 30 K for $M = \text{Ir}$ compound and from 5 to 18 K for $M = \text{Rh}$.

Knight shift as a function of magnetic susceptibility (Clogston-Jaccarino plot), depicted in Fig. 3.19, allows the determination of the hyperfine coupling constant B , through a linear fit with the expression $K \propto K_0 + B\chi$ in the high-temperature range. In general, the results show suppression of B with the doping of Nd at the Ce site. The hyperfine coupling B changed from $14.5 \text{ kOe}/\mu_B$ to $3.5 \text{ kOe}/\mu_B$ for the sample with Ir and from $25.2 \text{ kOe}/\mu_B$ to $24.8 \text{ kOe}/\mu_B$ on the Rh sample, which indicates a weaker interaction between the In(1) sites and the Ce atoms on the doped samples. These results lead to the interpretation that the electronic orbital interactions get more out-of-plane with the insertion of Nd. In other words, these results suggest that the

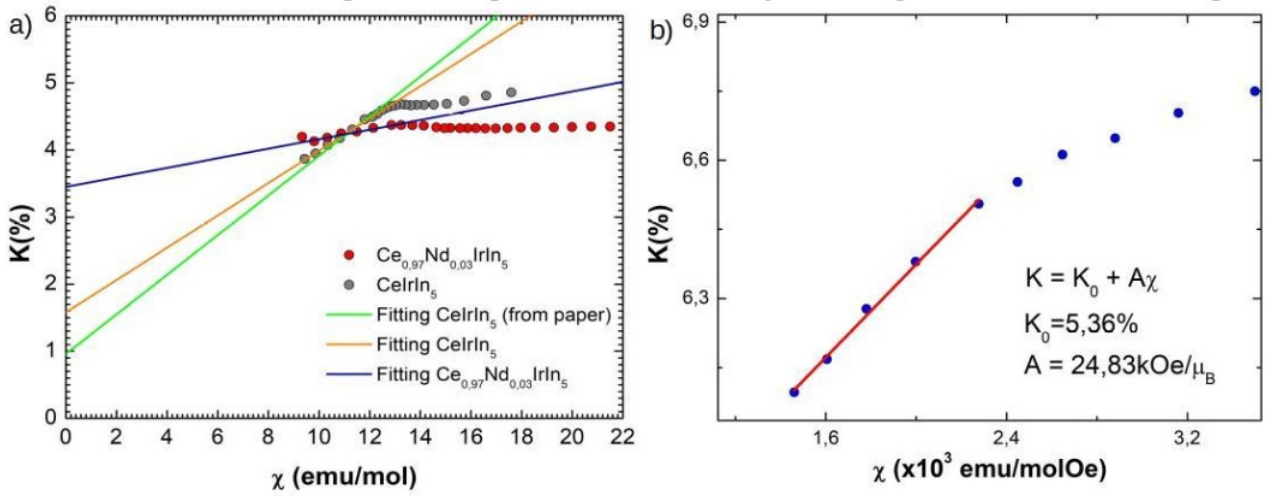


Figure 3.19: Knight shift as a function of magnetic susceptibility with their linear fit in the paramagnetic phase for (a) $\text{Ce}_{0.97}\text{Nd}_{0.03}\text{IrIn}_5$ and (b) $\text{Ce}_{0.97}\text{Nd}_{0.03}\text{RhIn}_5$. The hyperfine coupling is reduced with the substitution of Ce for Nd, as discussed in the main text. The fitting “from paper” in (a) is found at [79].

substitution of Ce for Nd favors the out-of-plane spin states, suppressing α in Eq. 3.1.1.

The reduction in α can be observed when one employs the scaling rule of Fig. 3.15. It must be pointed out however that such scaling should be taken with care for doping at the Ce site since it changes the CEF ground state and thus the energy balance. However, for a small doping level as 3%, such changes can be treated as perturbation and so, the linear scaling remains valid. Adding the B_1 values for the Nd doped samples to the scaling rule in eq. 3.3.2, one get the results referenced in Fig. 3.20

The observed values for α^2 are 0.38 and 0.14 for the systems with $M = \text{Rh}$ and $M = \text{Ir}$, respectively. Likely for the B_1 values, the wavefunction coefficient α is more suitable to changes in $\text{Ce}_{0.97}\text{Nd}_{0.03}\text{IrIn}_5$ than in $\text{Ce}_{0.97}\text{Nd}_{0.03}\text{RhIn}_5$. We claim that this is related to the higher electronic delocalization of CeIrIn_5 system [81].

3.3.5 Addressing the CeRhIn_5 Under Extreme Conditions in the Scaling Rule

As discussed, by using the scaling rule from eq. 3.3.2 one can obtain a clear prediction of the ground state wavefunction of a given electron. But can it be even more useful? To answer this

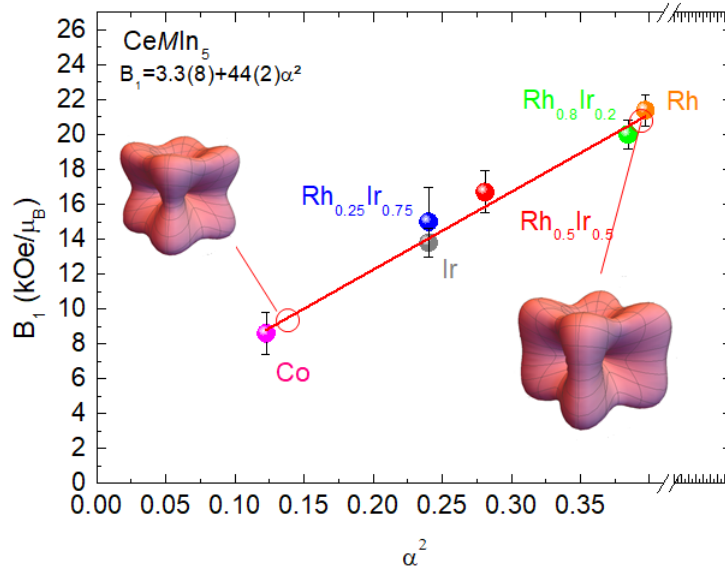


Figure 3.20: Hyperfine coupling versus α^2 with Nd doped data included. For $M = \text{Rh}$, the α^2 value is 0.14 and for $M = \text{Ir}$ it is 0.38. Also one can sketch the Ce orbitals by possessing this α values and, in fact, Nd doped orbitals are more out-of-plane.

question, it was addressed the reported CeRhIn_5 under pressure [82] and high magnetic field [78] NMR data to our scaling. The hyperfine couplings of CeRhIn_5 from ambient pressure up to approximately 2 GPa and also for magnetic fields of 44 T was included in the scaling graph of Fig 3.21.

The first evident result is that hydrostatic pressure seems to change the hybridization, and so the ground state, “moving” the CeRhIn_5 position in the phase diagram towards CeCoIn_5 . Therefore one can establish a qualitative relation between hydrostatic and chemical pressures through the scaling rule proposed in this thesis.

Furthermore, once one knows the hyperfine coupling dependency with pressure, magnetic field and α , dual relations between those three parameters can be established, as shown in Fig. 3.22 for the under pressure data. The polynomial fit was performed using the relation:

$$\alpha^2 = 0.41 - 0.31P + 0.07P^2 \quad (3.3.3)$$

Therefore, only by assuming that such scaling rule remains valid for Ce 115 systems under pressure,

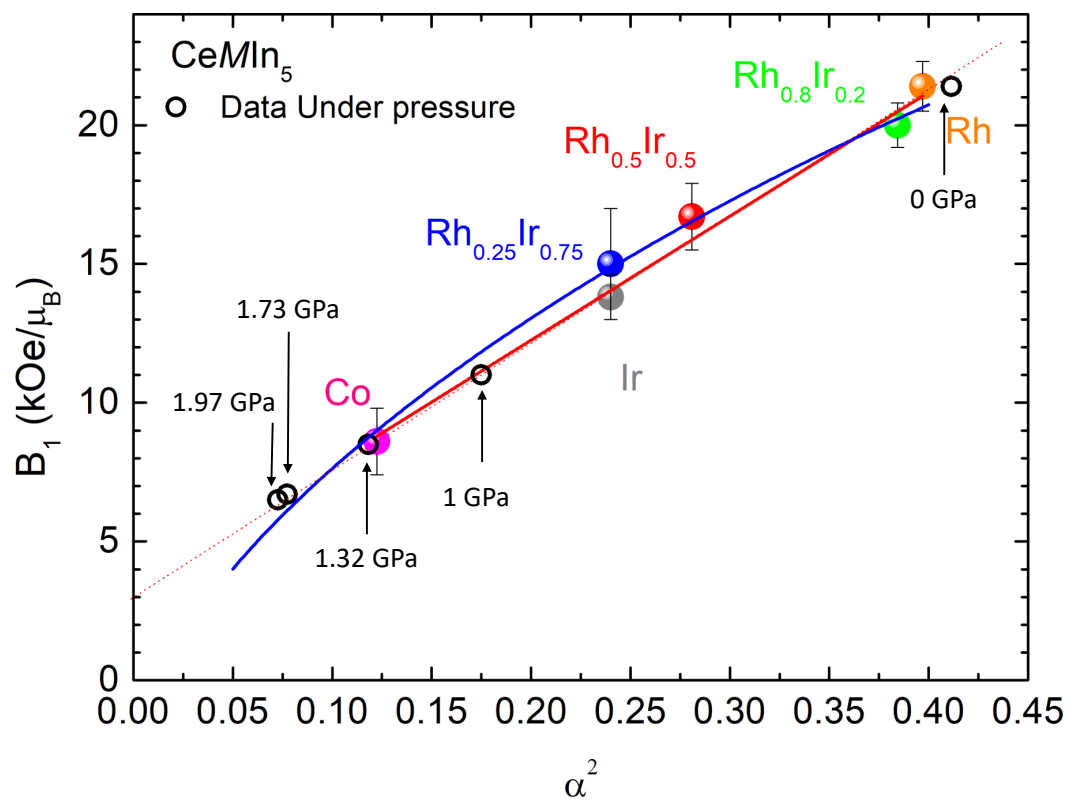


Figure 3.21: Hyperfine coupling versus α^2 with CeRhIn_5 NMR data under pressure (extracted from [82]). One can observe that the scaling holds true. Red line stands for the linear fit, while the blue one assumes a second order term. In terms of the least square method, the linear approximation is quite better.

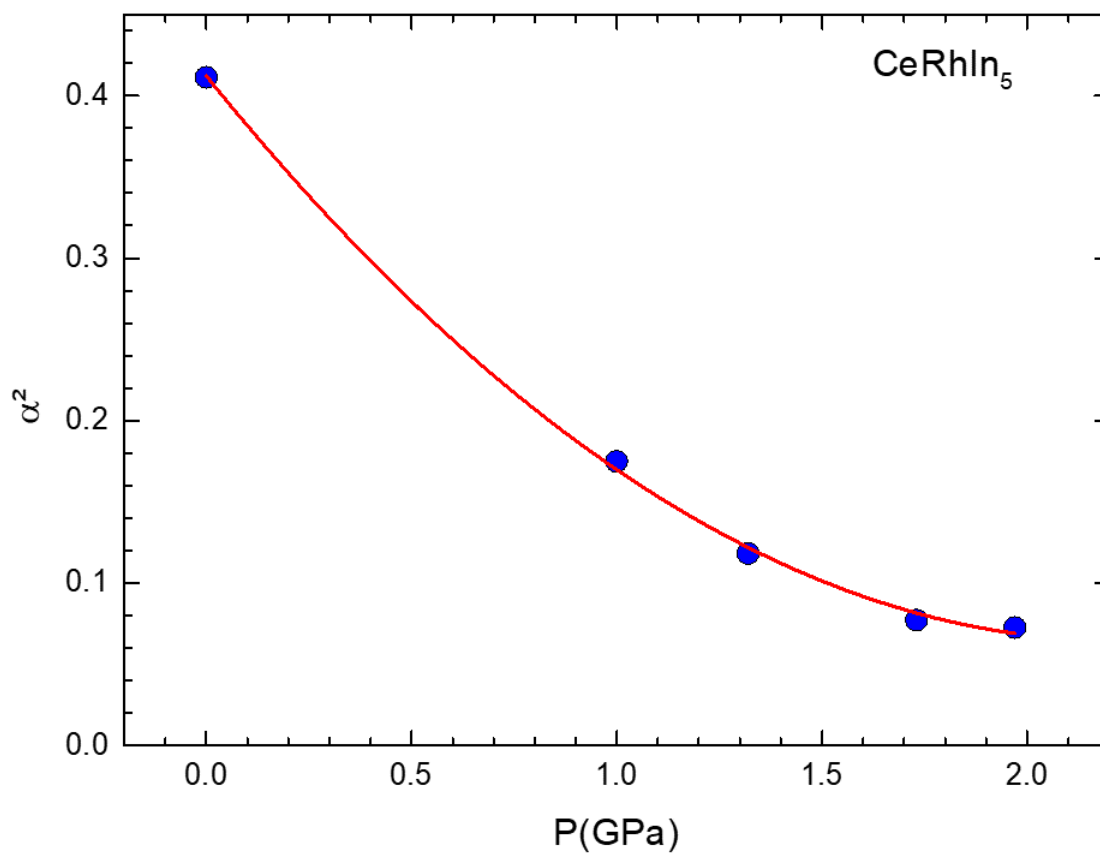


Figure 3.22: Scaling between the squared ground state wave function constant α and the external pressure for CeRhIn₅, assuming a 2nd order relation between them.

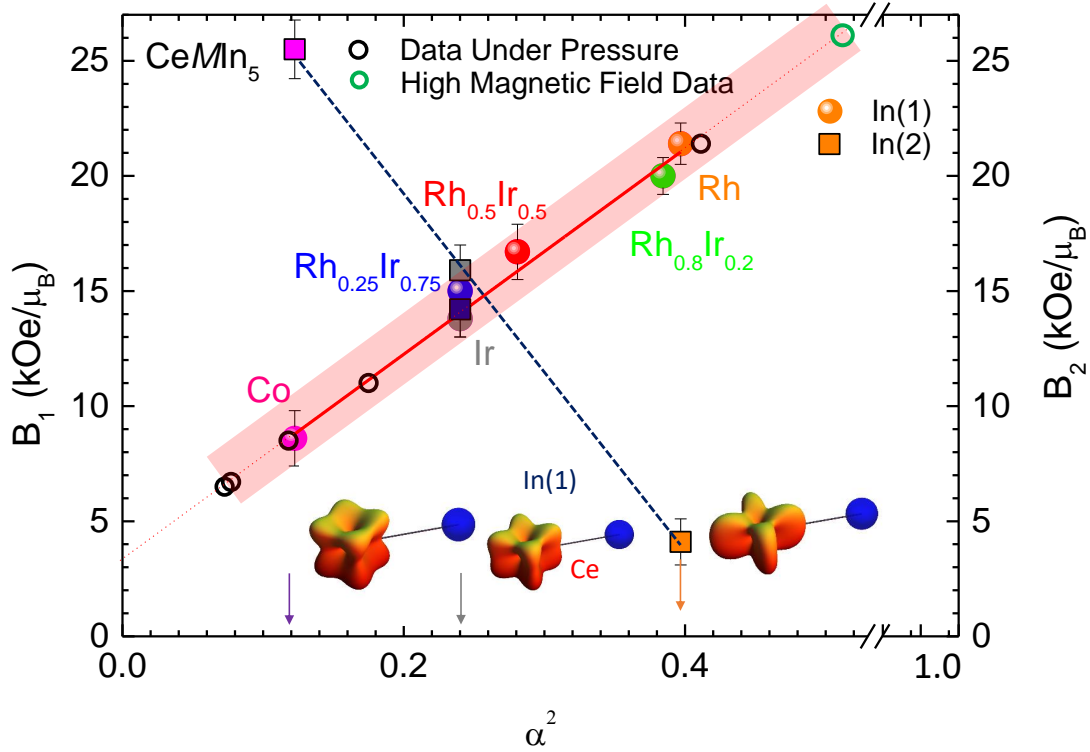


Figure 3.23: Hyperfine coupling versus α^2 for under pressure $CeRhIn_5$ or high magnetic field data included (extracted from [82] and [78]). The resultant Ce orbitals for α values addressing the pure compounds are also presented. The redish highlighted stripe is guide to the eyes.

one can estimate other important relations between fundamental properties of the ground-state wavefunction and control parameters such as chemical doping, hydrostatic pressure, and magnetic fields in $CeMIn_5$.

In summary, all main findings for the scaling rule of Ce 115 heavy fermion systems discussed here are finally presented in Fig. 3.23.

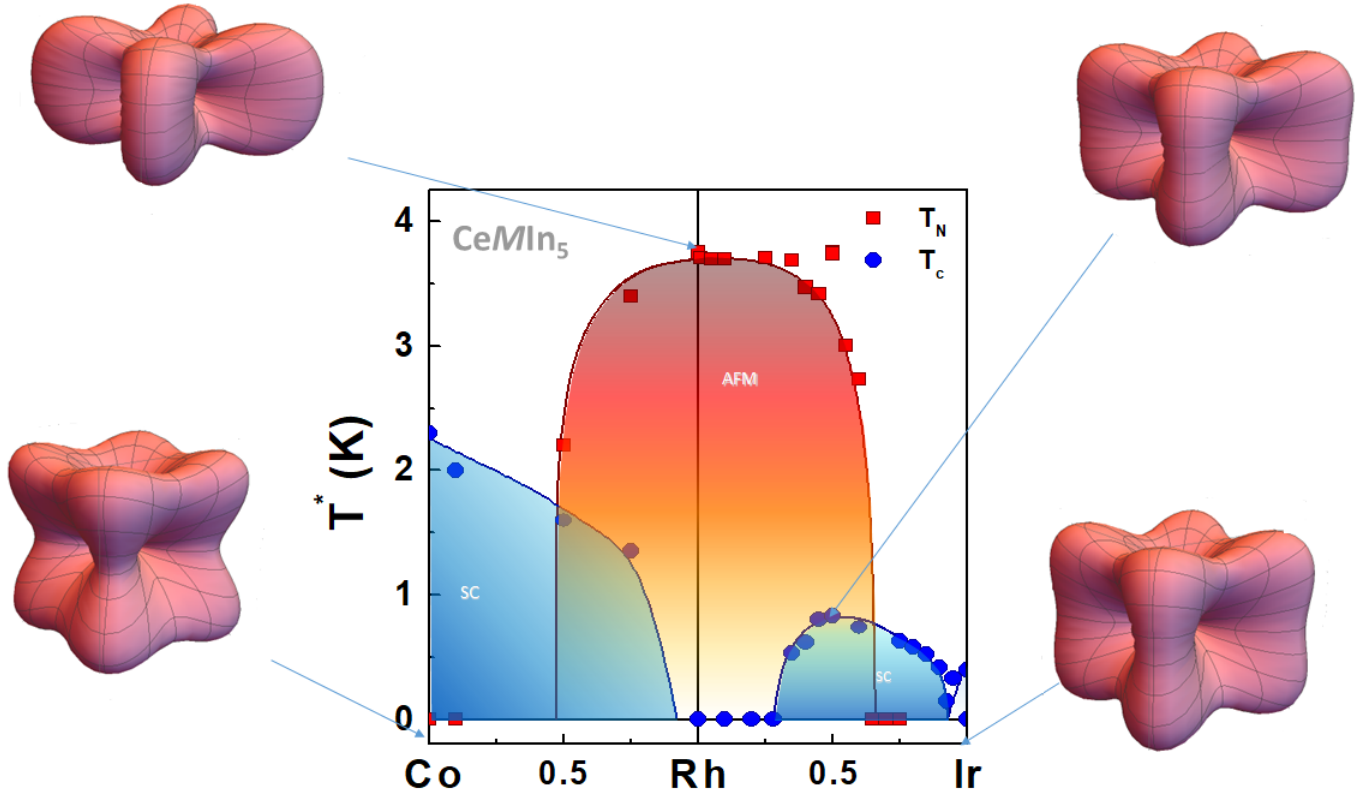


Figure 3.24: Phase diagram of $CeMIn_5$ family, modified from [68], with the Ce's orbitals representation from the data obtained in this thesis and related reports.

3.4 Conclusion and Perspectives

With such striking linear scaling rule presented in this work, one is now able to foresee how the orbitals evolve according to the ground state wavefunction of the heavy fermion compounds of Ce 115 family, as represented in Fig. 3.24. It is yet to be demonstrated that similar behavior is also extended to other heavy fermion systems.

In general, the results obtained in this thesis allow us to state that CEF effects play a fundamental role in the ground state of the Ce-115 family. This is strongly reflected in the high-temperature physical properties of these heavy fermion compounds and is crucial to unravel the physics near the QCP. This leads to a scenario in which the Doniach phase diagram itself is not sufficient to

account for all ingredients necessary to properly describe the HF systems since it does not consider the CEF effects.

From the materials point of view, it would be interesting to understand how the hyperfine coupling behaves for a smaller concentration of Neodymium in $CeMIn_5$. It seems that 3% of Nd content in $CeMIn_5$ was already too much, preventing us to determine whether the hyperfine coupling suppression is monotonic or not. What is known though is that $NdMIn_5$, at least for $M = Ir$ and Rh are, in principle, very difficult to be studied via NMR, due to the strong magnetic fluctuations which wipe out the In NMR signal, probably because of the fast T_2 relaxation times. Studies in the $M = Co$ site are the next step as they can further attest the hyperfine coupling evolution with the ground state wave function (α) of the compound. For $M = Ir$, a drop of 75% of the hyperfine coupling value was observed, while a much smaller one was found for $M = Rh$ (about 10%). This could be related to fluctuations in the superconducting state, which are even stronger in $CeCoIn_5$. So, to test this hypothesis, studies on $Ce_{0.97}Nd_{0.03}CoIn_5$ might be interesting.

Regarding the hyperfine coupling scaling with α , it is the definitive proof that CEF effects play an important role on the Ce $4f$ ground state of the Ce 115 systems. This study may be extended to other Ce-based compounds, with the most prominent examples, but not limited to, the Ce-112 and Ce-218 families. Studies of this sort could also be performed on other compounds with strong CEF effects. The extrapolation to $3d$ compounds however should be taken with care, since they generally present distinct CEF ground state wavefunctions (e_g and t_{2g}) and must not be applicable in this case.

From the linear scaling between B and α found in this investigation, one is also able to rise other theoretical relations between different control parameters and fundamental properties of these heavy fermion systems, in the same fashion as the relation between pressure and α^2 presented above. To name some, at the moment, the relations between B_2 , T^* and the ratio $\frac{a}{c}$ are being investigated. They are however a perspective to this work and need to be better developed in the near future.

Chapter 4

Investigations in Other Systems of Interest

Other systems that were under investigation during the course of this thesis are briefly mentioned in this chapter. Among them, there are two highlights, in which I was directly involved as the main investigator. This is the case of the insulating NaYF_4 nanoparticles, the cobalt based oxiborates, which are discussed in more details than the others. Also, the YCd_6 semi periodic crystals and the single crystals of MgB_2 are themes that are being explored in our NMR, respectively by the masters student Davi Zau and the undergrad Isadora Neme, which I strongly supported.

There were also some studies in which magnetic resonance was not the main used framework or which were not led by our NMR group. They will also be mentioned here, but with less focus, at section 4.3.

4.1 Insulating Nanoparticles

This section is devoted to the study of the insulating NaYF_4 nanoparticles. This study has been performed in collaboration with the post-docs of GPOMS at Unicamp, Dr. Eduardo Martinez, Dr. Ali Garcia-Flores and Dr. Michael Cabrera-Baes, which provided the high-quality samples and primary characterization, and also Prof. Thiago Branquinho, from UFABC, who supervised the

MAS-NMR experiments and data analysis. Both undoped and rare-earth doped NaYF_4 nanoparticles were studied to determine the influence of CEF effects. The main results are described below.

4.1.1 Introduction and Motivation

The technological advances exposed in our era is tremendous. In 1950, a computer has the size of an entire room and performed as a calculator, only solving simple math. Today, however, we have much more powerful notebooks and smartphones that perform the more diverse and complex demands. This is only possible due to the technological miniaturization of electronic components over the last decades. Eventually, a point is being reached in which such device miniaturization is becoming harder to be obtained. This is just a simple example why the study of nanoparticles is technologically important.

From a more scientific point of view, nanomaterials typically have a length of no more a dozen lattice parameters. Their electrons are so confined that they are called Quasi-zero-dimensional (Q-0D) materials, or even quantum materials. The fact is that, as shown in previous chapters, electron confinement leads to interesting and unconventional physical properties. This effect can be seen as an extra confinement bound to the electrons.

Take, for instance, the examples of heavy fermion compounds discussed in the previous chapter. When the orbitals are more spread along the Ce-In plane, the electronic interactions tend to happen in the plane. In other words, electrons are more likely to be present in the plane than out of it, so it is said that they are confined in the plane. But in such case, the samples are still bulk-like, meaning that they have a sizable length in all three directions and the electronic confinement happens only for energetic reasons. Consider, for instance, a material is composed by only one Ce-In plane. It does not matter how the orbitals behave in this situation, the electrons can only move within this plane. In this case, it is physically confined. That is what one does when growing samples like thin films, nanowires and nanoparticles.

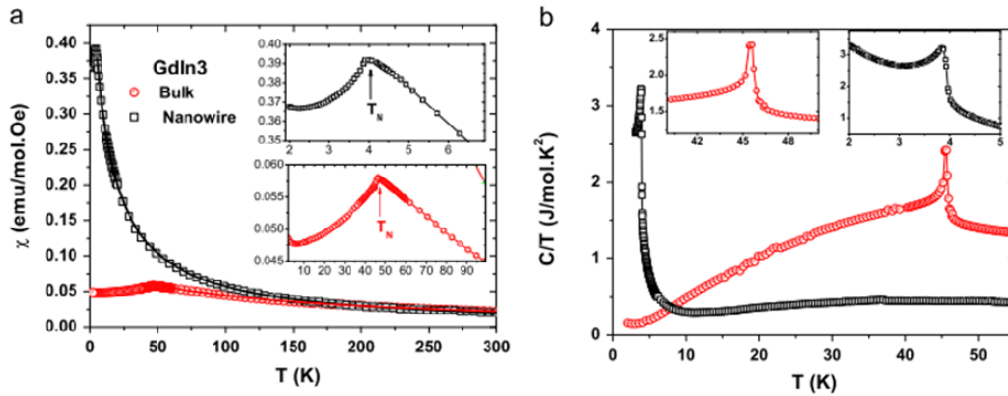


Figure 4.1: Magnetic susceptibility (panel a) and specific heat (panel b) versus temperature for GdIn₃ bulk and nanowire, investigated in our group, according to [83]. The results show an impressive reduction on T_N , indicating that physical confinement induces severe changes on the material’s physical properties.

But is physical confinement different from electronic confinement? That is exactly the question our group aims to answer lately by “miniaturizing” systems of our interest.

In a recent work, nanowires of GdIn₃ were successfully grown and investigated [83]. The samples demonstrate a very expressive reduction on T_N , as depicted in Fig. 4.1.

From the results, one can conclude that the physical properties and the fundamental electronic interactions inside a solid can be drastically affected by physical confinement. That is why our group started a quest in exploring nano-materials of intermetallic compounds. Among other, a more specific goal is to grow CeIn₃ (a well known bulk heavy fermion) in its nanostructured form, by a top-down method known as laser ablation. However, that is a very complicated matter, not directly related to this thesis.

Before measuring the nanostructured CeIn₃ with magnetic resonance, one would have to know how solid-state NMR would deal with nanoparticles (NPs) limitations, such as quantity, size, shape, core-shell or not core-shell, among many other experimental parameters. That is a motivation for the current work. Here, nanostructured NaYF₄ were explored to investigate how NMR is sensitive to such particles and what conclusions could be expected.

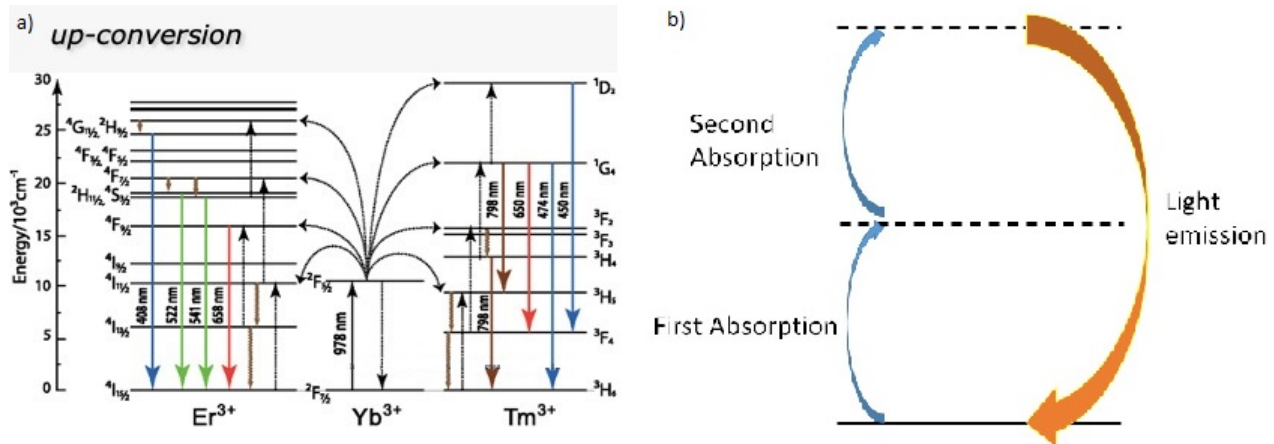


Figure 4.2: a) Energy levels of Er^{3+} , Yb^{3+} and Tm^{3+} electron system. The intermediate levels are metastable and can be reached by the absorption of a low-energy photon. However, if the electron absorbs another low-energy photon, it is promoted to a higher energy level. Then, the electron tends to decay, releasing all absorbed energy at once, leading to a higher energy emitted photon. Figure depicted after [85]. b) Schematic (simplified) view of the upconversion process.

Just because the NaYF_4 nanoparticles do not present heavy fermion behavior does not mean they are not interesting. These particles are well known to present the upconversion phenomenon, with several technological applications [84]. The upconversion phenomenon stands for the absorption of light in a given frequency and emission in a higher frequency. At a first glance, this process seems to violate energy conservation, but in fact, it is not true. The electrons absorb two or more low-energy photons and emit only one, at higher energy. The energy scaling of Fig. 4.2 helps to understand the process.

The main results we found out investigating this systems can be summarized as:

- Even in the cubic phase (NaYF_4), there are two atomic Na sites detected by NMR: One from the surface and another from the bulk of the material.
- The spin-lattice relaxation times do not seem to change considerably by changing the NP size.
- Upon doping with selected rare-earth, the relaxation rates (both spin-lattice and spin-spin) increases drastically, about three orders of magnitude for $\frac{1}{T_1}$, although they have nearly the same

increasing when compared with the undoped samples, Gd seems to have a slightly distinct effect.

For the next steps involving this fascinating area of nanoparticles, there is yet a lot of work to be done. First, one needs to understand the odds to observe surface states on the hexagonal particles β -NaYF₄, although already well known that such systems present two different nuclear sites for ²³Na, there is not a clear association with the possibility of surface states. Moreover, there is no work on relaxation times for such sites to attest is any difference between them. From the point of view of doped nanoparticles, the observed results for a different set of NPs with the same doping are to be confirmed, to ensure systematic. Also, it would be very interesting to measure what is the effect of smaller Rare Earth (RE) concentration, and see if the relaxation rate increase is monotonic. Size-dependent effects could also be interesting to establishing a relation between the reduction of T_1 , the RE doping and the surface/volume ratio. Furthermore, systematic RE doping effects are still lacking for hexagonal phase particles. Finally, it is worth emphasizing once again that all experiments shown and discussed in this section were performed at room temperature. It would be interesting to carry them out in different temperature conditions: It is known for instance that the upconversion effect is more efficient in higher temperatures, but how does the relaxation rate changes in this high T range is yet not known.

This first exploration in “a simpler” compound lead to important insights and methodology to work with more complex nanoparticles, such as CeIn₃, YbAl₄ and MgB₂, which are actually the aim of our group at this moment. So, this work was very relevant to establish the methods and procedures to work in this nanostructure world, which so seems to be a novel approach to investigating the complex physical properties of strongly correlated electrons systems.

A more detailed overview of the results in this systems is shown in Appendix I.

4.2 Cobalt-Based Ludwigites

The oxyborates, have strong similarities with the heavy fermions discussed before: both present strong CEF effects in a SCES system. However, the oxyborates presents totally distinct scenario. The notable difference is that the CEF here comes from a $3d$ metallic atom, which is typically several orders of magnitude stronger than that for $4f$ rare-earth. Also, the cobalt-based ludwigites are a quasi-one dimensional electronic system, while Ce-115 HFs are quasi-two dimensional layered compounds.

The idea to this study came after a neutron diffraction report by Daniele Freitas [21], in which an unexpected relatively low atomic moment was observed for Cobalt atom in the magnetic lattice. This lead the researches to believe there could be a high-spin to low-spin phase transaction induced by CEF. Since magnetic resonance, mainly ESR can be a smoking gun to observe this kind of phase transaction, since it acts directly in the conducting electron, our group technique came into play here. We not only found out such transition, but also other interesting topics about this system. More details on the results that lead to the conclusions discussed here are presented in Appendix K.

4.3 Systems Investigated in Collaborations

Here are the systems in which I was less directly involved or were explored by other groups as the main investigators.

4.3.1 YCd_6 Quasi-Periodic Crystals

This study is a collaboration with Profs. Michael Cabrera Baez and Carlos Rettori and have been lead by the master student Davi Zau from our NMR group. It consists of a comparison between the approximant crystalline form of YCd_6 and its quasi-periodic structure employing NMR.

It is a direct sequence of ESR experiments performed in our group [86], which proved that both approximant and the quasi-preiodic crystal has the same Korringa constant. So, the main focus here is to compare the Knight shift and spin-lattice relaxation times for both crystals. The preliminary results indicates that they has the same order of magnitude in the relaxation, but the Knight shift is not the same.

4.3.2 Single Crystals of MgB_2

This study is a collaboration with the undergraduate student Isadora Neme from our NMR group, and consist of the realization of NMR and ESR experiments on single crystals of MgB_2 . Although this system has been highly explored on its polycrystalline phase [47], just recently high-quality single crystals of them were synthesized. The main goal is to perform an angular dependent investigation, which is possible now with SCs. The experiments realization is work in progress in this moment. This work is also a collaboration with Profs Raquel Almeida and Paul Canfield from Ames Laboratory.

4.3.3 Er doped Au Nanoparticles

Although this study is technically in the Unicamp's resonance group, since was a collaboration with Prof. Carlos Rettori, I listed as a minor contribution of myself, since my activity was to

perform low-temperature ESR experiments on distinct batches of Er-doped Au nanoparticles.

Basically, this studies is trying to determine if the Er is trully “entering” in the Au nanoparticles or is intead attaching to its surface. This is important in the sense to confirm and extends the results obtained in “Absence of exchange interaction between localized magnetic moments and conduction-electrons in diluted Er^{3+} gold-nanoparticles” [87]. At the current state, we found out a strong sample dependency, indicating that we still need to put efforts in control the syntheses more properly

4.3.4 SmB_6 Topological Insulators

This study was a collaboration from our MR group with Profs. Dr. Pascoal Pagliuso and Carlos Rettori, and also with the ph.D. student Jean Souza. SmB_6 is a material that has been very explored since 1980 and has gained renewed attention due to the possible interplay between non-trivial topological states with the Kondo effect. In this study, ESR experiments on Re-doped samples, mainly with Er were carried out. This work lead to the publication “Metallic islands in the Kondo insulator SmB_6 ” [88], presented at Appendix J.

4.3.5 $\text{La}_3\text{Ir}_4\text{Sn}_{13}$ Heavy Fermions

This study was a cooperation with Profs. Dr. Leticie Ferreira, Marcos Ávila (UFABC) and Carlos Rettori and Karla Barbosa. The family $R_3M_3\text{Sn}_{13}$ is well known to present strong electronic correlation, with a complex phase diagram with non-conventional superconductivity, positive magneto-resistance, and charge density wave. In this study, the researchers were interested in the magnetic properties of slightly doped $\text{La}_{2.985}\text{Gd}_{0.015}\text{Ir}_4\text{Sn}_{13}$, which stands in the superconducting range. My contribution was to perform ESR experiment at low-temperature to extract the Korringa relation rate.

4.3.6 TmVO₄ Oxides

This study was cooperation with Prof. Dr. Nicholas Curro and Zhipan Wang at UC-Davis during my sandwich. TmVO₄ oxides present a strong Jahn-Teller effect at low temperatures, which leads to a structural transition at 2.2 K. Also, the Tm ion is submitted to strong CEF effects. Knight shift and spin-lattice relaxation experiments were performed and found a very strong anisotropy near the transition, which reflects the role of nematic fluctuations near the critical temperature. My contribution here was to perform Knight shift angular dependency experiments at low temperature range ($2\text{ K} < T < 5\text{ K}$). This investigation led to two works presented on March Meeting: “NMR Studies of TmVO₄” [89] and “NMR Studies of Nematicity in TmVO₄ and TmAsO₄” [90].

4.3.7 Fabre Bechgaard Organic Conductors

This study was performed in collaboration with Prof. Dr. Mariano de Souza, from Unesp and was once the main focus of this thesis. Although I invested more than half time of the period performing experiments on those, divergences on how to handle the results led then to be not shown here or anywhere else, apart from the keep up reports sent to FAPESP during the course of this thesis.

As a personal note, I find it unfortunate, but it is what it is.

Chapter 5

General Conclusions and Forewords

During the period of this thesis, we applied Magnetic Resonance (MR) Spectroscopy to several systems of interest within solid state physics, with particular emphasis to the heavy fermions of Ce-115 family. Although the HFs have been chosen as the main topic due to the relevance in the obtained results, deal with distinct systems was fundamental to my understand about MR in different frameworks. A good example is the work in nanoparticles (NPs), which has been performed using room temperature high resolution NMR (MAS and 3Q-MAS), which are quite different from the often designed solid state NMR experiments. Learning such complementary techniques was a great addition to my MR background.

As shown in chapter 3, we were able to measure the Knight Shift and magnetic susceptibility at low temperature range and through the Clogston-Jaccarino relation, extract the hyperfine coupling for $\text{Ce}_{1-x}\text{Nd}_x\text{Rh}_{1-x}\text{Ir}_x\text{In}_5$. Our NMR results provided key ingredients on the role of the crystalline field in the subtle balance between Kondo and RKKY interactions. The hyperfine interaction between nuclear and electronic spins in heavy fermions depends on the hybridization between $4f$ electronic orbitals and those in the vicinity of distant nuclei. In $\text{Ce}M\text{In}_5$ ($M = \text{Rh}, \text{Ir}, \text{Co}$), the hyperfine coupling with the two sites in the Ce crystalline electric field are both dependent on the transition metals in this matrix. We measured a series of $\text{CeRh}_{1-x}\text{Ir}_x\text{In}_5$ monocrystals and found that the hyperfine coupling reflects an orbital ground-state anisotropy of Ce $4f$ wave

functions. Furthermore, the most striking result of this study is a linear correlation between the transferred hyperfine coupling and the amplitude of the $4f$ Ce electronic orbitals in the plane. From a broader perspective, this behavior is related to the intensity of electronic hybridization controlling the change of states Localized-Delocalized related to the phenomenology of heavy fermions. In other words, our results provide direct proof that a transition from electrons to traveling is dominated by hybridization outside the Ce-In plane in this system. The opposite trend observed for the nuclei of In on the Ce-In plane (In (1)) and those outside the plane (In (2)) provides strong support to our interpretation.

Other studies were also important in the sense of establishing solid collaborations with several groups worldwide. Although our group already has strong collaboration with prof. Marcos Avila and Leticie Ferreira from UFABC, we established a strong collaboration with prof. Thiago Branquinho in the exploration of nanoparticles. I was fortunately able to visit his NMR lab a couple of times to perform MAS-NMR experiments on such systems. Also, a collaboration with Prof. Mucio Continentino, from CBPF, and Prof. Daniele Freitas from UFF has started with our ESR investigations in $\text{Co}_3\text{O}_2\text{BO}_3$. Afterwards, Prof. Eduardo Granado had also joined this collaboration, with a very important role in the investigations in this systems.

I'd like to emphasize the important collaboration with Prof. Nicholas Curro, from University of California - Davis, which resulted in the main investigation of this work. This collaboration was the beginning of a healthy interaction between Unicamp and UC. Not only it led to a great opportunity of doing an internship as a sandwich in my Ph.D., but also led to other relevant studies on TmVO_4 Oxides and opportunities to other students, as regarded in Appendix A.

Therefore I feel very satisfied with the results of this thesis. I feel like I have accomplish with sucess all the workplan and after this years of hard work, I consider myself able to follow the scientific career working with several different kinds of Magnetic Resonance in any laboratory around the world. Also, I highlight the relevant number of scientific collaborations established through this period, making a wide and relevant scientific network early in my career. Also, the

good and relevant results were obtained, which will certainly contribute and impact to the areas of investigation and help the scientific community (for the papers, please refer to appendix G).

I want to finish this text telling that I feel grateful for completing this five-year of hard work, full of challenges, but that could be surpassed by strong determination.

Bibliography

- [1] S. Bose, “*Planck’s law and light quantum hypothesis*” *Z. phys*, vol. 26, no. 1, p. 178, 1924.
- [2] A. Einstein, “*Quantum theory of the monatomic ideal gas*” *Sitzungsberichte der Preussischen Akademie der Wissenschaften, Physikalisch-mathematische Klasse*, pp. 261–267, 1924.
- [3] S. Balibar, “*The discovery of superfluidity*” *Journal of Low Temperature Physics*, vol. 146, pp. 441–470, 2007.
- [4] H. K. Onnes, “*research notebooks 56, 57*” Kamerlingh Onnes Archive, Boerhaave Museum, Leiden, the Netherlands, 1911.
- [5] D. Van Delft and P. Kes, “*The discovery of superconductivity*” *Physics Today*, vol. 63, no. 9, pp. 38–43, 2010.
- [6] H. K. Onnes, “*Isotherms of monatomic gases and their binary mixtures. i. isotherms of helium between+ 100 C and-217 C*” vol. 10, pp. 1907–1908, 1908.
- [7] K. Gavroglu and Y. Goudaroulis, “*Heike kamerlingh onnes’ researches at leiden and their methodological implications*” *Studies in History and Philosophy of Science Part A*, vol. 19, no. 2, pp. 243–274, 1988.
- [8] T. Broux, H. Ubukata, C. J. Pickard, F. Takeiri, G. Kobayashi, S. Kawaguchi, M. Yonemura, Y. Goto, C. Tassel, and H. Kageyama, “*High-pressure polymorphs of laho with anion coordination reversal*” *Journal of the American Chemical Society*, vol. 141, no. 22, pp. 8717–8720, 2019.
- [9] E. Snider, N. Dasenbrock-Gammon, R. McBride, M. Debessai, H. Vindana, K. Vencatasamy, K. V. Lawler, A. Salamat and R. P. Dias, “*Room-temperature superconductivity in a carbonaceous sulfur hydride*” *Nature*, vol. 586, pp. 373–377, 2020.
- [10] W. Meissner and R. Ochsenfeld, “*Ein neuer effekt bei eintritt der supraleitfähigkeit*” *Naturewissenschaften*, vol. 21, no. 44, pp. 787–788, 1933.
- [11] J. Bardeen, L. N. Cooper, and J. R. Schrieffer, “*Theory of superconductivity*” *Physical review*, vol. 108, no. 5, p. 1175, 1957.
- [12] J. Nagamatsu, N. Nakagawa, T. Muranaka, Y. Zenitani, and J. Akimitsu, “*Superconductivity at 39K in magnesium diboride*” *nature*, vol. 410, no. 6824, pp. 63–64, 2001.
- [13] J. G. Bednorz and K. A. Müller, “*Possible high T_c superconductivity in the Ba-La-Cu-O system*” *Zeitschrift für Physik B Condensed Matter*, vol. 64, no. 2, pp. 189–193, 1986.
- [14] N. Mott, “*Metal-insulator transition*” *Reviews of Modern Physics*, vol. 40, no. 4, p. 677, 1968.
- [15] P. W. Anderson, “*RVB theory of high T_c superconductivity*” *Novel Superconductivity* pp. 295–299, 1987.
- [16] P. Monthoux, A. Balatsky, and D. Pines, “*Toward a theory of high-temperature superconductivity in the antiferromagnetically correlated cuprate oxides*” *Physical review letters*, vol. 67, no. 24, p. 3448, 1991.

- [17] J. Custers, P. Gegenwart, H. Wilhelm, K. Neumaier, Y. Tokiwa, O. Trovarelli, C. Geibel, F. Steglich, C. Pépin, and P. Coleman, “*The break-up of heavy electrons at a quantum critical point*” *Nature*, vol. **424**, no. 6948, pp. 524–527, 2003.
- [18] P. Coleman, “*Heavy fermions and the kondo lattice: a 21st century perspective*” arXiv preprint arXiv:1509.05769, 2015.
- [19] M. N. Martin, T. Newman, M. Zhang, L. D. Sun, C. H. Yan, G. Y. Liu, and M. P. Augustine, “*Using NMR relaxometry to probe Yb^{3+} – Er^{3+} interactions in highly doped nanocrystalline NaYF_4 nanostructures*” *The Journal of Physical Chemistry C*, vol. **123**, no. 1, pp. 10–16, 2019.
- [20] C. W. Galdino, D. C. Freitas, C. P. C. Medrano, R. Tartaglia, D. Rigitano, J. F. Oliveira, A. A. Mendonça, L. Ghivelder, M. A. Continentino, D. R. Sanchez, and E. Granado, “*Magnetic, electronic, structural, and thermal properties of the $\text{Co}_3\text{O}_2\text{BO}_3$ ludwigite in the paramagnetic state*” *Phys. Rev. B*, vol. **100**, p. 165138, Oct 2019.
- [21] D. C. Freitas, C. P. C. Medrano, D. R. Sanchez, M. N. n. Regueiro, J. A. Rodríguez-Velamazán, and M. A. Continentino, “*Magnetism and charge order in the ladder compound $\text{Co}_3\text{O}_2\text{BO}_3$* ” *Phys. Rev. B*, vol. **94**, p. 174409, Nov 2016.
- [22] K. Andres, J. E. Graebner, and H. R. Ott, “*4*f*-virtual-bound-state formation in CeAl_3 at low temperatures*” *Phys. Rev. Lett.*, vol. **35**, pp. 1779–1782, Dec 1975.
- [23] C. Kittel, “*Introduction to solid state physics*” 2004.
- [24] F. Steglich, J. Aarts, C. D. Bredl, W. Lieke, D. Meschede, W. Franz, and H. Schäfer, “*Superconductivity in the presence of strong pauli paramagnetism: CeCu_2Si_2* ” *Phys. Rev. Lett.*, vol. **43**, pp. 1892–1896, Dec 1979.
- [25] H. von Löhneysen, “*Non-fermi-liquid behaviour in the heavy-fermion system*” *Journal of Physics: Condensed Matter*, vol. **8**, pp. 9689–9706, nov 1996.
- [26] H. v. Löhneysen, T. Pietrus, G. Portisch, H. G. Schlager, A. Schröder, M. Sieck, and T. Trappmann “*Non-fermi-liquid behavior in a heavy-fermion alloy at a magnetic instability*” *Phys. Rev. Lett.*, vol. **72**, pp. 3262–3265, May 1994.
- [27] N. D. Mathur, F. M. Grosche, S. R. Julian, I. R. Walker, D. M. Freye, R. K. W. Haselwimmer, G. G. Lonzarich, “*Magnetically mediated superconductivity in heavy fermion compounds*” *Nature*, vol. **394**, pp. 39–43, 1998.
- [28] J. J. Sakurai, “*Modern quantum mechanics: rev. ed.*” 1994.
- [29] G. Kotliar and D. Vollhardt, “*Strongly correlated materials: Insights from dynamical meanfield theory*” *Physics today*, vol. **57**, no. 3, pp. 53–60, 2004.
- [30] J. Hubbard, “*Electron correlations in narrow energy bands*” *Proceedings of the Royal Society of London. Series A. Mathematical and Physical Sciences*, vol. **276**, no. 1365, pp. 238–257, 1963.
- [31] R. Oerter, “*The theory of almost everything: The standard model, the unsung triumph of modern physics*” 2006.
- [32] R. L. Mössbauer, “*Kernresonanzfluoreszenz von gammastrahlung in ^{191}Ir* ” *Zeitschrift für Physik*, vol. **151**, no. 2, pp. 124–143, 1958.

- [33] M. A. Ruderman and C. Kittel, “*Indirect exchange coupling of nuclear magnetic moments by conduction electrons*” *Physical Review*, vol. **96**, no. 1, p. 99, 1954.
- [34] T. Kasuya, “*A theory of metallic ferro-and antiferromagnetism on Zener’s model*” *Progress of theoretical physics*, vol. **16**, no. 1, pp. 45–57, 1956.
- [35] K. Yosida, “*Magnetic properties of Cu-Mn alloys*” *Physical Review*, vol. **106**, no. 5, p. 893, 1957.
- [36] J. Kondo, “*Resistance minimum in dilute magnetic alloys*” *Progress of theoretical physics*, vol. **32**, no. 1, pp. 37–49, 1964.
- [37] S. Blundell, “*Magnetism in condensed matter*” 2003.
- [38] C. Slichter, “*Principles of magnetic resonance*” 1996.
- [39] A. Abragam, “*The principles of nuclear magnetism: Reprint with corrections*” 1989.
- [40] A. Abragam and M. H. L. Pryce, “*Theory of the nuclear hyperfine structure of paramagnetic resonance spectra in crystals*” *Proceedings of the Royal Society of London. Series A. Mathematical and Physical Sciences*, vol. **205**, no. 1080, pp. 135–153, 1951.
- [41] J. Keeler, “*Understanding nmr spectroscopy*” 2011.
- [42] M. H. Levitt, “*Spin dynamics: basics of nuclear magnetic resonance*” 2013.
- [43] Bruker, “*Bruker electronic paramagnetic resonance manual*” 2011.
- [44] S. Roeder and E. Fukushima, “*Experimental pulse NMR: A nuts and bolts approach*” Addison Wesley, Reading, Massachusetts, vol. **198**, no. 1, p. 207, 1981.
- [45] H. Alloul, “*NMR in strongly correlated materials*” arXiv preprint arXiv:1505.04699, 2015.
- [46] H. Alloul, “*NMR studies of electronic properties of solids*” arXiv preprint arXiv:1504.06992, 2015.
- [47] R. R. Urbano, “*Propriedades magnéticas de sistemas com elétrons fortemente correlacionados: MgB₂ supercondutor, CaB₆ semicondutor e, EuB₆ semi-metálico ferromagnético*” Ph. D. Thesis, 2004.
- [48] G. G. Lesseux, “*Ressonância magnética nuclear e eletrônica em sistemas de elétrons fortemente correlacionados*” Ph. D. Thesis, 2017.
- [49] N. J. Curro, “*Nuclear magnetic resonance studies of the high-temperature superconductors in the normal and superconducting states*” Ph. D. Thesis, 1998.
- [50] A. Schockley, “*Experimental study of knight shift trends in the heavy fermion compounds compounds CeMIn₅ (M=Ir, Rh, Co)*” Ph. D. Thesis, 2013.
- [51] A. P. Dioguardi, “*Nuclear magnetic resonance studies of the 122 iron-based superconductors*” Ph. D. Thesis, 2013.
- [52] N. R. apRoberts Warren, “*Investigating strong correlated electron behavior in heavy fermion cesium platinum indium and AFM insulator lanthanum nickel oxide*” Ph. D. Thesis, 2013.

- [53] T. Moriya and K. Ueda, “*Spin fluctuation spectra and high temperature superconductivity*” *Journal of the Physical Society of Japan*, vol. **63**, no. 5, pp. 1871–1880, 1994.
- [54] M. T. Heideman, D. H. Johnson, and C. S. Burrus, “*Gauss and the history of the fast fourier transform*” *Archive for history of exact sciences*, pp. 265–277, 1985.
- [55] J. Smith and E. Kmetko, “*Magnetism or bonding: A nearly periodic table of transition elements*” *Journal of the Less Common Metals*, vol. **90**, no. 1, pp. 83 – 88, 1983.
- [56] K. Hirsch, “*Electronic and magnetic properties of impurities embedded in non-magnetic finite hosts*” **06** 2013.
- [57] P. Coleman, “*Introduction to many-body physics*” 2015.
- [58] A. Sumiyama, Y. Oda, H. Nagano, Y. Onuki, K. Shibusaki, and T. Komatsubara, “*Coherent kondo state in a dense kondo substance: $Ce_xLa_{1-x}Cu_6$* ” *Journal of the Physical Society of Japan*, vol. **55**, no. 4, pp. 1294–1304, 1986.
- [59] N. F. Mott, “*Rare-earth compounds with mixed valencies*” *The Philosophical Magazine: A Journal of Theoretical Experimental and Applied Physics*, vol. **30**, no. 2, pp. 403–416, 1974.
- [60] S. Doniach, “*The kondo lattice and weak antiferromagnetism*” *Physica B+C*, vol. **91**, pp. 231 – 234, 1977.
- [61] T. Park, H. Yuan, M. Salmon, R. Movshovich, J. Sarrao, and J. Thompson, “*Hidden magnetism and quantum criticality in the heavy fermion superconductor $CeRhIn_5$* ” *Nature*, vol. **440**, p. 65, 2006.
- [62] Q. S. P. Coleman, C. Péin and R. Ramazashvili, “*How do fermi liquids get heavy and die?*” *J. Phys. Cond. Matt.*, vol. **13**, p. 273, 2001.
- [63] H. V. Lohneysen, A. Rosch, M. Vojta, and P. Wolf, “*Fermi-liquid instabilities at magnetic quantum phase transitions*” *Rev. Mod. Phys.*, vol. **79**, p. 1015, 2007.
- [64] P. Aynajian, E. H. S. Neto, A. Gyenis, R. E. Baumbach, J. D. Thompson, Z. Fisk, E. D. Bauer, A. Yazdani, “*Visualizing heavy fermions emerging in a quantum critical kondo lattice*” *Nature*, vol. **586**, pp. 373–377, 2020.
- [65] F. Steglich, J. Arndt, S. Friedemann, C. Krellner, Y. Tokiwa, T. Westerkamp, M. Brando, P. Gegenwart, C. Geibel, S. Wirth, O. Stockert, “*Superconductivity versus quantum criticality: what can we learn from heavy fermions?*” *J. Phys. Cond. Matt.*, vol. **2822**, p. 164202, 2010.
- [66] T. Willers, F. Strigari, Z. Hu, V. Sessi, N. B. Brookes, E. D. Bauer, J. L. Sarrao, J. D. Thompson, A. Tanaka, S. Wirth, L. H. Tjeng, and A. Severing, “*Correlation between ground state and orbital anisotropy in heavy fermion materials*” *Proceedings of the National Academy of Sciences*, vol. **112**, no. 8, pp. 2384–2388, 2015.
- [67] K. Iida, Y. Nagai, S. Ishida, M. Ishikado, N. Murai, A. D. Christianson, H. Yoshida, Y. Inamura, H. Nakamura, A. Nakao, K. Munakata, D. Kagerbauer, M. Eisterer, K. Kawashima, Y. Yoshida, H. Eisaki, and A. Iyo, “*Coexisting spin resonance and long-range magnetic order of Eu in $EuRbFe_4As_4$* ” *Phys. Rev. B*, vol. **100**, p. 014506, Jul 2019.

- [68] P. G. Pagliuso, C. Petrovic, R. Movshovich, D. Hall, M. F. Hundley, J. L. Sarrao, J. D. Thompson, and Z. Fisk, "Coexistence of magnetism and superconductivity in $CeRh_{1-x}Ir_xIn_5$ " Phys. Rev. B, vol. **64**, p. 100503, Aug 2001.
- [69] A. Llobet, A. D. Christianson, W. Bao, J. S. Gardner, I. P. Swainson, J. W. Lynn, J.-M. Mignot, K. Prokes, P. G. Pagliuso, N. O. Moreno, J. L. Sarrao, J. D. Thompson, and A. H. Lacerda, "Novel coexistence of superconductivity with two distinct magnetic orders" Phys. Rev. Lett., vol. **95**, p. 217002, Nov 2005.
- [70] S. Ohira-Kawamura, H. Shishido, A. Yoshida, R. Okazaki, H. Kawano-Furukawa, T. Shibauchi, H. Harima, and Y. Matsuda, "Competition between unconventional superconductivity and incommensurate antiferromagnetic order in $CeRh_{1-x}Co_xIn_5$ " Phys. Rev. B, vol. **76**, p. 132507, Oct 2007.
- [71] E. D. Bauer, J. D. Thompson, J. L. Sarrao, L. A. Morales, F. Wastin, J. Rebizant, J. C. Griveau, P. Javorsky, P. Boulet, E. Colineau, G. H. Lander, and G. R. Stewart, "Structural tuning of unconventional superconductivity in Pu_mGa_5 ($m = Co, Rh$)" Phys. Rev. Lett., vol. **93**, p. 147005, Sep 2004.
- [72] P. G. Pagliuso, D. J. Garcia, E. Miranda, E. Granado, R. Lora Serrano, C. Giles, J. G. S. Duque, R. R. Urbano, C. Rettori, J. D. Thompson, M. F. Hundley, and J. L. Sarrao, "Evolution of the magnetic properties and magnetic structures along the $rmln_{3n+2}$ ($r=Ce, Nd, Gd, Tb$; $m=Rh, Ir$; and $n=1,2$) series of intermetallic compounds" Journal of Applied Physics, vol. **99**, no. 8, p. 08P703, 2006.
- [73] P. F. S. Rosa, A. Oostra, J. D. Thompson, P. G. Pagliuso, and Z. Fisk, "Unusual kondo-hole effect and crystal-field frustration in Nd-doped $CeRhIn_5$ " Phys. Rev. B, vol. **94**, p. 045101, Jul 2016.
- [74] J. Remeika and Z. Fisk, "Handbook on the physics and chemistry of rare earths" vol. **12**, 1989.
- [75] "CeRhIn₅ crystal structure: Datasheet from "pauling file multinaries edition – 2012" in springermaterials (https://materials.springer.com/isp/crystallographic/docs/sd_1217779)" Copyright 2016 Springer-Verlag Berlin Heidelberg & Material Phases Data System (MPDS), Switzerland & National Institute for Materials Science (NIMS), Japan.
- [76] A. Aebischer, M. Hostettler, J. Hauser, K. Krämer, T. Weber, H. U. Güdel, and H.-B. Bürgi, "Structural and spectroscopic characterization of active sites in a family of light-emitting sodium lanthanide tetrafluorides" Angewandte Chemie International Edition, vol. **45**, no. 17, pp. 2802–2806, 2006.
- [77] S. Kawasaki, M. Yashima, Y. Mugino, H. Mukuda, Y. Kitaoka, H. Shishido, and Y. Onuki "Enhancing the superconducting transition temperature of $CeRh_{1-x}Ir_xIn_5$ due to the Strong coupling effects of antiferromagnetic spin fluctuations: An ^{115}In nuclear quadrupole resonance study" Phys. Rev. Lett., vol. **96**, p. 147001, Apr 2006.
- [78] G. G. Lesseux, H. Sakai, T. Hattori, Y. Tokunaga, S. Kambe, P. L. Kuhns, A. P. Reyes, J. D. Thompson, P. G. Pagliuso, and R. R. Urbano, "Orbitally defined field-induced electronic state in a kondo lattice" Phys. Rev. B, vol. **101**, p. 165111, Apr 2020.
- [79] K. R. Shirer, A. C. Shockley, A. P. Dioguardi, J. Crocker, C. H. Lin, N. apRoberts Warren, D. M. Nisson, P. Klavins, J. C. Cooley, Y.-f. Yang, and N. J. Curro, "Long range order and two-fluid

behavior in heavy electron materials” Proceedings of the National Academy of Sciences, vol. **109**, no. 45, pp. E3067–E3073, 2012.

[80] A. M. Clogston and V. Jaccarino, “*Susceptibilities and negative Knight shifts of intermetallic compounds*” Phys. Rev., vol. **121**, pp. 1357–1362, Mar 1961.

[81] C. Petrovic, R. Movshovich, M. Jaime, P. G. Pagliuso, M. F. Hundley, J. L. Sarrao, Z. Fisk, and J. D. Thompson, “*A new heavy-fermion superconductor CeIrIn₅ : A relative of the cuprates?*” Europhysics Letters (EPL), vol. **53**, pp. 354–359, Feb 2001.

[82] C. H. Lin, K. R. Shirer, J. Crocker, A. P. Dioguardi, M. M. Lawson, B. T. Bush, P. Klavins, and N. J. Curro, “*Evolution of hyperfine parameters across a quantum critical point in CeRhIn₅*” Phys. Rev. B, vol. **92**, p. 155147, Oct 2015.

[83] P. Rosa, L. de Oliveira, C. de Jesus, K. Moura, C. Adriano, W. Iwamoto, T. Garitezi, E. Granado, M. Saleta, K. Pirota, and P. Pagliuso, “*Exploring the effects of dimensionality on the magnetic properties of intermetallic nanowires*” Solid State Communications, vol. **191**, pp. 14 – 18, 2014.

[84] M. Giannini, F. A. Rueggeberg, R. R. Pacheco, R. R. Urbano, C. Rettori, A. F. Garcia-Flores, A. C. R. A. Lancellotti, G. G. Lesseux, J. R. Montero, E. D. Martínez, “*Nanopartículas com propriedades Ópticas de fluorescência e uso*” Patente, 2019.

[85] Z. Song, *et. al*, “Upconversion in hexagonal phase NaYF₄” J. Opt., vol. 18, 2012.

[86] M. Cabrera-Baes, M. A. Avila, C. Rettori, “Conduction electrons in aperiodic versus periodic structures: An ESR study of quasicrystalline i-Y(Gd)-Cd and its approximant Y(Gd)-Cd₆” Phys. Rev. B **100**, 1, 014207, 2019.

[87] G. G. Lesseux, W. Iwamoto, A. F. García-Flores, R. R. Urbano, and C. Rettori, “*Absence of exchange interaction between localized magnetic moments and conduction-electrons in diluted Er³⁺ gold nanoparticles*” Journal of Applied Physics, vol. **115**, no. 17, p. 17E128, 2014.

[88] J. C. Souza, P. F. S. Rosa, J. Sichelschmidt, M. Carlone, P. A. Venegas, M. O. Malcolms, P. M. Menegasso, R. R. Urbano, Z. Fisk, and P. G. Pagliuso, “*Metallic islands in the kondo insulator SmB₆*” Phys. Rev. Research, vol. **2**, p. 043181, Nov 2020.

[89] Z. Wang, Z. Mei, P. Menegasso, T. Kissikov, P. Massat, I. Fisher, and N. Curro, “*NMR Studies of TmVO₄*” in APS March Meeting Abstracts, vol. **2019** of APS Meeting Abstracts, p. B07.003, Jan. 2019.

[90] Z. Mei, Z. Wang, P. Menegasso, P. Massat, I. Fisher, and N. Curro, “*NMR Studies of Nematicity in TmVO₄ and TmAsO₄*” in APS March Meeting Abstracts, vol. **2019** of APS Meeting Abstracts, p. B07.004, Jan. 2019.

[91] <http://chiralqubit.eu/a-visit-to-the-zavoisky-museum>, Consulted at 2020-12-20.

Appendix A

Sandwich Ph. D. at UC - Davis

During my Ph. D. I fortunately had the chance to get involved into a Seed Grant project (UC Seed Grant: Uncovering the Role of Crystal Fields in Heavy Fermion Superconductors) about the investigation of Rare Earth doping into heavy fermions systems. This work has been done in a collaboration between the professors Ricardo Urbano, Pascoal Pagliuso and Nicholas Curro, from Unicamp and University of California, and it predicted an exchange between students from those institutes. In this context, part of my Ph.D. investigation has been done as a sandwich at UC-Davis, working at Prof. Curro's laboratory.

During this experience, I had the opportunity to travel to Davis and not only perform experiments there, but also being immerse into a different environment (both cultural and scientific) them I was before, and it was fundamental to my scientific and personal growth.

From the scientific point of view, I was totally independent at the laboratory, since my advisor was many miles away to support me there. It is worth mentioning that, when I arrived Professor Curro's lab, I had a lot of work to do, such as adapt the probes to our kind of experiments, deal with a new experimental setup and plan the experiments to be performed into a systematic and precise way. Two very important scientific contributions raised for this work: The first being the already mentioned studies on heavy fermions compounds, chosen as the theme of this thesis, and the second

one being the exploration of the vanadium oxides, which lead to relevant panels on March Meeting.

Apart from that, I had to work with a lot of Python coding, to control and execute the auto-tuner to the tank circuit in order to perform the frequency-sweep experiments for obtaining the spectra of the $CeMIn_5$ family. This was my first experience with high level programming, which lead me to conclude that I like programming as I like Physics itself, and had a decisive impact in my career, since after this period, I decided to stop working as a Scientist after finishing my Ph.D., and engage in software development.

Although this was a very good experience for me, it also gave robustness to the collaboration between our group at IFGW and UC-Davis, since after me, two students of our group has done a short to medium internship there. Unfortunately, this internship program is paused at the moment due to the pandemic, however, we have established a long term collaboration with UC.

Appendix B

Fundamental of continuous wave ESR experiments

This appendix is devoted to the practical aspects of an ESR spectroscopy experiment. Hereafter, the operation of a c. w. ESR spectrometer, the microwave bridge, the ESR cavity, the iris, the magnetic field controller, and the low-temperature system will be presented and discussed.



Figure B.1: Photograph of Zavoisky's experimental setup for the first ESR experiments ever performed. Figure taken from [91].

The Zeeman effect is known since 1896, but it took half a decade for the first ESR spectrometer to be built by Zavoisky in 1945. His experimental setup is shown in Fig. B.1. Such delay in the development of theory and experiment happened simply because there were not components to build a sensitive enough detector, which came

up only with the advent of the radar, during World War II.

The most simplified possible spectrometer consists of four basic elements: A sweepable **microwave source**, that emits the electromagnetic radiation to a **sample** of interest and a **detector**, to evaluate how much energy was absorbed. All of that in the presence of an external **magnetic field**. The source and the detector are put inside what is called a microwave bridge and the sample goes inside the microwave cavity, which is a device to enhance the signal.

B.1 The ESR Microwave Bridge

If one would compare an experimental ESR setup with a human body, the brain would definitively be the microwave bridge, as the heart would be the resonance cavity, preferentially with a very interesting sample inside. But first, let's stick to the brain, I mean, bridge. A diagram with its essential parts is drawn in Fig B.2.

The spectrometer consists of other parts such as power supplies and electronic protection to the

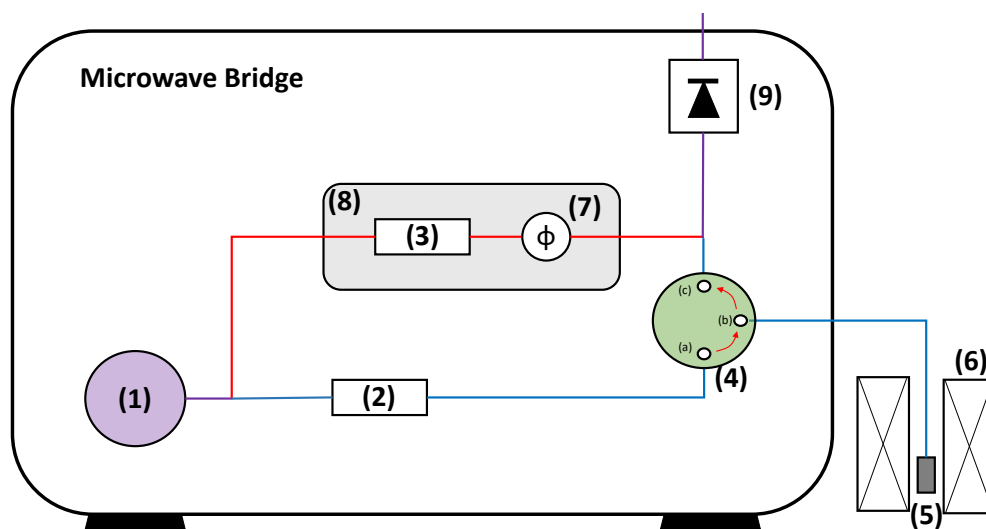


Figure B.2: Schematic function of the microwave bridge. (1) is the MW source; (2) and (3) are the power attenuators, (4) is the circulator, (5) is the resonance cavity (which stays out of the bridge), (6) is the electromagnet (actually it is not a part of the microwave bridge, but it is in the figure for reference), (7) is the lock-in amplifier of the reference arm (8) and (9) is the receptor diode. A detailed description of each component is presented in the main text.

components, but the most important ones, which are closely related to the Physics of the phenomena are hereafter discussed. The radiofrequency is produced on the microwave source (for types of those sources, please refer to Appendix C) and passes through an attenuator. Such attenuator is required because power-dependent experiments are very important and controlling the power level in the microwave generator is desired. So, what is done is produce a very high power microwave (about 0.5 W) and attenuate it through another electronic device to the desired power as well as avoid saturation of the spin system.

The attenuated microwave signal goes then to the circulator, which only allows it to pass from a to b and from b to c , but not from a to c directly. This is crucially important because our ESR setup (and the vast majority of them throughout the world) is reflective, not a transmissive one. This means that the initial power is compared to the power reflected by the sample. To reach the sample, the microwave signal passes from a to b in the circulator and then goes to the sample into the cavity; when the signal comes back from the sample to b , it goes through c in the circulator and then to the detector. If any signal passes from a to the detector, it would not carry information of the sample and then would disturb the experimental result. This is why the circulator is so important in the bridge.

Finally, the detector is generally a Schottky diode, which transforms the microwave signal that comes from the sample into a voltage that goes to the console to compose the spectrum in the PC. However, since the signal from the sample is very weak, the current in the diode is not enough to reach its optimal level of operation. Then, it is required an external bias source, which comes from the reference arm in the bridge. It has an internal attenuator that automatically sets the power to match the detector's linear operating current regime and a phase sensitive lock-in to match the same phase between the microwave coming from the sample and the reference arm. This arm is designed to optimize the work of the diode providing the best possible signal-to-noise ratio. Although many parameters can be controlled by the user, most of them are automatically controlled by the console and the bridge itself, and that is why the later is considered the brain, with an autonomic nervous system.

B.2 The ESR Resonant Cavity

The resonant cavity is simply a metallic box, with a rectangular or cylindrical shape, responsible to amplify the signal response from the sample. It also has a resonance frequency, in which the microwave power will be fully absorbed. The quality is defined by the Q factor, which is a ratio between the energy stored and the energy reflected per cycle of the microwave.

The “trapped” waves inside the cavity are referred to as standing waves and they have their electric and magnetic field components exactly 90 degrees out of phase. The vast majority of classical cavities is designed to have the samples exactly at a maximum magnetic standing field (the magnetic field required for the Zeeman interaction) and at a minimum electric field, since it could cause unwanted dielectric response, dissipating energy and lowering the quality factor (Q). That is the reason why small samples are usually desired for ESR since larger ones tend to “disturb” the cavity with a dielectric response. Therefore, high-frequency cavities are physically smaller and that is why they are more sensitive and “disturbable”.

The microwaves are coupled to the cavity by the iris. The iris size can be controlled by a plastic screw with a conducting tip. It determines the quantity of reflected radiation and the amount of radiation that passes into the cavity. Before the experiment, the cavity must be critically coupled to the microwave, this means that the microwave is exactly at the cavity’s resonance frequency and the Q factor is maximum. When the sample absorbs microwave energy, the coupling changes because less radiation is available, changing the cavity impedance and its Q . Since the cavity is now out of resonance condition and critical coupling regime, the microwave power will be reflected resulting in the ESR signal.

B.3 Magnetic Field

The ESR magnet used in the experiments of this thesis is a water refrigerated sweepable 2T electromagnet, but for ESR experiments at higher frequencies, i. e., THz frequency spectroscopy,

one may use superconducting magnets due to the higher field values required. The field sweep rate was automatically controlled by a microprocessor in the console. The sweep range is divided up to 4096 steps each one addressed with a voltage between those steps. The sweeping time is achieved by controlling how much time the sequence spends on each point. Also, to increase the sensitivity, the magnetic field is modulated. Such modulation amplitude must be chosen such as the ESR signal is not distorted over the modulation range (typically, the modulation value must be not higher than half of the ESR linewidth). The signal is then transformed into a sine wave, whose intensity is proportional to the slope of the signal. As a final result, one does not observe a conventional absorption Lorentzian, but its derivative.

A lock-in amplifier compares the modulated signal with a reference at the same frequency and, any signal coming from the sample not at this exact frequency is counted as noise and eliminated. The magnetic field modulation is induced by modulation coils in the walls of the cavity and its values range from 0.5 to 15 G.



Figure B.3: Photograph of the ESR setup used at GPOMS - IFGW - Unicamp for the experiments described in this thesis.

B.4 Temperature Control

Controlling the temperature as an external parameter is straightforward with this He gas flow system, at least on paper. One just need to put a cryostat inside their resonance cavity. In our ESR setup, X-band experiments are performed inside an Oxford flow cryostat. A transfer line is connected from the liquid helium Dewar to the cryostat. The cold helium gas flows through a needle valve, in the line to the cryostat and passes through the sample and cavity, removing heat and returning through another channel in the transfer line to the recovering tubes. This process can become more efficient if a diaphragm pump is installed on the return line.

Finally, Fig. B.3 is a photo of our experimental ESR setup illustrating the main components mentioned in this text.

Appendix C

Microwave and Radiofrequency Generators

Electromagnetic radiation covers a high spectrum of frequencies. On the high energy side, there are gamma waves and X-ray radiation. Visible Light, near-ultraviolet, and near-infrared occupy an intermediary energy range, while microwave (MW) and radiofrequency (RF) are on the bottom side of the spectra, being very large waves (with wavelength over thousands of kilometers) with the lowest energy in the electromagnetic waves spectra.

However, as pointed out in chapter 2, such waves are in the energy range of nuclear and electronic transitions, so they are very important for ESR and NMR experiments. Their generation, which happens inside our equipment will be briefly discussed here for an overview.

C.1 Microwave Generation

Microwaves are electromagnetic waves with typical wavelength in the range of 1 mm to 1 m, corresponding to a frequency between 300 and 0.3 GHz. So, they are situated between the infrared and radiofrequency on the electromagnetic spectra. As pointed out throughout chapter 2, a fundamental prerequisite for an ESR experiment is having a functional microwave generator.

There are several ways to produce microwaves and the first ones were the thermionic valves, as the magnetron and the Klystron. Both are based on heating electrons and making them oscillate between plates with a high voltage difference between them. The electrons are accelerated and produce MW radiation. The low-power models have been used as radar detectors, mainly during World War II, but given their simplicity and cheapness, these devices are still used in older TVs and microwave ovens.

For our technical ESR applications, however, the valves have been exchanged for diodes. Such substitution has happened in the late 60's with the advent of Field Effect Transistors (FETs). Now a days, however, new technology is being applied: The Gunn diode.

Gunn diodes possess a layer of the semiconducting material GaAs. This diode's $I-V$ curve presents a "negative resistance" branch, in which the current through the diode is decreased when the voltage is increased.

When a DC voltage is applied to bias the diode to the negative resistance region, this negative resistance cancels the load resistance, which is positive. The result is a circuit with zero differential resistance that produces spontaneous electric oscillations. such oscillation can be controlled by external parameters, such as the size of the GaAs layer, the applied bias voltage, and the coupling load, among others. Such control is very important to determine the oscillation frequency, and as a result, the frequency of the generated microwave. Note however that the MW's power depends on the number of oscillating electrons, which is not easily controlled. That's why the MWs are generated at high power and attenuated for power dependent ESR experiments.

Gunn diodes generally are capable of producing MWs in the $1 < f < 100$ GHz, which covers all the most employed ESR frequency bands.

C.2 Radiofrequency Generation

Radiofrequency radiation is as important for NMR as MWs are for ESR. They are also electromagnetic waves ranging from the lower energy branch of the spectrum. Their length can be as high as one thousand kilometers, but generally, most textbooks range them between 10 km and 1 m, covering a frequency range from 30 kHz to 300 MHz. They are less energetic than the MWs, which makes them much easier to produce. It is not by chance that they are used to transmit radio, television, cellphone, and internet signal all over the world. Many of them may be even passing not only through this piece of paper you are reading (or through the screen of your PC) and even through you. But that's nothing to worry about since these waves are generally low power ones and RF has low interaction with the matter.

Speaking about what is more important: Generating waves in the RF region is as easy as having a pulsed electric current source. One just has to turn on/off the source at the RF frequency to generate it. This can be achieved by employing transistors and diodes on the generators. Since one must "switch" on/off very fast, generally a small electrical current is employed, otherwise, the high voltage would be responsible for arcing in the generation switch. So, the typical process is to create low power waves and amplify them latter thought an RF amplifier.

It's worth mentioning however that very high power RFs can be created by more robust systems. The most recent example is the 5G internet signal, which is a very high power RF radiation. Its use is still under debate regarding if it could cause any harm to biological organisms by the time this thesis is finished.

Appendix D

NMR Hamiltonians and pulse sequences

In pulsed NMR, radiofrequency pulses are used to manipulate the spins ensemble. The “trick” is to use the coil that wraps the sample to “switch” between moments in which the RF pulse is turned on and moments in which it is turned off. One must be aware that RF produces a magnetic field inside the coil and switching it on and off changes the effective magnetic field over the spins ensemble. The effective magnetic field is given by the vector sum between the RF field (\vec{H}_1) and the magnet field (\vec{H}_0). Changing the effective field leads to a change in the Zeeman interaction. Stepping back a moment for the Zeeman hamiltonian, in the nuclear case one have:

$$H = \gamma \vec{H} \cdot \vec{I} = \omega_0 \hat{I}_z, \quad (\text{D.0.1})$$

which is valid when \vec{H} is parallel to the z axis.

From now on, the math behind how pulse sequences can control a spin ensemble will be shown. First, they are performed for an insulated spin in space and then generalized to an ensemble. It is known that the state of a spin can be written as $|\psi\rangle = c_\alpha|\alpha\rangle + c_\beta|\beta\rangle$, in which the kets $|\alpha\rangle$ and $|\beta\rangle$ correspond to the spinors for for up and down spin states:

$$|\alpha\rangle = \begin{pmatrix} 1 \\ 0 \end{pmatrix}; \quad \text{and} \quad |\beta\rangle = \begin{pmatrix} 0 \\ 1 \end{pmatrix}. \quad (\text{D.0.2})$$

Thus the action of the hamiltonian H over $|\alpha\rangle$ and $|\beta\rangle$ results in:

$$H|\alpha\rangle = \omega_0 \hat{I}_z |\alpha\rangle = \frac{1}{2} \omega_0 |\alpha\rangle, \quad (\text{D.0.3})$$

$$H|\beta\rangle = \omega_0 \hat{I}_z |\beta\rangle = -\frac{1}{2} \omega_0 |\beta\rangle. \quad (\text{D.0.4})$$

To calculate how the spin evolves in time under the influence of a given Hamiltonian, one must make use of the Schrödinger's equation:

$$\frac{d}{dt} |\psi\rangle = -\hat{H} |\psi\rangle \quad (\text{D.0.5})$$

If one considers that the field produced by the magnet is much more intense than the field from the coil, the Hamiltonian is:

$$\hat{H} = \omega_0 \hat{I}_z. \quad (\text{D.0.6})$$

If the spin would evolve from t_a to t_b , assuming a time difference τ and employing exponential operators:

$$|\psi(t_b)\rangle = e^{-i\omega_0\tau\hat{I}_z} |\psi(t_a)\rangle. \quad (\text{D.0.7})$$

But the term $e^{-i\omega_0\tau\hat{I}_z}$ can be written as a rotator around z axis, which is represented by $\hat{R}(\omega_0\tau)$:

$$\hat{R}(\omega_0\tau) = \begin{pmatrix} e^{-\frac{i\omega_0\tau}{2}} & 0 \\ 0 & e^{\frac{i\omega_0\tau}{2}} \end{pmatrix}, \quad (\text{D.0.8})$$

the effect of this operator is to rotate the spinnor on z axis by the angle $\omega_0\tau$.

Now suppose that τ has a fixed value, such as $(\omega_0\tau) = \frac{\pi}{2}$. Obviously, by doing that the generality is being lost, but τ is exactly the time that the pulse remains off, so it is a controllable experimental parameter and, in fact, the the relevant values for NMR are just $\theta = \frac{\pi}{2}$ and $\theta = \pi$; so for now consider $\hat{R}_z(\frac{\pi}{2})$.

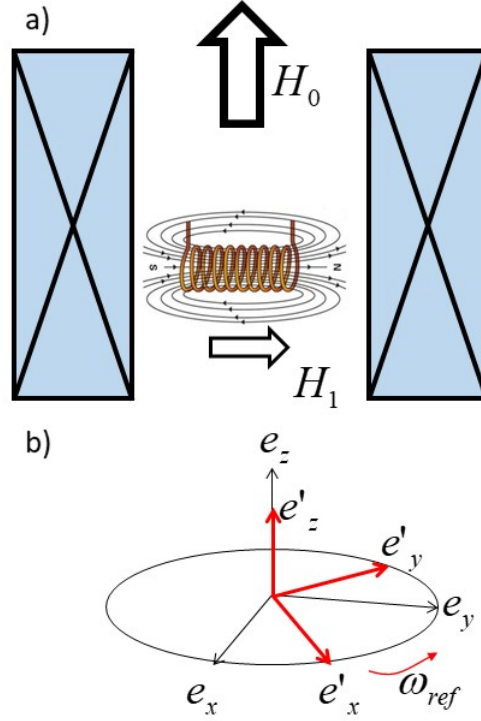


Figure D.1: a) Scheme of the magnetic fields \vec{H}_0 and \vec{H}_1 inside the magnet coils. b) Rotating frame. Note that $\hat{e}_z = \hat{e}'_z$, but \hat{e}'_x and \hat{e}'_y rotates around the z axis.

Now consider how $\hat{R}_z(\frac{\pi}{2})$ acts over the state $|\psi(t_a)\rangle = |\alpha\rangle$:

$$\hat{R}(\omega_0\tau) |\alpha\rangle = \begin{pmatrix} e^{-\frac{i\pi}{4}} & 0 \\ 0 & e^{\frac{i\pi}{4}} \end{pmatrix} \begin{pmatrix} 1 \\ 0 \end{pmatrix} = e^{-\frac{i\pi}{4}} |\alpha\rangle. \quad (\text{D.0.9})$$

Since the $e^{-\frac{i\pi}{4}}$ is just a phasor, it can be ignored and $|\alpha\rangle$ is simply an eigenstate of $\hat{R}_z(\frac{\pi}{2})$. This is actually an expected result. Since the hamiltonian is provided by a magnetic field on z -axis, its predictable that a spin on z -axis will continue there. However, consider now that $|\psi(t_a)\rangle = |+x\rangle$, i. e., the initial spin state is pointing towards x axis. The ket $|x\rangle$ is given by:

$$|+x\rangle = \frac{1}{\sqrt{2}} \begin{pmatrix} 1 \\ 1 \end{pmatrix}, \quad (\text{D.0.10})$$

so that

$$\hat{R}(\omega_0\tau)|+x\rangle = \begin{pmatrix} e^{-\frac{i\pi}{4}} & 0 \\ 0 & e^{\frac{i\pi}{4}} \end{pmatrix} \frac{1}{\sqrt{2}} \begin{pmatrix} 1 \\ 1 \end{pmatrix} = \frac{1}{2} \begin{pmatrix} 1-i \\ 1+i \end{pmatrix}, \quad (\text{D.0.11})$$

which is the $|+y\rangle$. So that $\hat{R}_z(\frac{\pi}{2})|+x\rangle = |+y\rangle$.

This means a 90-degree rotation on the xy plane, about the z axis.

Summarizing the previous two results and generalizing for any angle, for a fixed magnetic field along z axis, the spin rotates around the z axis. If the spin has any angle with the magnetic field, one of the components (parallel to z) does not rotate at all, while the component on the xy plane rotates around the z axis. Furthermore, that is exactly the explanation of the Larmor precession for a spin with a fixed magnetic field upon it.

Now the calculations will be repeated for a moment when the RF pulse is on, i. e., affecting the evolution of the spin state. The RF coil is mounted accordingly to the Fig. D.1, i. e., the magnetic field H , produced by the coil is perpendicular to H_0 . Consider for now that $\vec{H}_1 = H_1\hat{x}$. To make the calculations easier, a common trick is to use the rotating frame, which is a referential frame that is rotating around z axis with an angular velocity ω_R (please refer to Fig. D.1b).

All the states $|\psi\rangle$ on the statical frame can be rewritten on the rotating frame as:

$$|\psi\rangle^* = \hat{R}(\omega_R t)|\psi\rangle. \quad (\text{D.0.12})$$

Also, the hamiltonian \hat{H}_0 (from the external field) becomes:

$$\hat{H}_0 = \hat{H}_0^* = (\omega_0 - \omega_R)\hat{I}_z, \quad (\text{D.0.13})$$

and the hamiltonian from the RF field is:

$$\hat{H}_1^* = \gamma A_1(\hat{I}_x \cos \phi + \hat{I}_y \sin \phi), \quad (\text{D.0.14})$$

in which ϕ is the angle between H_1 and the static x -axis. So that the total hamiltonian on the rotating frame is:

$$\hat{H}^* = \hat{H}_0^* + \hat{H}_1^* = (\omega_0 - \omega_R)\hat{I}_z + \gamma A_1(\hat{I}_x \cos \phi + \hat{I}_y \sin \phi), \quad (\text{D.0.15})$$

but ϕ can be rewritten as $\omega_R t$:

$$\hat{H}^* = (\omega_0 - \omega_R)\hat{I}_z + \gamma A_1(\hat{I}_x \cos(\omega_R t) + \hat{I}_y \sin(\omega_R t)). \quad (\text{D.0.16})$$

So, ω_R is defined as the microwave's pulse frequency. It is another experimentally controlled parameter that can be chosen as $\omega_R = \omega_0$, the Larmor frequency. This is a different way to write the resonance condition in pulsed sequences, and such makes the first term on eq. D.0.16 equal to zero. It is as if the spin does not feel the external magnetic field at all.

Note that t is another experimental parameter, since it refers to the time the RF pulse remains on so, without loss of generality: $\omega_R t = \frac{\pi}{2}$, so that the total hamiltonian on the rotating frame (eq. D.0.16) can be simplified to:

$$\hat{H}^* = \gamma H_1 \hat{I}_x. \quad (\text{D.0.17})$$

Then, if the temporal evolution for $|\Psi_1\rangle^*$ is performed, prior to the pulse and $|\Psi_2\rangle^*$, after the pulse, it becomes:

$$|\Psi_2\rangle^* = \exp\{-iH_1\hat{I}_x\tau\} |\Psi_1\rangle^*, \quad (\text{D.0.18})$$

$$|\Psi_2\rangle^* = \hat{R}_x(\gamma H_1 \tau) |\Psi_1\rangle^*, \quad (\text{D.0.19})$$

using that $\gamma H_1 \tau = \theta$, and:

$$\hat{R}_x(\theta) = \begin{pmatrix} \cos \frac{\theta}{2} & -i \sin \frac{\theta}{2} \\ -i \sin \frac{\theta}{2} & \cos \frac{\theta}{2} \end{pmatrix}. \quad (\text{D.0.20})$$

\hat{R}_x is then a rotator of the spins around x -axis, so, considering $|\Psi_1\rangle^* = |\alpha\rangle$ and $\theta = \frac{\pi}{2}$, thus:

$$\hat{R}_x\left(\frac{\pi}{2}\right) |\alpha\rangle = e^{-i\frac{\pi}{4}} |-y\rangle. \quad (\text{D.0.21})$$

So that, the spin pointing towards z will now, after a $\frac{\pi}{2}$ pulse be on the xy plane. This is the reason why θ is called a flipping angle. After the pulse, H_1 is no more on and the resonance

conditions are not met, since $\omega_R = 0$. Then the Hamiltonian governing the system is now only H_0^* , in which the temporal evolution on the spin state will make it rotates continuously and undefined around z -axis.

Spins directions however mean nothing in the real world. One should extract some real quantity from our ensemble of spins, some measurable physical parameters. Fortunately, the NMR coil can detect tiny changes in magnetization. So, what must be done now is to calculate the expected value of the magnetization operator.

Any mean value in quantum mechanics can be calculated as $\langle Q \rangle = \sum_i \langle \psi_i | \hat{Q} | \psi_i \rangle$; and the coefficients of all the $|\psi_i\rangle$ s are known. The problem though is that our i is like 10^{20} spins, which makes such calculation a hard one.

Fortunately, there is a way to overcome this calculation: The density matrix $\hat{\rho}$, which is defined by:

$$\hat{\rho} = \sum_i |\psi_i\rangle \langle \psi_i|, \quad (\text{D.0.22})$$

and for a non-interacting $\frac{1}{2}$ spin system, thus:

$$\hat{\rho} = \begin{pmatrix} \langle c_\alpha c_\alpha^* \rangle & \langle c_\alpha c_\beta^* \rangle \\ \langle c_\beta c_\alpha^* \rangle & \langle c_\beta c_\beta^* \rangle \end{pmatrix} = \begin{pmatrix} \rho_\alpha & \rho_{xy}^* \\ \rho_{xy} & \rho_\beta \end{pmatrix}, \quad (\text{D.0.23})$$

in which the “ $\langle \rangle$ ” symbols means the mean values of the coefficients. Now to calculate the expected values the properties of the density operator may be used:

$$\langle Q \rangle = \text{Tr}(\hat{\rho}\hat{Q}). \quad (\text{D.0.24})$$

The magnetization components are than given by:

$$M_x = 4B^{-1} \text{Re}\{\rho_{xy}\}, \quad (\text{D.0.25})$$

$$M_y = 4B^{-1} \text{Im}\{\rho_{xy}\}, \quad (\text{D.0.26})$$

$$M_z = 2B^{-1}(\rho_\alpha - \rho_\beta), \quad (\text{D.0.27})$$

where $B = \frac{\hbar\omega_0}{k_B T}$.

For the equilibrium magnetization prior to the pulse, $\vec{M} = M\hat{z}$. Immediately after the pulse, $\vec{M}_z = M\hat{y}$; and as the system evolves to (3) (please refer to Fig. D.2), the magnetization evolves under the action of H_0 :

$$M_{x(3)} = M[\cos(\Omega_0 t) - \sin(\Omega_0 t)], \quad (\text{D.0.28})$$

$$M_{y(3)} = M[\sin(\Omega_0 t) + \cos(\Omega_0 t)], \quad (\text{D.0.29})$$

$$M_{z(3)} = M_{z(2)}. \quad (\text{D.0.30})$$

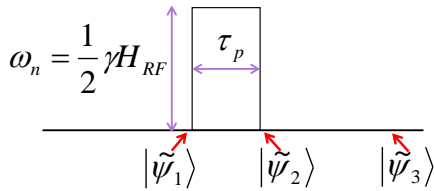


Figure D.2: Stages $|\Psi_1\rangle$, $|\Psi_2\rangle$ and $|\Psi_3\rangle$ represented accordingly to the pulse sequence. Time evolution of the state is given by Schrödinger's equation.

So that the magnetization of the ensemble evolves exactly like the single spin state.

Although the equations are correct, there are non-conservative processes that happens on the spin systems that prevent the spins to lays forever in the xy plane. Such give rise to the relaxation times T_1 and T_2 and are discussed on chapter 2.

Appendix E

Complementary Experimental Techniques

This appendix is devoted to a simple explanation of fundamental concepts for other experimental techniques employed in the research developed in this thesis.

E.1 X-ray Diffraction

X-ray experiments are usually the first ones to be performed on newly growth single crystal samples to characterize its crystallographic structure. It consists simply of focusing X-rays into a sample in a defined range of angles and detecting the diffracted photons. When the structure is periodic (single crystal), the Bragg's law, described by Eq. E.1.1 is satisfied

$$n\lambda = 2d \sin \theta, \tag{E.1.1}$$

where n is an integer, λ is the X-ray wavelength, θ is the incident X-ray angle and d is the distance between planes, which is the parameter to be determined.

X-ray diffraction experiments can be performed on crystals or powdered samples. The former is very hard and often require large sincrotron facilities to be performed. The later, performed on this thesis, is quite simple and can be done in a less complex bench top apparatus. The

used diffractometer is a Bruker D2 PHASER with Cu K_α radiation in a θ - 2θ (also called Bragg-Brentano) configuration.

E.2 Electrical Resistivity

Electrical resistivity has been performed on a commercial Quantum Design Physical Properties Magnetometer System - PPMS (9 or 14 T). The method employed was the four-points probe method which consists of putting four platinum wires over the sample and “gluing” them to the crystal’s surface with a conducting silver paste. Though a very small electric current is applied on the external wires while the voltage is measured between the two inner contacts. An illustration is presented at Fig. E.1. The resistance of the material is calculated through Ohm’s second law $R = \frac{V}{i}$.

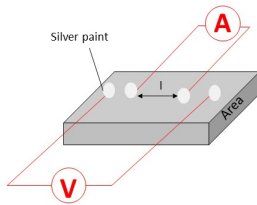


Figure E.1: Illustration of the four leads method to measure resistivity. This is the conventional method to ensure no wiring contribution to low-resistivity samples.

Possessing the resistance value R and the geometric properties of the sample, one can easily determine the electrical resistivity ρ by employing Ohm’s first law:

$$\rho = \frac{RA}{l}, \quad (\text{E.2.1})$$

where l is the distance between the inner contacts and A is the transverse area.

This method is way better than the conventional two-points probe method since it eliminates any extrinsic contributions from the wiring in the samples’ resistivity.

E.3 Specific Heat

Specific heat has been also measured on a Quantum Design PPMS (9 or 14 T). In solids the specific heat is determined as:

$$c_p = \frac{1}{m} \left(\frac{Q}{\partial T} \right)_P. \quad (\text{E.3.1})$$

Where the subscript index P stands for constant pressure, meaning that the volume of the solid can change over the process. Q is the heat quantity and T the temperature, while m is the crystal mass.

Specific heat is measured by thermal relaxation of the whole experimental system, which is composed by a thermometer and a heater under a metallic platform in which the sample is “glued” employing a grease with high thermal conductivity.

The measurement is performed by applying a well-known quantity of heat Q at constant power over a fixed period, and then measuring the temperature of the system versus time. The relaxation constant is associated with the $\frac{Q}{\partial T}$ rate.

To rule out contribution from the platform, the system with grease, without sample is measured first, generating a Debye-like specific heat curve which is called addenda. It is worth mentioning that the addenda have to be measured before any sample since it can be affected by the amount of grease and even by its position on the platform. After that, the whole system (platform + grease + sample) is measured and the obtained curve has the addenda subtracted.

E.4 Magnetic Measurements

The M versus T and M versus H experiments performed in the ludwigites with a commercial 7T Quantum Design Magnetic Properties Measurement System - MPMS SQUID magnetometer. The samples are generally placed inside a plastic tube, which is attached to a rod and inserted

into the cryostat.

The set is free to move between the superconducting magnet which produce an external magnetic field. The system also posses a pickup coil which collects the d.c. voltage generated by the sample motion, transforming the magnetic flux differential in d.c. electric current.

This coil is associated with a Josephson junction which is employed as an extremely sensitive current detector. The voltage is compared with a set internal reference to calculate its magnetization with a typical precision of 10^{-6} emu.

For the experiments on heavy fermions though, a higher magnetic field was required, to ensure the similar values to NMR magnetic field and rule out any unexpected field effects. Then, such experiments were performed using a VSM insert into the PPMS system. In this method, the sample vibrates in a high frequency inside the magnetometer, producing an a.c. voltage to the pickup coil. Although it is possible to use this technique to gather information about the a.c. magnetization, only d.c. component were considered in the investigations of this thesis.

Appendix F

Mathematica Code for Orbital Sketching

During Chapter 3 of this thesis, a lot of orbitals have been sketched through the value of alpha. This has been performed by using Mathematica, a Wolfram's software that allows complex calculations and fitting through scripts. The routine used to calculate the wavefunctions shown here through pictures, but is also available in my GitHub through the link:

[https : //github.com/PauloMenegasso/MathematicaCode](https://github.com/PauloMenegasso/MathematicaCode)

```

1  \setminus[Alpha] |5/2>- \setminus[Beta] |-3/2>
2  This can be re-written as:
3  \setminus[Alpha] (Sqrt[6/7]|3,3,1/2,-1/2> -Sqrt[(1/7)]|3,2,1/2,+1/2>) -
4  \setminus[Beta]( Sqrt[2/7]|3,-1,1/2,-1/2> -Sqrt[(5/7)]|3,-2,1/2,+1/2> )
5
6  Now if we take the overlap with spin up: -Sqrt[(1/7)]\setminus[Alpha] Y[3,2]
7  +Sqrt[5/7]\setminus[Beta] Y[3,-2] and with spin-down:
8  Sqrt[6/7]\setminus[Alpha]Y[3,3]-Sqrt[2/7]\setminus[Beta] Y[3,-1]
9  B=0T (B//c)
10
11 \setminus[Psi]1 = -Sqrt[(1/7)] Sqrt[0.596] *
12   SphericalHarmonicY[3, 2, \setminus[Theta], \setminus[Phi]] +
13   Sqrt[5/7] Sqrt[0.404]*SphericalHarmonicY[3, -2, \setminus[Theta], \setminus[Phi]]
14 \setminus[Psi]2 =
15   Sqrt[6/7]*Sqrt[0.596]*SphericalHarmonicY[3, 3, \setminus[Theta], \setminus[Phi]] -
16   Sqrt[2/7]*Sqrt[0.404]* SphericalHarmonicY[3, -1, \setminus[Theta], \setminus[Phi]]
17 \setminus[Psi]3 = -Sqrt[(1/7)] Sqrt[0.596] *
18   SphericalHarmonicY[3, -2, \setminus[Theta], \setminus[Phi]] +
19   Sqrt[5/7] Sqrt[0.404]*SphericalHarmonicY[3, 2, \setminus[Theta], \setminus[Phi]]
20 \setminus[Psi]4 =
21   Sqrt[6/7] Sqrt[0.596] *SphericalHarmonicY[3, -3, \setminus[Theta], \setminus[Phi]] -
22   Sqrt[2/7] Sqrt[0.404]*SphericalHarmonicY[3, 1, \setminus[Theta], \setminus[Phi]]
23
24 SphericalPlot3D[
25   Conjugate[\setminus[Psi]1]*\setminus[Psi]1 /. {\setminus[Alpha] -> 0.46}, {\setminus[Theta], 0,
26   Pi}, {\setminus[Phi], 0, 2 Pi}, PlotRange -> All]
27 SphericalPlot3D[
28   Conjugate[\setminus[Psi]2]*\setminus[Psi]2 /. {\setminus[Alpha] -> 0.46}, {\setminus[Theta], 0,
29   Pi}, {\setminus[Phi], 0, 2 Pi}, PlotRange -> All]

```

```

30
31 SphericalPlot3D[
32   Conjugate[\setminus\Psi]3*\setminus\Psi]3 /. {\setminus[Alpha] -> 0.46}, {\setminus[Theta], 0,
33   Pi}, {\setminus[Phi], 0, 2 Pi}, PlotRange -> All]
34 SphericalPlot3D[
35   Conjugate[\setminus\Psi]4*\setminus\Psi]4 /. {\setminus[Alpha] -> 0.46}, {\setminus[Theta], 0,
36   Pi}, {\setminus[Phi], 0, 2 Pi}, PlotRange -> All]
37
38 SphericalPlot3D[
39   Conjugate[\setminus\Psi]2*\setminus\Psi]2 + Conjugate[\setminus\Psi]1*\setminus\Psi]1 +
40   Conjugate[\setminus\Psi]3*\setminus\Psi]3 +
41   Conjugate[\setminus\Psi]4*\setminus\Psi]4 /. {\setminus[Alpha] ->
42   Sqrt[0.2116]}, {\setminus[Theta], 0, Pi}, {\setminus[Phi], 0, 2 Pi},
43   PlotRange -> All]
44
45 SphericalPlot3D[
46   Conjugate[\setminus\Psi]2*\setminus\Psi]2 + Conjugate[\setminus\Psi]1*\setminus\Psi]1 +
47   Conjugate[\setminus\Psi]3*\setminus\Psi]3 +
48   Conjugate[\setminus\Psi]4*\setminus\Psi]4 /. {\setminus[Alpha] -> Sqrt[
49   0.2116]}, {\setminus[Theta], 0, \setminus\Pi]}, {\setminus[Phi], 0, 2 \setminus\Pi]},
50   PlotStyle -> RGBColor[1., 0.61, 0.68], PlotRange -> All]
51
52 Manipulate[
53   SphericalPlot3D[
54     Conjugate[\setminus\Psi]2*\setminus\Psi]2 +
55     Conjugate[\setminus\Psi]1*\setminus\Psi]1 /. {\setminus[Alpha] -> x}, {\setminus[Theta], 0,
56     Pi}, {\setminus[Phi], 0, 2 Pi}, PlotRange -> All], {x, 0, 01}]
57

```

Appendix G

Scientific resultant from the investigations on this thesis

This appendix contains the articles prepared during this thesis. While some of them have already been published, some of them are in their final stage. After the list, a full draft is presented in each case.

1 - Nuclear Magnetic Resonance as a Probe for Electrical Crystal Field Scaling on Ce Based Heavy Fermions, P. Menegasso, I. Vinograd, Z. Wang, S. Mormon, P. Pagliuso, R. R. Urbano, N. J. Curro. Submitted to PRL (2021). This article is presented at Appendix H.

2 - Probing Surface Effects on α -NaYF₄ Nanoparticles by Nuclear Magnetic Resonance. T. Queiroz, M. Cabrera-Baez, P. Menegasso, E. Martines, A. Garcia-Flores, C. Rettori, R. R. Urbano. Accepted for publication in Journal of Physical Chemistry C (J. Phys. Chem. C 2020, 124, 17, 9523–9535). This article is presented at Appendix I.

3 - Metallic islands in Kondo insulator SmB₆. J. C. Souza, P. F. S. Rosa, J. Sichelschmidt, M. Carlone, P. A. Venegas, M. O. Malcolms, P. Menegasso, R. R. Urbano, C. Rettori, Z. Fisk, and P. G. Pagliuso. This article is presented at Appendix J.

4 - Magnetic Resonance Probing Spin Fluctuations in Cobalt Homometallic Ludwigites, P. Menegasso, G. G. Lesseaux, M. A. Continentino, D. C. Freitas, C. Rettori, R. R. Urbano (in preparation). This article is presented at Appendix K.

Articles regarding Nd doping on $CeMIn_5$ and rare earth doping on α - $NaYF_4$ nanoparticles are still under finalization. That is why they are not listed above.

Appendix H

Scientific Work on Heavy Fermions

This appendix brings the preprint of the paper submitted with the heavy fermions studies, detailed on chapter 3.

Hyperfine Couplings as a Probe of Orbital Anisotropy in Heavy Fermion Materials

P. Menegasso,¹ J. C. Souza,¹ I. Vinograd,² Z. Wang,² S. P. Edwards,² P. G. Pagliuso,¹ N. J. Curro,² and R. R. Urbano¹

¹*Instituto de Física “Gleb Wataghin”, UNICAMP, Campinas-SP, 13083-859, Brazil*

²*Department of Physics, University of California, Davis, California 95616, USA*

Overlap between neighboring atomic wavefunctions is a central feature of conducting solids. In heavy fermion materials, f -electron orbitals in the lattice lie on the boundary between fully localized and hybridized in an energy band. This dichotomy gives rise to a range of behaviors including antiferromagnetism, unconventional superconductivity, and the ability to tune from one ground state to the other continuously. Measuring the degree of this hybridization by traditional methods is challenging and indirect. We utilize a new approach using NMR to determine the magnetic couplings between the f -electrons and neighboring nuclear spins in a series of $\text{CeRh}_{1-x}\text{Ir}_x\text{In}_5$ crystals, and find that the hybridization is strongly directional dependent in this important class of superconducting heavy fermion materials. Our results demonstrate that hyperfine coupling measurements provide a quantitative measure of orbital anisotropy.

I. INTRODUCTION

Heavy fermion metals are characterized by strong electron-electron interactions that can be tuned across a quantum phase transition between localized f -electron magnetism and itinerant heavy-mass Fermi liquid behavior [1–3]. The crossover between these two extremes is controlled by the degree to which the f -electron orbitals hybridize with neighboring atoms to form dispersive bands [4–7]. Theoretical models typically assume that variables such as pressure or doping (‘chemical pressure’) indirectly modify the small wavefunction overlap between the Ce $4f$ electrons and itinerant conduction electron bands, which consequently alter the low energy degrees of freedom [8–11]. Detailed information about this hybridization has required complex quantum chemistry calculations [12], or indirect analysis of experiments [13–15].

The tetragonal CeMIn_5 ($M = \text{Co}, \text{Rh}, \text{Ir}$) materials are prototypical heavy fermion systems, exhibiting quantum criticality, antiferromagnetism and unconventional superconductivity across a phase diagram that can be tuned with pressure, magnetic field, or substitution at the transition metal site [16–19]. One of the outstanding mysteries in these materials is how the transition metal M changes the $4f$ hybridization, and hence the ground state. Similar physics is at play in the actinide PuMGa_5 ($M = \text{Co}, \text{Rh}$) materials, where the superconducting transition temperature is an order of magnitude larger [20–22]. For parts of the phase diagram where the ground state is superconducting, T_c appears to correlate with the lattice anisotropy at ambient pressure [23, 24]. However, this relationship breaks down when the ground state evolves towards antiferromagnetism.

Recently, an X-ray absorption spectroscopy (XAS) study probed the nature of the Ce $4f$ crystalline electrical field (CEF) ground state wavefunctions for several different $\text{CeRh}_x\text{Ir}_{1-x}\text{In}_5$ crystals [14]. These studies revealed a change in the shape of the wavefunction, lending support to the idea that hybridization to the $4f$ electron is strongly momentum-dependent [12, 13]. Electronic

structure calculations indicated that the momentum dependence affects the hybridization with the in-plane $\text{In}(1)$ and out-of-plane $\text{In}(2)$ $5p$ electrons differently, leading to multiple hybridization gaps at low temperature. Surprisingly, the $\text{In}(2)$ appear to be more strongly coupled to the $4f$ moments, suggesting that substitution at the M site may affect this coupling and hence the nature of the ground state.

In order to investigate the nature of this hybridization in more detail, we have measured the NMR Knight shift in $\text{CeRh}_x\text{Ir}_{1-x}\text{In}_5$ for both $\text{In}(1)$ and $\text{In}(2)$ sites. The In nuclear spins ($I = 9/2$) experience a transferred hyperfine field to the Ce $4f$ moments that reflects the hybridization to the $4f$ state [25, 26]. The hyperfine coupling between a nuclear spin \mathbf{I} at $\mathbf{r} = 0$ and an electronic spin at \mathbf{r} is given by:

$$\mathcal{H}_{hyp} = g\mu_B\gamma\hbar\mathbf{I} \cdot \left(\frac{8\pi}{3}\delta(\mathbf{r})\mathbf{S} + 3\frac{\mathbf{r}(\mathbf{S} \cdot \mathbf{r})}{r^5} - \frac{\mathbf{S}}{r^3} \right), \quad (1)$$

where γ is the nuclear gyromagnetic ratio and μ_B is the Bohr magneton. The first term is the Fermi contact term relevant for s -orbitals, and the second and third terms constitute a dipolar interaction with the electron spin. Typically both contact and dipolar terms are present, as well as multiple electron spins, leading to an effective hyperfine coupling tensor that in practice is determined empirically and contains both Fermi-contact and dipolar components. Often the magnitude of the dipolar component exceeds the direct dipolar field for a localized spin by at least an order of magnitude - e.g. in this case the dipolar field of a moment located at the origin of the Ce atom. This enhancement is due to hybridization of the orbitals of the unpaired electron spin with the relevant orbitals surrounding the nucleus. These so-called *transferred* hyperfine couplings depend sensitively on the electronic wavefunction [27].

In heavy fermions, there are two sets of electronic spins: those associated with the itinerant conduction electrons, \mathbf{S}_c , and with the $4f$ orbitals, \mathbf{S}_f . There are different hyperfine coupling tensors to these two degrees of freedom: $\mathcal{H}_{hyp} = g\mu_B\gamma\hbar\mathbf{I} \cdot (\mathbb{A} \cdot \mathbf{S}_c + \sum_i \mathbb{B}_i \cdot \mathbf{S}_f(\mathbf{r}_i))$,

where \mathbb{A} corresponds to an on-site coupling to the conduction electron spins [28], and \mathbb{B}_i are the transferred couplings to the nearest neighbor $4f$ spins. The transferred couplings can be determined by comparing the Knight shift and bulk susceptibility as a function of temperature and field direction, and have been well documented for the stoichiometric CeMIn_5 materials [15, 28–30]. Surprisingly, the transferred coupling $B_{cc}(1)$ for the In(1) site decreases by a factor of three between $M=\text{Rh}$ to $M=\text{Co}$, whereas $B_{cc}(2)$ for the In(2) site increases by the same factor. A similar evolution of $B_{cc}(1)$ has been observed in CeRhIn_5 under modest hydrostatic pressure as the ground state evolves from antiferromagnetic to superconducting [31]. *Such a large variability in transferred hyperfine couplings constants has not been observed in other strongly correlated superconductors, such as the cuprates, iron pnictides or chalcogenides.* We posit that in the CeMIn_5 materials the transferred hyperfine couplings arises due to the hybridization between the Ce $4f$ ground state orbital and the In $5p$ states, and that the variations in coupling constant reflect changes to the CEF parameters.

II. RESULTS

High-quality single crystals of $\text{CeRh}_x\text{Ir}_{1-x}\text{In}_5$ with multiple values of doping, x , were grown via the flux method technique [32, 33]. Single crystals of tetragonal shape were selected manually and polished to remove In flux from the surface. Powder x-ray diffraction measurements confirmed the expected tetragonal phase without evidence of spurious phases.

A. Magnetic Susceptibility

Figure 1 shows the bulk magnetic susceptibility, χ , of a series of single crystals of $\text{CeRh}_{1-x}\text{Ir}_x\text{In}_5$ between 4 and 300 K. χ varies strongly between 4 and 300 K, reflecting the localized nature of the Ce $4f$ electrons. For $T > 50$ K, χ is well-described by local moments in a tetragonal crystal field, with an effective exchange interaction, as discussed in [35]. This behavior is modified at low temperature due to the crystal field splitting, the Kondo interaction, and the exchange interaction among the Ce orbitals, all of which depend on the doping, x . As x increases the ground state evolves from antiferromagnetic below $T_N = 3.8$ K ($x = 0$) to superconducting below $T_c = 0.4$ K ($x = 1$), with a possible quantum phase transition near $x = 0.3$ [36]. de Haas-van Alphen measurements and band structure calculations indicate that the $4f$ electrons become more itinerant, and this trend is reflected in the overall decrease in the magnitude of χ over this range [37, 38].

The behavior of an isolated Ce $4f$ electron spin in a tetragonal environment is given by $\mathcal{H}_{CEF} = b_{20}\hat{O}_2^0 + b_{40}\hat{O}_4^0 + b_{44}\hat{O}_4^4$, where \hat{O}_n^m are the Stevens operators and

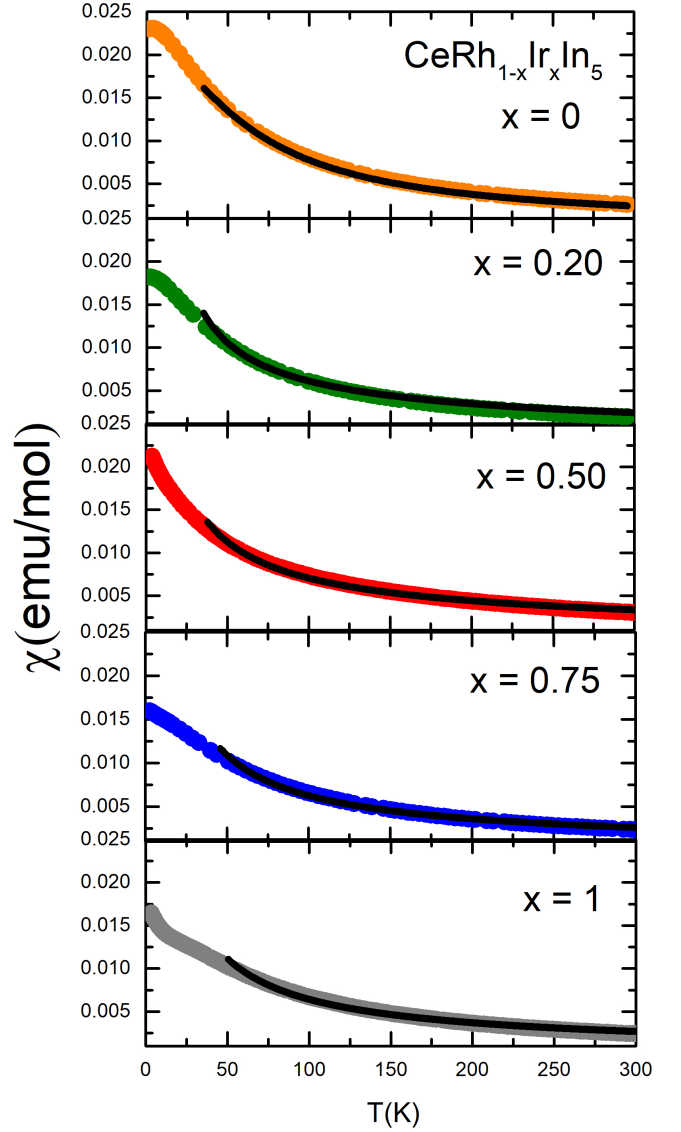


FIG. 1. Bulk susceptibility along the c axis of $\text{CeRh}_{1-x}\text{Ir}_x\text{In}_5$ versus temperature. The solid lines are fits to the high temperature data, as described in the text.

b_{nm} are parameters that characterize the crystal field. The $J = 5/2$ multiplet is split into three Kramers' doublets: $\Gamma_7^{(1)}$, $\Gamma_7^{(2)}$, and Γ_6 . The ground state $\Gamma_7^{(1)}$ wavefunctions can be expressed as:

$$|\psi(\Gamma_7^{(1)})\rangle = \alpha \left| \pm \frac{5}{2} \right\rangle + \sqrt{1 - \alpha^2} \left| \mp \frac{3}{2} \right\rangle, \quad (2)$$

where α characterizes the degree of mixing between the J_z manifolds and controls the degree of spatial anisotropy of the orbital. $\alpha_c^2 = 1/6$ for cubic symmetry ($b_{44} = 4b_{40}$ and $b_{20} = 0$). α^2 increases as the CEF potential becomes more tetragonal, and the orbital shape becomes more two-dimensional.

The magnetic susceptibility of the f moments is given by $\chi_{ff}^{-1} = \chi_{ff0}^{-1} + \lambda$, where λ is a mean-field param-

TABLE I. EFG, Hyperfine, and CEF Parameters for $\text{CeRh}_{1-x}\text{Ir}_x\text{In}_5$ and CeCoIn_5 . Values for $x = 0$, $x = 1$, and CeCoIn_5 are reproduced from [28], [29], and [34]. Hyperfine couplings are given in units of kOe/μ_B .

x	$\nu_{zz}(1)$ (MHz)	$\nu_{zz}(2)$ (MHz)	$\eta(2)$	$B_{cc}(1)$	$B_{cc}(2)$	b_{20} (meV)	b_{40} (meV)	$ b_{44} $ (meV)	α^2
0	6.78	16.665	0.445	21.4	4.1	-0.928	0.052	0.128	0.407
0.20	6.4(5)	17.3(8)	0.45	20.0(2.0)	--	-0.961	0.057	0.118	0.37
0.50	6.3(5)	16.5(8)	0.45	16.7(4)	--	-0.996	0.061	0.107	0.28
0.75	6.0(5)	17.3(8)	0.45	15.0(4.0)	--	-1.154	0.068	0.86	0.26
1	6.07	18.17	0.46	13.8	15.9	-1.197	0.069	0.088	0.250
CeCoIn_5	8.173	15.489	0.386	8.9	28.1	-0.856	0.063	0.089	0.129

ter that captures both the exchange and Kondo interactions, and χ_0 is determined by the local moments in \mathcal{H}_{CEF} [39]. We assume that the f-moments dominate the magnetic response and fit the susceptibility data for $T > 50$ K to extract the fitting parameters b_{20} , b_{40} , b_{44} and λ , as detailed in Table I. The α^2 values are determined by the eigenvectors of \mathcal{H}_{CEF} with these fit parameters. Although fitting the susceptibility data is an indirect and less-precise approach to extracting the CEF parameters than direct XAS measurements, our values agree well with published results [14].

B. NMR Spectra

NMR experiments were carried out in a high-homogeneity fixed-field magnet with field $H_0 = 11.7294$ T for a range of temperatures down to 5 K. Samples were mounted with $\mathbf{H}_0 \parallel c$, and radiofrequency pulses of varying duration (1.9 -2.2 μs) were used. Spectra at multiple frequencies were acquired and summed over a broad range to identify multiple satellites of each In site.

Figure 2 shows ^{115}In NMR spectra of $\text{CeRh}_{1-x}\text{Ir}_x\text{In}_5$ for several different values of x at 5K. In ($I = 9/2$) has nine transitions for each site, and all transitions are split by the quadrupolar interaction [31]. The In sites were identified by fitting the spectra using the nuclear spin Hamiltonian:

$$\mathcal{H} = \gamma \hbar \mathbf{I} \cdot (1 + \mathbf{K}) \cdot \mathbf{H}_0 + \frac{h\nu_{zz}}{6} [3I_z^2 - \hat{I}^2 + \eta (\hat{I}_x^2 - \hat{I}_y^2)] \quad (3)$$

where $\gamma = 0.93295$ kHz/G is the gyromagnetic ratio, I_α are the nuclear spin operators, \mathbf{K} is the Knight shift tensor, ν_{zz} is the largest eigenvalue of the EFG tensor, and η is the asymmetry parameter. The (x, y, z) coordinates are defined in the usual manner such that $|\nu_{zz}| > |\nu_{xx}| > |\nu_{yy}|$. For the In(1), z corresponds to the c axis, and for the In(2), z corresponds to the direction normal to unit cell face containing the In(2) atom, whereas x corresponds to the other in-plane direction perpendicular to c . The resonance frequencies of the In(1) depend on K , the field orientation, and ν_{cc} . The In(2) resonances are more complex due to the non-zero EFG asymmetry parameter, $\eta = |\nu_{xx}| - |\nu_{yy}| / |\nu_{zz}|$, and misorientations from $\mathbf{H}_0 \parallel c$ split the In(2) resonances giving rise to double peaks. Furthermore, local disorder and mixing of the Rh

and Ir in the doped samples are responsible for multiple In(2) sites and create complex NMR spectra.

To fit the spectra, we assume the direction of \mathbf{H}_0 is described by the spherical polar angles (θ, ϕ) with respect to the c axis, and perform an exact diagonalization of Eq. 3. The peaks are fit to Voigt functions. The EFG values agree with previous measurements [36]. Although we are able to fit the full In(1) spectra, there are several peaks that are not fully identified. These are likely due to In(2) sites associated with local disorder due to the non-stoichiometry of Rh and Ir. Note that when $\theta \neq 0^\circ$ the In(2) sites split into two peaks. Moreover, because the In(2) has non-axial symmetry, the resonance frequencies are strong functions of the relative orientation between \mathbf{H}_0 and the EFG tensor. Local disorder at an In(2) site can affect both the magnitude of the EFG tensor components and the orientation of the principle EFG axes. Nevertheless, these sites are not relevant for understanding the behavior of the hyperfine coupling and we focus our analysis solely on the sites that have been clearly identified. Fig. 3 shows the temperature dependence of specific well-defined resonances. There are clear shifts of the resonance frequencies with increasing temperature. We assume that the EFG remains temperature independent and that the temperature dependence arises solely from the Knight shift.

C. Knight shift

The Knight shift of the In(1), K_1 , is shown in Fig. 4 as function of temperature and doping, x , for field aligned along the c -direction. K_1 decreases with x , similar to χ , although there are small deviations at low temperature. For the hyperfine interaction in heavy fermions, the Knight shift is given by $K = A\chi_{cc} + (A+B)\chi_{cf} + B\chi_{ff}$, where χ_{cc} , χ_{ff} , and χ_{cf} are contributions from the conduction electrons, the f -moments, and their interaction, respectively [25]. Here we write $B = nB_{cc}$, where n is the number of nearest neighbor f sites ($n = 4$ for In(1) and 2 for In(2)), and B_{cc} corresponds to the c -axis component of the tensor \mathbb{B} . The total susceptibility is $\chi = \chi_{cc} + 2\chi_{cf} + \chi_{ff}$. For sufficiently high temperatures $T > T^*$ the first two contributions to the shift can be ignored and $K \approx B\chi$. A plot of K_1 versus χ yields a straight line for $T > T^*$ with slope B_1 , as shown in

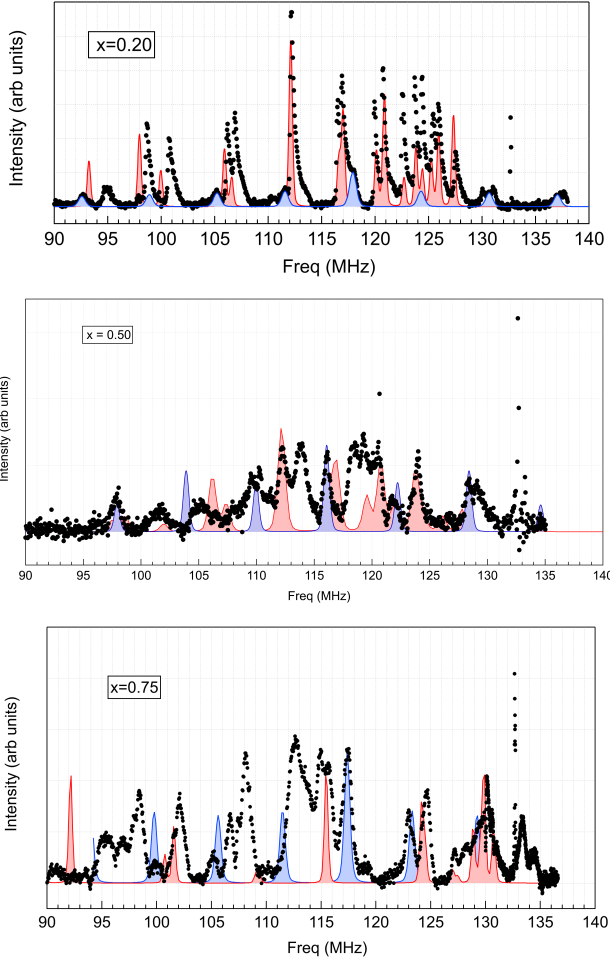


FIG. 2. NMR spectrum for $\text{CeRh}_{1-x}\text{Ir}_x\text{In}_5$ with $x = 0.20$ (top), $x = 0.50$ (middle), and $x = 0.75$ (lower). Fits to the In(1) sites are shown in blue and those for the In(2) sites are shown in red. The fit parameters for $x = 0.20$ are: $\theta = 4 \pm 3^\circ$, $\phi = 8 \pm 3^\circ$, $K_c(1) = 7.8 \pm 0.1\%$, $K_c(2) = 2.5 \pm 0.1\%$, $\nu_{zz}(1) = 6.41 \pm 0.5$ MHz, $\nu_{zz}(2) = 17.3 \pm 0.5$ MHz, and $\eta(2) = 0.45 \pm 0.02$. The fit parameters for $x = 0.50$ are: $\theta = 8.3 \pm 3^\circ$, $\phi = 11 \pm 3^\circ$, $K_c(1) = 6.2 \pm 0.2\%$, $K_c(2) = 2.8 \pm 0.5\%$, $\nu_{zz}(1) = 6.32 \pm 0.2$ MHz, $\nu_{zz}(2) = 16.57 \pm 0.5$ MHz, and $\eta(2) = 0.45 \pm 0.02$. The fit parameters for $x = 0.75$ are: $\theta = 6 \pm 3^\circ$, $\phi = 0^\circ$, $K_c(1) = 7.3 \pm 0.2\%$, $K_c(2) = 5.4 \pm 0.8\%$, $\nu_{zz}(1) = 6.0$ MHz, $\nu_{zz}(2) = 17.28 \pm 0.5$ MHz, and $\eta(2) = 0.45 \pm 0.02$.

Fig. 5. Fig. 6 shows the Knight shift for the In(2) for $x = 0.75$. We are unable to reliably extract the In(2) Knight shift for the other dopings due to misalignments and spectral overlap with other sites.

There are two important trends evident in Fig. 5. First, the slope decreases with increasing x , and gets even smaller in CeCoIn_5 . Secondly, there is a breakdown in the linear relationship below a temperature T^* . This deviation signals the onset of coherence at low temperatures, where χ_{cc} and χ_{cf} can no longer be ignored. As x increases from 0 to 1, the deviation evolves from curving upwards (pure CeRhIn_5) to downwards (undoped CeIrIn_5), and becomes more pronounced for CeCoIn_5 .

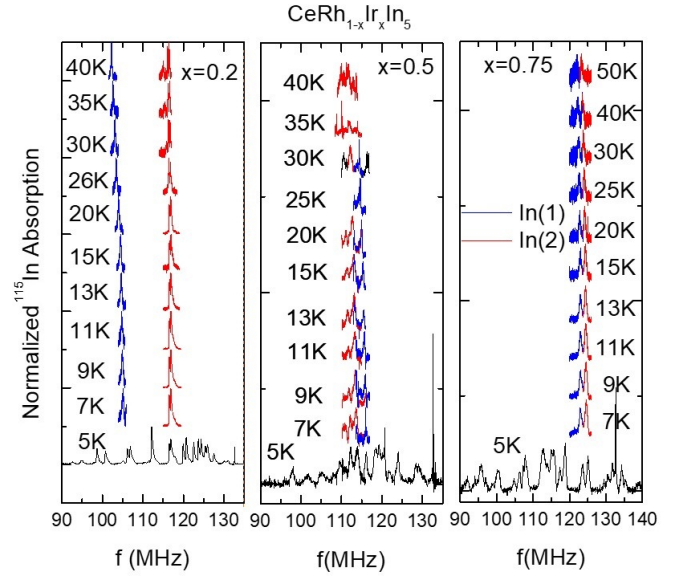


FIG. 3. Spectra of $\text{CeRh}_{1-x}\text{Ir}_x\text{In}_5$ for $x = 0.20$, $x = 0.50$ and $x = 0.75$ for several different temperatures for $H_0 = 11.7$ T along the c direction. Blue indicates In(1) and red indicates In(2). Slight misalignments cause the In(2) spectra to split. Details of the spectral fitting are provided in the supplemental information.

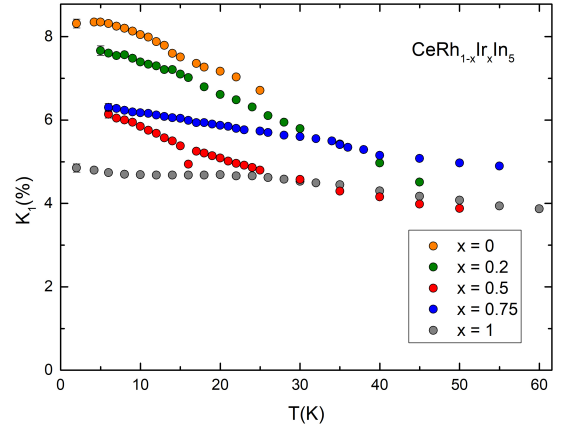


FIG. 4. In(1) Knight shift versus temperature. Data for the $x = 0$ and $x = 1$ are reproduced from [28].

For intermediate values of $x \approx 0.5$, there is no clear evidence of such a deviation in the data. This behavior reflects changes in the relative size of the on-site A coupling to the transferred B coupling, as well as the growth of heavy fermion coherence, as discussed below.

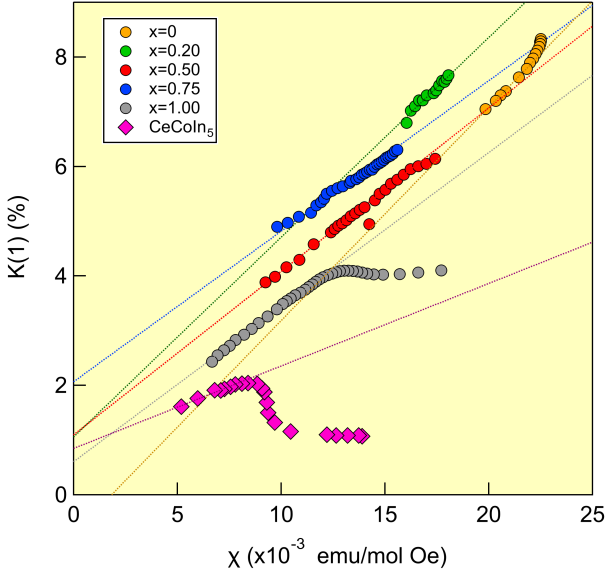


FIG. 5. In(1) Knight shift versus magnetic susceptibility. Dotted lines are fits to the high temperature ($T > T^*$) data. Data for CeCoIn₅ is reproduced from [40].

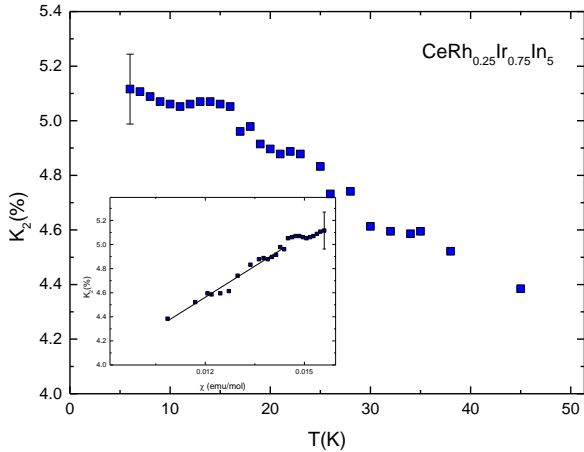


FIG. 6. In(2) Knight shift versus temperature for $x = 0.75$. The inset shows $K(2)$ versus χ and the solid line is the best fit to the high temperature data.

III. DISCUSSION

We can now examine how the hyperfine coupling correlates with the CEF ground state orbital shape. Fig. 7 shows B_1 and B_2 versus α^2 using the parameters extracted from the fits to the Knight shift and susceptibility. The solid lines in Fig. 7 are linear fits to the data, including the value for CeCoIn₅. As α^2 increases, the orbitals become more oblate, the lobes pointing along the In(1) directions become more extended, and the transferred hyperfine coupling to the In(1) nucleus increases.

In order to understand this behavior quantitatively, we consider a simple model in which the transferred coupling

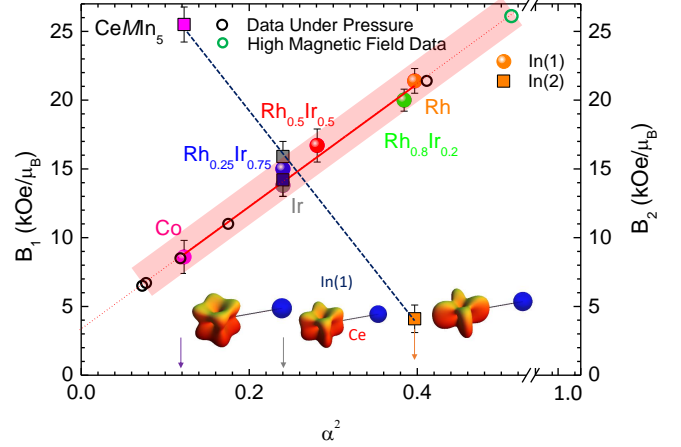


FIG. 7. The transferred hyperfine coupling to the In(1) and In(2) as a function of α^2 . The solid lines are fits to $B_{1,2}(\alpha^2) = B_{1,2}(0) + \kappa_{1,2}\alpha^2$, where $B_1(0) = 3.3(8)$ kOe/ μ_B , $B_2(0) = 32(1)$ kOe/ μ_B , $\kappa_1 = 44(2)$ kOe/ μ_B and $\kappa_2 = -59(2)$ kOe/ μ_B . The open black circles represent CeRhIn₅ under pressure and are taken from Ref. [31] and inferring the α^2 values using the fit to the ambient-pressure data (shown in Fig. 8). The open green circle represents CeRhIn₅ at high fields above 31 T, taken from Ref. [41]. The insets at the bottom show how the spatial form of the Ce 4f wavefunction evolves as α^2 changes.

is directly proportional to the magnitude squared of the Ce 4f wavefunction along the Ce-In(1) bond direction. The angular dependence of this probability is given by the function $f_\alpha(\theta, \phi) = \sum_{m_S} |\langle \theta, \phi, m_S | \psi(\Gamma_7^{(1)}) \rangle|^2$, shown as insets in Fig. 7 for various values of α . The wavefunction is given by Eq. 2, where

$$|J_z\rangle = \sum_{m_L=-3}^3 \sum_{m_S=-1/2}^{1/2} C_{m_L, m_S} |L, m_L\rangle |S, m_S\rangle \quad (4)$$

and C_{m_L, m_S} are the appropriate Clebsch-Gordan coefficients for $L = 3$ and $S = 1/2$. Along the Ce-In(1) bond direction $f_\alpha(\theta = \frac{\pi}{2}, \phi = \frac{\pi}{4}) \sim 1 + 4\alpha^2 + 2\sqrt{5}\alpha^2(1 - \alpha^2)$. This function grows over the range $0.2 \lesssim \alpha^2 \lesssim 0.8$, in agreement with our observation that the hyperfine coupling increases with α^2 .

Direct measurements of the In(2) hyperfine coupling are challenging in the doped materials. However, it is insightful to consider the values for the pure CeRhIn₅, CeIrIn₅ and CeCoIn₅ versus α^2 , as well as for the $x = 0.75$ sample measured here. In contrast to the In(1), B_2 is largest when the orbital lobes extend out of the plane and decreases with increasing α^2 . The exact value of θ to use for $f_\alpha(\theta, \phi)$ depends on the position of the In(2) within the unit cell, however it can be well-approximated as $f_\alpha(\theta \approx \frac{3\pi}{4}, \phi = 0) \sim 51 - 6\alpha(6\alpha + \sqrt{5 - 5\alpha^2})$. This quantity decreases as α^2 increases, which again agrees with the behavior observed in Fig. 7. These results reveal directly how the hybridizations to the in-plane In(1) and

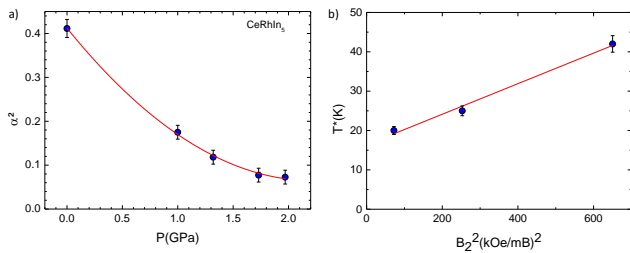


FIG. 8. (upper) α^2 inferred from the pressure dependence of B_1 in [31] using the relationship measured at ambient pressure in Fig. 7. The solid line is a guide to the eye. (lower) The coherence temperature T^* versus B_2^2 . The solid line is given by $T^* = 16.3(2) + 0.039(3)B_2^2$.

out-of-plane In(2) sites evolve as the ground state orbital anisotropy changes.

Similar changes in the transferred hyperfine couplings were observed in CeRhIn₅ under hydrostatic pressure [31]. In this case, B_1 decreases from 25.6 to 5.2 kOe/ μ_B between ambient pressure and ~ 2 GPa, which is close to the value observed in pure CeCoIn₅. Using the linear relationship between B_1 and α^2 we observe under ambient pressure in Fig. 7, we infer the pressure dependence of α^2 in Fig. 8(a). These results imply that pressure changes the CEF parameters so that the Ce wavefunction lobes extend more out of the plane, becoming more cubic-like. This observation is consistent with the fact that at this pressure, CeRhIn₅ becomes superconducting with T_c similar to CeCoIn₅, and develops a large Fermi surface [17, 37]. On the other hand, the data imply that the α^2 becomes smaller than $\alpha_c = 1/6$ which may be unphysical. It should be noted, however, the values for B_1 in [31] were determined based on the assumption that the In(2) hyperfine coupling did not change under pressure. Because there is no independent susceptibility data under pressure, it was only possible to directly extract the ratio of $B_1(P)$ to $B_2(P)$, rather than their independent values. Nevertheless, the trend under hydrostatic pressure is similar to that observed with ‘chemical pressure’. A possible explanation for the behavior of the In(2) hyperfine coupling is that under pressure the wavefunction acquires an admixture of the $\Gamma_7^{(2)}$ excited states due to the Kondo coupling, similar to recent observations in CeCoIn₅ [42]. Because the $\Gamma_7^{(2)}$ state is rotated 45 degrees relative to the $\Gamma_7^{(1)}$ state, any admixture would dramatically affect the hyperfine couplings B_1 and possibly B_2 . Future measurements of the In(2) Knight shift for in-plane fields in CeRhIn₅ will be necessary to check this scenario.

The Knight shift anomaly observed in Fig. 5 reflects the growth of $K_{HF}(T)$ below T^* , where $K_{HF}(T) \propto (A - B)(1 - T/T^*)^{3/2}[1 + \ln(T^*/T)]$ [28]. As B_1 increases with α^2 , the sign of $K_{HF}(T)$ changes from positive to negative, and vanishes when the transferred coupling equals the on-site coupling, A . Previously, $A \approx 14$ kOe/ μ_B was estimated in CeCoIn₅ [29]. Since this quantity reflects a combination of a Fermi-contact interac-

tion plus core-polarization from the Indium 5p orbitals, it should only weakly depend on doping or transition metal element. Thus, the observation that the Knight shift anomaly is small or absent in CeRh_{1-x}Ir_xIn₅ for $x \approx 0.5$ in Fig. 5 likely reflects the fact that $B_1 \approx A$ in this range. On the other hand, there is a clear growth of both the magnitude of K_{HF} and the onset temperature, T^* , as α^2 decreases in CeIrIn₅ and CeCoIn₅. T^* is approximately the temperature where the entropy reaches $R \ln 2$, and has been shown empirically related to the Kondo coupling, J , as $T^* = 0.45J^2\rho$, where ρ is the density of conduction electron states [19]. Since the Kondo coupling arises due to hybridization of the 4f orbital, it is natural to expect that $J \propto \alpha^2$, and thus $T^* \sim B_2^2$, as demonstrated in Fig. 8(b). This observation supports previous dynamical mean-field theory (DMFT) calculations of CeIrIn₅ that indicated the hybridization gap for the Ce-In(2) band dominates that for the in-plane Ce-In(1) band [12]. The Kondo hybridization, which drives the low temperature correlated behavior, is thus directly controlled by the shape of the Ce 4f orbitals.

IV. SUMMARY

We have measured the Knight shift and magnetic susceptibilities for several single crystals of CeRh_{1-x}Ir_xIn₅, and found that the transferred hyperfine couplings to the In(1) and In(2) vary linearly with α^2 , where α describes the admixture between the $|J_z = -\frac{3}{2}\rangle$ and $|J_z = +\frac{5}{2}\rangle$ states of the Ce 4f ground state wavefunction. The hyperfine coupling to the In(1) is enhanced as α^2 grows and the wavefunction extends out of the plane. The coupling to the In(2), on the other hand, decreases as α^2 increases. These results provide direct proof that the hybridization between the 4f wavefunction and the In 5p orbitals is controlled by the orbital anisotropy. This observation also offers an explanation for the abrupt decrease in the In(1) Knight shift at 30 T, where the magnetic field induces changes to the crystal field ground state orbital [41], and for the pressure-dependence of the coupling to the In(1). A detail that has not been considered in our analysis is that it is possible that the Kondo coupling to the excited state $\Gamma_7^{(2)}$ manifold alters the shape of the 4f orbital, which may play a role in the pressure dependence of the ratio B_1/B_2 under pressure [31]. Further experiments exploring all components of the hyperfine coupling tensor will be important to better characterize this hybridization, especially under pressure. This study establishes transferred hyperfine interactions as an important probe of hybridization anisotropy in heavy fermion materials, and may provide a more straightforward approach to determine the crystal field parameters.

ACKNOWLEDGMENTS

The authors gratefully acknowledge support from the UC Davis Seed Grant program and FAPESP (Grants No. 2016/14436-3, 2018/11364-7, 2017/10581-1 and 2012/05903-6). RRU acknowledges CNPq Grant No

309483/2018-2. PGP acknowledges CNPq Grant No 304496/2017-0. We acknowledge helpful discussions with T. Kissikov and P. Klavins. Work at UC Davis was partially supported by the NSF under Grant No. DMR-1807889.

-
- [1] S. Doniach, The Kondo lattice and weak antiferromagnetism, *Physica* **91B**, 231 (1977).
- [2] Z. Fisk, D. W. Hess, C. J. Pethick, D. Pines, J. L. Smith, J. D. Thompson, and J. O. Willis, Heavy-electron metals: new highly correlated states of matter., *Science* **239**, 33 (1988).
- [3] G. R. Stewart, Non-Fermi-liquid behavior in d - and f -electron metals, *Rev. Mod. Phys.* **73**, 797 (2001).
- [4] P. Coleman and A. J. Schofield, Quantum criticality, *Nature* **433**, 226 (2005).
- [5] Q. M. Si, S. Rabello, K. Ingersent, and J. L. Smith, Locally critical quantum phase transitions in strongly correlated metals, *Nature* **413**, 804 (2001).
- [6] J. Custers, P. Gegenwart, H. Wilhelm, K. Neumaier, Y. Tokiwa, O. Trovarelli, C. Geibel, F. Steglich, C. Pepin, and P. Coleman, The break-up of heavy electrons at a quantum critical point, *Nature* **424**, 524 (2003).
- [7] P. Gegenwart, Q. Si, and F. Steglich, Quantum criticality in heavy-fermion metals, *Nat. Phys.* **4**, 186 (2008).
- [8] J. R. Schrieffer and P. A. Wolff, Relation between the Anderson and Kondo hamiltonians, *Phys. Rev.* **149**, 491 (1966).
- [9] M. Vekic, J. Cannon, D. Scalapino, R. Scalettar, and R. Sugar, Competition between antiferromagnetic order and spin liquid behavior in the two-dimensional periodic Anderson model at half-filling, *Phys Rev. Lett.* **74**, 2367 (1995).
- [10] M. Jiang, N. J. Curro, and R. T. Scalettar, Universal Knight shift anomaly in the periodic Anderson model, *Phys. Rev. B* **90**, 241109 (2014).
- [11] N. C. Costa, T. Mendes-Santos, T. Paiva, N. J. Curro, R. R. dos Santos, and R. T. Scalettar, Coherence temperature in the diluted periodic Anderson model, *Phys. Rev. B* **99**, 195116 (2019).
- [12] J. Shim, K. Haule, and G. Kotliar, Modeling the localized-to-itinerant electronic transition in the heavy fermion system CeIrIn₅, *Science* **318**, 1615 (2007).
- [13] K. S. Burch, S. V. Dordevic, F. P. Mena, A. B. Kuzmenko, D. van der Marel, J. L. Sarrao, J. R. Jeffries, E. D. Bauer, M. B. Maple, and D. N. Basov, Optical signatures of momentum-dependent hybridization of the local moments and conduction electrons in Kondo lattices, *Phys. Rev. B* **75**, 054523 (2007).
- [14] T. Willers, F. Strigari, Z. Hu, V. Sessi, N. B. Brookes, E. D. Bauer, J. L. Sarrao, J. D. Thompson, A. Tanaka, S. Wirth, L. H. Tjeng, and A. Severing, Correlation between ground state and orbital anisotropy in heavy fermion materials, *Proc. Natl. Acad. Sci.* **112**, 2384 (2015).
- [15] A. C. Shockley, K. R. Shirer, J. Crocker, A. P. Dioguardi, C. H. Lin, D. M. Nisson, N. apRoberts Warren, P. Klavins, and N. J. Curro, NMR evidence of anisotropic Kondo liquid behavior in CeIrIn₅, *Phys. Rev. B* **92**, 085108 (2015).
- [16] J. Thompson, R. Movshovich, Z. Fisk, F. Bouquet, N. Curro, R. Fisher, P. Hammel, H. Hegger, M. Hundley, M. Jaime, P. Pagliuso, C. Petrovic, N. Phillips, and J. Sarrao, Superconductivity and magnetism in a new class of heavy-fermion materials, *J. Magn. Magn. Mater.* **226**, 5 (2001).
- [17] T. Park, F. Ronning, H. Q. Yuan, M. B. Salmón, R. Movshovich, J. L. Sarrao, and J. D. Thompson, Hidden magnetism and quantum criticality in the heavy fermion superconductor CeRhIn₅, *Nature* **440**, 65 (2006).
- [18] T. Park, V. A. Sidorov, F. Ronning, J.-X. Zhu, Y. Tokiwa, H. Lee, E. D. Bauer, R. Movshovich, J. L. Sarrao, and J. D. Thompson, Isotropic quantum scattering and unconventional superconductivity, *Nature* **456**, 366 (2008).
- [19] Y.-F. Yang, Z. Fisk, H.-O. Lee, J. D. Thompson, and D. Pines, Scaling the Kondo lattice, *Nature* **454**, 611 (2008).
- [20] J. L. Sarrao, L. A. Morales, J. D. Thompson, B. L. Scott, G. R. Stewart, F. Wastin, J. Rebizant, P. Boulet, E. Colineau, and G. H. Lander, Plutonium-based superconductivity with a transition temperature above 18 K, *Nature* **420**, 297 (2002).
- [21] F. Wastin, P. Boulet, J. Rebizant, E. Colineau, and G. H. Lander, Advances in the preparation and characterization of transuranium systems, *J. Phys.: Condens. Matter* **15**, S2279 (2003).
- [22] N. Curro, T. Caldwell, E. Bauer, L. Morales, M. Graf, Y. Bang, A. Balatsky, J. Thompson, and J. Sarrao, Unconventional superconductivity in PuCoGa₅, *Nature* **434**, 622 (2005).
- [23] P. Pagliuso, R. Movshovich, A. Bianchi, M. Nicklas, N. Moreno, J. Thompson, M. Hundley, J. Sarrao, and Z. Fisk, Multiple phase transitions in Ce(Rh,Ir,Co)In₅, *Physica B* **312-313**, 129 (2002).
- [24] E. D. Bauer, J. D. Thompson, J. L. Sarrao, L. A. Morales, F. Wastin, J. Rebizant, J. C. Griveau, P. Javorsky, P. Boulet, E. Colineau, G. H. Lander, and G. R. Stewart, Structural tuning of unconventional superconductivity in PuMGa₅ (M=Co,Rh), *Phys. Rev. Lett.* **93**, 147005 (2004).
- [25] N. J. Curro, Hyperfine interactions in the heavy fermion CeMIn₅ systems, *New J. Phys.* **8**, 173 (2006).
- [26] N. J. Curro, B.-L. Young, R. R. Urbano, and M. J. Graf, Hyperfine fields and magnetic structure in the B phase of CeCoIn₅, *J. Low Temp. Phys.* **158**, 635 (2010).
- [27] S. Renold, S. Pliberšek, E. Stoll, T. Claxton, and P. Meier, First-principles calculation of electric field gradients and hyperfine couplings in YBa₂Cu₃O₇, *EPJ B* **23**, 3 (2001).

- [28] K. R. Shirer, A. C. Shockley, A. P. Dioguardi, J. Crocker, C. H. Lin, N. apRoberts Warren, D. M. Nisson, P. Klavins, J. C. Cooley, Y.-f. Yang, and N. J. Curro, Long range order and two-fluid behavior in heavy electron materials, *Proc. Natl. Acad. Sci.* **109**, E3067 (2012).
- [29] N. Curro, B. Young, J. Schmalian, and D. Pines, Scaling in the emergent behavior of heavy-electron materials, *Phys. Rev. B* **70**, 235117 (2004).
- [30] S. Kambe, Y. Tokunaga, H. Sakai, H. Chudo, Y. Haga, T. D. Matsuda, and R. E. Walstedt, One-component description of magnetic excitations in the heavy-fermion compound CeIrIn₅, *Phys. Rev. B* **81**, 140405 (2010).
- [31] C. H. Lin, K. R. Shirer, J. Crocker, A. P. Dioguardi, M. M. Lawson, B. T. Bush, P. Klavins, and N. J. Curro, Evolution of hyperfine parameters across a quantum critical point in CeRhIn₅, *Phys. Rev. B* **92**, 155147 (2015).
- [32] C. Petrovic, R. Movshovich, M. Jaime, P. G. Pagliuso, M. F. Hundley, J. L. Sarrao, Z. Fisk, and J. D. Thompson, A new heavy-fermion superconductor CeIrIn₅: A relative of the cuprates?, *EPL* **53**, 354 (2001).
- [33] P. G. Pagliuso, C. Petrovic, R. Movshovich, D. Hall, M. F. Hundley, J. L. Sarrao, J. D. Thompson, and Z. Fisk, Coexistence of magnetism and superconductivity in CeRh_{1-x}Ir_xIn₅, *Phys. Rev. B* **64**, 100503 (2001).
- [34] T. Willers, Z. Hu, N. Hollmann, P. O. Körner, J. Gerner, T. Burnus, H. Fujiwara, A. Tanaka, D. Schmitz, H. H. Hsieh, H.-J. Lin, C. T. Chen, E. D. Bauer, J. L. Sarrao, E. Goremychkin, M. Koza, L. H. Tjeng, and A. Severing, Crystal-field and Kondo-scale investigations of CeMIn₅ (M=Co, Ir, and Rh): A combined x-ray absorption and inelastic neutron scattering study, *Phys. Rev. B* **81**, 195114 (2010).
- [35] P. G. Pagliuso, D. J. Garcia, E. Miranda, E. Granado, R. Lora Serrano, C. Giles, J. G. S. Duque, R. R. Urbano, C. Rettori, J. D. Thompson, M. F. Hundley, and J. L. Sarrao, Evolution of the magnetic properties and magnetic structures along the R_mMIn_{3m+2} (R=Ce, Nd, Gd, Tb; M=Rh, Ir; and m = 1, 2) series of intermetallic compounds, *J. Appl. Phys.* **99**, 08P703 (2006).
- [36] S. Kawasaki, M. Yashima, Y. Mugino, H. Mukuda, Y. Kitaoka, H. Shishido, and Y. Ōnuki, Enhancing the superconducting transition temperature of CeRh_{1-x}Ir_xIn₅ due to the strong-coupling effects of antiferromagnetic spin fluctuations: An ¹¹⁵In nuclear quadrupole resonance study, *Phys. Rev. Lett.* **96**, 147001 (2006).
- [37] H. Shishido, R. Settai, H. Harima, and Y. Ōnuki, A drastic change of the fermi surface at a critical pressure in CeRhIn₅: dHvA study under pressure, *J. Phys. Soc. Jpn.* **74**, 1103 (2005).
- [38] Y. Haga, Y. Inada, H. Harima, K. Oikawa, M. Murakawa, H. Nakawaki, Y. Tokiwa, D. Aoki, H. Shishido, S. Ikeda, N. Watanabe, and Y. Ōnuki, Quasi-two-dimensional fermi surfaces of the heavy fermion superconductor CeIrIn₅, *Phys. Rev. B* **63**, 060503 (2001).
- [39] K. Haule, Quantum Monte Carlo impurity solver for cluster dynamical mean-field theory and electronic structure calculations with adjustable cluster base, *Phys. Rev. B* **75**, 155113 (2007).
- [40] N. Curro, B. Simovic, P. Hammel, P. Pagliuso, J. Sarrao, J. Thompson, and G. Martins, Anomalous NMR magnetic shifts in CeCoIn₅, *Phys. Rev. B* **64**, 180514 (2001).
- [41] G. G. Lesseux, H. Sakai, T. Hattori, Y. Tokunaga, S. Kambe, P. L. Kuhns, A. P. Reyes, J. D. Thompson, P. G. Pagliuso, and R. R. Urbano, Orbitally defined field-induced electronic state in a Kondo lattice, *Phys. Rev. B* **101**, 165111 (2020).
- [42] M. Sundermann, A. Amorese, F. Strigari, B. Leedahl, L. H. Tjeng, M. W. Haverkort, H. Gretarsson, H. Yavaş, M. M. Sala, E. D. Bauer, P. F. S. Rosa, J. D. Thompson, and A. Severing, Orientation of the ground-state orbital in CeCoIn₅ and CeRhIn₅, *Phys. Rev. B* **99**, 235143 (2019).

Appendix I

Detailed study on Insulating Nanoparticles

This appendix brings the paper published on Undoped Insulating Nanoparticles, along with the current study (still unpublished) about the Rare Earth Doped particles.

Probing Surface Effects on α -NaYF₄ Nanoparticles by Nuclear Magnetic Resonance

Thiago B. de Queiroz,* Michael Cabrera-Baez,* Paulo Menegasso, Eduardo D. Martinez, Ali F. García Flores, Carlos Rettori,* and Ricardo R. Urbano*



Cite This: *J. Phys. Chem. C* 2020, 124, 9523–9535



Read Online

ACCESS |



Metrics & More



Article Recommendations



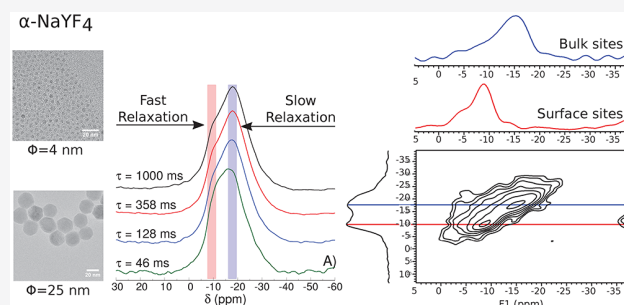
Supporting Information

ABSTRACT: The structural properties of insulating α -NaYF₄ (cubic) nanoparticles with size ranging within 4–25 nm were investigated by high-resolution ²³Na and ¹⁹F solid-state nuclear magnetic resonance (NMR) spectroscopy under magic angle spinning (MAS) with single-pulse (SP-MAS), spin-echo (SE-MAS), inversion recovery, and 3Q-MAS experiments. The ²³Na SP-MAS spectra show a broad peak around –18 ppm with a shoulder around –9 ppm, which becomes more prominent for the smallest nanoparticles. The ²³Na nuclei resonating around –9 ppm demonstrate a longitudinal relaxation time of a few milliseconds, while the ones resonating around –18 ppm are on the order of 50–125 ms. This feature is noticed for all studied nanoparticles,

but it is more evident for the smallest ones ($\phi \lesssim 7$ nm), especially among the batches with higher polydispersity. On the basis of these relaxation times, field-dependent measurements, and ²³Na 3Q-MAS, we attributed the signal around –18 ppm to ²³Na in the bulk of the nanoparticles and the signal around –9 ppm to surface or/and sites near defects, featuring higher fluctuations in the electric field gradient (EFG). The ²³Na 3Q-MAS spectra provide evidence for two (and sometimes three) distinct Na sites in α -NaYF₄ with similar quadrupole coupling but slightly different chemical shifts. The ¹⁹F SE-MAS spectra show a broad peak around –75 ppm with a small shoulder around –120 ppm corresponding to only $\approx 1\%$ of the signal. The peak around –75 ppm is attributed to the stoichiometric NaYF₄ composition, and its broadening is attributed to a distribution of Na- and Y-rich environments. The minor shoulder around –120 ppm is associated with the F-deficient NaYF₄ structure. The ¹⁹F spin–spin relaxation time indicates some degree of mobility of the fluorine atoms, possibly due to the presence of F vacancies triggering hopping-like ion motion. The signal related to the F-deficient structure is greatly enhanced for the smallest nanoparticles ($\phi = 4$ nm), i.e., along with the increase of ²³Na surface effects and defects. Therefore, we correlate several NMR techniques to provide a fundamental structural view for nanoparticles used as upconversion host systems with prominent technological applications. Particularly for α -NaYF₄, significant surface effects and defects must be expected for nanoparticles with dimensions in the order of few nanometers ($\phi \lesssim 7$ nm).

1. INTRODUCTION

The design and development of nanocrystalline compounds are currently very attractive research topics due to their use in numerous technological applications.^{1–3} An example is the rare earth (RE) doped NaYF₄ nanoparticles (NPs) that display interesting features arising from interactions between doping ions.^{4,5} It makes these NPs suitable host materials in upconversion processes, whereby incident infrared radiation is converted into visible light.^{4,5} This nanocrystalline compound can be synthesized in two crystallographic phases:⁶ cubic (α -phase) and hexagonal (β -phase). A recent study of the macro- and microscopic properties of doped β -NaYF₄ nanoparticles revealed the important role of the electrostatic potential around the dopant ions in the optical properties, leading to a better comprehension of the upconversion efficiency.⁷ Despite these significant advances, many aspects of the structure of the nanoparticles are of current interest. For instance, there were



significant disagreements concerning the structure of the β -NaYF₄ nanoparticles. Different space groups have been proposed to fit the X-ray diffraction (XRD) patterns observed for the bulk material,⁸ and NMR as a technique sensitive to the local characteristics of the structure was employed to finally conclude that it is formed as $P63/m$ space group.⁹

Although the β -phase has been more extensively investigated because of its efficient upconversion emission, the cubic α -NaYF₄ NP is postulated as the simplest structure to understand fundamental properties^{10,11} such as surface effects in the

Received: January 28, 2020

Revised: March 18, 2020

Published: April 8, 2020



structure. Previous NMR studies^{12,13} investigated structural properties of undoped and rare earth doped NPs, evaluating the quality of the crystals formed and the influence of the dopant in the crystalline lattice parameter and spin diffusion. Despite the completeness of these studies, no size dependence on the structural properties influenced by surface effects was reported though they are among the fundamental features of nanoscaled materials. Focused on that issue, we synthesized undoped α -phase NaYF₄ NPs with sizes ranging from 4 to 25 nm and characterized them by XRD, transmission electron microscopy (TEM), and ²³Na and ¹⁹F NMR. In particular, we associate spectral resolution with dissimilar relaxation times to probe subtle ²³Na site distortions and defects as a function of particle size and polydispersity.

2. EXPERIMENTAL DETAILS

2.1. Synthesis of the Nanoparticles. Pure cubic α -NaYF₄ NPs were synthesized by different methods to obtain a variety of particle sizes. For the smallest NP (named NP A) the coprecipitation method was performed following the process described by Wang et al.¹⁴ and Liu et al.¹⁵ Briefly, 4 mL of a 0.2 M Y(CH₃COO)₃ aqueous solution was added in a three-neck round-bottom flask together with 7.2 mL of oleic acid (OA, technical grade, Sigma-Aldrich) and 16.8 mL of 1-octadecene (ODE, 90%, Sigma-Aldrich). Under magnetic stirring, the mixture was heated to 120–140 °C to evaporate the water content and then cooled to room temperature. At this point, a freshly prepared mixture containing 2 mL of a 1 M NaOH methanol solution and 8 mL of 0.4 M NH₄F solution in methanol was rapidly injected. The flask was heated to 50 °C for 30 min and then sealed. The temperature was raised to 100 °C, and a vacuum pump was connected. After 15 min, the vacuum pump was turned off, a condenser was mounted, and the temperature was increased to 260 °C under an argon flux and maintained for 20 min. The flask was then removed from the mantle and allowed to cool to room temperature. This method, typically used for the synthesis of small hexagonal-phase NPs, was performed at a lower temperature to delay the phase transformation from small cubic nuclei to larger hexagonal NPs.

For the syntheses of NPs of intermediate size (NP B, C, and D), thermal decomposition of trifluoroacetates was performed by adapting the methods reported in ref 6. For NP B, 1 mmol of Na(CF₃COO) (98%, Aldrich) and 1 mmol of Y(CF₃COO)₃ (99.99%, Aldrich) were added to 9.9 mL of oleylamine (OLA, technical grade, Sigma-Aldrich), 9.5 mL of OA, and 19.2 mL of ODE in a three-neck round-bottom flask. The mixture was heated to 120–140 °C with vigorous magnetic stirring under vacuum for 30 min in a temperature-controlled electromantle to reduce the water and oxygen content. Then, under argon flux, the solution was heated to a final temperature of 310 °C and maintained at this temperature for 30 min. The same procedure was performed for the synthesis of NP C. We report the characterization of NPs B and C, despite their analogous preparation, to observe how sensitive the batches are to uncontrolled preparation conditions (as ambient temperature, temperature fluctuations in the oven, and so on). For NP D, the final temperature was reduced to 300 °C, and the reaction time was extended up to 60 min. The lower temperature set in this case explains the smaller size obtained, as both nucleation and growth rates are strongly reduced at lower temperatures.

For the synthesis of the NP F, the largest NP in our study, a different procedure was performed, based on ref 16. First, a

solution, labeled as solution X, was prepared in a round-bottom flask containing 2.5 mmol of Na(CF₃COO), 2.5 mmol of Y(CF₃COO)₃, 5 mL of ODE, and 10 mL of OA. Solution Y was prepared in a separate three-neck round-bottom flask containing a mixture of 10 mL of OA and 15 mL of ODE. Both solutions were heated to 125 °C with vigorous magnetic stirring and kept at this temperature for 30 min under vacuum to remove residual water and oxygen. Afterward, solution Y was heated to 310 °C under an argon flux and maintained at this temperature while solution X was transferred dropwise at a rate of 1 mL min⁻¹ by using a custom-made syringe pump. After mixing the solutions, the temperature was lowered to 305 °C and maintained for 1 h under an argon atmosphere. To obtain intermediate-size NPs (11 nm), NP E was prepared by the same procedure, but the volumes of ODE and OA in solution Y were increased 1.5 times, as dilution affects the nucleation and growth process during the injection of solution X.

In all cases, after the reaction time was completed, the flask was removed from the mantle for cooling to room temperature. An excess amount of ethanol was added, and the NPs were extracted by centrifugation. A washing procedure was performed two times by dispersing the NPs in ethanol and centrifuging. An additional washing step to dissolve and eliminate residual NaF was performed by using a mixture of ethanol–water (50% v/v).

2.2. XRD and TEM. The powder XRD measurements of the α -NaYF₄ NPs were performed in a Bruker Phaser D2 diffractometer with Cu K α radiation ($\lambda = 1.5418$ Å) using a silicon plate with zero background. The scan range was set from 20° to 60° with a step size of 0.02° and a count time of 5 s. TEM analyses were performed using a JEOL JEM 2100F HRP (TEM-FEG) operating at 200 kV. For the analysis, the NPs were dispersed in toluene and dropped on a carbon film. Size counting statistics were measured semiautomatically by using the ImageJ software.¹⁷ For each batch, about 200 NPs were measured on the TEM images.

2.3. ¹⁹F and ²³Na Solid-State NMR. ²³Na SP-MAS, SE-MAS, inversion recovery, and 3Q-MAS experiments were conducted in a Varian VNMRS 500 MHz spectrometer, with magnetic flux density of 11.7 T, operating at the resonance frequency of 132.2 MHz with MAS of 15 kHz and at room temperature (25 °C). For the SP-MAS, a $\pi/2$ pulse length of 3.5 μ s was employed by using regular radio-frequency (rf) power such that nutation frequency was 71.4 kHz strength. The use of short excitation pulses corresponding to flip angles smaller than 30° resulted in identical spectra. For the SE-MAS and inversion recovery, low rf power were used to preferentially excite central transitions (CT) such that we obtained $\pi/2$ pulses of 12.5 μ s with nutation frequency of 20 kHz strength (nutation experiments using such power resulted in regular sine functions). 3Q-MAS experiments were obtained by the three-pulse z -filtered sequence,^{18–21} with a hard excitation of 5.3 μ s and reconversion pulse of 1.8 μ s (short pulses at nutation frequency of 100 kHz strength) and a detection pulse selective of the central transition of 15 μ s (nutation frequency of 16.6 kHz strength), using a time increment τ_1 of 66.7 μ s. ²³Na 3Q-MAS were not performed in NPs C and E since these time-demanding experiments would not provide any further information. Relaxation delays of 2 s were used in the SP-MAS, SE-MAS and inversion recovery experiments, while 1 s was used in the 3Q-MAS. Chemical shifts are reported relative to Na⁺ (NaCl 1 M aqueous solution) at 0 ppm by using solid NaCl as secondary reference at 7.21 ppm.²² The NPs B and C

present NaF as an impurity in the ^{23}Na spectra even after ethanol washing as well as in the XRD (for NP C), but this could be finally eliminated by washing out the samples with water. The ^{23}Na experiments were acquired by accumulating from 64 to ~ 1600 scans, depending on the amount of sample available. The spectra were deconvoluted by using the software DMFIT.²³ Additional ^{23}Na SP-MAS experiments were performed in Agilent DD2 and Bruker Avance Neo spectrometers at magnetic flux densities of 5.64 and 14.1 T, with the ^{23}Na resonating at 64.1 and 158.8 MHz. All details on these experiments were similar to the ^{23}Na SP-MAS described above, except for the use of the Agilent 1.6 mm and Bruker 1.3 mm probes. The use of such probes allowed us to perform experiments at variable MAS spinning frequencies, up to 35.7 kHz. The use of ^{19}F TPPM decoupling²⁴ in the ^{23}Na NMR experiments did not result in higher resolved spectra, independently of decoupling pulse power or phase angle.

^{19}F MAS NMR spectra were measured in the same Agilent DD2 spectrometer with ^{19}F resonating at 228.04 MHz. The spectra were recorded in 1.6 mm rotors spinning at 35.7 kHz by using a rotor-synchronized spin-echo sequence. The ^{19}F spectra were obtained after two rotor cycles for the echo formation (56 μs), which reproduces the SP-MAS spectra without significant background and baseline distortions. For spin–spin relaxation times (T_2) the SE-MAS was obtained after a range of 2–46 rotor cycles for the echo formation (i.e., with interpulse delay times, τ , ranging from 56 to 1288 μs). Relaxation delays of 160 s were used with $\pi/2$ pulses of 1.15 μs length (nutating frequency of 217.4 kHz strength). The relaxation delay was long enough to perform experiments after full relaxation in all samples, since the NPs with the larger sizes present relatively long ^{19}F T_1 (in particular, NP F shows $T_1 \approx 30$ s, as estimated from inversion recovery experiments). Up to 128 scans were accumulated, and the chemical shifts are reported relative to CFCl_3 by using solid NaF as a secondary reference at -224 ppm.²⁵

3. RESULTS AND DISCUSSION

3.1. XRD and TEM Characterization: Particle Size and Lattice Parameter. Figure 1 presents the XRD pattern for the $\alpha\text{-NaYF}_4$ NPs (see Table 1 for size/label relation as obtained from XRD line broadening and TEM images counting). The peak positions correspond to the reported standard patterns of cubic $\alpha\text{-NaYF}_4$ (JPCDS)⁶ without any additional peak

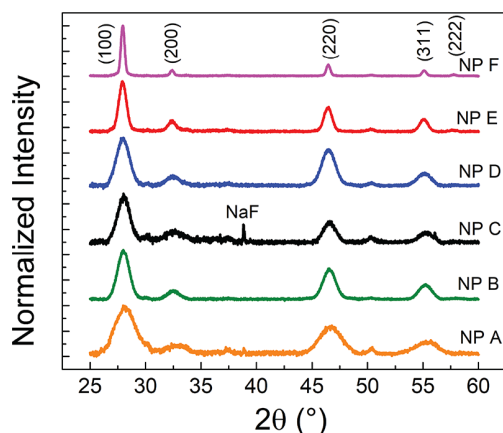


Figure 1. XRD patterns of NPs A–F, with peaks indexed according to the cubic structure of $\alpha\text{-NaYF}_4$ (JPCDS Card No. 77-2042).

Table 1. Size of the Nanoparticles Estimated by XRD and TEM Images (Diameters in nm)

method ^a	NP A	NP B	NP C	NP D	NP E	NP F
XRD	4(1)	7(1)	7(1)	6(1)	11(1)	20(2)
TEM	4(1)	9(2)	12(9)	7(1)	11(7)	25(5)

^aNote the difference in the deviations annotated in parentheses: For the XRD, it is presented the standard deviation between experimental data and the Debye–Scherrer formula, while for the TEM it is presented the full width at half-maximum (FWHM) of the Gaussian distribution fitted to the data (σ_{FWHM}).

associated with impurities, except for the NP C that shows NaF impurities. In fact, ^{23}Na NMR demonstrates that the NPs B and C, as prepared, contain adsorbed NaF. This contaminant could be finally eliminated by washing out the samples with water (as commented in sections 2.3 and 3.2). The lattice constants of all NPs were calculated to be 5.47(1) Å, in agreement with bulk $\alpha\text{-NaYF}_4$. The broadening of the diffraction peaks is related to the small size of $\alpha\text{-NaYF}_4$ nanoparticles. Using the Debye–Scherrer formula, one obtains a group of smaller NPs with an average crystallite size of 4(1), 7(1), 7(1), and 6(1) nm for NPs A, B, C, and D, respectively, and a group of larger NPs, with sizes of 11(1) and 20(2) nm for NPs E and F, respectively.

Figure 2 displays the room temperature TEM images of the NPs. Images in high resolution show lattice fringes (insets) indicating the crystalline nature of the NPs, clearly revealed by fast Fourier transform patterns. For all NPs the interplane distances match those of the cubic structure, with 3.1 Å corresponding to d -spacing for the lattice plane (111) and 1.89 Å for the (220).

More detailed information about the particle size can be obtained from statistical analyses of the TEM images. Figure 3 shows the particle size distributions for the NPs calculated from size counting on more than 200 NPs taken from several images, with the histograms fitted to Gaussian distributions (see Table 1 for size parameters derived from the Gaussian fittings). NPs A, B, C, D, E, and F are characterized by particle size centered at 4(1), 9(2), 12(9), 7(1), 11(7), and 25(5) nm, respectively. The size dispersions are indicated in parentheses and were defined as the FWHM of the Gaussian distribution. The NPs A, D, and F present relatively narrow particle size distribution, around 20% of their particle size. The NPs B, C, and E present broader particle size distribution. For instance, NP B presents high counts ($\approx 20\%$) for particles ranging from 7 to 11 nm, while for NP C this range is from 10 to 17 nm. This results from small variations in the temperature during the preparation of the NPs, demonstrating that the formation of the NPs is highly sensitive to this parameter.^{6,15}

The first finding from the comparison between XRD and TEM data is that for particles with higher polydispersity (NPs B and C) the Debye–Scherrer model has limited accuracy. The XRD peaks are not only broadened by a reduction in particle size but also due to polydispersity, defects, and possibly local distortions from the cubic phase.²⁶ In the following, we discuss the surface effects and the presence of sites nearby defects as influenced by two parameters: particle size (contrasting NPs A, D, and F) and particle size distribution (or polydispersity).

3.2. ^{23}Na Solid-State NMR. Figure 4 shows the room temperature ^{23}Na SP-MAS spectra of the NPs and respective deconvolutions. The spectrum of the NP F extends from -5 to -30 ppm with the center of gravity at -18.8 ppm. It is

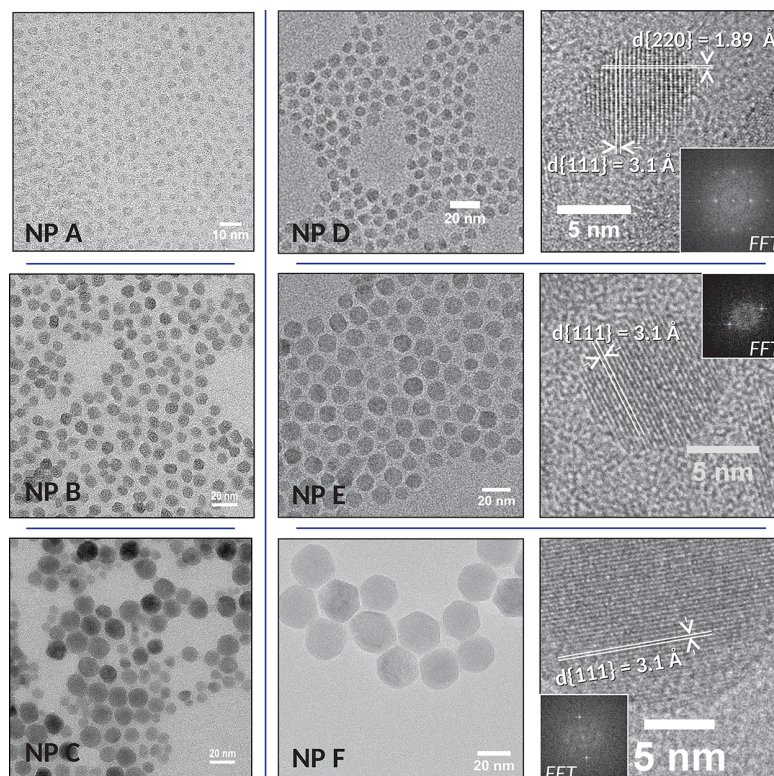


Figure 2. TEM images of the α - NaYF_4 NPs at low magnification (first and second rows) and selected high-magnification TEM images (third column) with lattice fringes as insets for NPs D, E, and F.

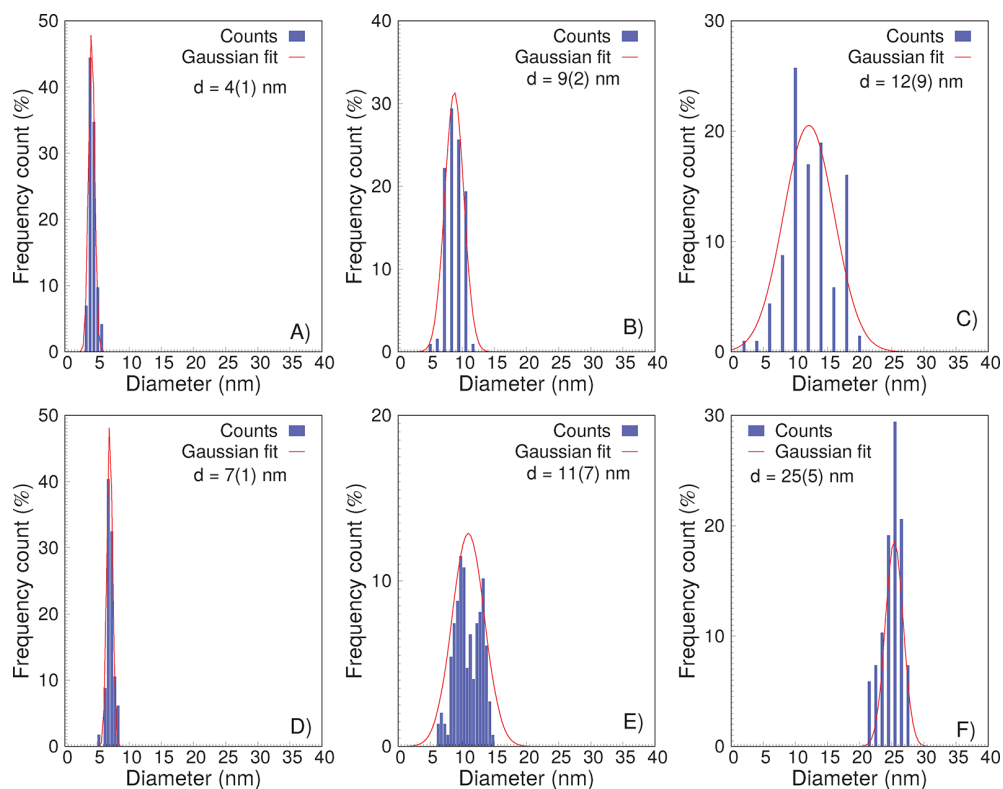


Figure 3. Particle size statistics from TEM images of the α - NaYF_4 NPs with histograms fitted to Gaussian distributions. The mean sizes are indicated with the FWHM of the Gaussian distribution fitted to the data indicated in parentheses.

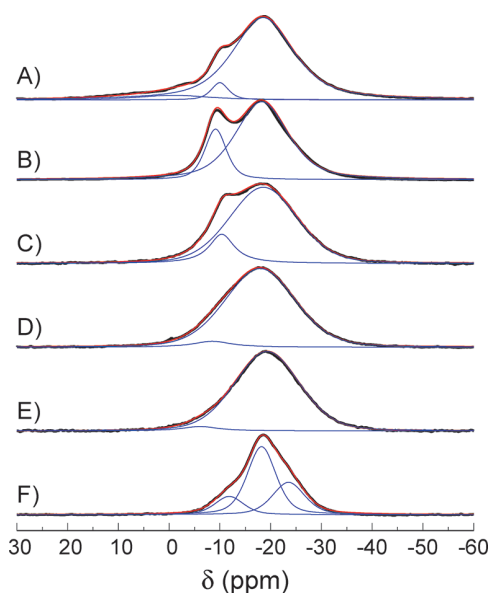


Figure 4. ^{23}Na SP-MAS spectra and respective deconvolutions of the NPs. See Table 2 for deconvolution details. The detected resonances are mostly from CT due to selective excitation.

comparable to the spectra reported by Arnold et al.¹² obtained for NPs of similar size. In the regime of “fast” MAS, a ^{23}Na isotope should resonate at a frequency shift that is a composition of the isotropic chemical shift ($\delta_{\text{CS}}^{\text{iso}}$) and the quadrupolar isotropic shift ($\delta_{\text{Q}}^{\text{iso}}$), i.e., according to $\delta_{\text{CG}} = \delta_{\text{CS}}^{\text{iso}} + \delta_{\text{Q}}^{\text{iso}}$. The line broadening should be dominated by the second-order term of the quadrupolar coupling since dipolar interactions and chemical shift anisotropy would be averaged out by the MAS. We have measured NP B and NP F at various MAS (see the Supporting Information),²⁷ and around a MAS of 5 kHz the spectra show resolution similar to the ones at MAS of 15 kHz, which is already at the highest possible resolution.

Arnold et al.¹² assumed the condition of “fast” MAS at 25 kHz and that second-order quadrupole broadening is of secondary importance (considering the cubic structure). From quantum chemical calculations and the measurements at different magnetic fields they attributed most of the spectral broadening to the chemical shift distributions due to local dissimilarities around the ^{23}Na , as follows: Around the Na atoms there are eight possible nearest neighbors (n.n.) and 12 near to nearest neighbors (n.n.n.). The n.n. are F atoms or vacancies, and the n.n.n. are Na or Y atoms. The Na and Y are

statistically distributed such that the observed ^{23}Na can have 3 Na and 9 Y atoms in the second coordination sphere, or 4 Na and 8 Y, and so on (F vacancies are not noted for the undoped NP, and Na/Y vacancies are considered negligible). The differences in the Na site with respect to the n.n.n. are the main reason for the spectral broadening due to a distribution of isotropic chemical shift. They interpreted their quantum chemical results correlating the chemical shifts at higher frequencies (around -10 ppm) to the rich Na coordinated sites (approximately 8 Na and 4 Y atoms) and at lower frequencies (around -20 ppm) to the poorly occupied Na coordinated sites. However, the correlation is not so obvious (see Figure S.1 of ref 12), as pointed out by the authors themselves. For example, an observed ^{23}Na with 7 Na neighbors appears over the whole range of chemical shifts. Thus, the line broadening is correctly associated with the statistical distribution of Na and Y atoms in the cubic lattice of the $\alpha\text{-NaYF}_4$ NPs (resulting in a $\Delta\delta_{\text{CS}}^{\text{iso}}$), but it should be also affected by local distortions generated by such a distribution (resulting in a $\Delta\delta_{\text{Q}}^{\text{iso}}$, as discussed below).⁴ Second-order quadrupolar broadening maybe be hidden by these local inhomogeneities since the structure approaches to the cubic one.

Now, assuming the presence of slightly distinct Na sites in the $\alpha\text{-NaYF}_4$ lattice (with respect to the Y/Na ratio in the neighborhood and local distortions from the cubic structure), the spectra should be simulated by a composition (convolution) of Lorentzian resonances representing each site. In this approach we are neglecting anisotropic terms coming from the anisotropic chemical shift and second-order quadrupolar coupling. The first term is averaged out by the fast MAS, and the second-order quadrupolar broadening is small in comparison with the chemical shift distribution, as discussed below. This more formal treatment of the NMR resonance lines as compositions of Lorentzian resonances and further Gaussian distribution envelope, done in two steps, are demonstrated in the Appendix. Alternatively, one may also represent an inhomogeneous line broadening by combining Lorentzian and Gaussian distribution representing different sites in one Lorentzian/Gaussian envelop. In this context, a larger amount of Gaussian over Lorentzian weights means a broader distribution of Na sites with respect to their local structure (distortions) or Na/Y ratios. We used this approach in this work because of its simplicity and because both approaches lead to the same conclusions.

There are few differences between the spectra of the undoped NP measured by Arnold et al.¹² and of the NP F reported here. The spectrum of the NP F can also be described by an envelope

Table 2. Best Fitting Parameters from Numerical Deconvolution of the ^{23}Na SP-MAS Spectra of the NPs

NP	δ (ppm)	σ_{FWHM} (ppm)	$X(\text{G}, \text{L})^a$	A^b (%)	δ (ppm)	σ_{FWHM} (ppm)	$X(\text{G}, \text{L})^a$	A^b (%)	δ (ppm)	σ_{FWHM} (ppm)	$X(\text{G}, \text{L})^a$	A^b (%)
A	-1.3	19.3	0.5	6	-10.0	4.0	0.5	5	-18.5	14.1	0.4	89
B					-9.1	5.0	0.5	21	-18.2	12.2	0.5	79
C					-10.4	6.0	0.0	16	-18.6	15.7	0.8	84
D					-8.5	8.8	0.0	5	-17.9	16.2	0.8	95
E					-6.1	8.6	0.0	4	-19.3	15.1	0.8	96
F ^c	-11.8	6.6	0.6	15	-18.2	6.7	0.6	56	-23.5	7.4	0.6	29

^a $X(\text{G}, \text{L})$ means the ratio between Gaussian (X) and Lorentzian ($1 - X$) in the curve; i.e., $X = 0$ stands for a full Lorentzian distribution and $X = 1$ for a full Gaussian distribution. ^b A (%) is the contribution in area of the peak to the whole spectrum. ^cNote that for NP F the three deconvoluting peaks describe a superposition of chemical shifts due to the ^{23}Na local site variations in the bulk of the NP, as detailed in the text, and they are not attributed to surface effects or defects. This interpretation is based on the quantum chemical calculations performed in ref 12 and our relaxation results. It is a coincidence that such a superposition of chemical shifts results in a band with three features that can be represented by three Gaussian/Lorentzian distributions.

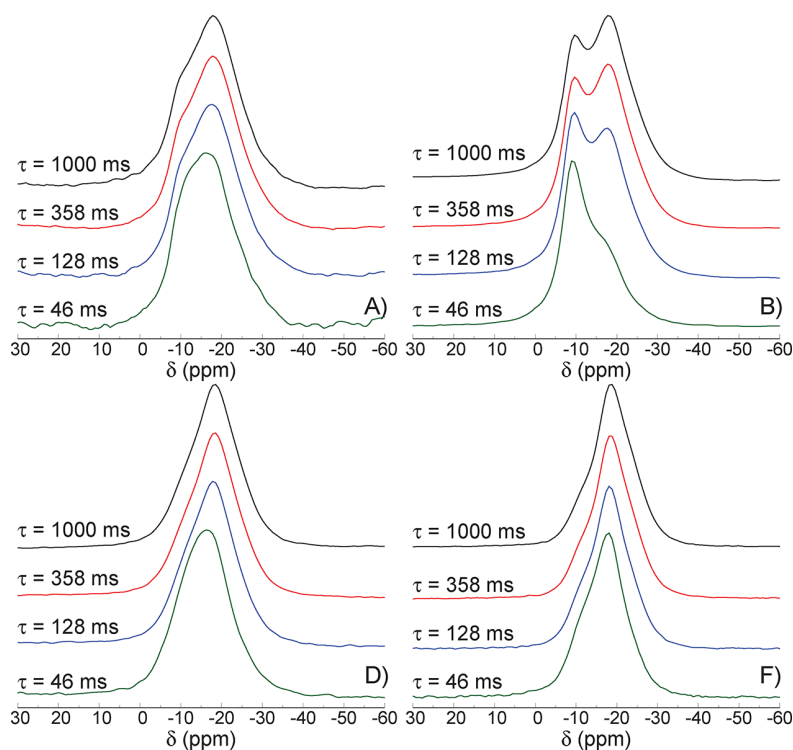


Figure 5. Inversion recovery spectra of NPs A, B, D, and F, obtained after various interpulse delay times. The spectra of NPs C and E do not contribute further to the discussion and are omitted. The detected resonances are mostly from CT due to selective excitation.

with three features, here simulated by three distributions composed by combinations of Gaussian and Lorentzian distributions. The best fit is obtained by combining $X = 0.6$ with Gaussian and $1 - X = 0.4$ Lorentzian (refer to Table 2 for deconvolution details). Note that the three features do not assign distinguishable ^{23}Na sites, but they appear as an overlap of many contributions. Our spectrum is slightly narrower than the one reported by Arnold et al.,¹² despite their higher MAS and magnetic field. This is possibly due to the less (or absent) contamination or spurious phases and narrower particle size distribution in our NP F, in contrast to the particles studied by Arnold et al.¹² (for instance, σ_{FWHM} is 5 nm for NP F and ~ 8 nm in ref 12). Furthermore, our spectrum is shifted by ~ 7 ppm to higher frequencies (by visually interpolating their data to $\nu_0 = 132.2$ MHz). This apparent difference is due to their choice of referencing solid NaCl at 0 ppm and not the conventional NaCl 1 M aqueous solution at 0 ppm and solid NaCl at 7.21 ppm.

The ^{23}Na NMR spectra change considerably for the NPs smaller than the NP F. The spectrum of the NP E, for instance, can be fairly well represented by two distinguishable signals: an intense and broad peak around -18 ppm and a small peak at -6 ppm (with a contribution of 4% for the integrated intensity). The X is 0.8 for the peak around -18 ppm and 0 for the peak at -6 ppm, meaning that the former signal has a higher Gaussian contribution (Table 2), thus, with more ^{23}Na site variations. As the NPs become smaller and/or with higher polydispersity, the small peak around -6 ppm becomes more prominent and can be distinguished around -9 ppm instead. Interestingly, NP A, the smallest one, shows an extended band to even higher frequencies (around 0 ppm). As further validated below, the wide peak around -18 ppm represents the ^{23}Na in the bulk of the NPs A-E with the site variations similar to those described by Arnold et al.¹² This peak contains all the features displayed

for NP F, though less distinguishable, related to the smaller particle sizes. The small peak at higher frequency, around -6 ppm (or -9 ppm), is associated with the higher surface/bulk ratio (and/or polydispersity) and can be interpreted as Na surface sites or sites nearby defects.

For the ^{23}Na spectra of the NPs among those with higher polydispersity, NPs B, C, and E, the contribution from the peak at -9 ppm is 21%, 16%, and 4%, respectively. Accordingly, the contribution from the sites assigned as surface or nearby defects decrease as particle size increases. A similar trend can be drawn for the NPs with low polydispersity, NPs A, D, and F: While no signal related to surface/defect sites is attributed to the NP F, for NP D and A this peak contributes with 5% and 11%, respectively. Finally, we can compare the two smallest NPs with low and high polydispersity: NP A has 11% of contribution from surface/defect sites, while NP B has 21%. Although NP B is, on average, larger than NP A, the surface effects or defect sites on the former are more noticeable. It means that these sites are also related to polydispersity; i.e., the experimental conditions that lead to higher polydispersity also lead to higher probabilities of Na sites nearby defects.

Figure 5 shows the inversion recovery spectra of representative samples, NPs A, B, D, and F, recorded after several delay times between the inversion pulse (π) and the excitation pulse ($\pi/2$). For each NP, the spectra recorded after an interpulse delay time of 1 s resemble those obtained from the SP-MAS because they were recorded after full relaxation. However, for NP A and, most remarkably, for NP B, the peak at -9 ppm becomes more pronounced for shorter evolution times. With the NP B, for instance, this peak turns into the most intense for delay times as short as 46 ms. Therefore, the resonance signal at -9 ppm has a much shorter spin–lattice relaxation time. Similar behavior is observed for the NPs C (not

shown), D, and E (not shown), although with the peak around -9 ppm less pronounced. For NP F, the inversion recovery spectra are nearly independent of evolution times, indicating for negligible effects from the surface or defective sites in comparison to the bulk ones (Figure 5).

There are numerous effects influencing the ^{23}Na longitudinal relaxation.^{28,29} In general, the longitudinal relaxation of quadrupolar nuclei is not single exponential but governed by $2I$ rates.^{30,31} The initial excitation conditions also influence the observed magnetic relaxation, particularly, differentiating the situations of complete saturation of both CT and satellite transitions (STs) from the selective saturation of the CT.^{29,30,32–34} In the latter case, as approximately in our experiments, the return to equilibrium of the magnetization can be described by only $I + 1/2$ rates (if $2I$ is odd).³⁰ The $(I + 1/2)$ -exponential behavior of the relaxation is a function of the spin–lattice transition probabilities involving single- and double-quantum processes, $W_1 = W(m = 1)$ and $W_2 = W(m = 2)$, which themselves depend on the specific form of the relaxation mechanism and are functions of temperature and crystal orientation.³⁰ Next, the relaxation process might be due to fluctuations of the dipolar couplings (magnetic relaxation) and/or to the quadrupolar coupling to the time-modulated EFG (quadrupolar relaxation).³⁵ The first mechanism is observed in cubic structures or for nuclei with small quadrupole moment. The second mechanism is dominant in imperfect cubic and more distorted structures, and an interplay of both effects is also possible.³⁵ For a crystallite under fast MAS, i.e., when the rotor period is much shorter than T_1 , the orientational dependence of the transition rates is averaged to a characteristic value (W_1^{avg} and W_2^{avg}).³⁶ The statement holds approximately for polycrystalline samples.³⁶ For perfect cubic crystals (and sometimes also for imperfect cubic crystals), W_1^{avg} can be regarded as equal to W_2^{avg} , and the relaxation behavior approaches a single exponential.^{30,37–40} In addition, MAS activates zero-crossing conditions between ST and CT during the rotation periods (first-order spin-exchange transitions),^{28,29,32,34} adding a further relaxation channel, increasing the apparent magnetic relaxation rate.³⁴ On top of that, the local distortions in the ^{23}Na sites of the $\alpha\text{-NaYF}_4$ NPs, as previously described, would lead to a distribution of relaxation rates, adding further dispersion in the magnetization recovery data.

Our experimental method does not allow to discriminate the different contributions to the relaxation patterns; neither is it in the scope of this work. However, our results highlight the main mechanism that drives the differences in the longitudinal magnetization dynamics between the two characteristic ^{23}Na sites: surface or defects in contrast to bulk sites. Based on the typical relaxation times found for the studied NPs, comparable to similar structures in terms of quadrupolar coupling,^{41,42} the changes in longitudinal relaxation at room temperature for the $\alpha\text{-NaYF}_4$ NPs are mainly driven by the quadrupole mechanism.^{35,43} The considerable EFGs are created by local distortions and the modulation of the quadrupole coupling by lattice vibrations, especially for ^{23}Na sites in the bulk. One expects faster relaxation times for the sites on the surface and/or defects, given that the nuclear motion and impurities as protons from adsorbed water are also contributing to the relaxation of the magnetization.^{33,44,45}

We can assign T_1 as the characteristic time in which the magnetization returns to equilibrium after a selective CT inversion according to

$$M_z(\tau) = M_0\{1 - f[e^{-(\tau/T_1)^\lambda}]\} \quad (1)$$

where M_0 is the initial magnetization, $f < 2$ accounts for incomplete M_0 inversion after the π pulse, and λ accounts for differences between W_1 and W_2 (though we assume $W_1 \sim W_2$, considering the pseudocubic structure of the NPs),³⁰ the contribution from spin exchange transitions and the dispersion of these relaxation rates due to local distortions and inhomogeneities caused by the surface/bulk interface.

Figure 6 shows the integrated intensity of the deconvoluted peaks as a function of τ for all studied NPs. The adjusted curves,

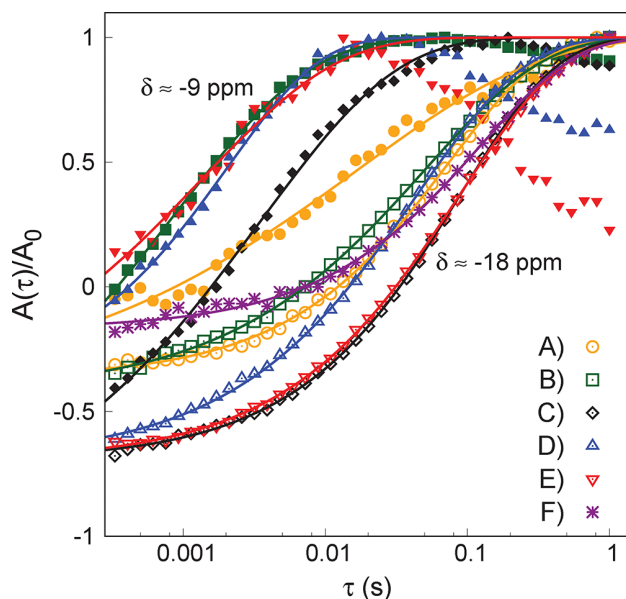


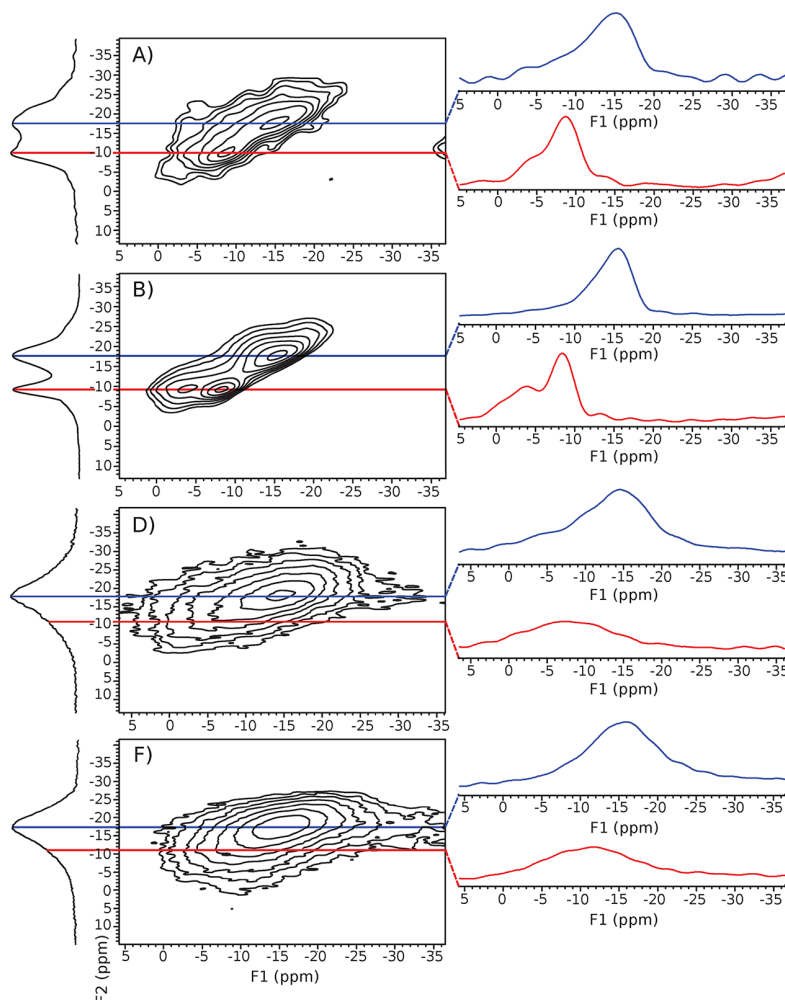
Figure 6. ^{23}Na inversion recovery integrated intensity as a function of interpulse delay time and fits according to eq 1 for all NPs. Solid symbols are due to the signal at -9 ppm and open symbols to the signal at -18 ppm. Note that the signals at -9 ppm show a decrease in intensity at long interpulse delay times ($\tau \geq 0.02$ s). This effect is more pronounced for the NPs that present the smallest ratios between the surface or defect signals with respect to bulk signals ($A(\delta_{-9\text{ppm}})/A(\delta_{-18\text{ppm}})$). These downturns occur because the peaks representing the bulk sites dominate the spectra at long delay times, obscuring the small peaks at -9 ppm which are underestimated in the deconvolution.

according to eq 1, are in good agreement with the experimental data (the obtained parameters are indicated in Table 3). The signals around -9 ppm exhibit a T_1 of 17 ms for NP A and within 1–3.5 ms for NPs B, C, D, and E. The signals around -18 ppm show T_1 more than 1 order of magnitude longer, within 50–125 ms, except for NP A, which shows a more moderate difference in T_1 .

Because the NPs present only cubic crystallographic phase (as observed by XRD), though locally distorted, the signal around -18 ppm with longer relaxation times is attributed to ^{23}Na in the bulk sites of the nanoparticles. The peak around -9 ppm with shorter relaxation times is related to sodium atoms on the surface or nearby defects. Considering that the dominant spin–lattice relaxation mechanism is the quadrupole coupling to the time-modulated EFG and that the quadrupolar couplings of both sites are quite similar (see 3Q-MAS results below), the differences in relaxation times must be associated with the dynamics of the EFG. The surface sites and/or sites nearby defects demonstrate a more intense fluctuation of the EFG,

Table 3. Fitting Parameters According to Eq 1 of Deconvoluted ^{23}Na Inversion Recovery Integrated Intensity as a Function of Interpulse Delay Time

parameter	NP A	NP B	NP C	NP D	NP E	NP F
$T_1^{(-9\text{ppm})}$ (ms)	17(3)	0.9(3)	3.4(6)	2.1(1)	1.3(9)	
$\lambda^{(-9\text{ppm})}$	0.34(2)	0.45(6)	0.45(4)	0.7(3)	0.5(1)	
$f^{(-9\text{ppm})}$	1.44(8)	1.43(1)	1.70(1)	1.69(1)	1.70(1)	
$T_1^{(-18\text{ppm})}$ (ms)	74(1)	51.2(6)	90.4(6)	45.2(5)	90.0(7)	125(2)
$\lambda^{(-18\text{ppm})}$	0.65(1)	0.52(1)	0.64(1)	0.57(1)	0.60(1)	0.65(1)
$f^{(-18\text{ppm})}$	1.36(1)	1.9(3)	2.0(1)	1.4(5)	1.5(4)	1.17(1)

**Figure 7.** ^{23}Na 3Q-MAS spectra of the representative samples, NPs A, B, D, and F, with projection of the signal attributed to the bulk of the NPs (≈ -18 ppm) onto the isotropic dimension (in blue) and projection of the signal attributed to the surface/defects (≈ -10 ppm, in red).

caused by thermal lattice vibrations (spin–phonon interactions) and the motion of defects, oleic acid molecules attached to the yttrium sites on the surface,⁴⁶ and polar sorbate molecules^{44,45} (as in the external layers of the nanoparticles). As expected, the NP F presents the longest spin–lattice relaxation, 125 ms, for the peak at -18 ppm, indicating that the bulk structure of the largest particle is also the most symmetric one.

To further investigate the structural differences of the sites attributed to the surface and/or defects and bulk sites, we performed 3Q-MAS. In the well-established 3Q-MAS experiments,^{18,19} it is possible to resolve the contribution from $\delta_{\text{CS}}^{\text{iso}}$ and $\delta_{\text{Q}}^{\text{iso}}$ to the total shift δ_{CG} of the MAS NMR spectrum.

Succinctly, this is done by composing the signal from appropriate instant frames after echo pulses that access single and triple coherences in which anisotropic terms on the system evolution are canceled out.^{18,19} Thus, the regular MAS spectrum is collected in the direct dimension (F2) and correlated to an isotropic spectrum obtained in the indirect dimension (F1). After a shear transformation in F1, these shifts are described by^{47,48}

$$\delta_{\text{F1}} = \delta_{\text{CS}}^{\text{iso}} - \frac{10}{17} \delta_{\text{Q}}^{\text{iso}} \quad (2)$$

which yield

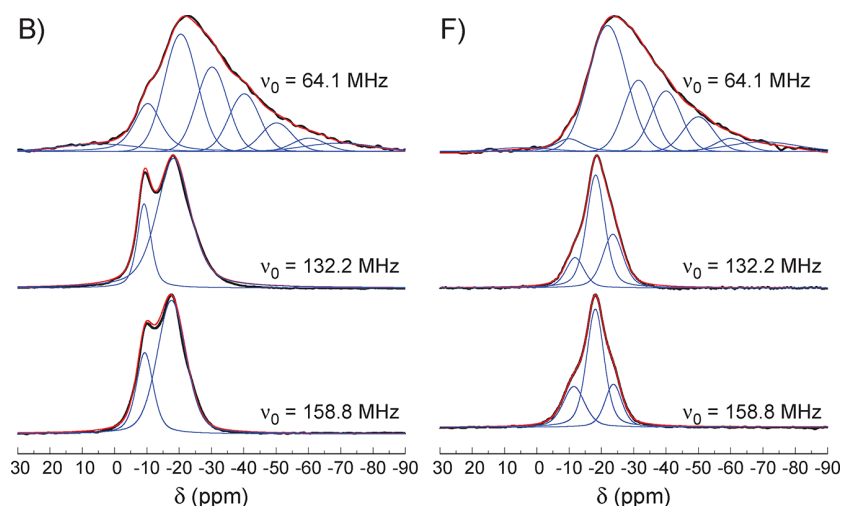


Figure 8. Field dependence of the ^{23}Na SP-MAS spectra at 15 kHz and respective deconvolutions for representative NPs A and F. The detected resonances are mostly from CT due to selective excitation.

$$\delta_{\text{CS}}^{\text{iso}} = \frac{17}{27}\delta_{\text{F1}} + \frac{10}{27}\delta_{\text{CG}} \quad (3)$$

From $\delta_{\text{Q}}^{\text{iso}}$ it is possible to calculate the second-order quadrupolar effect parameter (P_{Q}) since

$$\delta_{\text{Q}}^{\text{iso}} = -\frac{P_{\text{Q}}^2}{\nu_0^2}\beta(I)10^6 \quad (4)$$

with

$$\beta(I) = \frac{204}{680} \frac{[I(I+1) - 3/4]}{[2I(2I-1)]^2} \quad (5)$$

which is a measure of the magnitude of the EFG⁴⁹ (ν_0 is the Larmor frequency and I is the nuclear spin number).

Figure 7 shows the 3Q-MAS spectra of representative samples, NPs A, B, D, and F, with projections on the isotropic dimension (F1) taken from the slice when the direct dimension (F2) is around -18 ppm (in blue, on top) and -9 ppm (in red, on bottom). For the NP A, the most intense signal at -18 ppm is correlated to an isotropic signal at -15 ppm. The shoulder observed in the direct dimension at -10 ppm is correlated to an isotropic signal at -8.6 ppm with a shoulder around -4 ppm. This is also observed for the NP B, with the small shoulder around -4 ppm in the isotropic dimension even more visible. The contribution from lower frequencies is less remarkable for the other nanoparticles (NPs D and F), but a small isotropic peak around -6 ppm remains distinguishable when the peak around -9 ppm in the direct dimension is projected onto the isotropic dimension.

The calculated isotropic chemical shift of the bulk site is around -16 ppm for all samples and around -8 ppm for the surface sites and/or defects.⁴⁷ The calculated quadrupolar coupling constant for bulk sites is small, and ranges about 1.2–1.0 MHz, as also previously estimated.¹² It is slightly smaller for the surface/defect sites, around 0.4–1.1 MHz, and slightly higher for the shoulder extending to higher frequencies, around 1.6–2.0 MHz. These estimates are taken from the line broadening in the direct and indirect dimensions. The similar EFG between the sites, within their ranges, indicates that the site distortions in both environments are not substantial.

Figure 8 shows the field dependence of the ^{23}Na SP-MAS spectra at 15 kHz with respective deconvolutions for NPs A and F. As expected, the low field spectra taken at $\nu_0 = 64.1$ MHz ($B_0 = 5.64$ T) are the broadest ones and extend from -5 to -70 ppm, mostly because the spectra are compositions of chemical and quadrupolar shifts and the line broadening is proportional to the $\Delta\delta_{\text{CS}}^{\text{iso}} + \Delta\delta_{\text{Q}}^{\text{iso}}$. Because $\delta_{\text{Q}}^{\text{iso}}$ is proportional to P_{Q}^2/ν_0^2 (eq 4), at low field (and thus low ν_0) the distribution of P_{Q} between the sites is evidenced ($\Delta_{\text{Q}} \sim 1/\nu_0^2$). In addition, the broadening of the central transition line is inversely proportional to B_0 in second-order quadrupolar coupling (not averaged out by the MAS).⁵⁰ This contribution depends on the asymmetric parameter of the EFG, and it is probably less important since the structure identified by XRD is cubic, though locally distorted. The spectra of both samples are similar, but for NP A there is an enhanced shoulder around -10 ppm and a small contribution extending up to 15 ppm, which are contributions from surface/defect sites. The spectra taken with $\nu_0 = 158.8$ MHz ($B_0 = 14.1$ T) are similar to the previous ones with $\nu_0 = 132.2$ MHz ($B_0 = 11.7$ T), except that the signal attributed to the bulk sites becomes closer to the peak attributed to the surface/defect sites. The smaller shift of the peaks attributed to surface and/or defects as magnetic field increases indicates a smaller quadrupolar coupling, as obtained from the 3Q-MAS experiments. From the center of gravity of the spectra at $B_0 = 5.64$ T, and taking the assigned peaks for other magnetic fields, the ^{23}Na in the bulk and surface sites or nearby defects of NP A demonstrate a P_{Q} of 1.8(4) and 0.4(2) MHz, respectively, with a $\delta_{\text{CS}}^{\text{iso}}$ of $-14.1(5)$ and $-9.0(2)$ ppm (see data fit to eq 2 in combination with eqs 4 and 5 in the Supporting Information).²⁷ For NP F, the $\delta_{\text{CS}}^{\text{iso}}$ is $-14.76(4)$ ppm and P_{Q} is 1.7(1) MHz, in agreement with the 3Q-MAS experiments.

Overall, our results can be analyzed as follows: The ^{23}Na spectra of the NPs present a broad peak at -18 ppm due to the α - NaYF_4 bulk phase. The spectral broadening is dominated by the chemical shift distribution associated with Na sites that are different relative to first and second neighbors,¹² in addition to slight local site distortions from the cubic lattice, resulting in a distribution of quadrupolar shift. Upon decreasing the size of the NPs to <10 nm, another low-field (high-frequency) signal emerges, implying the presence of a less shielded environment. The large difference in spin–lattice relaxation rates between

bulk and surface sites cannot be explained only by the different EFG in these regions. It has to be associated with the dynamics (fluctuations) of the EFG related to distinct vibrational modes in the bulk and surface sites.^{45,51,52} The increased mobility of Na ions is also observed for confined NaNO₂ in nanoporous materials,^{53,54} which have the same size scale as the NPs investigated here. Thus, ionic motion in the surface sites of the NPs might also play a role in the relaxation rates.

Interesting studies in a similar fashion as ours have been reported. For semiconducting nanoparticles such as CdSe (a closer system to the one presented here) Thayet and collaborators⁵⁵ have also observed a ⁷⁷Se line broadening and possibly spectral resolution for “bulk” and “surface” sites via relaxation time analyses in the same fashion as reported here. They have interpreted that the paramagnetic contribution to the chemical shielding is attenuated in small particles due to their higher energy gap, leading to shifted resonance lines.⁵⁵ In addition, the structural differences between the bulk and surface in the NPs are also analyzed in a general way by taking into account the site distortions at the surface for other nanoparticles.^{56,57} Lo et al.⁵⁸ have found similar results for LaF₃ NPs with sizes of 8–10 nm, but only a line broadening was noticed in the ¹³⁹La and ¹⁹F spectra when compared to the bulk materials. Their spectra do not display sufficient resolution to distinguish bulk from surface site contributions, although a biexponential behavior of *T*₁ was justified by surface effects. They observed longitudinal relaxation times ~2 orders of magnitude shorter than that of bulk samples, with the relaxation process driven by quadrupole interactions in addition to a small influence of paramagnetic impurities. Perhaps studies in smaller LaF₃ NPs would lead to a discernible spectral and relaxation time resolutions as those reported in this work.

3.3. ¹⁹F Solid-State NMR. Figure 9 shows the ¹⁹F SE-MAS spectra of all NPs. The spectrum of NP F, for instance, shows a broad peak centered at –75 ppm, extending from approximately –50 to –95 ppm, with a small shoulder around –120 ppm, accounting for 1% of the integrated intensity. The dominant peak can be represented by three Gaussian/Lorentzian peaks (see deconvolution details in the Supporting Information).²⁷ This spectrum is very similar to that of Arnold et al. for the undoped α -NaYF₄ NP¹² and ~10 ppm shifted to higher frequencies relative to the one obtained by Bessada et al.⁵⁹ for bulk α -NaYF₄ (centered at –85 ppm). From quantum chemical calculations, Arnold et al.¹² assigned the ¹⁹F resonances to defects free α -NaYF₄, where the fluorine is 4-fold-coordinated as FN_{*x*}Y_{4–*x*} (*x* = 0, 1, 2, 3, 4). The resonances at high frequencies are related to Na-rich sites (around 0 ppm), the ones at low frequencies to Y-rich sites (around –75 ppm), and those at intermediate frequencies (around –50 ppm) to sites with similar Na/Y ratios in addition to an overlap of the two sites previously described. The main peak in the NP F spectrum can be interpreted according to Arnold et al.¹² Again, the spectral line broadening is attributed to a distribution of δ_{CS}^{iso} due to local site variations coming from variable Na/Y cell occupancies. At the MAS employed here, this effect dominates over the anisotropic chemical shift (and distributions) and dipolar broadening. In fact, the spin–spin relaxation time of the main peak is around 0.7 ms (Supporting Information),²⁷ corresponding to a homogeneous broadening of only 0.5 kHz, while its σ_{FWHM} is \approx 7 kHz.

The interpretation of the small shoulder at –120 ppm is grounded on the work of Bessada et al.⁵⁹ in NaF–YF₃ melts. The ¹⁹F resonance of the stoichiometric NaYF₄ melt is observed

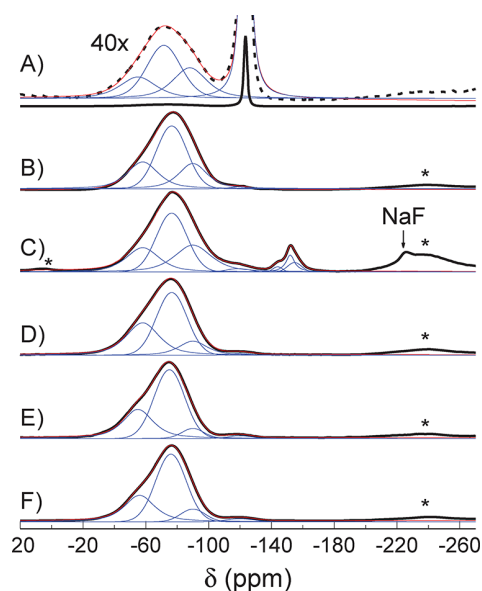


Figure 9. ¹⁹F SE-MAS spectra and respective deconvolutions of all NPs studied, taken after 56 μ s interpulse delay time. Spinning sidebands are indicated by asterisks. The deconvolutions, presented in the Supporting Information,²⁷ are not considering the spinning sidebands due to their low intensity (\leq 1%, except for NP C) and because the detailed quantitative information about this contribution is not relevant for the discussion.

around –75 ppm, while in YF₃-rich compositions the ¹⁹F resonances are observed at higher frequencies and in NaF-rich compositions at lower frequencies. The resonances at –120 ppm are noticed for NaF–YF₃ melts with molar contents of 0.3 for the YF₃ and 0.7 for the NaF. To form a α -NaYF₄ structure with such stoichiometry (as confirmed from the XRD and ²³Na NMR results), it is necessary to form fluorine-deficient sites. Thus, the small shoulder at –120 ppm is assigned to fluorine in Na-rich sites of the α -NaYF₄ structure in the presence of fluorine vacancies. This indicates the presence of mobile fluorines, first suggested by Roy and Roy.¹⁰ Accordingly, this peak has longer spin–spin relaxation times in comparison to that at –75 ppm (\approx 1 ms, see the Supporting Information).²⁷

The NPs E, D, and B present ¹⁹F spectra similar to the NP F. The spectrum of NP C shows additional resonances around –150 and –224 ppm, contributing to \approx 10% and 1% of the spectrum weight, respectively. The resonances around –150 ppm are tentatively attributed to additional species of free fluorine in Na-rich NaF–YF₃ composition (YF₃ \leq 20%),⁵⁹ possibly as amorphous structures formed in the crystal interstices (since they are not detected by XRD). The peak at –224 ppm is due to remaining NaF present in the NP despite the extensive washing procedure of the NP.

The ¹⁹F spectrum of the NP A is the most distinct one. It has \approx 75% of the spectrum composed by the peak at –120 ppm and a broadening in the peak at –75 ppm attributed to the stoichiometric α -NaYF₄. Thus, \approx 75% of the fluorines are attributed to fluorine in Na-rich sites, and consequently, the broadening in the peak around –75 ppm is due to the presence of Y-rich sites and fluorine vacancies.

Interestingly, the indication of small contents of fluorine vacancies for NPs B–F (\approx 1%) and high contents for the NP A (\approx 75%) points to fluorine ionic motion,⁶⁰ as previously predicted.^{61,62} The easy decoupling between ²³Na and ¹⁹F in

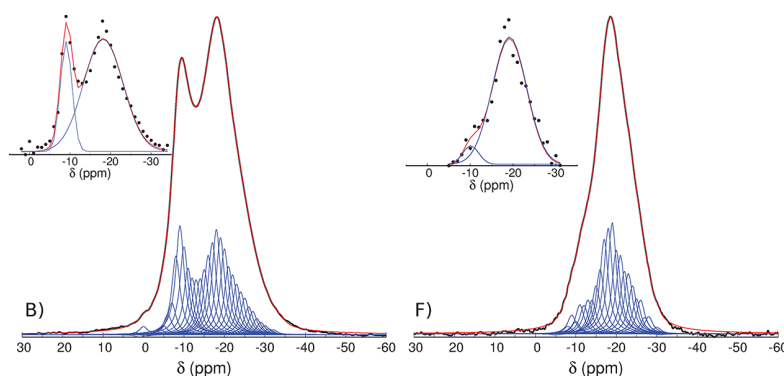


Figure 10. ^{23}Na SP-MAS spectra of the NPs B and F and deconvolutions as an envelop of Lorentzian resonances with line width of 2.5 ppm spaced by 2 ppm. Insets show the Gaussian fits of the Lorentzian resonances.

our measurements also indicates fast motion of fluorines. For instance, the ^{23}Na – ^{19}F dipolar coupling is estimated as 4–6 kHz for static nuclei in the unit cell, while ≈ 5 kHz of MAS was sufficient to average out this interaction in the ^{23}Na spectra (see the Supporting Information).²⁷ Temperature-dependent NMR is a promising lead to characterize the ion conductivity in the α - NaYF_4 NPs, particularly because ion mobility might be largely enhanced in small NPs.⁶³ Note, however, that line broadening will not be the appropriate parameter to probe such dynamics since the spectra of the NPs are dominated by inhomogeneous broadening. Therefore, the relaxation rates obtained from echo experiments will rather be the most suitable parameter to characterize ion mobility as a function of particle size and polydispersity.

4. CONCLUSIONS

We synthesized and characterized cubic α - NaYF_4 nanoparticles in a wide range of particle sizes (4–25 nm). We performed a systematic method to evaluate site differences in nanoparticles due to defects and surface effects, combining various and very sensitive NMR techniques. ^{23}Na and ^{19}F were used as local probes for the site-selective spectral analysis, spin–lattice and spin–spin relaxation times, and multiquantum experiments. Upon varying the nanoparticle size and carrying out these locally sensitive experiments, we were able to unveil small but not less important structural changes due to surface effects in this particular system. Moreover, the presented methodology may be extended to other nanoparticle systems. The structural effects are more prominent in the smallest particles ($\phi \lesssim 7$ nm), especially when the preparation conditions lead to broader particle size distribution ($\sigma_{\text{FWHM}} \gtrsim 20\%$ of their mean size). This is important when site symmetry breaking is desired while avoiding defects, as for upconversion host systems used for technological applications.

APPENDIX. NMR SPECTRA SIMULATED AS A GAUSSIAN DISTRIBUTION OF LORENTZIAN RESONANCE LINES

Figure 10 shows the spectra of the NPs B (left) and F (right) simulated by a sum of Lorentzian resonances spaced 1 ppm apart by using a fixed width of 2.5 ppm. The line width was chosen according to the shortest spin–spin relaxation time of the ^{23}Na in the different sites, 1 ms, estimated from SE-MAS experiments (see the Supporting Information).²⁷ The shift of 1 ppm between Lorentzian resonances was chosen to reproduce the smoothness of the experimental spectra. The amplitudes of

the Lorentzian resonances were plotted as a function of chemical shift, and these data were simulated by two Gaussian distributions (inset to Figure 10). For NP B, the Gaussian distributions are centered at -9.0 and -18.2 ppm, with weight contributions of 22% and 78%, respectively. For NP F the Gaussian lines are centered at -10.1 and -19.5 ppm, with weight contributions of 6% and 94%, respectively. This data analysis corresponds to the following interpretation: The Na sites of either bulk or surfaces of the NPs are composed by sites that are slightly different due to distortions or Na/Y neighboring composition. Each site has a first-order spin–spin relaxation, as expected, due to dipolar and quadrupolar interactions. Thus, each site contributes to a Lorentzian resonance signal. However, the sites show a chemical shift and quadrupolar shift distribution, which is better represented by a Gaussian distribution of sharp Lorentzian lines. The surface/bulk ratio obtained by this rigorous method is similar to that obtained by combining Gaussian and Lorentzian distributions, as described in the text. For instance, the SP-MAS spectrum of the NP B presents 21% of contribution from the peak centered at -9.1 ppm and 79% from the peak at -18.2 ppm (Table 2).

ASSOCIATED CONTENT

Supporting Information

The Supporting Information is available free of charge at <https://pubs.acs.org/doi/10.1021/acs.jpcc.0c00776>.

^{23}Na NMR measurements at various MAS, estimates of spin–spin relaxation times, ^{23}Na σ_{CG} as a function of Larmor frequency, and deconvolution data of the ^{19}F NMR spectra (PDF)

AUTHOR INFORMATION

Corresponding Authors

Thiago B. de Queiroz – Centro de Ciências Naturais e Humanas, Universidade Federal do ABC, 09510-580 Santo André, SP, Brazil; orcid.org/0000-0003-3775-954X; Email: thiago.branquinho@ufabc.edu.br

Michael Cabrera-Baez – Departamento de Física, Universidade Federal de Pernambuco, 50670-901 Recife, PE, Brazil; Email: mcabrera@df.ufpe.br

Carlos Rettori – Centro de Ciências Naturais e Humanas, Universidade Federal do ABC, 09510-580 Santo André, SP, Brazil; Email: rettori@ifi.unicamp.br

Ricardo R. Urbano – Instituto de Física “Gleb Wataghin”, UNICAMP, 13083-859 Campinas, SP, Brazil; Email: urbano@ifi.unicamp.br

Authors

Paulo Menegasso – Instituto de Física “Gleb Wataghin”, UNICAMP, 13083-859 Campinas, SP, Brazil

Eduardo D. Martinez – Centro Atómico Bariloche, Comisión Nacional de Energía Atómica (CNEA), Consejo Nacional de Investigaciones Científicas y Técnicas (CONICET), San Carlos de Bariloche, Argentina; orcid.org/0000-0002-5834-4389

Ali F. García Flores – Instituto de Física “Gleb Wataghin”, UNICAMP, 13083-859 Campinas, SP, Brazil

Complete contact information is available at: <https://pubs.acs.org/10.1021/acs.jpcc.0c00776>

Notes

The authors declare no competing financial interest.

ACKNOWLEDGMENTS

The authors acknowledge the Brazilian funding agencies São Paulo Research Foundation (FAPESP) and National Council for Scientific and Technological Development (CNPq) for support: UFABC Tematico 2011/19924-2, UNICAMP Tematico 2012/04870-7, FAPESP 2016/15780-0, FAPESP 2016/14436-3, Fapesp 2018/21025-5, and CNPq Universal Project 404951/2016-3. TEM was performed at LNNano, Centro Nacional de Pesquisa em Energia e Materiais (CNPEM) in Campinas, SP, Brazil. R.R.U. acknowledges JP FAPESP 2012/05903-6 and CNPq 307668/2015-0. Additional images of electron microscopy were obtained by a collaboration with INCT/INOMAT (National Institute for Complex Functional Materials financed by Grant 2014/50906-9, FAPESP). The authors are grateful to the Multiuser Central Facilities (UFABC) for the experimental support. Special thanks go to Dr. Antoine Champetier de Ribes from University of California, Davis, for proofreading the article and Prof. Hellmut Eckert and Prof. José Schneider from the Physics Institute of São Carlos, University of São Paulo (IFSC/USP), for making available the NMR facilities and for valuable discussions and suggestions.

ADDITIONAL NOTE

^aNote that Δ usually represents the chemical shift anisotropy. Here Δ refers to a distribution of isotropic chemical shift ($\Delta\delta_{CS}^{iso}$) and quadrupolar shift ($\Delta\delta_Q^{iso}$).

REFERENCES

- (1) Sun, C.-J.; Xu, Z.; Hu, B.; Yi, G. S.; Chow, G. M.; Shen, J. Application of NaYF₄:Yb, Er upconversion fluorescence nanocrystals for solution-processed near infrared photodetectors. *Appl. Phys. Lett.* **2007**, *91*, 191113.
- (2) Chen, X.; Zhao, Z.; Jiang, M.; Que, D.; Shi, S.; Zheng, N. Preparation and photodynamic therapy application of NaYF₄:Yb, Tm-NaYF₄:Yb, Er multifunctional upconverting nanoparticles. *New J. Chem.* **2013**, *37*, 1782–1788.
- (3) Cui, X.; Mathe, D.; Kovács, N.; Horváth, I.; Jauregui-Osoro, M.; Torres Martin de Rosales, R.; Mullen, G. E. D.; Wong, W.; Yan, Y.; Krüger, D.; et al. Synthesis, Characterization, and Application of Core-Shell Co_{0.16}Fe_{2.84}O₄NaYF₄(Yb, Er) and Fe₃O₄NaYF₄(Yb, Tm) Nanoparticle as Trimodal (MRI, PET/SPECT, and Optical) Imaging Agents. *Bioconjugate Chem.* **2016**, *27*, 319–328.
- (4) Aebischer, A.; Hostettler, M.; Hauser, J.; Krämer, K.; Weber, T.; Güdel, H. U.; Bürgi, H.-B. Structural and Spectroscopic Characterization of Active Sites in a Family of Light-Emitting Sodium

Lanthanide Tetrafluorides. *Angew. Chem., Int. Ed.* **2006**, *45*, 2802–2806.

(5) Zhou, B.; Shi, B.; Jin, D.; Liu, X. Controlling upconversion nanocrystals for emerging applications. *Nat. Nanotechnol.* **2015**, *10*, 924.

(6) Mai, H.-X.; Zhang, Y.-W.; Si, R.; Yan, Z.-G.; Sun, L.-d.; You, L.-P.; Yan, C.-H. High-Quality Sodium Rare-Earth Fluoride Nanocrystals: Controlled Synthesis and Optical Properties. *J. Am. Chem. Soc.* **2006**, *128*, 6426–6436.

(7) García-Flores, A. F.; Matias, J. S.; Garcia, D. J.; Martínez, E. D.; Cornaglia, P. S.; Lesseux, G. G.; Ribeiro, R. A.; Urbano, R. R.; Rettori, C. Crystal-field effects in Er³⁺- and Yb³⁺-doped hexagonal NaYF₄ nanoparticles. *Phys. Rev. B: Condens. Matter Mater. Phys.* **2017**, *96*, 165430.

(8) Hirsh, D. A.; Johnson, N. J. J.; van Veggel, F. C. J. M.; Schurko, R. W. Local Structure of Rare-Earth Fluorides in Bulk and Core/Shell Nanocrystalline Materials. *Chem. Mater.* **2015**, *27*, 6495–6507.

(9) Sobolev, B. P.; V. P. P., D. A. Mineev Low-temperature hexagonal modification of NaYF₄ having the gagarinite structure. *Dokl. Akad. Nauk SSSR* **1963**, *150*, 791–794.

(10) Roy, D. M.; Roy, R. Controlled Massively Defective Crystalline Solutions with the Fluorite Structure. *J. Electrochem. Soc.* **1964**, *111*, 421–429.

(11) Mathews, M.; Ambekar, B.; Tyagi, A.; Köhler, J. High temperature X-ray diffraction studies on sodium yttrium fluoride. *J. Alloys Compd.* **2004**, *377*, 162–166.

(12) Arnold, A. A.; Terskikh, V.; Li, Q. Y.; Naccache, R.; Marcotte, I.; Capobianco, J. A. Structure of NaYF₄ Upconverting Nanoparticles: A Multinuclear Solid-State NMR and DFT Computational Study. *J. Phys. Chem. C* **2013**, *117*, 25733–25741.

(13) Martin, M. N.; Newman, T.; Zhang, M.; Sun, L. D.; Yan, C. H.; Liu, G. Y.; Augustine, M. P. Using NMR Relaxometry to Probe Yb³⁺-Er³⁺ Interactions in Highly Doped Nanocrystalline NaYF₄ Nanoparticles. *J. Phys. Chem. C* **2019**, *123*, 10–16.

(14) Wang, F.; Deng, R.; Liu, X. Preparation of core-shell NaGdF₄ nanoparticles doped with luminescent lanthanide ions to be used as upconversion-based probes. *Nat. Protoc.* **2014**, *9*, 1634–1644.

(15) Liu, J.; Chen, G.; Hao, S.; Yang, C. Sub-6 nm monodisperse hexagonal core/shell NaGdF₄ nanocrystals with enhanced upconversion photoluminescence. *Nanoscale* **2017**, *9*, 91–98.

(16) Boyer, J.-C.; Cuccia, L. A.; Capobianco, J. A. Synthesis of Colloidal Upconverting NaYF₄: Er³⁺/Yb³⁺ and Tm³⁺/Yb³⁺ Monodisperse Nanocrystals. *Nano Lett.* **2007**, *7*, 847–852.

(17) Schneider, C. A.; Rasband, W. S.; Eliceiri, K. W. NIH Image to ImageJ: 25 years of image analysis. *Nat. Methods* **2012**, *9*, 671–675.

(18) Frydman, L.; Harwood, J. S. Isotropic Spectra of Half-Integer Quadrupolar Spins from Bidimensional Magic-Angle Spinning NMR. *J. Am. Chem. Soc.* **1995**, *117*, 5367–5368.

(19) Medek, A.; Harwood, J. S.; Frydman, L. Multiple-Quantum Magic-Angle Spinning NMR: A New Method for the Study of Quadrupolar Nuclei in Solids. *J. Am. Chem. Soc.* **1995**, *117*, 12779–12787.

(20) Brown, S. P.; Heyes, S. J.; Wimperis, S. Two-Dimensional MAS Multiple-Quantum NMR of Quadrupolar Nuclei. Removal of Inhomogeneous Second-Order Broadening. *J. Magn. Reson., Ser. A* **1996**, *119*, 280–284.

(21) Amoureux, J.-P.; Fernandez, C.; Steuernagel, S. ZFiltering in MQMAS NMR. *J. Magn. Reson., Ser. A* **1996**, *123*, 116–118.

(22) Koller, H.; Engelhardt, G.; Kentgens, A. P. M.; Sauer, J. 23Na NMR Spectroscopy of Solids: Interpretation of Quadrupole Interaction Parameters and Chemical Shifts. *J. Phys. Chem.* **1994**, *98*, 1544–1551.

(23) Massiot, D.; Fayon, F.; Capron, M.; King, I.; Le Calvé, S.; Alonso, B.; Durand, J.-O.; Bujoli, B.; Gan, Z.; Hoatson, G. Modelling one- and two-dimensional solid-state NMR spectra. *Magn. Reson. Chem.* **2002**, *40*, 70–76.

(24) Bennett, A. E.; Rienstra, C. M.; Auger, M.; Lakshmi, K. V.; Griffin, R. G. Heteronuclear decoupling in rotating solids. *J. Chem. Phys.* **1995**, *103*, 6951–6958.

- (25) Zheng, A.; Liu, S.-B.; Deng, F. 19F Chemical Shift of Crystalline Metal Fluorides: Theoretical Predictions Based on Periodic Structure Models. *J. Phys. Chem. C* **2009**, *113*, 15018–15023.
- (26) Hargreaves, J. S. J. Some considerations related to the use of the Scherrer equation in powder X-ray diffraction as applied to heterogeneous catalysts. *Catalysis, Structure & Reactivity* **2016**, *2*, 33–37.
- (27) See the supporting information at <http://dx.doi.org/address> for ²³Na NMR measurements at various MAS, estimates of spin–spin relaxation times, ²³Na σ_{CG} as a function of Larmor frequency, and deconvolution data of the ¹⁹F NMR spectra.
- (28) Kwak, H.-T.; Srinivasan, P.; Quine, J.; Massiot, D.; Gan, Z. Satellite transition rotational resonance of homonuclear quadrupolar spins: magic-angle effect on spin-echo decay and inversion recovery. *Chem. Phys. Lett.* **2003**, *376*, 75–82.
- (29) Makrinich, M.; Gupta, R.; Polenova, T.; Goldbourt, A. Saturation capability of short phase modulated pulses facilitates the measurement of longitudinal relaxation times of quadrupolar nuclei. *Solid State Nucl. Magn. Reson.* **2017**, *84*, 196–203.
- (30) Andrew, E. R.; Tunstall, D. P. Spin-Lattice Relaxation in Imperfect Cubic Crystals and in Non-cubic Crystals. *Proc. Phys. Soc., London* **1961**, *78*, 1.
- (31) Hubbard, P. S. Nonexponential Nuclear Magnetic Relaxation by Quadrupole Interactions. *J. Chem. Phys.* **1970**, *53*, 985–987.
- (32) Woessner, D.; Timken, H. The influence of MAS on spin-lattice relaxation curves and nuclear spin excitation of half-integer spin quadrupolar nuclei in solids. *J. Magn. Reson. (1969-1992)* **1990**, *90*, 411–419.
- (33) Mikushev, V. M.; Ulyashev, A. M.; Charnaya, E. V.; Chandoul, A. Controlled Massively Defective Crystalline Solutions with the Fluorite Structure. *Phys. Solid State* **2002**, *44*, 1044–1049.
- (34) Yesinowski, J. P. Finding the true spin–lattice relaxation time for half-integral nuclei with non-zero quadrupole couplings. *J. Magn. Reson.* **2015**, *252*, 135–144.
- (35) Suter, A.; Mali, M.; Roos, J.; Brinkmann, D. *J. Phys.: Condens. Matter* **1998**, *10*, 5977–5994.
- (36) Apperley, D. C.; Markwell, A. F.; Frantsuzov, I.; Illott, A. J.; Harris, R. K.; Hodgkinson, P. NMR characterisation of dynamics in solvates and desolvates of formoterol fumarate. *Phys. Chem. Chem. Phys.* **2013**, *15*, 6422–6430.
- (37) Gordon, M. I.; Hoch, M. J. R. Quadrupolar spin-lattice relaxation in solids. *J. Phys. C: Solid State Phys.* **1978**, *11*, 783–795.
- (38) Okubo, N.; Igarashi, M.; Yoshizaki, R. Relaxation of ²⁷Al NMR in Aluminium Tribromide due to Raman Process. *Z. Naturforsch., A: Phys. Sci.* **1996**, *51*, 277–282.
- (39) Igarashi, M.; Okubo, N.; Hashimoto, S.; Cha, D. J.; Yoshizaki, R. ²³Na Spin-Lattice Relaxation Measurements in Dehydrated Na-X Zeolite. *Z. Naturforsch., A: Phys. Sci.* **1996**, *51*, 657–661.
- (40) Yesinowski, J. P. Magnetization-recovery experiments for static and MAS-NMR of $I = 3/2$ nuclei. *J. Magn. Reson.* **2006**, *180*, 147–161.
- (41) Bonera, G.; Borsa, F.; Rigamonti, A. Nuclear Quadrupole Spin-Lattice Relaxation and Critical Dynamics of Ferroelectric Crystals. *Phys. Rev. B* **1970**, *2*, 2784–2795.
- (42) Jung, J.; Han, O.; Choh, S. Temperature dependence of ²³Na NMR quadrupole parameters and spin-lattice relaxation rate in NaNO₂ powder. *Solid State Commun.* **1999**, *110*, 547–552.
- (43) Weber, M. Nuclear quadrupole spin-lattice relaxation in solids. *J. Phys. Chem. Solids* **1961**, *17*, 267–277.
- (44) Haase, J.; Pfeifer, H.; Oehme, W.; Klinowski, J. Longitudinal NMR relaxation of ²⁷Al nuclei in zeolites. *Chem. Phys. Lett.* **1988**, *150*, 189–193.
- (45) Haase, J.; Park, K. D.; Guo, K.; Timken, H. K. C.; Oldfield, E. Nuclear magnetic resonance spectroscopic study of spin-lattice relaxation of quadrupolar nuclei in zeolites. *J. Phys. Chem.* **1991**, *95*, 6996–7002.
- (46) Zhou, J.; Wen, S.; Liao, J.; Clarke, C.; Tawfik, S. A.; Ren, W.; Mi, C.; Wang, F.; Jin, D. Activation of the surface dark-layer to enhance upconversion in a thermal field. *Nat. Photonics* **2018**, *12*, 154–158.
- (47) Massiot, D.; Touzo, B.; Trumeau, D.; Coutures, J.; Virlet, J.; Florian, P.; Grandinetti, P. Two-dimensional magic-angle spinning isotropic reconstruction sequences for quadrupolar nuclei. *Solid State Nucl. Magn. Reson.* **1996**, *6*, 73–83.
- (48) Amoureux, J.-P.; Huguenard, C.; Engelke, F.; Taulelle, F. Unified representation of MQMAS and STMAS NMR of half-integer quadrupolar nuclei. *Chem. Phys. Lett.* **2002**, *356*, 497–504.
- (49) Slichter, C. P. *Principles of Magnetic Resonance*, 3rd ed.; Springer-Verlag: Berlin, 1990; Chapter 10, p x.
- (50) Ashbrook, S. E.; Duer, M. J. Structural information from quadrupolar nuclei in solid state NMR. *Concepts Magn. Reson., Part A* **2006**, *28A*, 183–248.
- (51) Oshima, C.; Aizawa, T.; Souda, R.; Ishizawa, Y. Microscopic surface phonons of MgO(1 0 0) surface. *Solid State Commun.* **1990**, *73*, 731–734.
- (52) Lagos, M. J.; Trügler, A.; Hohenester, U.; Batson, P. E. Mapping vibrational surface and bulk modes in a single nanocube. *Nature* **2017**, *543*, 529–532.
- (53) Tien, C.; Charnaya, E. V.; Lee, M. K.; Baryshnikov, S. V.; Sun, S. Y.; Michel, D.; Böhlmann, W. Coexistence of melted and ferroelectric states in sodium nitrite within mesoporous sieves. *Phys. Rev. B: Condens. Matter Mater. Phys.* **2005**, *72*, 104105.
- (54) Baryshnikov, S. V.; Tien, C.; Charnaya, E. V.; Lee, M. K.; Michel, D.; Böhlmann, W.; Stukova, E. V. Dielectric Properties of Mesoporous Sieves Filled with NaNO₂. *Ferroelectrics* **2008**, *363*, 177–186.
- (55) Thayer, A. M.; Steigerwald, M. L.; Duncan, T. M.; Douglass, D. C. NMR Study of Semiconductor Molecular Clusters. *Phys. Rev. Lett.* **1988**, *60*, 2673–2676.
- (56) Lianos, P.; Thomas, J. Cadmium sulfide of small dimensions produced in inverted micelles. *Chem. Phys. Lett.* **1986**, *125*, 299–302.
- (57) Kortan, A. R.; Hull, R.; Opila, R. L.; Bawendi, M. G.; Steigerwald, M. L.; Carroll, P. J.; Brus, L. E. Nucleation and Growth of CdSe on ZnS Quantum Crystallite Seeds, and Vice Versa, in Inverse Micelle Media. *J. Am. Chem. Soc.* **1990**, *112*, 1327–1332.
- (58) Lo, A. Y. H.; Sudarsan, V.; Sivakumar, S.; van Veggel, F.; Schurko, R. W. Multinuclear Solid-State NMR Spectroscopy of Doped Lanthanum Fluoride Nanoparticles. *J. Am. Chem. Soc.* **2007**, *129*, 4687–4700.
- (59) Bessada, C.; Rakhmatullin, A.; Rollet, A.-L.; Zanghi, D. High temperature NMR approach of mixtures of rare earth and alkali fluorides: An insight into the local structure. *J. Fluorine Chem.* **2009**, *130*, 45–52.
- (60) Wang, F.; Grey, C. P. Probing the Mechanism of Fluoride-Ion Conduction in LaF₃ and Strontium-Doped LaF₃ with High-Resolution 19F MAS NMR. *Chem. Mater.* **1997**, *9*, 1068–1070.
- (61) Ramana Reddy, M. V.; Narasimha Reddy, K. Characterization and electrical behaviour of NaYF₄ thin films. *physica status solidi (a)* **1986**, *95*, K193–K197.
- (62) Shareefuddin, M.; Jamal, M.; Chary, M. N. Solid state battery with pure and doped sodium yttrium fluoride as the solid electrolyte. *J. Phys. D: Appl. Phys.* **1995**, *28*, 440–442.
- (63) Patro, L.; Hariharan, K. Fast fluoride ion conducting materials in solid state ionics: An overview. *Solid State Ionics* **2013**, *239*, 41–49.

I.1 Rare-earth doping

Another potential interest of the NaYF_4 particles is the substitution of the rare-earth Y by other rare-earth elements and how this could be related to the upconversion process. In other words, it is possible to investigate whether there is a relation between RE CEF and the upconversion phenomena on these particles.

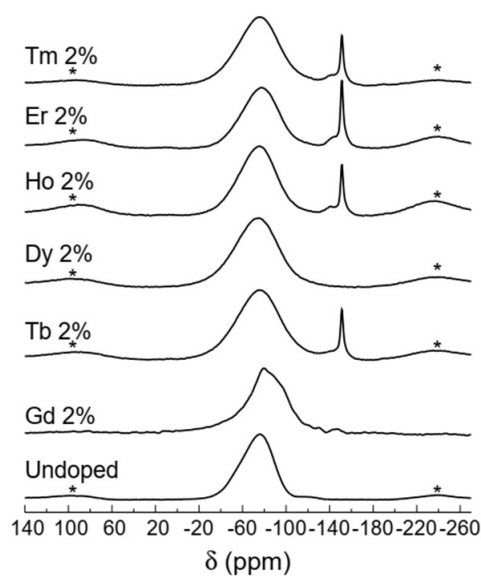


Figure I.1: ^{19}F MAS spectra for 7 nm rare-earth doped NaYF_4 at rotating frequency of 15 kHz. The asterisks are spinning sidebands and the sharp resonance line near -140 ppm is from residual NaF on the NPs surface, which can be eliminated by washing the NPs.

Following the room temperature relaxation time study of the $\alpha\text{-NaYF}_4$, the very same kind of experiments were performed with 2% nominal doping of Gd, Td, Dy, Ho, Er and Tm. Experiments of magnetic susceptibility as a function of time on such samples have shown that the real RE concentration inside the NPs is quite near the nominal values, with a maximum dispersion of 0.2% in the Dy case. Also, preliminary X-Ray and TEM points towards a sample size of 7(1) nm with very small dispersion.

The MAS-NMR experiments have been performed once again in collaboration with Prof. Thiago Branquinho from UFABC, and similar systematic have been employed with some punctual differences: In the inversion recovery measurements, the undoped particles require a higher time saturation pulse length ($13\ \mu\text{s}$), while doped ones need smaller times ($2.5\ \mu\text{s}$). For spin-spin relaxation times (T_2), spin-echo sequences with variable time between pulses have been employed. Also, experiments at ^{19}F site have been performed by Professor Branquinho in an Agilent DD2 spectrometer with ^{19}F resonating at 228.04 MHz.

Fig. I.1 depicts the spectra of the RE doped samples. The

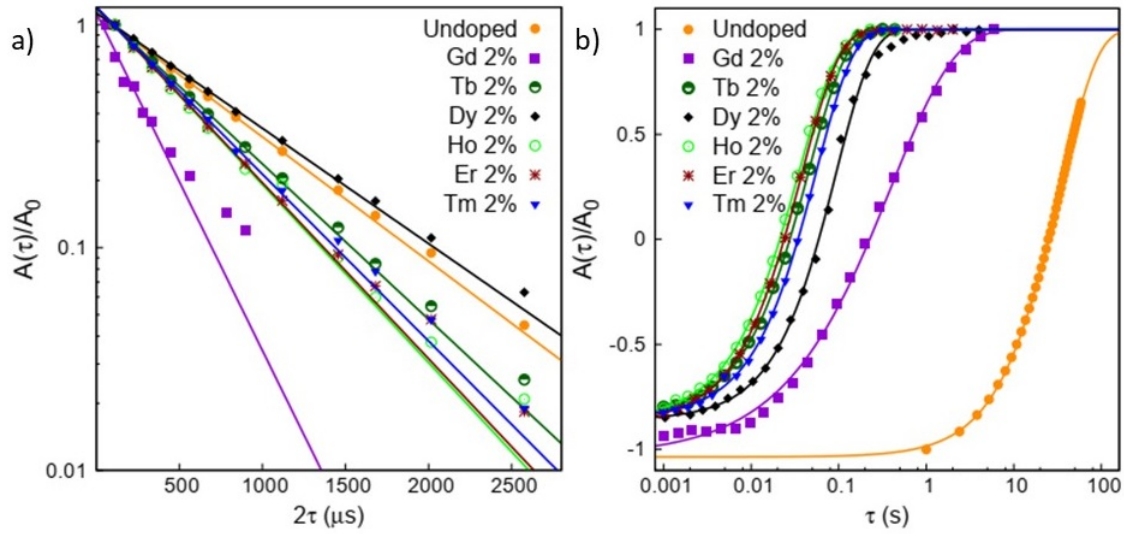


Figure I.2: *a)* In-plane relative magnetization for ^{19}F as a function of time for RE doped NaYF_4 for a series of RE. The fitting to obtaining the spin-spin relaxation times are shown. *b)* Out of plane relative magnetization for ^{19}F as a function of time for RE doped NaYF_4 . The fitting to obtaining the spin-lattice relaxation times are shown.

asterisks represent the spinning sidebands and the thin line at -150 ppm stands for the residual contaminant NaF , which can be removed by washing the NPs with water, as pointed out before. The observable result is expected:

The increased linewidth on the RE doped samples, which happens because of the insertion of dilute magnetic moments, which tends to reduce the spin-spin relaxation times, increasing the linewidth.

However, when the relaxation times (both spin-spin and spin-lattice) were measured, a change of two orders of magnitude have been observed between undoped and RE doped particles. The values obtained are presented in Table I.1. The results are summarized in Fig. I.2. Panel *a* and *b* stands for the ^{19}F xy and z magnetization ratio as a function of time, from which the relaxation times were fitted.

While T_2 values do not present an expressive discrepancy, changing from $778 \mu\text{s}$ to approximately $500 \mu\text{s}$, the T_1 values change from 45 seconds to approximately 40 ms at the sodium site. A change of nearly three orders of magnitude. The variance is more or less the same for the fluorine site, as

Table I.1: Spin-lattice and spin-spin relaxation times for RE doped nanoparticles, for both ^{19}F and ^{23}Na sites.

heightDoping	Y	Gd	Tb	Dy	Ho	Er	Tm
$T_1(^{23}\text{Na})$ (s)	45.2(5)	0.4(1)	0.045(1)	0.08(5)	0.039(7)	0.037(9)	0.057(4)
$T_1(^{19}\text{F})$ (s)	35.5(1)	0.40(1)	0.045(1)	0.094(2)	0.035(1)	0.038(1)	0.055(1)
$T_2(^{23}\text{Na})$ (ms)	0.75(1)	0.12(5)	0.27(5)	0.09(2)	0.25(4)	0.26(3)	0.27(2)
$T_2(^{19}\text{F})$ (ms)	0.78(1)	0.29(3)	0.62(1)	0.84(1)	0.54(1)	0.55(1)	0.58(1)

can be noted from the values in Table I.1.

A fundamental aspect to be observed however, lies in the spectra of doped NPs. While for pure samples a couple of lines are observed as pointed out in the previous section, such distinction is not possible in doped ones, since the line broadening overcomes each other line, leading to an inconclusive scenario in which distinction cannot be done. So, we are treating here an average relaxation time, which has both bulk and surface components. One must remember, however, that higher relaxation times are dominated by bulk component, so that bulk relaxation is being considered in this discussion.

Comparing the value between different rare-earths, an expressive change in the relaxation rates is not observed among the considered ones, except to of Gd and Dy. On the latter, there could be a spurious effect due to an underdoping, since a concentration of 1.8% of Dy was observed, instead of 2%. However for the Gd case, there are no arguments to confront the data so far and there are indicatives that, in fact, there is something special around this RE. The results are still under discussion since this part of the work is in progress but the initial interpretation is that the Gd effective spin state ($S = \frac{7}{2}$) is being affected by the hyperfine coupling between the RE electrons with the nuclei of F and Na, leading to severe changes in the relaxation rates.

Appendix J

Scientific Work on SmB_6

This appendix brings the paper published on SmB_6 , performed as a collaboration with our group, as described in the main text.

Metallic islands in the Kondo insulator SmB_6

J. C. Souza^{1,2,*}, P. F. S. Rosa³, J. Sichelschmidt², M. Carlone⁴, P. A. Venegas⁵, M. O. Malcolms⁶, P. M. Menegasso¹, R. R. Urbano¹, Z. Fisk⁶, and P. G. Pagliuso¹

¹Instituto de Física “Gleb Wataghin,” UNICAMP, 13083-859, Campinas, São Paulo, Brazil

²Max Planck Institute for Chemical Physics of Solids, D-01187 Dresden, Germany

³Los Alamos National Laboratory, Los Alamos, New Mexico 87545, USA

⁴POSMAT, Faculdade de Ciências, UNESP, C.P. 473, 17033-360, Bauru, São Paulo, Brazil

⁵Departamento de Física, Faculdade de Ciências, UNESP, C.P. 473, 17033-360, Bauru, São Paulo, Brazil

⁶Department of Physics and Astronomy, University of California, Irvine, California 92697, USA



(Received 2 June 2020; accepted 7 October 2020; published 3 November 2020)

The predicted interplay between Kondo physics and nontrivial topology in SmB_6 has stimulated many experimental reports, some of which are in apparent contradiction. The origin of the dispute may lie in the fragility of the Kondo insulating phase in the presence of Sm vacancies (Kondo holes) and/or natural impurities, such as Gd^{3+} . In this work, we locally investigate this fragility for Al flux grown $\text{Sm}_{1-x}\text{Gd}_x\text{B}_6$ single crystals ($0 \leq x \leq 0.02$) by combining electron spin resonance (ESR) and complementary bulk measurements. The Gd^{3+} ESR spectra in a highly dilute regime ($x \sim 0.0004$) display the features of an insulating cubic environment. Remarkably, a metallic ESR line shape is observed for more concentrated samples ($x \geq 0.004$), even though these systems are still in a reasonably dilute regime and show insulating dc electrical resistivity. Our data indicate that the Kondo insulating state is destroyed locally around impurities before a global percolation occurs. This result not only explains the discrepancy between dc and ac conductivity but also provides a scenario to explain the presence of quantum oscillations in magnetization in the absence of quantum oscillations in electrical resistivity.

DOI: [10.1103/PhysRevResearch.2.043181](https://doi.org/10.1103/PhysRevResearch.2.043181)

I. INTRODUCTION

The Kondo insulator SmB_6 has attracted a lot of interest for almost half a century due to numerous puzzling properties such as the physics of the hybridization gap, the mixed-valence ground state, nonzero specific heat at low temperatures, the crystalline electrical field ground state, and the saturation in the resistivity under $T \approx 4$ K [1]. The interest was renewed following the prediction that SmB_6 is a topological Kondo insulator (TKI) [2,3]. Many experimental results support a TKI phase [4–10], but this classification remains a matter of contention [11]. Conflicting experimental results for SmB_6 further complicate classification schemes.

For instance, quantum oscillations in magnetization are observed in floating-zone grown samples, whereas they are absent in aluminum flux grown ones [12–14]. Electrical conductivity measurements also appear to be conflicting. A bulk-activated insulating behavior is obtained in dc electrical resistance measurements [15], while ac conductivity measurements show localized states with conductivities orders of magnitude higher than the dc measurements [16–18].

These discrepancies naturally invite a discussion regarding the role of impurities and defects in SmB_6 . Raman spectroscopy measurements explored the effect of Sm vacancies and argued for a breakdown of the Kondo insulating phase for small numbers of Sm vacancies [19,20]. However, Corbino disk dc resistance measurements have shown that Sm vacancies do not affect the thermally activated bulk behavior of flux-grown SmB_6 , indicating that the bulk may be immune to disorder in the dc limit [15]. The effect of Sm vacancies acting as “Kondo holes” [21], i.e., an isolated nonmagnetic impurity in a Kondo lattice [22–25], also has consequences for the formation of a possible TKI phase [19]. On the one hand, low-energy spin excitons could destroy the protection of the gapless surface states [26]. On the other hand, Kondo holes are argued to enable quasiparticle interference patterns that reveal the heavy surface states in recent scanning tunneling spectroscopy (STS) measurements [27]. Furthermore, STS results showed that Gd^{3+} impurities in SmB_6 destroy the surface states locally, and the effect percolates for $x \geq 0.03$ [28].

An outstanding question is whether magnetic impurities such as Gd^{3+} , which is a natural impurity in Sm, could also display effects similar to the Sm vacancies on the hybridization gap of SmB_6 . In order to properly address this question, the use of a microscopic technique that locally probes the effects of Gd^{3+} in SmB_6 is highly desirable. Recent experimental results by Fuhrman *et al.* were explained assuming the possibility of a dynamic screening of localized Gd^{3+} moments, which is unexpected due to the $\text{Gd}^{3+} 4f^7$ electronic

*jcsouza@ifi.unicamp.br

Published by the American Physical Society under the terms of the [Creative Commons Attribution 4.0 International](https://creativecommons.org/licenses/by/4.0/) license. Further distribution of this work must maintain attribution to the author(s) and the published article’s title, journal citation, and DOI.

configuration, which carries no orbital moment and is particularly stable [29,30].

The Gd^{3+} spin is a standard probe in electron spin resonance (ESR) experiments; however, to the best of our knowledge, there is no report of ESR in highly dilute samples ($x \leq 0.0004$), except the observation by Wiese *et al.* [31] of an anomalous spectrum of Gd^{2+} for concentrations down to 200 parts per million. This spectrum most likely originates from the resonance of a Gd^{2+} ion within an oxide impurity phase on the crystal surface [32]. Other reports are not reproducible [33,34], which begs for a revisited experimental investigation.

Here we present ESR and complementary macroscopic measurements of high-quality flux-grown $\text{Sm}_{1-x}\text{Gd}_x\text{B}_6$ single crystals with nominal concentrations $x = 0, 0.0004, 0.004,$ and 0.02 . From magnetic susceptibility data and using the ESR-determined actual Gd^{3+} concentrations, we extracted a Gd^{3+} magnetic moment that is close to the theoretically expected value. In the highly dilute regime ($x = 0.0004$) at $T = 4$ K, the Gd^{3+} ESR shows seven symmetrical Lorentzian lines typical of a cubic insulating environment. Increasing the Gd^{3+} concentration to $x = 0.004$, a single asymmetrical line shape appears, which is characteristic of metallic samples for which the microwave skin depth is smaller than the sample size [35–37]. These results suggest that Gd^{3+} ions could close the hybridization gap locally, while the resultant metallic islands do not affect the global hybridization gap in this concentration range.

II. METHODS

Single-crystalline samples of $\text{Sm}_{1-x}\text{Gd}_x\text{B}_6$ were synthesized by the Al flux grown technique as described elsewhere [15]. The samples had a typical size of ~ 700 μm wide, 300 μm high, and 120 μm thick. Magnetic susceptibility measurements were carried out in superconducting quantum interference device (SQUID) and SQUID vibrating-sample magnetometers. Specific heat measurements were performed in a commercial small-mass calorimeter system. Electrical resistivity was measured using a standard four-point technique with a dc bridge. ESR measurements were performed on single crystals in an X-band ($\nu \cong 9.4$ GHz) spectrometer equipped with a goniometer and a He flow cryostat in the temperature range of $2.6 \leq T \leq 40$ K at very low power of $P = 0.21$ mW. In order to calibrate the ESR intensity in our spectrometer to estimate the actual Gd^{3+} concentrations, we used a standard weak-pitch sample with 0.79×10^{14} spins/ cm^3 and a g value $g_{\text{ref}} = 2.002(1)$. The samples were etched before the ESR measurements in a mixture of hydrochloric and nitric acids in a proportion of 3:1 to remove any possible impurities on the surface of the crystals due to Al flux. We did not polish any crystals in this study. The mass of the studied samples ranged from 0.3 to 4 mg. We performed our experiments on 20 different crystals from five different batches and found no sample dependence. The concentration x used below refers to the nominal concentration value.

III. RESULTS AND DISCUSSION

Figure 1 summarizes the bulk macroscopic properties of $\text{Sm}_{1-x}\text{Gd}_x\text{B}_6$ with $x = 0.0004, 0.004,$ and 0.02 . The top panel

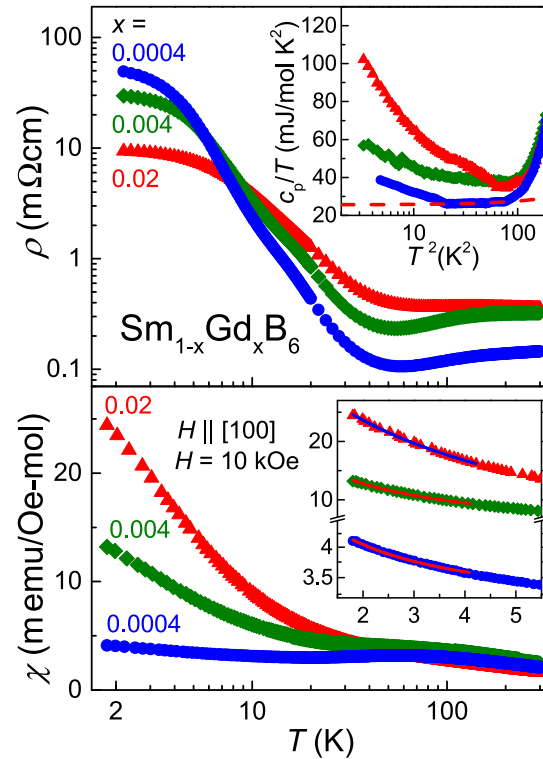


FIG. 1. Temperature dependences of dc electrical resistivity ρ , specific heat c_p , and dc magnetic susceptibility χ for $\text{Sm}_{1-x}\text{Gd}_x\text{B}_6$ with x as indicated. For χ , the magnetic field $H = 10$ kOe is applied parallel to the [100] direction. The lower inset shows χ at low temperatures. For χ , the solid lines are the best fits obtained considering a Curie-Weiss plus a Pauli T -independent term. For c_p the red dashed line shows, for $x = 0.0004$, how we estimated the γ value.

of Fig. 1 shows the resistivity as a function of temperature. At low temperatures, the three concentrations show a saturation in the resistivity, consistent with the undoped compound [5,6]. This is expected because the saturation disappears only for Gd^{3+} concentrations of $x \geq 0.03$ [5,28]. Using the value of the resistivity at 4 K, we estimate the skin depth in a first approximation of the investigated samples to be $\delta_D = \sqrt{\rho/\pi f \mu} \approx 90, 80,$ and 50 μm for $x = 0.0004, 0.004,$ and 0.02 , respectively. These estimated values should be taken with extreme care as recent magnetotransport measurements have shown that sub-surface cracks create additional conduction channels in SmB_6 , which affects the maximum resistivity value obtained [38]. A more dedicated investigation would be appropriate to compare resistivity values of our results with undoped samples. Consequently, we are probably underestimating the skin depth, which may be even larger than the sample size (≈ 350 μm). Finally, it is important to notice that all samples show a similar gap in the resistivity, which agrees with previous Corbino disk measurements and the effects of Sm vacancies on the resistivity of SmB_6 [15].

The low-temperature specific heat c_p is shown as a function of T^2 in the inset in the top panel of Fig. 1. By extrapolating the high- T c_p data towards $T \rightarrow 0$ K, we estimate the Sommerfeld coefficients $\gamma \sim 20, 30,$ and 35 mJ/mol K^2 for $x = 0.0004, 0.004,$ and 0.02 , respectively. The red dashed

line exemplifies the extrapolation for $x = 0.0004$. These values should be taken with care, especially comparing samples with different Gd^{3+} concentrations. It has been reported that undoped samples can show very distinct γ values [14] and disorder could play a role in the Sommerfeld coefficient [39]. More importantly, the low-temperature increase of c_p is related to a Kondo-impurity-like behavior, which is similar to previous reports for $\text{Sm}_{1-x}\text{La}_x\text{B}_6$, $\text{Sm}_{1-x}\text{B}_6$, and $\text{Sm}_{1-x}\text{Gd}_x\text{B}_6$ [29,40]. Although this increase has been attributed to a local screening of the Gd^{3+} ions [29], the local destruction of the Kondo lattice by a nonscreened ion, which is a Kondo hole effect, also provides a reasonable explanation for this increase [41]. We should note that it appears to be additional entropy into the system when we compare $\text{Sm}_{1-x}\text{La}_x\text{B}_6$ and $\text{Sm}_{1-x}\text{Gd}_x\text{B}_6$, which was reported before [29,40]. This additional entropy, for example, might arise from antiferromagnetic (AFM) exchange field fluctuations and/or a possible Gd^{3+} interaction with local conduction electrons at ultralow T (approximately millikelvins).

The magnetic susceptibility as a function of temperature is shown in the bottom panel of Fig. 1. A clear x -dependent Curie-Weiss-like behavior is observed at low temperatures, whereas at higher temperatures the behavior of the magnetic susceptibility data is consistent with undoped SmB_6 [42,43]. Above $T \approx 5$ K the data start to deviate from the Curie-like behavior, which means that the Gd^{3+} contribution is not the most dominant one. We have used the low-temperature region, $T \leq 4$ K, to isolate the contribution from the Gd^{3+} ions themselves, as shown in the inset in the bottom panel of Fig. 1.

In order to extract the magnetic moment of Gd^{3+} and compare it to the expected values, we have used the measured concentration x_{meas} of our samples using ESR. In an ESR experiment we can estimate the number of resonant spins N_{spins} , comparing the ESR intensity I with a well-known reference. The relationship between the sample A ESR intensity and the B reference can be written as [44]

$$\frac{I_A}{I_B} = \frac{N_{\text{spins}}^A}{N_{\text{spins}}^B} \left(\frac{g_A}{g_B} \right)^2 \left[\frac{S_A(S_A + 1)}{S_B(S_B + 1)} \right] \left(\frac{T_B}{T_A} \right), \quad (1)$$

where g is the g value, S is the spin moment, and T is the temperature. The ESR intensity I is obtained by double integrating our Gd^{3+} ESR spectrum. The g value is a parameter extracted from the Gd^{3+} ESR resonance field, which is obtained by fitting our Gd^{3+} ESR spectrum using an admixture of absorption and dispersive derivatives. We will discuss the Gd^{3+} ESR g value in more detail below. Figure 2 shows the Gd^{3+} ESR spectra for $\text{Sm}_{1-x}\text{Gd}_x\text{B}_6$ with $x = 0$ and 0.0004 at 4 K. The Gd^{3+} ESR spectrum for $x = 0.0004$ is resolved; that is, it contains seven distinct Lorentzian line shapes. This spectrum is the resonance of the Gd^{3+} fine structure ($S = 7/2$, selection rule $\Delta m = \pm 1$) and is characteristic of an insulating environment having a skin depth larger than the sample size. The red solid line is a simulation considering a cubic crystal field spin Hamiltonian with a crystal field parameter (CFP) $b_4 = -9.5(3)$ Oe [37]. Even though the γ values obtained are not the smallest reported in the literature for SmB_6 samples, they do not affect our results. The insulating Gd^{3+} ESR line shape reinforces the clear insulating bulk environment

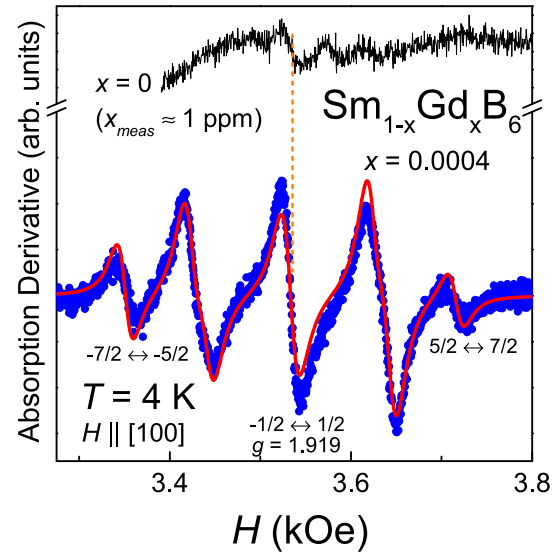


FIG. 2. X-band Gd^{3+} ESR spectra for $\text{Sm}_{1-x}\text{Gd}_x\text{B}_6$ single crystals with $x = 0$ and 0.0004 . The field H is applied parallel to the [100] direction. The dashed line shows the g value of the $-1/2 \leftrightarrow 1/2$ resonance. The red solid line is a simulation assuming a cubic insulator spin Hamiltonian with a CFP $b_4 = -9.5(3)$ Oe [37].

in our samples. For the undoped compound we were able to observe a resonance with a very similar g value compared with $x = 0.0004$, as shown by the orange dotted line in Fig. 2. This is an indication that this resonance could, most likely, be coming from Gd^{3+} or Eu^{2+} natural impurities in the undoped compound. Using Eq. (1), the measured concentration x_{meas} estimated was ≈ 1 part per million, which is extremely low and shows the good quality of the undoped single crystals. We also did not observe an ESR signal from disordered Sm^{3+} as reported by previous studies [45,46].

For the Gd^{3+} -doped compound ESR spectra, as shown in Fig. 2, using Eq. (1), we were able to estimate the actual concentrations of Gd^{3+} based on N_{spins} : $x_{\text{meas}} = 0.00034(1)$, $0.0039(1)$, and $0.0189(1)$. Using these values, we fit the χ data for different concentrations with a Curie-Weiss law plus a Pauli T -independent term in the range of $2 \leq T \leq 4$ K (see the inset in the bottom panel of Fig. 1). The obtained magnetic moments are $\mu_{\text{Gd}} = 8.0(1)\mu_B/\text{Gd}$, $8.2(1)\mu_B/\text{Gd}$, and $7.94(2)\mu_B/\text{Gd}$ for $x = 0.0004$, 0.004 , and 0.02 , respectively. Thus, the full theoretically expected moments for Gd^{3+} are observed.

Our Gd^{3+} ESR spectra as displayed in Fig. 2 do not support the scenario of a Gd^{3+} dynamic screening. The ESR should be observable only for temperatures above the single-impurity Kondo regime ($T \gg T_K$), for which the Gd^{3+} local moment is well defined [47]. Furthermore, we do not observe the ESR spin dynamics expected for a single-impurity Kondo ion [47] or for a Kondo ion lattice [48,49]. Therefore, these results do not corroborate the scenario of dynamic Gd^{3+} screening proposed by Fuhrman *et al.* [29].

Besides supplying information on spin dynamics, the Gd^{3+} ESR linewidth ΔH also provides information on disorder and sample quality. For $x = 0.0004$, the Gd^{3+} resonance of the central line at $T = 4$ K, which corresponds to the $-1/2 \leftrightarrow 1/2$ transition, has a linewidth $\Delta H = 17(2)$ Oe. When the fine

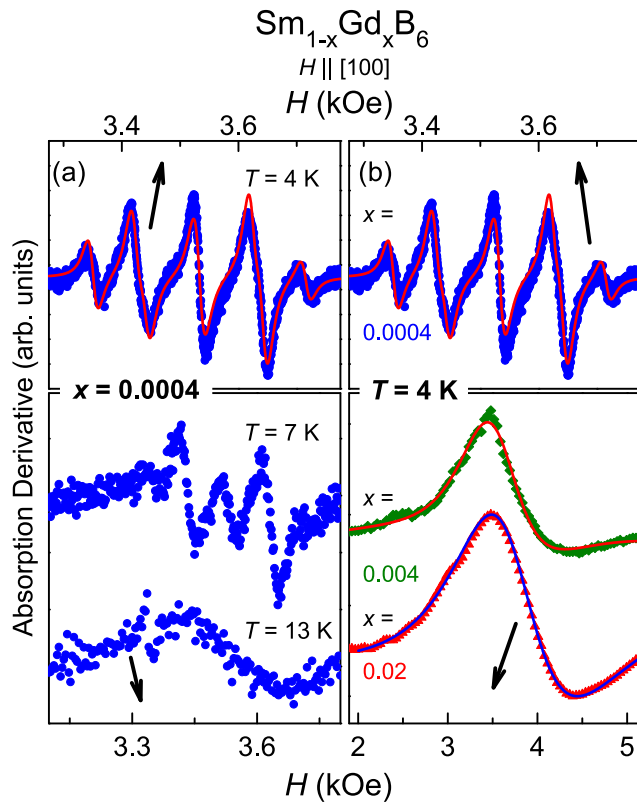


FIG. 3. Gd^{3+} X-band ESR spectra (a) T and (b) x dependences for $\text{Sm}_{1-x}\text{Gd}_x\text{B}_6$, with x indicated in the panels. The field H is applied parallel to the $[100]$ direction. The solid lines are the best fit obtained to the spectra using an admixture of absorption and dispersion derivatives for $x = 0.004$ and 0.02 [37]. For $x = 0.0004$ the same fit as in Fig. 2 is shown.

structure is collapsed into one resonance by varying the angle with respect to the applied magnetic field H [37,44], we obtain $\Delta H = 19(2)$ Oe [Fig. S2(a)]. This is consistent with samples known as good insulators [50]. Further, the Gd^{3+} linewidth at $T = 4$ K has a similar value when compared with previous results for Er^{3+} -doped SmB_6 [42,51].

Figure 3(a) shows the Gd^{3+} ESR line shape evolution as a function of temperature for $\text{Sm}_{1-x}\text{Gd}_x\text{B}_6$ for $x = 0.0004$. As temperature increases, the seven lines merge into one line, which is a narrowing due to the interaction of the Gd^{3+} $4f$ local moments and the conduction electrons, known as exchange narrowing [37,44,52]. However, as has already been shown for Kondo insulators [53,54], it is necessary to take into account the influence of the valence fluctuation of $\text{Sm}^{2.6+}$ at the Gd^{3+} site to fully describe the narrowing effect.

The most intriguing change in the line shape occurs when, at constant temperature, the Gd^{3+} concentration is increased from $x = 0.0004$ to 0.004 and 0.02 . As shown in Fig. 3(b), the Gd^{3+} ESR spectra at $T = 4$ K for $x = 0.004$ and 0.02 display a single asymmetrical Lorentzian line shape, also known as Dysonian line shape [35–37], with no Gd^{3+} fine structure. This line shape is characteristic of a metallic environment, where the skin depth is much smaller than the thickness of the sample. At the same temperature, the $x = 0.0004$ sample still displays the seven distinct Lorentzian line shapes expected for

an insulator. Therefore, the local environment surrounding the Gd^{3+} ions is changing as a function of the Gd^{3+} concentration. At the same time this is not indicated in resistivity data, where the thermally activated bulk behavior still remains. As shown in the top panel of Fig. 1, both the T dependence of the resistivity data and skin depth are very similar for all concentrations, especially when we compare $x = 0.0004$ and 0.004 , showing a similar indirect gap without any apparent change in the insulating ground state.

The remarkable change in the local Gd^{3+} environment happens between $x = 0.0004$ and 0.004 . In order to understand the origin of such evolution, it is useful to compare it with nonmagnetic insulator Gd^{3+} - and Eu^{2+} -doped CaB_6 [55–57], where the Kondo effect does not play a role.

In CaB_6 , the local insulator-to-metal evolution as a function of Gd^{3+} was interpreted as the introduction of an extra electron to the system, with Gd^{3+} ions acting as electron donors and creating a hydrogenlike bound state within the gap. The bound states overlap and form a percolative network; that is, there is a change in the ground state of the system. In that case, for higher Gd^{3+} concentrations ($0.003 \leq x \leq 0.01$), the ESR results were always consistent with the metallic resistivity data [55]. This is in contrast to the situation for Gd^{3+} -doped SmB_6 , as stated above. The introduction of Eu^{2+} in CaB_6 gives rise to a localized split-off bound state, with the Fermi energy lying in the gap of the semiconductor. This impurity state percolates only with $x \geq 0.3$, when the ground state becomes a ferromagnetic metal; however, it is possible to observe an Eu^{2+} Dysonian line shape for $x \geq 0.15$ [56,57].

SmB_6 is not expected to host a hydrogenlike doping mechanism [58]. Furthermore, the nonparabolic band structure of SmB_6 leads to a significant increase of the calculated density of impurities required for percolation [59]. Hence, the origin of the insulator-to-metal evolution in SmB_6 should differ from that in CaB_6 . Our results agree with these two propositions. If the origin of the metallic islands and consequent evolution were due to a Gd^{3+} -induced hydrogenlike in-gap bound state, we should expect an evolution from insulating to metallic resistivity, i.e., a change in the ground state of the compound, or a striking change in the hybridization gap value, which is not observed.

Remarkably, the insulator-to-metal evolution is also noticed in the ESR response of $\text{Sm}_{1-y}\text{Eu}_y\text{B}_6$ samples. The Eu^{2+} ESR spectrum of $y = 0.0004$ shows a cubic insulator environment, with a well-defined Eu^{2+} hyperfine structure and a CFP $b_4 \approx -50$ Oe [43]. For higher concentrations, e.g., $y = 0.01$, the Eu^{2+} fine structure collapses, and we obtain a Dysonian line shape. Previous reports have shown that a metallic antiferromagnetic ground state for $\text{Sm}_{1-y}\text{Eu}_y\text{B}_6$ appears only at or above $y = 0.4$, at least one order of magnitude higher than what it is observed by electron spin resonance [60]. The Gd^{3+} - and Eu^{2+} -doped SmB_6 results suggest that there is not a percolation in the system, but a local effect which does not affect the global hybridization gap.

One alternative scenario is that the Gd^{3+} ions are not screened by conduction electrons, although they occupy a Sm site. Instead of screening, these substitutions locally close the hybridization gap at the Gd^{3+} site, increasing the local density of states and/or the local number of carriers. As already stated, this Kondo hole effect of Gd^{3+} is consistent with the

low- T magnetic susceptibility and specific heat measurements shown in Fig. 1, as well with the scaling proposed by Fuhrman *et al.* [29]. Such an effect could have two different local manifestations: the first one, which is more unlikely due to the small amount of Gd^{3+} , resides in the possibility of local in-gap impurity states [17,18].

The natural scenario we propose is related to the formation of a bound state at the Gd^{3+} site. This state should affect locally the hybridization gap around the Gd^{3+} ions due to translational symmetry breaking. In other words, this substitution should create a spatial oscillation of the hybridization gap near the impurity [24]. In the highly diluted case, such metallic islands are small and separated, in the sense that the Gd^{3+} spins have a spin relaxation mechanism mediated by phonons. Hence, we obtain a Gd^{3+} ESR spectrum as expected for a cubic insulating environment. Based on previous theoretical reports [24], we propose that when there is quantum interference between such metallic islands, due to the increase of Gd^{3+} concentration, effectively, the islands grow in size and, as a consequence, the carriers will have mobility to enable metallic properties in the ESR line shape and ESR line parameters, which will lead to a local effect and will not reflect in the global properties of the system, such as dc resistivity. Naturally, a percolation should occur at higher concentrations. While for Gd^{3+} -doped SmB_6 we know that samples with $x = 0.05$ still present an insulating behavior [29], La^{3+} -doped samples will show a metallic-insulating transition at $x \sim 0.3$ [40]. Eu^{2+} -doped samples have a metallic-insulating transition at $x \sim 0.4$ [60].

Despite the local change in the environment, a more systematic in-depth theoretical investigation might need to introduce inhomogeneous effects, which may arise due to Gd^{3+} ions in different magnetic states [44]. Such effects may distort the ESR line shape asymmetry and linewidth. Although inhomogeneous effects should, in principle, play a role in fully describing the Gd^{3+} ESR spectrum evolution, the possibility of new mechanisms should be a motivation for further theoretical works.

The intriguing question arising from the Kondo holes physics is related to the effects of metallic islands in a TKI. Would the metallic islands have a nontrivial topology? From an ESR viewpoint, the fingerprint of a nontrivial topological state could be related to the appearance of an ESR diffusivelike line shape for the signal of the ESR local moment probe [61]. However, one of the main ingredients for such an unusual effect is a phonon-bottleneck regime, which is not present in these studied Gd^{3+} concentrations. Therefore, we cannot extract any information about the topology of the system from an ESR perspective for the studied samples. Further experiments exploring different Gd^{3+} concentrations could be valuable in order to clarify this pressing question from our results.

In ESR, the linewidth ΔH is proportional to $1/T_2$, where T_2 is the spin-spin relaxation time. Hence, using an admixture of absorption and dispersive derivatives to fit the Gd^{3+} ESR line shapes, we can extract ΔH and obtain information about the interaction between the Gd^{3+} $4f$ local moments and their environment; that is, we can extract the ESR spin dynamics. The solid lines in Fig. 3(b) indicate the fit for $x = 0.004$ and 0.02 . In order to exclude crystal field effects, the T dependence

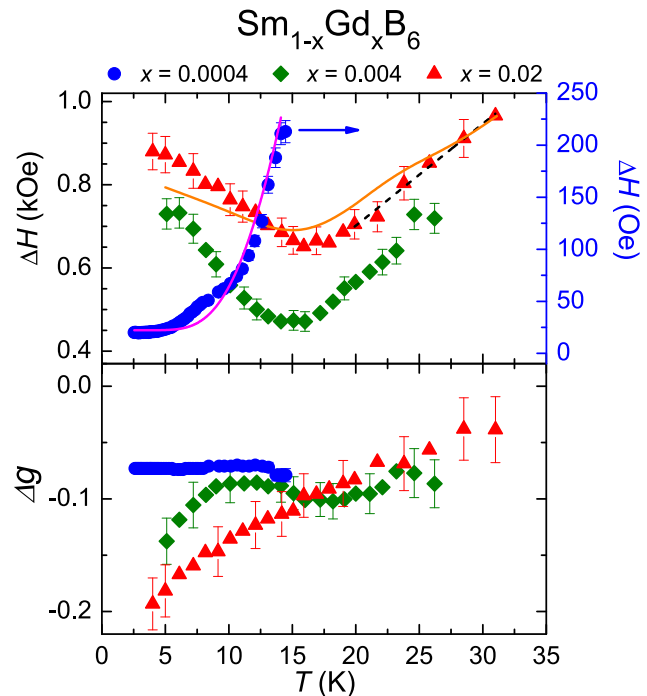


FIG. 4. Top: T dependence of the Gd^{3+} ESR linewidth ΔH for the $\text{Sm}_{1-x}\text{Gd}_x\text{B}_6$ compound with $x = 0.0004, 0.004,$ and 0.02 . While the external magnetic field was applied into the $[100]$ direction for $x = 0.004$ and 0.02 , for $x = 0.0004$ the magnetic field was applied 30° from the $[100]$ direction in the (110) plane (collapsed ESR spectrum). The solid lines are fits explained in the text. The dotted line is a guide to the eye. Bottom: Δg as a function of temperature.

of ΔH for $x = 0.0004$ was obtained when the Gd^{3+} ESR spectrum is collapsed into one resonance [44]. The top panel of Fig. 4 shows the evolution of the linewidth ΔH as a function of temperature.

For the highly diluted $x = 0.0004$ sample, it is possible to observe an exponential dependence of the Gd^{3+} ESR linewidth as a function of temperature. The interconfigurational fluctuation model (ICF) [62–64] shows that the fluctuation between the $4f^n$ and $4f^{n+1}$ configurations of the Sm ions provokes a fluctuating field at the Gd^{3+} site, which explains the exponential increase of ΔH ,

$$\Delta H = \Delta H_0 + bT + Ae^{-E_{\text{ex}}/T}, \quad (2)$$

where ΔH_0 is the residual Gd^{3+} linewidth, b is the Korringa relaxation rate [37,44], E_{ex} is the excitation energy of the Sm ions, and A is a constant. The Korringa relaxation b is related to the spin-flip scattering relaxation mechanism which arises from the interaction between conduction electrons and the Gd^{3+} $4f$ local moments [37,44]. We obtain $b = 0$ Oe/K and $E_{\text{ex}} = 56$ K (magenta solid line), which is, notably, of the order of the hybridization gap [15]. This result is another microscopic hint that Gd^{3+} ions are not introducing extrinsic charge in-gap states when substituting Sm ions in SmB_6 .

Comparing the linewidth ΔH for all samples, we can see a clear difference between the highly dilute system ($x = 0.0004$) and the other two Gd^{3+} concentrations. The relaxation changes dramatically when the Gd^{3+} sites start to

interact, which can be verified in trying to use the same ICF model for $x = 0.02$ (orange solid line). In this case, considering a phenomenological exchange interaction between Gd^{3+} sites with an internal exchange field $H_{\text{ex}} = 20$ Oe [63], we obtain a Korringa relaxation rate $b = 1.5(5)$ Oe/K and $E_{\text{ex}} = 110(10)$ K, which are two times larger than those for $x = 0.0004$. This clearly indicates that the model does not necessarily apply for higher Gd^{3+} concentrations, where the correlation between the metallic islands covers the effect of interconfigurational fluctuations.

As already mentioned, from the admixture of absorption and dispersive derivative fitting we can also extract the Gd^{3+} resonance field H_0 . Consequently, we obtain the Gd^{3+} experimental g value $g_{\text{exp}} = h\nu/\mu_B H_0$, where h is the Planck constant and μ_B is the Bohr magneton. The bottom panel of Figure 4 shows the temperature dependence of Gd^{3+} , $\Delta g = g_{\text{exp}} - g_{\text{insulator}}$, where $g_{\text{insulator}} = 1.993(1)$ for an isolated Gd^{3+} ion [44]. In metals, for the simplest scenario [65–67], the g shift Δg is given by $\Delta g = J_{fs}\eta(E_F)$ [37], where J_{fs} is the effective exchange interaction between the $4f$ local moments and the conduction electrons and $\eta(E_F)$ is the DOS at the Fermi level for one spin direction. Positive g shifts are expected due to the ferromagnetic (atomic) interaction between the $4f$ local moments and s and/or d conduction electrons. Negative g shifts are obtained when the contribution at the Fermi level comes from p and/or f conduction electrons since their magnetic interaction with the $4f$ local moments occurs via a virtual bound state [68] and, consequently, an antiferromagnetic (covalent) exchange interaction appears [37,68]. In the simplest scenario for metals it is crucial to note that the Korringa relaxation b , which is extracted from ΔH T dependence, is also proportional to the exchange interaction between the $4f$ local moments and the conduction electrons. In other words, $b \propto J_{fs}^2 \eta^2(E_F)$ when we neglect \mathbf{q} dependence or multiband effects [37]. Another crucial point is that internal ferromagnetic or antiferromagnetic fields can also shift the resonance field, generating apparent positive or negative g shifts.

$\Delta g = -0.074(2)$ for $x = 0.0004$ is T independent. Since the Korringa relaxation at this concentration is negligible and the spin relaxation is phonon mediated, this negative value most likely is due to the interaction between the Gd^{3+} and $\text{Sm}^{2.6+}$ $4f$ electrons. In other words, our results indicate that there is no relevant overlap between the Gd^{3+} $4f$ and conduction electron wave functions at these investigated temperatures, which is in agreement with our scenario. Since the magnetic contribution of the $\text{Sm}^{2.6+}$ is T independent at this temperature range, it behaves like a constant AFM internal field at the Gd^{3+} site, which is consistent with recent magnetic dichroism results [69]. In this scenario, the AFM net local field at the Gd^{3+} site would be $H^{\text{net}} = 130(5)$ Oe.

For the higher-concentration samples there is a clear decrease of the Gd^{3+} Δg towards low temperatures. This is an indication of an exchange interaction between the Gd^{3+} sites, which is expected to be negative since GdB_6 is an antiferromagnetic compound with $T_N \approx 15$ K [70]. The possibility of Gd-Gd interactions for such small Gd^{3+} concentrations ($x = 0.004$) is also suggested by STS studies which show that defects in SmB_6 have a “healing length” of ~ 2 nm [28]. If we assume that this would also characterize the bulk and not

just the surface, the affected volume around a defect could be of the order of ~ 500 unit cells. It is worth noting that Gd-Gd interaction for $x = 0.004$ and 0.02 is also reflected in the low- T increase of the linewidth, as shown in the top panel of Fig. 4, although this increase does not scale with the Gd^{3+} concentration.

As discussed above, due to the correlation between the metallic regions, the local density of carriers may become mobile and start to play a role in the relaxation mechanism, resulting in a finite value of the Korringa relaxation rate even at lower temperatures for $x = 0.004$ and 0.02 . As a consequence, the Gd^{3+} ESR turns into a single Dysonian line shape with a small Korringa relaxation; that is, the environment changes from insulatorlike to a metalliclike. Although these local effects can be seen, the global hybridization gap is not affected, as shown by dc resistivity data.

This ESR scenario helps us to understand the apparent discrepancy between ac and dc conductivity data [15–18,38]. The local response of the metallic islands will not affect the global hybridization gap due to the lack of percolation; hence, at the dc limit it is only possible to observe an insulating behavior. Recent theoretical models argue that such localized states could produce quantum oscillations in the magnetization, which is a plausible way to understand the presence of quantum oscillations in magnetization and the absence in resistivity [12,38]. Defects, such as Sm vacancies and natural magnetic impurities, are responsible for localized metallic islands, which allegedly could produce such oscillations [71]. Although recent theoretical results indicate that the reported oscillations could be supported by the bulk band structure of this compound [72], our results are also consistent with the emergence of quantum oscillations from bulk impurities [71]. In contrast to this theoretical proposition [72], we should note that SmB_6 does not show a magnetic ordered state at ambient pressure [73,74]. Finally, the Kondo hole scenario for Gd^{3+} is also valid for Eu^{2+} -doped SmB_6 and is a plausible way to explain the scaling as a function of Gd^{3+} concentration in SmB_6 described by Fuhrman *et al.* [29,41].

Our results show that there is a local insulator-to-metal evolution in Gd^{3+} -doped SmB_6 at very low concentrations. This observation was possible only because we are directly probing the Gd^{3+} in the bulk locally.

IV. CONCLUSION

In summary, we performed electron spin resonance and complementary macroscopic measurements in the Kondo insulator $\text{Sm}_{1-x}\text{Gd}_x\text{B}_6$ with $x = 0, 0.0004, 0.004$, and 0.02 . The Gd^{3+} ESR spectra at 4 K for different concentrations showed two clearly different behaviors. For $x = 0.0004$ we observed an insulatorlike Gd^{3+} ESR line shape, while for $x = 0.004$ and 0.02 we obtained a Dysonian metallic line shape, characteristic of a conductive environment. Hence, the hybridization gap at the Gd^{3+} site collapses, which can result in an effective formation of larger metallic islands as a function of magnetic impurity concentration. This scenario is consistent with the observed ESR spin dynamics and shift of ESR g factors. These localized states explain the discrepancy between dc and ac conductivity measurements and can also provide a different point of view regarding quantum oscillations in this

system. Further experiments, such as ESR in “neutral” doping samples, e.g., Gd^{3+} - Sr^{2+} and Eu^{2+} - La^{3+} dopings, and NMR measurements in Gd^{3+} -doped SmB_6 could be valuable to understand the evolution of the metallic islands in more detail.

ACKNOWLEDGMENTS

We acknowledge constructive discussions with C. Rettori and S. M. Thomas. This work was supported by

FAPESP (São Paulo, Brazil) Grants No. 2018/11364-7, No. 2017/10581-1, No. 2016/14436-3, No. 2013/17427-7, No. 2012/04870-7, and No. 2012/05903-6; CNPq Grants No. 309483/2018-2, No. 442230/2014-1, No. 304649/2013-9, and No. 141026/2017-0; CAPES; and FINEP-Brazil. Z.F. acknowledges the funding from NSF Grant No. 1708199. Work at Los Alamos National Laboratory (LANL) was performed under the auspices of the U.S. Department of Energy, Office of Basic Energy Sciences, Division of Materials Science and Engineering.

- [1] M. Dzero, J. Xia, V. Galitski, and P. Coleman, *Annu. Rev. Condens. Matter Phys.* **7**, 249 (2016).
- [2] M. Dzero, K. Sun, V. Galitski, and P. Coleman, *Phys. Rev. Lett.* **104**, 106408 (2010).
- [3] V. Alexandrov, M. Dzero, and P. Coleman, *Phys. Rev. Lett.* **111**, 226403 (2013).
- [4] M. Sundermann, H. Yavaş, K. Chen, D. J. Kim, Z. Fisk, D. Kasinathan, M. W. Haverkort, P. Thalmeier, A. Severing, and L. H. Tjeng, *Phys. Rev. Lett.* **120**, 016402 (2018).
- [5] D.-J. Kim, J. Xia, and Z. Fisk, *Nat. Mater.* **13**, 466 (2014).
- [6] D.-J. Kim, S. Thomas, T. Grant, J. Botimer, Z. Fisk, and J. Xia, *Sci. Rep.* **3**, 3150 (2013).
- [7] M. Neupane, N. Alidoust, S.-Y. Xu, T. Kondo, Y. Ishida, D. J. Kim, C. Liu, I. Belopolski, Y. J. Jo, T.-R. Chang *et al.*, *Nat. Commun.* **4**, 2991 (2013).
- [8] J. Jiang *et al.*, *Nat. Commun.* **4**, 3010 (2013).
- [9] N. Xu *et al.*, *Nat. Commun.* **5**, 4566 (2014).
- [10] S. Wolgast, Ç. Kurdak, K. Sun, J. W. Allen, D.-J. Kim, and Z. Fisk, *Phys. Rev. B* **88**, 180405(R) (2013).
- [11] P. Hlawenka *et al.*, *Nat. Commun.* **9**, 517 (2018).
- [12] B. S. Tan *et al.*, *Science* **349**, 287 (2015).
- [13] G. Li *et al.*, *Science* **346**, 1208 (2014).
- [14] S. M. Thomas, X. Ding, F. Ronning, V. Zapf, J. D. Thompson, Z. Fisk, J. Xia, and P. F. S. Rosa, *Phys. Rev. Lett.* **122**, 166401 (2019).
- [15] Y. S. Eo, A. Rakoski, J. Lucien, D. Mihaliov, C. Kurdak, P. F. S. Rosa, and Z. Fisk, *Proc. Natl. Acad. Sci. USA* **116**, 12638 (2019).
- [16] B. Gorshunov, N. Sluchanko, A. Volkov, M. Dressel, G. Knebel, A. Loidl, and S. Kunii, *Phys. Rev. B* **59**, 1808 (1999).
- [17] N. J. Laurita, C. M. Morris, S. M. Koohpayeh, P. F. S. Rosa, W. A. Phelan, Z. Fisk, T. M. McQueen, and N. P. Armitage, *Phys. Rev. B* **94**, 165154 (2016).
- [18] N. J. Laurita *et al.*, *Physica B (Amsterdam, Neth.)* **536**, 78 (2019).
- [19] M. E. Valentine, S. Koohpayeh, W. A. Phelan, T. M. McQueen, P. F. S. Rosa, Z. Fisk, and N. Drichko, *Phys. Rev. B* **94**, 075102 (2016).
- [20] M. E. Valentine, S. Koohpayeh, W. A. Phelan, T. M. Queen, P. F. S. Rosa, Z. Fisk, and N. Drichko, *Physica B (Amsterdam, Neth.)* **536**, 60 (2018).
- [21] M. H. Hamidian *et al.*, *Proc. Natl. Acad. Sci. USA* **108**, 18233 (2011).
- [22] R. Sollie and P. Schlottmann, *J. Appl. Phys.* **69**, 5478 (1991).
- [23] P. Schlottmann and C. S. Hellberg, *J. Appl. Phys.* **79**, 6414 (1996).
- [24] J. Figgins and D. K. Morr, *Phys. Rev. Lett.* **107**, 066401 (2011).
- [25] H.-F. Lü, H.-Z. Lu, S.-Q. Shen, and T.-K. Ng, *Phys. Rev. B* **87**, 195122 (2013).
- [26] A. Arab, A. X. Gray, S. Nemsak, D. V. Evtushinsky, C. M. Schneider, D.-J. Kim, Z. Fisk, P. F. S. Rosa, T. Durakiewicz, and P. S. Riseborough, *Phys. Rev. B* **94**, 235125 (2016).
- [27] H. Pirie *et al.*, *Nat. Phys.* **16**, 52 (2020).
- [28] L. Jiao, S. Röbber, D. Kasinathan, P. F. S. Rosa, C. Guo, H. Yuan, C.-X. Liu, Z. Fisk, F. Steglich, and S. Wirth, *Sci. Adv.* **4**, eaau4886 (2018).
- [29] W. T. Fuhrman, J. R. Chamorro, P. A. Alekseev, J.-M. Mignot, T. Keller, J. A. Rodriguez-Rivera, Y. Qiu, P. Nikolić, T. M. McQueen, and C. L. Broholm, *Nat. Commun.* **9**, 1539 (2018).
- [30] W. T. Fuhrman and P. Nikolić, *Phys. Rev. B* **101**, 245118 (2020).
- [31] G. Wiese, H. Schäffer, and B. Elschner, *Europhys. Lett.* **11**, 791 (1990).
- [32] J. C. Souza, P. F. S. Rosa, U. Burkhardt, M. König, Z. Fisk, P. G. Pagliuso, S. Wirth, and J. Sichelschmidt, *JPS Conf. Proc.* **30**, 011021 (2020).
- [33] S. Kunii, T. Uemura, Y. Chiba, T. Kasuya, and M. Date, *J. Magn. Magn. Mater.* **52**, 271 (1985).
- [34] K. Kojima, M. Kasaya, and Y. Koi, *J. Phys. Soc. Jpn.* **44**, 1124 (1978).
- [35] G. Feher and A. F. Kip, *Phys. Rev.* **98**, 337 (1955).
- [36] F. J. Dyson, *Phys. Rev.* **98**, 349 (1955).
- [37] S. Barnes, *Adv. Phys.* **30**, 801 (1981).
- [38] Y. S. Eo, S. Wolgast, A. Rakoski, D. Mihaliov, B. Y. Kang, M. S. Song, B. K. Cho, M. Ciomaga Hatnean, G. Balakrishnan, Z. Fisk, S. R. Saha, X. Wang, J. Paglione, and Ç. Kurdak, *Phys. Rev. B* **101**, 155109 (2020).
- [39] S. Sen, N. S. Vidhyadhiraja, E. Miranda, V. Dobrosavljević, and W. Ku, *Phys. Rev. Research* **2**, 033370 (2020).
- [40] M. Orendáč, S. Gabáni, G. Pristáš, E. Gažo, P. Diko, P. Farkašovský, A. Levchenko, N. Shitsevalova, and K. Flachbart, *Phys. Rev. B* **96**, 115101 (2017).
- [41] J. M. Lawrence, T. Graf, M. F. Hundley, D. Mandrus, J. D. Thompson, A. Lacerda, M. S. Torikachvili, J. L. Sarrao, and Z. Fisk, *Phys. Rev. B* **53**, 12559 (1996).
- [42] G. G. Lesseux, P. F. S. Rosa, Z. Fisk, P. Schlottmann, P. G. Pagliuso, R. R. Urbano, and C. Rettori, *AIP Adv.* **7**, 055709 (2017).
- [43] See Supplemental Material at <http://link.aps.org/supplemental/10.1103/PhysRevResearch.2.043181> for additional magnetic susceptibility data and Eu^{2+} ESR spectra.
- [44] A. Abragam and B. Bleaney, *Electron Paramagnetic Resonance of Transition Ions* (Clarendon, Oxford, 1970).

- [45] T. Uemura, Y. Chiba, M. Hagiwara, and M. Date, *J. Phys. Soc. Jpn.* **55**, 3737 (1986).
- [46] T. S. Altshuler and M. S. Bresler, *J. Exp. Theor. Phys.* **88**, 1019 (1999).
- [47] K. Baberschke and E. Tsang, *Phys. Rev. Lett.* **45**, 1512 (1980).
- [48] P. Schlottmann, *Magnetochemistry* **4**, 27 (2018).
- [49] B. I. Kochelaev, *Low Temp. Phys.* **43**, 76 (2017).
- [50] H. A. Buckmaster and Y. H. Shing, *Phys. Status Solidi A* **12**, 325 (1972).
- [51] H. Sturm, B. Elschner, and K.-H. Höck, *Phys. Rev. Lett.* **54**, 1291 (1985).
- [52] P. W. Anderson and P. R. Weiss, *Rev. Mod. Phys.* **25**, 269 (1953).
- [53] F. A. Garcia, P. A. Venegas, P. G. Pagliuso, C. Rettori, Z. Fisk, P. Schlottmann, and S. B. Oseroff, *Phys. Rev. B* **84**, 125116 (2011).
- [54] P. A. Venegas, F. A. Garcia, D. J. Garcia, G. G. Cabrera, M. A. Avila, and C. Rettori, *Phys. Rev. B* **94**, 235143 (2016).
- [55] R. R. Urbano, C. Rettori, G. E. Barberis, M. Torelli, A. Bianchi, Z. Fisk, P. G. Pagliuso, A. Malinowski, M. F. Hundley, J. L. Sarrao, and S. B. Oseroff, *Phys. Rev. B* **65**, 180407(R) (2002).
- [56] G. A. Wigger, C. Beeli, E. Felder, H. R. Ott, A. D. Bianchi, and Z. Fisk, *Phys. Rev. Lett.* **93**, 147203 (2004).
- [57] R. R. Urbano, P. G. Pagliuso, C. Rettori, P. Schlottmann, J. L. Sarrao, A. Bianchi, S. Nakatsuji, Z. Fisk, E. Velazquez, and S. B. Oseroff, *Phys. Rev. B* **71**, 184422 (2005).
- [58] A. Rakoski, Y. S. Eo, K. Sun, and Ć. Kurdak, *Phys. Rev. B* **95**, 195133 (2017).
- [59] B. Skinner, *Phys. Rev. Mater.* **3**, 104601 (2019).
- [60] S. Yeo, K. Song, N. Hur, Z. Fisk, and P. Schlottmann, *Phys. Rev. B* **85**, 115125 (2012).
- [61] G. G. Lesseux *et al.*, *J. Phys.: Condens. Matter* **28**, 125601 (2016).
- [62] L. L. Hirst, *Phys. Kondens. Mater.* **11**, 255 (1970).
- [63] T. Gambke, B. Elschner, and L. L. Hirst, *Phys. Rev. Lett.* **40**, 1290 (1978).
- [64] P. A. Venegas and G. E. Barberis, *Phys. Rev. B* **46**, 911 (1992).
- [65] C. Rettori, S. B. Oseroff, D. Rao, P. G. Pagliuso, G. E. Barberis, J. Sarrao, Z. Fisk, and M. Hundley, *Phys. Rev. B* **55**, 1016 (1997).
- [66] J. G. S. Duque, E. M. Bittar, C. Adriano, C. Giles, L. M. Holanda, R. Lora-Serrano, P. G. Pagliuso, C. Rettori, C. A. Pérez, R. Hu, C. Petrovic, S. Maquilon, Z. Fisk, D. L. Huber, and S. B. Oseroff, *Phys. Rev. B* **79**, 035122 (2009).
- [67] P. G. Pagliuso, C. Rettori, J. L. Sarrao, A. Cornelius, M. F. Hundley, Z. Fisk, and S. B. Oseroff, *Phys. Rev. B* **60**, 13515 (1999).
- [68] D. Davidov, C. Rettori, A. Dixon, K. Baberschke, E. P. Chock, and R. Orbach, *Phys. Rev. B* **8**, 3563 (1973).
- [69] W. T. Fuhrman, J. C. Leiner, J. W. Freeland, M. van Veenendaal, S. M. Koohpayeh, W. A. Phelan, T. M. McQueen, and C. Broholm, *Phys. Rev. B* **99**, 020401(R) (2019).
- [70] S. Kunii, K. Takeuchi, I. Oguro, K. Sugiyama, A. Ohya, M. Yamada, Y. Koyoshi, M. Date, and T. Kasuya, *J. Magn. Magn. Mater.* **52**, 275 (1985).
- [71] H. Shen and L. Fu, *Phys. Rev. Lett.* **121**, 026403 (2018).
- [72] R. Zhang, B. Singh, C. Lane, J. Kidd, Y. Zhang, B. Barbiellini, R. S. Markiewicz, A. Bansil, and J. Sun *et al.*, [arXiv:2003.11052](https://arxiv.org/abs/2003.11052) (2020).
- [73] A. Barla, J. Derr, J. P. Sanchez, B. Salce, G. Lapertot, B. P. Doyle, R. Ruffer, R. Lengsdorf, M. M. Abd-Elmeguid, and J. Flouquet, *Phys. Rev. Lett.* **94**, 166401 (2005).
- [74] Y. Zhou, P. F. S. Rosa, J. Guo, S. Cai, R. Yu, S. Jiang, K. Yang, A. Li, Q. Si, Q. Wu, Z. Fisk, and L. Sun, *Phys. Rev. B* **101**, 125116 (2020).

Appendix K

Scientific Work on Cobalt Based Ludwigites

This appendix brings the paper published on Cobalt Based Ludwigites, performed as a collaboration with Prof. Mucio Continentino and Prof. Daniele Freitas, as described in the main text.

Magnetic Resonance Probing Spin Fluctuations in Cobalt Homometallic Ludwigites

P. Menegasso¹, G. G. Lesseaux², M. A. Continentino⁴, D. C. Freitas³, C. Rettori¹, R. R. Urbano¹

¹*Instituto de Física “Gleb Wataghin”, UNICAMP, Campinas-SP, 13083-859, Brazil*

²*Ames Laboratory and Department of Physics and Astronomy, Iowa State University, Ames, Iowa 50011, USA*

³*Centro Brasileiro de Pesquisas Físicas, Rua Dr. Xavier Sigaud 150 - Urca, 22290-180, Rio de Janeiro, RJ, Brazil*

⁴*Universidade Federal Fluminense, Rua Miguel de Frias 9 - Niterói, 24220-900, Rio de Janeiro, RJ, Brazil*

(Dated: March 5, 2020)

The homo and heterometallic oxyborates were explored via magnetic resonance studies with the main goals to *i*—unreveal the interplay between the metallic ion valence and the absence of magnetic ordering at $\text{Co}_3\text{O}_2\text{BO}_3$ in disagreement with its parent compound $\text{Fe}_3\text{O}_2\text{BO}_3$ and *ii*—to confirm the possibility of a high to low spin transition in the Co homometallic compound which have been recently proposed in the literature [1]. We probed single crystals and powder of $\text{Co}_3\text{O}_2\text{BO}_3$ via nuclear magnetic resonance (NMR) and electron spin resonance (ESR). Our results for $\text{Co}_3\text{O}_2\text{BO}_3$ demonstrate a spin fluctuation crossover from a paramagnetic regime to a phase with short ranged magnetic fluctuations near 80 K, which could be of the very same kind observed for the homometallic $\text{Fe}_3\text{O}_2\text{BO}_3$ [2]. However, the ESR experiments reveal that such transition may be the recent proposed high-spin to low-spin transition on Co3+ sites. *g*-shift also reveal that Co^{2+} is sensitive to an internal field increase around the same transition temperature which is another strong indicative of a local magnetic ordering.

PACS numbers: 76.30.-v, 71.20.Lp

I. INTRODUCTION

Systems with low dimensionality always drew the attention of scientific community due to the realization of non-trivial physical properties, which gets even more interesting in presence of strong electronic correlation (SEC). Examples of systems which couple both phenomena are the high- T_C cuprates [3], organic conductors [4] and more recently the oxyborates ludwigites [5]. The latter has gained a renewed attention through the discovery of charge ordering [6, 7], partial magnetic ordering [2, 8] and non conventional magnetic, structural properties [5, 9–11] and more recently their outstanding property to increase the efficiency of carbon nanotubes for energy storage [12]. The oxyborates compounds have also been intensively investigated both experimentally and theoretically over the last decade due to its unusual magnetic properties, generated by the SEC and also magnetic frustration on the triangular coordination boron site.

Such oxyborates may crystallize in structures of calcite, warwickite, huntite, norbergite and our object of study, the ludwigites (space group $Pb\bar{3}m$) [13, 14]. The latter family consist systems with $\text{M}_2\text{M}'\text{O}_2\text{BO}_3$ in which M and M' are respectively a divalent and trivalent intermetallic ions, both occupying four nonequivalent positions [15]. This 3LL structures leads to low dimensionality and the stacking of such structures features the a -axis. It is believed that M ions presents electronic valence 2+ while M' is 3+. The b -axis follows a zig-zag chain and the c -axis is perpendicular to a and b . A representation of the lattice is shown at Fig. 1. Among the ludwigites, the only homometallic compounds present $M = M' = \text{Fe}$ or Co and besides the structural similarities between them and the chemical equivalence of Fe and Co, they

exhibit different magnetic and electrical properties [16].

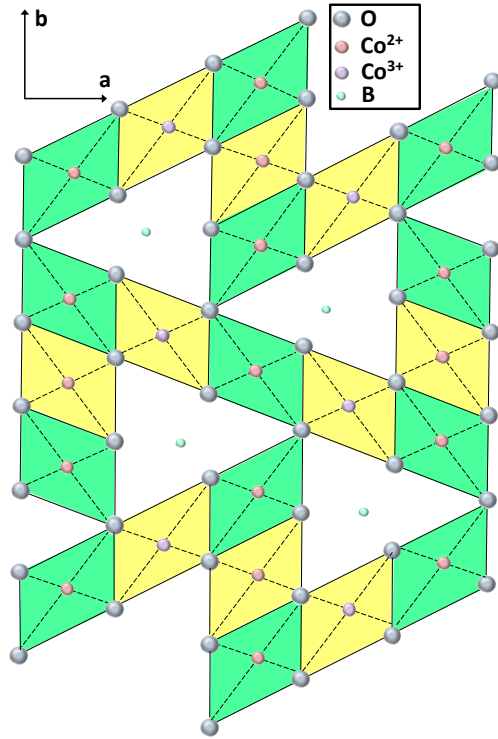


FIG. 1: Structure of $\text{Co}_3\text{O}_2\text{BO}_3$. Oxygen, Cobalt (2+), Cobalt (3+) and boron are respectively represented by blue, red, purple and green spheres. Black lines, both solid and dashed, indicate chemical bonding. The Co ions stands in an octahedral symmetry, thus the CEF favors t_{2g} as the fundamental state. a -axis is featured along the 3LL direction given quasi-one-dimensional character to the compound.

This fact has been intriguing researches of the area since the discovery of homometallic Co compound and so far no satisfactory explanation has been given.

Several studies have been carried out in the mixed region on $\text{Co}_2\text{Co}_{1-x}\text{Fe}_x\text{O}_2\text{BO}_3$ [15, 18] as well. So far, the compounds with Fe are probed to present a charge ordering transition at $T = 283\text{K}$ [15] and also two magnetic sublattices which orders orthogonally at 110 and 70 K [7, 15], which can be explained by the ions electronic valence, stating that the Fe^{3+} orders at higher temperature than the Fe^{2+} . Until now, to the best of our knowledge, the sample with Co show only one magnetic ordering at $T_N = 42\text{K}$ [16] featuring weak ferromagnetism with easy axis along ab plane [19], which presents ferrimagnetism [1]. Also, a high temperature ($T_C = 440\text{K}$) charge ordering state have recently been discovered [17].

The inequivalent magnetic ordering has been considered the most striking difference between both homometallic systems and many efforts have been made to unreveal what mechanism is behind such contrast. Magnetic susceptibility experiments as function of temperature has shown a deviation from Curie-Weiss (CW) law starting at 80 K [16] and also probed the systems to have a AFM ground state. Furthermore, an anomaly at 17K in M versus T was pointed out by Ivanova *et al*[19]. However, any kind of signature was observed at the latter cited temperatures via specific heat measurements [16], indicating that long ranged magnetic ordering is not established. Recent studies on neutron diffraction [1] suggests that Co^{3+} suffers a high to low spin transition, resulting in a low temperature phase with no effective spin on the ion. This scenario would explain the absence of magnetic ordering in ions Co^{3+} .

In this context, magnetic resonance (MR) experiments, both nuclear and electronic, are the *smoking gun* experiment to definitively comprove such scenario. This work aims to study the $\text{M}_2\text{M}'\text{O}_2\text{BO}_3$ behavior via MR for $M = M' = \text{Co}$ and $M = \text{Co}$, $M' = \text{Sn}$ systems. At first glance, ESR experiments was expected to confirm the high to low spin phase transition early proposed by means of analysing the resonances of electrons effective spin.

II. EXPERIMENT

Needle-like single crystals of $\text{Co}_3\text{O}_2\text{BO}_3$ with typical dimensions of $50 \times 50 \times 500 \mu\text{m}$ were obtained by employing the methods described at [16]. The desired crystals were grind, aligned inside a quartz tube and submitted to Q-Band ($f \approx 34\text{GHz}$) ESR experiments on a model Elexsys E500 spectrometer supplied by Bruker equipped with a goniometer and a helium flow cryostat capable of measuring within the range $4 < T < 300\text{K}$, sweeping the magnetic field up to 1,9955 T. The spectra were measured from room temperature (RT) down to 10 K, sweeping the magnetic field from 0 to 18 kG pointing perpendicularly

to the needle direction (a -axis). Angular dependence experiments has been carried out at 30, 60 and 90 K and no anisotropic effect has been observed since such rotation was perpendicular to the easy axis (not shown). The very same assembly was submitted to X-Band ($f \approx 9.4\text{GHz}$) ESR experiments and too much noise has been observed. The single crystals were milled and turned into a powder which was fixed inside the ESR quartz tube. The powder sample presented a higher signal-noise ratio, increasing the quality of the spectra. Similarly, the single crystals of Sn doped ludwigites were milled and dissolved into paraffin for X-band ESR experiments. The paraffin was measured previously to each experiment and provided no spurious ESR signal.

Both single crystals and powder samples have been submitted to NMR experiments in a Redstone spectrometer supplied by Tecmag equipped with an open-cycle Janis cryostat capable of working in the range $4 < T < 300\text{K}$ with 0.01 K precision and with a superconducting magnet capable of producing field up to 12.1 T. The spectra of ^{11}B has been measured in the range $4 < T < 160\text{K}$ sweeping the magnetic field from 1.8 to 8 T at 4 K. The coil used to produce the NMR radio-frequency (RF) pulse was made of AGW 26 eneaed copper wire and kapton tape with diameter of 1.5 mm, length of $\approx 6\text{mm}$ and resonance frequency of 60.2 MHz. NMR signal was obtained using spin-echo pulse sequence [20] due to systems' short spin-spin relaxation time T_2 . ^{11}B Spin dynamics measurements through relaxation times has been carried out for the same temperature range using magnetization saturation method in a permanent field of 4.4 T. NMR data was analysed using MagRes 2000 software.

$\vec{M} \times \vec{H}$ and magnetic susceptibility measurements were carried out in randomly oriented single crystals fixed on paraffin using a comercial SQUID magnetometer supplied by Quantum Design operating in the range $4 < T < 300\text{K}$ and magnetic field up to 7 T.

The powder XRD measurements of the samples were carried out in a Bruker Phaser D2 diffractometer with $\text{Cu K}\alpha$ radiation ($\lambda = 1.5418 \text{ \AA}$) using a zero background silicon plate. Scan range was set from 10-80 degrees with a step size of 0.05 degrees and a count time of 2 s.

III. RESULTS AND DISCUSSION

The NMR results are depicted in Fig. 2a. Outstandingly the ^{59}Co , nucleus known to be quite proper for NMR experiments with gyromagnetic ratio (γ) of 10.03 MHz/T, presented a relatively weak signal with $H_{\text{Res}} = 5.797\text{T}$, with a temperature independent shift of approximately 0.23kG from the expected value for metallic Co. Such a weak signal indicates strong magnetic fluctuation on the site which was probed by spin dynamics experiments on ^{59}Co site with a very short spin-spin relaxation time when compared with solids

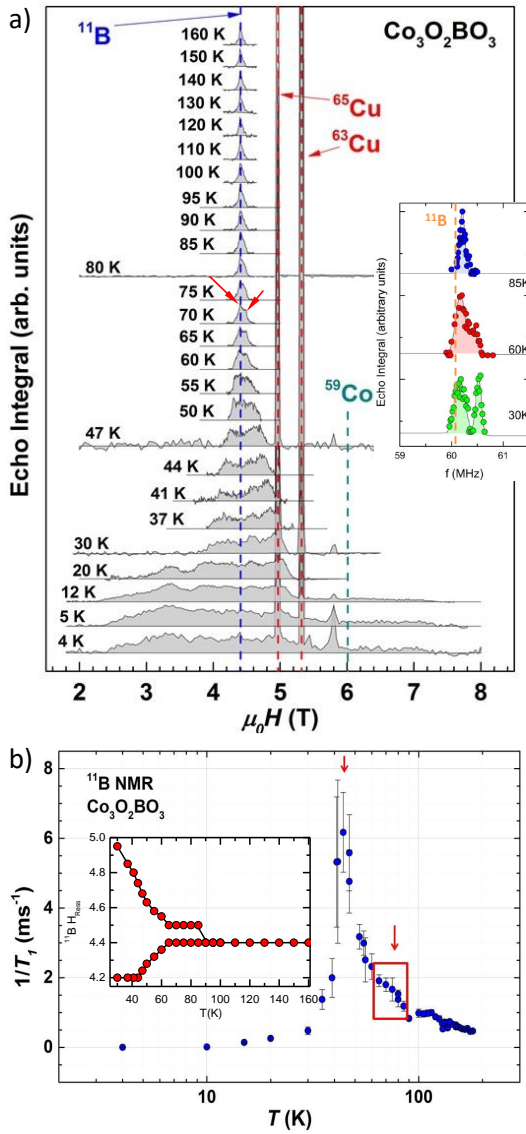


FIG. 2: a) NMR spectra of ^{59}Co and ^{11}B for the range $4 < T < 160$ K. The copper signal is shown at 4 K by means of comparison and the dashed line displays the calculated resonance position using the tabulated values of gyromagnetic ratio. Line broadening is observed below 80 K and provides a clear indication of internal field distribution. The red arrows indicate the line splitting that also happens below 80 K. *Inset*: NMR powder spectra of ^{11}B for 85, 60 and 30 K feature the same observations of SC spectra. b) $1/T_1$ as a function of temperature for ^{11}B . Not only a maximum associated with T_N is observed in 42 K but also a pronounced anomaly in 80 K.

($T_2 \approx 20 \mu\text{s}$). However, the ^{11}B ($\gamma = 13.655 \text{ MHz/T}$) nuclei have proved themselves to be sensitive to the system's magnetism as can be seen in its NMR spectra also presented in Fig. 2a. At 160 K the line width is 255 kHz, and it increases impressively as temperature goes down, specially below 44 K near the AFM phase

transition, indicating internal field distribution.

Below 80 K the line splits into two others, shown by the red arrows at 70 K spectra. Such split is also enhanced as temperature is reduced and indicates that the boron nucleus, given its $3/2$ spin, is under the effect of symmetry breaking, generating inequivalent sites with different local electric fields. The ^{11}B resonance also shows a small chemical shift being close to the expected field, represented by the blue dashed line. The ^{63}Cu and ^{65}Cu arise from the copper coil and are shown at the 4 K spectra for means of comparison.

Spin dynamics experiments on ^{11}B reveal a short spin-lattice relaxation time near T_N , featuring the maximum presented in Fig. 2b as expected. Interestingly, an anomaly at $1/T_1$ is observed at $T \approx 80$ K as shown by the red square in the figure.

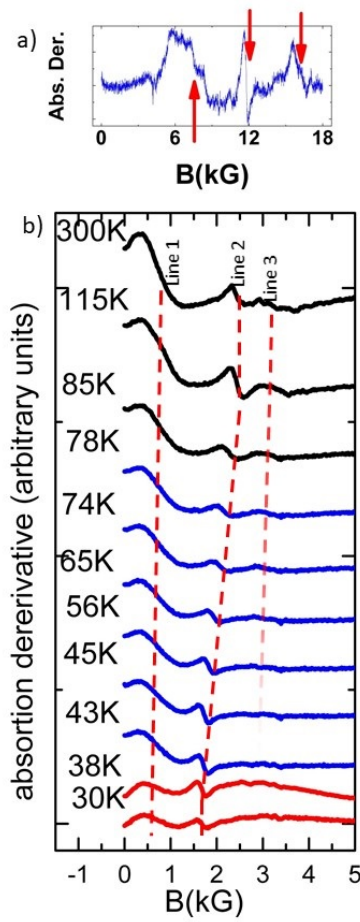
Furthermore, NMR experiments have been carried out in powder samples dissolved in paraffin and the spectra are shown in the inset to Fig. 2a. The same behavior observed in the SCs, with a line split near 80 K and line broadening below 44 K, is presented in the powder spectra. This is an indication that, apart from anisotropic effects, the physical properties remain unchanged due to milling of the crystals.

The same features observed in NMR spectra and spin dynamics are confirmed by ESR experiments. Firstly, even at RT, three resonance lines are observed. The behavior is most like the same for Q-band (Fig. 3)a and X-band (Fig. 3)c. At the figure, the spectra intensity at 275 and 73 K have been multiplied by a factor 20 for visualization reasons. We also measured the $\text{Co}_{2.5}\text{Sn}_{0.5}$ doped sample (not shown) in order to observe the g value ($g = \hbar f / \mu_0 B_{\text{Res}}$) which is close to 2.1, the expected value for Co^{2+} low spin [21], allowing us to prove that the doped sample presents just one valence for Co. In this context, the presence of three resonance lines on a pure sample is a clear indication that more cobalt valences are present. In fact, the number of spins in each X-band resonance was calculated in comparison between the strong pitch and the undoped sample, the given numbers are:

- Line 1: 1.7×10^{18} spins;
- Line 2: 6.4×10^{17} spins;
- Line 3: 2.2×10^{17} spins;

and the estimated total number of spins for the sample measured is in the order of magnitude of 2×10^{18} . It is notorious that line 2 has three times more spins than line 3 which is an indication that these lines may be indeed associated with Co^{2+} and Co^{3+} , since stoichiometrically the first is two times more abundant in the sample leading to conclude that CEF plays an important role for the determination of fundamental physical properties on ludwigites.

Also, by taking the ESR spectra and the fore-given arguments, there is a clear association of the resonance lines 2 and 3 respectively to Co^{2+} and Co^{3+} at high spin



3.jpg

FIG. 3: *a)* ESR Q-band spectra of $\text{Co}_3\text{O}_2\text{BO}_3$ at RT. Three resonance lines ($g = 3.30, 2.11$ and 1.54) are indicated by the arrows. *b)* ESR X-band spectra of $\text{Co}_3\text{O}_2\text{BO}_3$ for the range $30 < T < 300$ K. Three resonance lines ($g = 7.8, 2.8$ and 2.1) are observed even at RT. This three resonances are signatures of an intermediate field scenario as discussed in the main text.

state since the values of g are very closed to the expected ones[21] and line 3 resonance vanishes at ≈ 80 K what could be associated to a high to low spin transition, knowing that at the latter Co^{3+} present zero effective spin, since the octahedral symmetry leads t_{2g} at the ground state and the ion has six electron on d shell. However, there is still the first large resonance line at lower fields (higher g) which is not explained by this scenario, but, X-Ray experiments have been performed (not shown) and found out a tiny contamination (about $1 \mu\text{g}$) of spurious Co_3O_4 , which should be attached to the needle-like samples. We emphasize that, since they are very distinct from the investigated compound on ESR and doesn't present B in the composition for the NMR, such spurious compound is not relevant to our conclusions. Moreover, as the pure sample is cooled, the resonance positions remain constant down to 80 K, temperature in which a shift

is observed for higher values of g as shown by the red dashed lines for resonances 1 and 2.

Due to the weak signal a considerable mass of $\text{Co}_3\text{O}_2\text{BO}_3$ has to be used for ESR experiments ($m \approx 1.0(1)$ mg) and this was harmful for Q-band experiments, leading to a non-optimal coupling between sample and cavity ($Q \approx 400$). For this reason the signal became very unstable in Q-band spectra (not shown) but even so, the very same behavior is observed as shown by the g values dependance with the temperature for the three resonance lines on X and Q-bands, presented in Fig. 4. Also, the

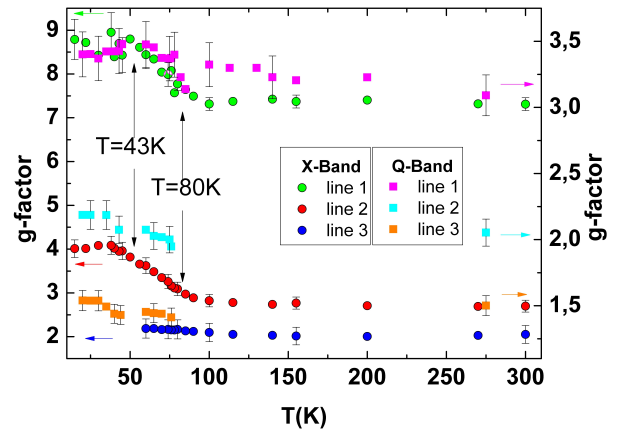


FIG. 4: g values for the three resonances of homometallic ludwigite $\text{Co}_3\text{O}_2\text{BO}_3$ as function of temperature in X- and Q-bands. The values remain constant from RT down to 80 K, in which the values for lines 1 and 2 increase down to 43 K, when a plateau is achieved. The behavior is essentially the same in both bands, as expected, however the values are higher in X-band, indicating dependence with the magnetic field, a fact that favours intermediate field as discussed in the main text.

line shift begins at 80 K and a plateau is reached at $T_N \approx 43$ K for both bands, the resonance presents a scaling behavior. Interestingly enough, the g values are different at X and Q bands, indicating a strong dependence of the resonances with the applied external magnetic field.

Also, the values g_X/g_Q were calculated and some results are presented in table 1.

TABLE I: g_X/g_Q values as function of temperature for the undoped sample 3 resonances at 300 and 30 K.

line #	g_X/g_Q (300K)	g_X/g_Q (30K)
1	2.25	2.57
2	1.33	1.88
3	1.36	1.51 (@60K)

This dependence with external magnetic field strengthens is not clearly understood yet, given that a pure CEF effect would not be dependent on external field even for a systems with strong magnetism as the ludwigites.

Magnetization experiments have been carried out as function of magnetic field up to 4 T with SCs randoly

dispersed at paraffin. Results are depicted in Fig. 5 and reveal paramagnetic behavior for $T > 44$ K, comprovig that the magnetic fluctuations are short ranged and thus undetectable to macroscopic techniques. The inset to the figure displays inverse magnetic susceptibility as function of temperature, measured at 4.4 T. A deviation from Curie-Weiss law starts out at 80 K as shown by the fitted red line, which was expected according to other literature results [16].

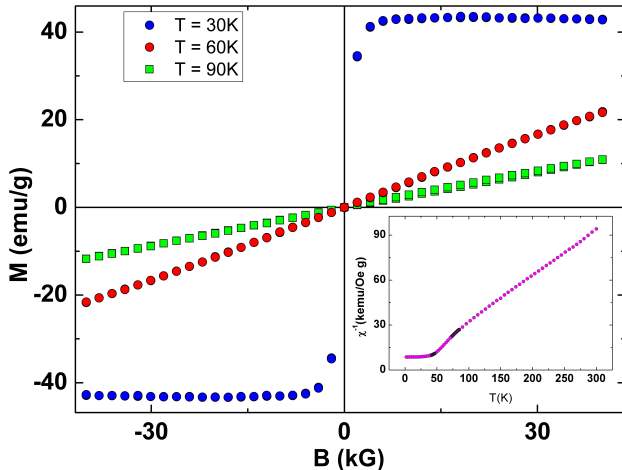


FIG. 5: Magnetization versus magnetic field up to 4 T at 30, 60 and 90 K. SC was randomly dispersed in paraffin and long-ranged magnetic ordering was observed only below T_N . Inset: Inverse susceptibility as function of temperature at 4.4 T. A deviation from CW law was observed.

IV. CONCLUSION

In summary, magnetic resonance experiments presented at this work were pioneers to unveil a crossover to a regime of strong short-ranged magnetic fluctuations in $\text{Co}_3\text{O}_2\text{BO}_3$ in the temperature range $44 < T < 80$ K. Such fluctuations are proved by NMR spin dynamics experiments which reveal a very short spin-spin relaxation time ($T_2 \approx 20 \mu\text{s}$) and an anomaly at spin-lattice relaxation time 80 K that would be the origin of the high spin to low spin phase transition not only on Co^{3+} but in both cobalt sites. However, regardless of the mechanism, the results presented here are the definitive proof of the high-to-low spin phase transition. This result is a fundamental step in order to understand the similarities between Co and Fe homometallic ludwigites since was the first to approximate both via magnetic ordering. The presence of three resonance lines in the ESR spectra indicates an intermediate field scenario in detriment of a high to low spin transition. Furthermore, the different g values between Q and X bands ESR are an evidence of external magnetic field dependence.

V. ACKNOWLEDGMENTS

This work was supported by FAPESP (SP-Brazil) Grants No 2016/14436-3, No 2012/05903-6, CNPq Grants No xxxxxxxx CAPES and FAPERJ (RJ-Brazil) Grants No xxxxxxxx. The authors acknowledge Carlos Galdino, Eduardo Granado and Pascoal Pagliuso for valuable physical discussion on the subject.

- [1] D. C. Freitas, C. P. C. Medrano, D. R. Sanchez, M. Nuñez Regueiro, J. A. Rodriguez-Velmazn, M. A. Continentino, Phys. Rev. B **94** 174409 (2016).
- [2] J. C. Fernandes, R. B. Guimarães, M. A. Continentino, L. Ghivelder, R. S. Freitas, Phys. Rev. B **61** R850(R) (2000).
- [3] J. G. Bednorz, K. A. Müller, Zeitschrift für Physik B Condensed Matter **64**, 189 (1986).
- [4] H. Seo, J. Merino, H. Yoshioka, M. Ogata, J. Phys. Soc. Jpn. **75** 051009 (2006).
- [5] M. A. Continentino, J. C. Fernandes, R. B. Guimarães, B. Boechat and A. Saguia, *Frontiers in Magnetic Materials* Springer, Berlin, p. 385 (2005).
- [6] M. Mir, R. B. Guimarães, J. C. Fernandes, M. A. Continentino, A. C. Doriguetto, Y. P. Mascarenhas, J. Ellena, E. E. Castellano, R. S. Freitas and L. Ghivelder, Phys. Rev. Lett. **87**, 147201 (2001).
- [7] P. Bordet and E. Suard, Phys. Rev. B **79**, 144408 (2009).
- [8] R. B. Guimarães, M. Mir, J. C. Fernandes, M. A. Continentino, H. A. Borges, G. Cernicchiaro, M. B. Fontes, D. R. S. Candela and E. Baggio-Saitocitch, Phys. Rev. B **60**, 6617 (1999).
- [9] M. Angst, P. Khalifah, R. P. Herrmann, H. J. Xiang, M.-H. Whangbo, V. Varadarajan, J. W. Brill, B. C. Sales and D. Mandrus, Phys. Rev. Lett. **99** 086403 (2007).
- [10] I. Leonov, A. N. Yaresko, V. N. Antonov, J. P. Attfield and V. I. Anisimov, Phys. Rev. B **72**, 014407 (2005).
- [11] I. Leonov, A. N. Yaresko, V. N. Antonov, J. P. Attfield and V. I. Anisimov, Phys. Rev. B **74**, 176402 (2006).
- [12] E. Fabbri, A. Haberer, K. Waltar, R. Kotz, and T. J. Schmidt, Cat. Sci. Tech. **4**, 3800 (2014).
- [13] R. Norrestam, K. Nielsen, I. Sotofte and N. Thorup, Z. Kristallog. **189**, 33 (1989).
- [14] J. C. Fernandes, R. B. Guimarães, M. Mir, M. A. Continentino, H. A. Borges, G. Cernicchiaro, M. B. Fontes and E. M. Biaggio-Saitivich, Physica B **281**, 694 (2000).
- [15] J. Bartolom, A. Arauzo, N. V. Kazak, N. B. Ivanova, S. G. Ovchinnikov, Yu. V. Knyazev and I. S. Lyubutin, Phys. Rev. B **83**, 144426 (2011).
- [16] D. C. Freitas, M. A. Continentino, R. B. Guimarães, J. C. Fernandes, J. Ellena and L. Ghivelder, Phys. Rev. B **77**, 184422 (2008).
- [17] C. W. Galdino, D. C. Freitas, C. P. C. Medrano, R. Tartaglia, D. Rigitano, J. F. Oliveira, A. A. Mendonça, L. Ghivelder, M. A. Continentino, D. R. Sanchez, and E. Granado, Phys. Rev. B
- [18] N. B. Ivanova, N. V. Kazak, Yu. V. Knyazev, D. A. Velikanov, L. N. Bezmaternykh, S. G. Ovchinnikov, A. D. Vasiliev, M. S. Plutunov, J. Bartolom and G. S. Patrin, J. Exp. Theor. Phys. **113**, 1015 (2011).

- [19] N. B. Ivanova, A. D. Vasil'ev, D. A. Velikanov, N. V. Kazak, S. G. Ovchinnikov, G. A. Petrakovskii and V. V. Rudenko, *Phys. Solid State* **51**, 966 (2007).
- [20] E. L. Hahn, *Phys. Rev.* **80**, 580 (1950).
- [21] A. Abragam, B. Bleaney, *Electron Paramagnetic Resonance of Transition Ions*, Clarendon Press, Oxford (1970).

Appendix L

Scientific Events

During this thesis, a lot of works have been submitted to different Scientific Conferences. I attended personally only to the first one, however, was directly involved in the work presented on the other ones by co-authors. Also, I'm inserting some of the conferences in which we had the works approved but didn't attend, mainly last year due to the Covid-19 pandemic.

1 - International Conference on Strongly Correlated Electron Systems (SCES-2017), from 17th to 21st July 2017, in Prague, Czech Republic, where a poster was presented with the title: Magnetic ordering of $\text{Co}_3\text{O}_2\text{BO}_3$ ludwigite via magnetic resonance. Authors: P. Menegasso, G. Lesseux, D. Freitas, M. Continetino, C. Rettori, and R. R. Urbano.

2 - XXIII Latin American Symposium on Solid State Physics (SLAFES), from 10th to 13rd April 2018, Bariloche, Argentina (presented by M. Cabrera-Baez). Poster: Surface Effects in -NaYF_4 nanoparticles: A NMR study. Authors: T. B. de Queiroz, M. Cabrera-Baez, E. D. Martínez, P. Menegasso, A. Garcia-Flores, R. R. Urbano, e C. Rettori.

3 - American Physics Society March Meeting 2019, from 4th to 8rd March 2019, Boston, United States (presented by Z. Wang). Poster: NMR Studies of Nematicity in TmVO_4 and TmAsO_4 . Authors: Z. Mei, Z. Wang, P. Menegasso, P. Massat, I. Fisher, N. Curro

4 - International Conference on Strongly Correlated Electron Systems (SCES-2019), from 23rd to 28th September 2019, Okayama, Japan (Withdrawn), the poster submitted was: Effects of Nd doping in CeMIn₅ (M = Rh and Ir): an NMR study. Authors: P. Menegasso, Z. Wang, T. Kissikov, P. Pagliuso, N. Curro, and R. R. Urbano.

5 - Magnetism and Magnetic Materials Conference (MMM-2019), from 4th to 8th November 2019, in Las Vegas, United States (not attended), the poster submitted was: Effects of Nd doping in CeMIn₅ (M = Rh and Ir): An NMR study. Authors: P. Menegasso, Z. Wang, T. Kissikov, P. Pagliuso, N. Curro, and R. R. Urbano.

6 - Encontro de Outono SBF 2020, postponed, Bonito, Brazil (Withdrawn). Poster: Magnetic Resonance Probing Spin Fluctuations in Cobalt Homometallic Ludwigites. Authors: P. Menegasso, G. Lesseux, M. Continetino, D. Freitas, C. Rettori and R. R. Urbano.

7 - Encontro de Outono SBF 2020, Bonito, Brazil (presented by D. Zau). Poster: Novel NMR studies on i-Y-Cd quasicrystal and its approximant YCd₆. Authors: D. Zau, P. Menegasso, M. Cabrera-Baez, C. Rettori, R. R. Urbano.

8 - Encontro de Outono SBF 2020, Bonito, Brazil (presented by K. Barbosa). Poster: Effects of magnetic impurities in superconducting La_{3x}Gd_xIr₄Sn₁₃. Authors: K. Barbosa, I. Bianchi, P. Menegasso, C. Rettori, M. Avila, F. Ferreira, and L. Mendonça-Ferreira